CHAPTER 6

SLAG RESISTANCE OF MAGNESIA-GRAPHITE COMPOSITES

6.1 Introduction

Magnesia-carbon (graphite) bricks have found wide practical applications as refractories for steelmaking furnaces by virtue of their excellent resistance to thermal shock and corrosion resistance to slags. The improvement in thermal shock resistance when graphite is added to an oxide refractory has been discussed in the previous chapter, and here we review some current thoughts as to how graphite improves the corrosion resistance of the magnesia-graphite brick. Furthermore, the results of limited experiments carried out in this work on slag attack of composites containing 80 parts magnesia, 20 parts graphite, of different types, and 5 parts pitch, using a static reaction test method at 1500°C and 1650°C are reported. An industrial steel slag was used in these tests.

However, before discussing the possible slag attack mechanisms in the magnesia-graphite composites, it is appropriate to describe briefly the fundamental principles of slag attack on refractories in general.

6.1.1 Slag Attack of Refractory Materials

Oxide refractories are readily wetted by most slags, which are mixtures of oxides themselves. However, liquid metals have higher surface energies than most solid oxides and therefore the interfacial energy between the solid oxide refractory and the liquid metal is high and therefore liquid metals do not wet and spread on the oxide[89]. Since the slag wets the refractory oxide, it will penetrate into the pore structure by capillary suction.

The wetting of a solid surface by a liquid is determined by the surface energies involved. For example, consider the situation of a drop of liquid on a surface as shown in Figure 6.1.1. At equilibrium, in surface tension terms, the energy balance is given as:

$$\gamma_{SV} = \gamma_{SL} + \gamma_{LV} \cos \theta$$

where γ_{SV} is the solid-vapour interfacial energy of the system;
γ_{SL} is the solid-liquid interfacial energy;
γ_{LV} is the liquid-vapour interfacial energy; and
θ is the contact angle.

Because the sign of cos θ changes as θ passes through 90°, this equation applies whether the liquid wets the solid ($\theta < 90°$) or does not wet the solid ($\theta > 90°$)[90]. "It can be seen that wetting is determined by whether the solid-liquid interfacial energy is greater or less than the solid vapour interfacial energy, and the degree of wetting depends on the value of the liquid-vapour interfacial energy".[90] Kingery[89] and Budworth[90] give a relationship between the surface energies in the system and explain that the "relationships between the surface energies determine the wetting behaviour and spreading tendency according to a spreading coefficient S:

$$S_{SL} = \gamma_{SV} - (\gamma_{LV} + \gamma_{SL}) \ .$$

For spreading to occur, it is necessary that S_{SL} be positive". The degree of wetting, given by θ, the contact angle, does, however, depend on the liquid-vapour interfacial energy.

Figure 6.1.1(a) illustrates a situation where the liquid does not wet the solid, in which case $\gamma_{SV} > \gamma_{SL}$, i.e. $\theta > 90°$, while Figure 6.1.1(b) illustrates the wetting of a solid by a liquid, i.e., $\gamma_{SV} < \gamma_{SL}$ and $\theta < 90°$.

The effect of liquid-vapour interfacial energy and the wetting angle on liquid penetration, in this case slag, into a network of capillary system is best explained by considering how the capillary action draws slag into the pore structure of the refractory. The suction pressure of one cylindrical capillary is given by the equation:

$$P = \frac{2\gamma_{LV} \cos \theta}{r}$$

where P is the suction pressure, r is the radius of the capillary, γ_{LV} is the liquid-vapour interfacial energy. The rate of penetration will depend on the contact angle, the viscosity of the liquid (γ_{LV}) and the pore structure of the matrix, in addition to the hydrostatic head of the slag.

The descriptions above have indicated briefly how an oxide is wetted by a slag. However, the slag attack of oxide refractories in practice is more complicated than can be presented in mathematical equations. Several mechanisms are known to be at play when a slag is in contact with a refractory oxide. Cooper[91] argued that corrosion of oxide refractories by slags often occurs, not by dissolution or evaporation of the oxide, but by the penetration of the solid by some, or all, of the species from the fluid. The liquid phase may be pulled into the open porosity of the solid by capillary forces, as already discussed above, and species from the fluid will diffuse both down the grain boundaries and into the bulk of the solid. Therefore, such processes can cause deterioration of the solid by:

(a) completely encasing a volume of the solid by the liquid phase and this will cause the solid to be washed into the dynamic liquid;

(b) causing either an expansion or contraction of the solid with the associated development of the stresses and ultimately fracture, hence spalling of the refractory not by thermal gradient, but by virtue of introducing foreign matter in the structure, which inevitably changes the linear thermal expansion coefficient of the refractory. This phenomenon has been observed before in checker bricks[92] and basic oxygen furnace refractories[93] ; for instance, where the deterioration of the bricks were observed to be due to the presence of foreign matter;

(c) introduction of species in the structure which may cause the change of the chemistry in the refractory. This may be in the form of changing the calcium/silica molar ratio (C/S) away from the controlled value which may result into the reduction of the hot modulus of rupture due to the formation of low melting phases in the refractory.

The above sections have briefly outlined some of the mechanisms by which slags corrode refractory oxides in general and the fundamental principles which lead to the corrosion of refractories by slags have been indicated. It is therefore necessary at this point to review some of the literature available on the corrosion mechanisms of magnesia-graphite refractories by slags in the steelmaking plants.

6.1.2 Slag corrosion of magnesia-graphite refractories

It was recognised in the early 1970s that the presence of residual carbon from pitch contributed to the resistance of slag attack by physically occupying the interstices of the refractory grains which would otherwise be empty in the absence of pitch. It was also proposed then that because the carbon is not wetted by the slag, penetration of the slag could not take place as θ was greater than 90° and therefore capillary suction pressure will be low (see Section 6.1.1). It was further proposed[94] that the presence of residual carbon suppresses the penetration of iron oxide from the slag into the refractory, which would form low melting calcium ferrite eutectics by reacting with CaO in the refractory, e.g., in dolomite blocks. A proposal was further made[94,95] that the residual carbon reduces iron oxide in the slag to metallic iron which itself is unreactive to the refractory. However, the wear of these refractories was thought to be accompanied by decarburization of the residual carbon[94], which is precisely what would be expected if the above mechanism is correct.

Some five years ago, Cooper[96] demonstrated the non-wetting characteristics of natural flake graphite by a molten slag. He showed globules of flux stand, without spreading, on graphite flakes after heating to 1500°C. In the refractory industry, it is now accepted that natural flake graphite improves the corrosion of the composite brick in which it is contained by inhibiting infiltration of the molten slag. However, various interpretations still exist as to how this improved resistance to infiltration of the slag into the composite comes about. To date, there are six theories which have been advanced to explain this phenomenon. These theories are listed below and no attempt will be made to describe these processes in detail as this is beyond the scope of this work:

(a) The reduction of iron oxide to metallic iron by the carbon in the brick, and since iron is unreactive to a ceramic oxide it will inhibit any further penetration of any melt after the iron itself has solidified in the brick matrix on reaching the colder parts of the brick[95] .

(b) As discussed above, natural flake graphite is not wetted by most of the molten slag. Therefore, any infiltration by the slag into the composite will physically be blocked by this mechanism, as long as graphite is not oxidized[96,97,98].

(c) The reduction of Fe_2O_3 to FeO by the carbon in the brick. In this process ferric oxide (Fe_2O_3) which has a lower contact angle on MgO is reduced to ferrous oxide (FeO) by the carbon monoxide produced by the partial oxidation of the carbon phase in the brick[99] . Ferrous oxide has higher contact angle than Fe_2O_3 on MgO and by increasing the contact angle the infiltration of the slag into the magnesia brick is reduced.

(d) The CO produced in the carbon containing brick due to partial oxidation of the carbon phase in the brick produces high pressures which prohibit the penetration of the slag by virtue of pressure build-up in the brick[99,100].

(e) Pressure build-up due to reduction of MgO and C into gases. Here the slag penetration is inhibited again by the pressure produced from CO which itself reduces MgO to Mg gas and this pressure, as in (d), is thought to hold back any possible slag penetration from the hot surface[101].

(f) Inhibition of penetration of slag by the dense layer of MgO. In this mechanism, the reduced MgO to Mg gas diffuses towards the hot face where the oxygen partial pressure is higher and the Mg vapour is reoxidized to MgO to form a dense layer (non-porous) of MgO behind the hot face of the brick, effectively sealing off any further slag infiltration beyond this layer[102] These mechanisms have been summarized by Barthel et al.[103] and are shown as Figure 6.1.2.

The mechanisms of corrosion of carbon-containing refractory bricks indicated above are complex and many and cannot therefore be studies in real environment. Further, some of these mechanisms, in addition to many other factors, may be taking place simultaneously during service. Therefore, slag attack mechanisms are best studied in laboratories in which variables can be controlled. The section below lists some of the methods used in research laboratories to investigate various slag attack mechanisms.

6.1.3 Laboratory Slag Tests

The service lives of steelmaking refractories vary greatly and depend mainly on the quality of the refractory, the composition of the slag and the operating conditions in general, such as melting time, temperature, agitation of molten slag and metal. All these variables cannot be studied simultaneously, therefore laboratory tests are carried out in which measurements and process and slag attack mechanism variables can be controlled precisely, making it possible to determine the controlling mechanism of the process than it would have been in the field. It follows then that if the effect of corrosion mechanism variables, refractory composition or properties are known, then the lifetime of the refractory lining in the field may possibly be predicted.

The disadvantages with laboratory tests, however, are that the tests are conducted over a short period of time and it is, therefore, not possible to duplicate actual operation practices and conclusions and results so obtained may not be reliable, because, as already pointed out earlier on, the number of variables affecting refractory life can be enormous in real practice. This problem is usually overcome by establishing industrial and research and development laboratories in which the research laboratory results can be put to the test in a semi-industrial practice. The laboratory slag test methods which are commonly used are listed below.

Slag test methods can be divided into two parts[104]; static and dynamic tests. The static slag tests are those in which the slag is not moving while the dynamic tests are those in which the slag is moving about on the test specimen.

6.1.4 The Static Slag Test Methods

The following are some of the static test methods carried out on refractory test specimens in laboratories:

(a) The reaction test method[105] in which the specimen is examined whether it reacted with a slag or not;

(b) The cup test method[104,105]. This is the method which was used in this part of the work and will be described in detail in Section 6.1.6 later.

(c) The static "pencil" or "finger" slag test[104] is that in which the "pencil" is dipped in a molten slag at a test temperature and the specimen is examined whether a reaction with the slag and penetration of the slag occurred, or not.

6.1.5 Dynamic Slag Test Methods

The dynamic methods used for slag attack tests are listed below as well:

(a) The rotating pencil test[106,107,108,109] in which the pencil-like specimen is moved about in the slag at the test temperature.

(b) The drip test method involves dripping of a melted slag on the refractory test piece[110].

(c) Rotating furnace slag test. This method involves lining a furnace with test specimens and when the slag is melted, the furnace is rotated about its axis as long as is required [111].

In this work, cup test method was used to test slag resistance of various specimens containing the same amount of graphite but of different types. This method is described fully in the following section.

6.1.6 The Cup Test Method

This test is usually performed by drilling a hole part-way through a brick or specimen, filling the hole with a slag, and then firing the brick to the test temperature for a few hours. The specimen is then cut in half through the longitudinal axis of the hole. The reaction zone is examined using various techniques, such as, reflected light microscopy, X-ray diffraction (XRD), etc. Because the test is isothermal and the amount of slag is small, no convection currents are set up, and the test is essentially static; therefore slag attack on a new brick surface proceeds comparatively quickly to start with, but later on, it is usually retarded by the reaction products which prevent the reaction between the slag and the brick. However, a lot of data can be obtained to help, mostly, eliminate unsuitable brick or specimen. The examination of the slagged specimen is usually intended to establish:

(a) whether or not the slag wetted the refractory, i.e., infiltration did or did not take place in the brick;

(b) whether the slag was absorbed into the pores more by one refractory than by another, due to differences in pore size distribution, type of the refractory, microstructure texture, etc;

(c) whether all the liquid slag was absorbed in the brick matrix or whether it rapidly penetrated the brick. The depth of penetration may be established.

(d) whether shrinkage or expansion accompanied the reaction, giving an indication to the vulnerability of the brick to thermal spalling during service;

(e) whether bloating or other signs of gas evolution occurred; and

(f) what new phases were formed.

From this method valuable information can be extracted to help in establishing the likely chemical behaviour of the brick when in contact with the molten slag used in the test at the test temperature.

Because of the ease with which cup test slag tests can be conducted, in addition to the limited time in this work, limited slag test experiments, using the cup test method, were carried out on the magnesia-graphite composites at two test temperatures, 1500°C and 1650°C. The sections below describe the experimental work carried out and the discussion of the results.

6.2 Slag Test Experiments on the Magnesia-Graphite Composites

In this part of the work, the composition of the composites was kept constant at 80 parts MgO + 20 parts graphite and 5 parts pitch, but different types of graphite were used. All the five graphites used in the strength test measurements were used in making slag test specimens separately. Furthermore, only two extreme n-values, i.e. $n = 0.3$ and 1.0, were used because at these n-values, the physical properties and the observed microstructural texture, as already discussed in the previous two chapters, were found to be significantly different due to large percentage variations of the quantities of fine magnesia fractions between the two n-values. These experiments were intended to investigate whether composites containing different types of graphite reacted differently with the slag at the same n-value and at the same test temperature. Furthermore, the experiments were aimed at investigating the effect of varying the size of magnesia grains in the composite by varying n-value, hence examining the effect of microstructural variation on slag attack resistance by examining the amount of penetration and/or reaction of the slag after firing at the test temperature.

The slag used in this work was an industrial stainless steel melting slag obtained from British Steel Corporation (BSC) indicated to have come from "an ex-BSC small plant with a mark number 161R". The slag was supplied together with its chemical analysis and this is shown in Table 6.2. When this slag was analysed, as-received and after firing in a reducing atmosphere, by X-ray technique, the major phases detected in both cases were gehlenite in solid solution with akermanite ($2CaO.Al_2O_3.2SiO_2$ + $MgO.2CaO.2SiO_2$), fosterite ($2MgO.SiO_2$), lime (CaO), magnesio chromite ($MgO.Cr_2O_3$), MgO, iron oxide (hematite), iron (α-phase), calcium iron oxide (CaO.FeO), alumina (Al_2O_3).

6.2.1 Specimen Preparation

All specimens were prepared by Method 3 described in Section 4.2.2(iii) of Chapter 4. Two specimens containing the same type of graphite were tested for slag resistance at each of the two temperatures, 1500°C and 1650°C.

6.2.2 Mixing and Pressing of the Specimens

The mixing of the composites was carried out as described in Section 5.3.3.1(b) of Chapter 5 and after mixing, 50 g batches were weighed out and pressed into cylindrical discs, as described in Section 4.2.4(ii), but now an attachment was made to the plunger of the pressing die so that the pressed discs had holes half-way through the specimen formed *in situ* at the centre of the cross-sectional area of one of the flat surfaces in which a slag was to be filled in.

After pressing, the specimens were put into the oven, set at 110°C, and left there for 24 h before being filled with the slag ready for firing. To increase the amount of slag that could be filled in the specimen hole, the slag was pressed into cylindrical discs as well in a pressing die whose plunger diameter was equal to the diameter of the hole. After several experiments, it was found that 10 g slag discs could just fill the hole of the test specimens.

6.2.3 Firing of the Specimens

After fitting the slag discs in the test specimens, the specimens were fired in the same manner as described in Section 5.3.3.4 of Chapter 5.

The specimens which were fired to 1650°C were first fired to 850°C, as described in Section 4.2.6(ii) of Chapter 4 and then fired to 1650°C in a gas furnace, made available to the author with kind permission of the Dyson Group Research and Development Laboratories, Sheffield, UK, and soaked for 3 h at temperature before switching off the furnace and cooling to room temperature.

6.2.4 Preparation of Specimens for Microscopic Examination

The fired specimens were cut in half and then mounted in Araldite as described in Section 4.3. The specimens were mounted in such a way that the cut surface was to be the polished surface to enable examination of the entire length of the cut surface. Plate 6.2.4 shows the cut surfaces of two specimens and the features in this plate will be discussed later.

6.3 Results and Discussion

The effect of the slag on the composites was evaluated qualitatively using reflected light microscopy, scanning electron microscopy (SEM) and in some specimens, X-ray diffraction (XRD).

Plate 6.2.4 shows two specimens of the same composition and type of graphite, A, at $n = 1.0$, but reacted at two different temperatures, 1500°C and 1650°C. Specimen No. 1 is that reacted at 1500°C and No. 2 at 1650°C. Specimens No. 1(a) and 2(a) show the plan view, showing where the slag was, while specimens No. 1(b) and 2(b) show the cut surfaces.

The cut surfaces of the specimens reacted at 1500°C show that there was no penetration of the slag or the slag was too viscous to infiltrate into the brick matrix. Specimens reacted at 1650°C still show a slag/ specimen boundary but diminished. From visual inspection of these plates it is not possible to say whether the slag did or did not penetrate the specimen matrix. What is also interesting to note is that specimen,1(a), seems to show that the slag is about to flow over the specimen. This view is confirmed by 2(a), reacted at 1650°C, in which the slag has covered the flat surface of the specimen. This situation could only arise if the slag is unable to infiltrate the brick matrix and would therefore rise to the top by capillary action. This view is confirmed by the cut surfaces which show that the centre of the cup does not have more slag than the walls of the cup as it would be expected if the slag remained in the cup during firing. However, the slag cannot rise to the top by capillary suction because it does not wet the graphite, unless the area immediately in contact with the slag does not contain graphite. As Plate 6.2.4 shows, the slag rose to the top and therefore it is reasonable to argue that the inner walls of the cup containing the slag had their graphite removed by oxidation of the graphite by the gases from the slag at the time of melting before reaching "equilibrium" conditions at the test temperature.

The other mechanism by which the amount of slag could have been reduced at 1650°C, is by reduction of some of the oxide phases to gaseous phases, such as Mg, SiO, etc., by the coke in which the specimens were covered. The coke particles were in direct contact both with the specimens and the top part of the slag sample discs inserted in the holes of the test specimens. Further, some of the slag which was in direct contact with graphite flakes could have been reduced in a similar manner.

6.3.1 Specimens Containing MgO only and MgO + Pitch

To investigate the effect of graphite on slag resistance, it was necessary to test the effect of this slag on specimens without graphite. This was achieved by preparing specimens containing different grain size magnesia fraction mixtures only and magnesia mixtures with pitch.

Plates 6.3.1(i)(a) and 6.3.1(i)(b) show slagged specimens of magnesia compacts at n = 0.3 and n = 1.0 respectively, reacted at 1500°C. The specimens containing a large amount of fine magnesia (Plate 6.3.1(a)) show a lot of magnesia grains floating in the slag. Two mechanisms of slag attack can be inferred here. Firstly, the magnesia grains are detached from the matrix by the penetration of the slag between grain boundaries and the species in the infiltrate react with the silicate impurities in the grain boundaries of the magnesia grains, producing a high amount of liquid phase which otherwise would have been very low. Then the erosion of the grains takes place. Secondly, once these grains are floating in the molten slag, dissolution of the grains takes place. This is clearly demonstrated by the rounding off of the edges of the grains floating in the slag.

Plate 6.3.1(i)(b) is also that of magnesia compacts only but prepared at n = 1.0 and reacted at 1500°C. The slag has penetrated the matrix but there is a definite slag line at the contact point, implying that the slag penetration has been inhibited more than it was with specimens prepared at n = 0.3. This is, presumably, due to large magnesia grains which do not present a large surface area for the reactions described above to take place efficiently.

The bright phase, round white globules, is metallic iron (Fe) reduced by the coke, since all specimens were covered in coke during firing. The dentritic phase in the slag contains several phases detected by X-ray analysis. When the slag/specimen interface was X-rayed the following phases were detected:

(a) Magnesium oxide (MgO) had the strongest relative intensities, obviously from the specimen.

(b) Gehlenite in solid solution with akermanite, i.e. $2CaO.Al_2O_3.SiO_2$

+ $MgO.2CaO.2SiO_2$ respectively. This phase had the second strongest relative intensities to those of MgO lines.

(c) Monticellite ($CaO.MgO.SiO_2$) had the largest number of d-values detected and had the third strongest relative intensities.

(d) Di-calcium ferrite was also detected with only 3 to 4 lines observed.

(e) Magnesium chromium oxide was difficult to confirm because only 2 lines were detected.

Quite clearly the slag, when in contact with MgO, produced almost as many phases as when received, see Section 6.2. Perhaps the significant development is the formation of monticellite which is a low melting phase at the expense of fosterite which has disappeared completely, but detected in the slag before the reaction test was carried out.

Plates 6.3.1(i)(c) and (d) show the specimens of magnesia + pitch prepared at $n = 0.3$ and $n = 1.0$ respectively and reacted at 1500°C. Plate 6.3.1(i)(c) shows that there is slight reduction in the reaction between the slag and the magnesia, at least on this micrograph. Although this specimen had a very high amount of fine magnesia grains ($n = 0.3$), the slag/specimen interface is clearly visible (compare this with Plate 6.3.1(i)(a)). As before, the bright phase is metallic iron and the dendritic phase contains many phases, as discussed above.

Plate 6.3.(i)(d) is for the specimen of MgO + pitch at $n = 1.0$. The plate emphasizes the point that the slag will infiltrate easily between the grains and corrode the smaller grains which may be providing the necessary grain-to-grain contact which keeps the structure firm, as there is no chemical bond between the grains coated with pitch, as

discussed in the previous chapter. It follows then that if these areas were occupied by a non-reactive phase with the slag, then the slag resistance of the brick could be improved upon, since large magnesia grains are not easily corroded. With the extent of slag attack observed in the above specimens, no attempt was made to slag specimens without graphite at 1650°C.

6.3.2 Composites Containing Graphite Reacted at 1500°C

In this part of the work, composites containing different types of graphite but of the same composition and prepared at $n = 0.3$ and $n = 1.0$, were qualitatively examined for slag attack resistance at 1500°C.

The microstructure texture of composites containing different types of graphite, for the same n-value, after slag tests, did not show any significant difference as has been shown elsewhere in this work. Therefore not all composites containing different types of graphite are reported, rather only those features which were significant in explaining the most likely reactions to have taken place between the slag and the composite at the firing temperature.

Plate 6.3.2(i)(a) shows a composite specimen containing ~ 20 $^{W}/o$ graphite D, for $n = 0.3$, at 1500°C. The slag (S) is seen at the top right hand corner of the plate. Here the slag has gone round the graphite flakes attacking the magnesia grains deep into the specimen as it can be seen near the bottom right hand corner of the plate. What is significant is that the extent of the reaction is not the same as that shown in Plate 6.3.1.(i)(a) where a lot of small magnesia grains are seen floating in the slag. Further, the amount of iron (Fe) reduced has increased as seen at the top of the plate. This is not very easy to deduce from the plates, but if Plates 6.3.1(i)(b)-(d) are compared with

Plate 6.3.2(i)(a), it can be seen that small globules of iron (white round phase) are scattered within the slag in Plates 6.3.1(i)(b)-(d), while a large band of iron lies across almost the entire area between the specimen and the slag in Plate 6.3.2(i)(a) and this was typical of most of the graphite-containing specimens examined in this work.

On examining the area of the specimen slightly below the field of view shown in Plate 6.3.2(i)(a), i.e. bottom right-hand corner of this micrograph, at a higher magnification, the extent of slag penetration can be appreciated. The magnesia grains are surrounded by the liquid slag as shown in Plate 6.3.2(i)(b).

Plate 6.3.2(i)(c) shows a specimen (n = 1.0) containing ~ 20 $^{w}/_{o}$ graphite D reacted at 1500°C. The slag has not penetrated the area below that on which it is resting because this area is occupied by graphite flakes. Equally interesting to note is that the metallic iron resulting from the reduction of Fe_2O_3 or FeO by either the graphite or coke, or both, during firing, is seen to be in contact with the graphite flakes at some points. This is surprising as one would expect the metallic iron to dissolve the graphite at the point of contact. However, this is a postmortem examination, and the micrographs may not be representing the position of these phases at test temperature. For instance, there could have been a thin film of slag separating the graphite and the metal (iron) at temperature, but during cooling this liquid slag shrunk on solidifying into cavities from which the graphite may have shrunk away itself, leaving a false picture of contact between the slag and the graphite in places where the graphite was unable to shrink or, indeed, the metal shrinking into the cavities left by the graphite. Clearly the situation is more complex than has been described here and the factors can only be established by studying the microstructure at test temperatures using hot stage microscopy.

Plate 6.3.2(i)(d) is of the same specimen as that shown in Plate 6.3.2(i)(c) but of a different field of view. The plate shows that the amount of iron reduced is much higher than in the specimen without graphite. It also shows that the slag has not penetrated between the graphite flakes. In Section 6.3.1 (see Plate 6.3.1(i)(d)), it was proposed that if the interstices between large grains were filled with a non-reactive phase to a slag, the slag resistance of the brick could be increased because the slag will not infiltrate between the big grains and it would require a longer time to corrode the large magnesia grains, therefore Plate 6.3.2(i)(c) seems to prove this point because graphite is unreactive to the slag and it is not wetted by the slag, hence no penetration of the composite by the slag. Plate 6.3.2(i)(e) is of a composite specimen (n = 1.0) containing graphite C reacted at 1500°C. The gap between the magnesia grains is occupied by the graphite and the slag cannot penetrate between these MgO grains, again emphasizing the importance of graphite in improving slag attack resistance of the composite.

From the microstructure of the specimens reacted at 1500°C discussed above, it has been shown that when graphite was added to the magnesia, the reaction between the slag and the specimen was less than in specimens containing MgO or MgO + pitch. Furthermore, the penetration of the slag was effectively hindered at higher n-values than at low n-values, because large magnesia grains are not easily corroded by the slag while the slag cannot penetrate between the large magnesia grains since these areas are occupied by graphite which is not wetted by the slag. Compare Plates 6.3.2(i)(a) and (b), n = 0.3, with Plates 6.3.2(i)(c) and (d), n = 1.0.

6.3.3 Composites Reacted at 1650°C

Plate 6.3.3(i) shows a slagged specimen containing ~ 20 $^w/o$ graphite M (n = 0.3) and reacted at 1650°C. The reaction was substantial but only at the contact point of the specimen, as there seems to be no reaction at the bottom right-hand corner of the photomicrograph. Plate 6.3.3(ii)(a) is a field of view less than a millimetre below the bottom left-hand corner of Plate 6.3.3.(i) and the extent of the reaction is not as vigorous as shown in Plate 6.3.3(i) which is specimen/slag interface. Below the large graphite flake, encircled area, a liquid is visible between magnesia grains. This is possibly not liquid due to slag penetration but arising from the liquid sintering of the fine magnesia grains (n = 0.3). The two plates also show some contact between the slag and the graphite, and Plate 6.3.3(ii)(b) is further evidence of graphite-slag "contact" and graphite-iron "contact". To investigate further whether there is a real physical contact of the metallic iron and the slag with the graphite flakes, a field of view of the flake surrounded by a slag in Plate 6.3.3(i) was observed under higher magnification, as shown in Plate 6.3.3(iii). In the middle of this plate, encircled, a bright white phase (Fe) is evidently in contact with small graphite flakes, and to the right of this phase (Fe), the slag is seen to be in contact with the flakes as well. About 2 cm below this area, in a rectangle, a solid, presumably liquid slag at test temperature, seems to have conformed to the shapes of the interlaminar cracks of the graphite flakes. Plate 6.3.3(iv) shows a flake situated deep in the slag after a reaction test at 1650°C.

Plate 6.3.3(v) is the microstructure of a specimen containing 20 $^w/o$ graphite M (n = 1.0) at the slag/specimen contact point after firing at 1650°C. The reaction between the magnesia and the slag is higher than in specimens fired at 1500°C for the same n-value. In this plate, some of the graphite flakes are virtually floating in the slag. Surprisingly though, about a millimetre below this zone, bottom of Plate 6.3.3(v), the specimen does not show any sign of the presence of a slag and this field of view is depicted in Plate 6.3.3(vi).

To try and quantify the extent of slag reactions and penetration in the magnesia composites, specimens reacted at 1650°C were examined under the scanning electron microscope (SEM). Little success was achieved because the contrast between magnesia grains and the slag at any magnification other than the lowest on the instrument, was poor. Therefore, meaningful results on the type of reactions or depth of slag penetration could only have been achieved by micro-analysis of the specimen using electron probe-microanalysis. Therefore, a qualitative analysis of the specimens was carried out as was done with reflected light microscopy.

Plate 6.3.3(vii) shows the interface between the slag and the specimen (n = 0.3) containing 20 $^{w}/o$ graphite A. Although the extent of reactions seem to be high in the previous plates already described, when observed under low magnification, the reactions could be considered as minor in practical terms. The slag in this plate is the curved feature (s) on the right-hand side of the vertical white line.

The field at which the two lines cross was examined at a higher magnification and this is shown as Plate 6.3.3(viii). The grey phase on the left-hand side of the vertical line is the slag (s) and the dark phase on the right is a graphie flake (G) and the contact between the slag and graphite flake is obvious at room temperature, at least.

6.3.4 Summary of Results

From the microstructural features described above, it has been shown that the presence of graphite hinders the penetration of the slag. However, it has been shown that if the amount of graphite-graphite contacts is less, as has been shown at lower n-values (n = 0.3), the slag can still penetrate the specimen by reacting with the fine magnesia grains which form a continuous matrix at these low n-values. When the n-value is high, the graphite phase becomes continuous and since the slag does not wet the graphite, slag infiltration will not take place unless:

(a) the slag dissolves the magnesia grains first, which will inevitably loosen the structure and the graphite flakes will float into the slag;

(b) the graphite is oxidized by the oxygen literated from the slag or reduced oxide phase in the specimen or brick.

Although the plates have shown some physical contact between the slag and the graphite, the fact that the slag did not penetrate into the interior of the specimen in areas where graphite was present, Plate 6.3.2(i)(e), is a clear indication that graphite is not wetted by the slag.

Another interesting observation from the above specimens is that in the absence of graphite in the test specimens, little amount of metallic iron was observed, but when specimens containing graphite were tested for slag resistance, the amount of metallic iron reduced from the slag increased. From this observation, the proposal[95] made in Section 6.1.2(a) which leads to reduction in slag penetration could be real, although the information obtained in this work is not adequate to give a conclusive view over this proposal. No other mechanisms proposed in

Section 6.1.2 were observed or inferred in this work because of various reasons, among them is that the specimens were too small to realise differential partial pressure of the gases in different parts of the brick; hence dense layers of MgO near the hot face (in these specimens temperature graident within each specimen was, probably, zero, as otherwise proposed[102] in Section 6.1.2(f)) was not observed.

CHAPTER 7

GENERAL CONCLUSIONS AND SUGGESTIONS FOR FUTURE WORK

7.1 Conclusions

Relationships between microstructure and some properties of MgO-graphite materials have been studied in this work. Firstly, the characteristics of the raw materials and the components of the MgO-graphite composites were evaluated.

7.1.1 The powder densities of all the graphites used in this work were similar, varying only between 2.22×10^3 and 2.25×10^3 kg/m^3. Graphites with higher ash contents showed slightly higher densities than those with low ash contents (see Table 2.3.1(ii) and 2.3.3(i). The density of the coked pitch showed the expected increase from its raw state to the fired state, i.e., from 1.36×10^3 kg/m^3 to 2.0×10^3 kg/m^3 after coking at 1500°C. On the other hand, the density of the resin (P41) and the mixed resin (PR67 + P41) increased only from 1.30×10^3 and 1.40×10^3 to 1.40×10^3 and 1.80×10^3 kg/m^3 respectively. The low increase in the density of the coked resins is due to the existence of closed pores which are absent in the coked pitch as discussed in Section 2.4.6.

7.1.2 The specific surface areas (SSA) df the graphites examined in this work did not vary very much with sieve size for the same graphite. However, there were significant differences in SSA between different types of graphite, with coarse graphites showing the largest specific surface areas (see Table 2.3.4(ii)).

The specific surface area of a coked resin (P41) was found to be higher than that of the pitch coke. But when these coked binders were ground to less than 75 μm, their SSA were found to be the same.

7.1.3 The oxidation characteristics of the four graphites were different. Generally, graphites containing large amounts of fines, i.e. < 150 μm, oxidized faster than those with large flakes as discussed in Section 2.4.5(i) in detail and Figure 2.4.5(i) shows the oxidation behaviour of the graphites.

The coked resin P41, was found to have much lower oxidation resistance than the coked pitch. The low oxidation resistance of the coked resin may be due to the opening up of pores during the oxidation reactions, therefore presenting a larger surface area for the reaction than pitch coke. This point is highlighted in Section 2.4.5(ii) while Figure 2.4.5(ii) illustrates the oxidation characteristics of the two materials.

7.1.4 From the literature cited in this thesis, it has been shown that there is need to determine the aspect ratio of the natural flake graphite used in the refractories industry.

A novel method of determining aspect ratio (maximum length/thickness) of graphite has been developed in which length and thickness distributions of flakes were determined using a microscope and a graphics tablet connected to a computer as described in Section 3.2.3. This method was applied to the four graphites A, B, C and D.

The length measurement distributions were found to be symmetrical and the flake lengths followed the sieve size distribution, i.e., flakes retained on coarse sieve sizes were found to be longer than those retained on fine sieve mesh sizes as expected. However, thickness distributions did not bear any relationship with the sieve size distributions. For instance, a graphite sample which had a large amount of fines, by sieve analysis, did not necessarily have thinner flakes than the coarse ones.

The aspect ratio of a graphite sample was determined by plotting the mode of its length against the mode of its thickness in each sieve cut. This plot produced a straight line indicating that the aspect ratio was a constant for each graphite sample.

The aspect ratios of the four graphites determined in this work were found to be between 15 and 45, with graphite A and B showing the highest ratios. The results of the aspect ratio measurements are discussed fully in Section 3.3 of Chapter 3.

7.1.5 A detailed study was made of the compaction of magnesia-graphite mixtures. Following the establishment of the effect of MgO size distributions on porosity of compacts using a relationship derived by Andreasen[46], i.e.,

$$y = 100\left(\frac{d}{D}\right)^{n} ,$$

where y is the percent of the material with size d, D is the diameter of the largest size fraction in the grain mixture and n (n-value) is the exponent that can be used to vary the proportion of coarse material to fine material, graphite was introduced in the magnesia grain mixture in a number of ways and its effect evaluated. Specifically, three methods were used:

(a) Method 1 involved the replacement of the amounts of magnesia ($^{w}/o$) equivalent to the amount of graphite required to be introduced in a given sieve range such that the final mixture contained 80 $^w/o$ MgO + 20 $^w/o$ graphite (Section 4.2.2(i)).

(b) Method 2 involved replacing all the magnesia grains less than 150 μm at each n-value, as a result the amount of graphite was different for each n-value (see Section 4.2.2(ii)).

(c) Method 3. Here the graphite was added to the magnesia mixture as determined by Andreasen's expression (see Section 4.2.2(iii)).

In general the effects of adding graphite and/or binder to a magnesia grain mixture were as follows:

(a) When graphite was introduced into the magnesia grain mixture (as described in Section 4.2.2), the porosity of the resulting composite was lower than that of the pure magnesia compacts, both in the green and fired state. However, the porosity of these composites was found to increase by an amount of about 5% after firing. This increase in porosity was attributed to the expansion of the graphite flakes on firing (see Section 4.4.3).

(b) Of the three methods, indicated above, of introducing natural flake graphite in the magnesia grain mixture, Method 3 gave the lowest porosity of the composite both in the green and fired state of the composite.

(c) The microstructure of the magnesia graphite composites was found to vary with n-value. At lower n-values, i.e. composites with high amount of fine magnesia, the graphite phase was found to be dispersed because of the fine MgO grains separating the graphite flakes. However, at high n-values the graphite phase was seen to be the continuous phase, mostly filling the cavities between big MgO grains.

(d) When varying amounts of binder were added to a composite of a fixed magnesia/graphite ratio, the green porosity decreased with increasing binder content because the binder was able to fill the pores in the matrix. Furthermore, the presence of a fluid material (the composites containing binders were warmed during pressing) at the time of pressing acted as a lubricant between particles and facilitated packing. However, after firing these binder-containing specimens, the porosity was found to increase with increasing binder content, due to increased volatile matter evolved from the binders.

Although the bulk volume increased after firing, this increase was not a function of the amount of binder added, but was due largely to the expansion of the graphite. However, cured resin restrained this expansion and volume increase was lower (Figures 4.4.4(i)(c) and (ii)(c)). These results are discussed in Section 4.4.4.

7.1.6 (i) The strength of the fired magnesia compacts (1500°C) was found to fall with increasing n-value, typically from 25 MPa at $n = 0.3$ to 8 MPa at $n = 1.0$. The relative elastic modulus, $Ef(\nu)$, (see Section 5.4) showed the same trend as strength as shown in Figure 5.5.1(a) and (d). This fall in strength and $Ef(\nu)$ towards high n-values was attributed to the reduction in the load bearing area. However, when pitch was used as a binder in the magnesia grain mixtures, the strength fell by a factor of about 10 while the modulus fell by a factor of about

4. This drastic fall in strength was thought to be due to the loss of the ceramic bond in the matrix due to a lack of bonding of carbon to the oxide, as discussed fully in Section 5.5.2. On introducing a small amount of graphite ~ 10 ^{w}/o into the magnesia grain mixture containing pitch, the strength of the resulting composite was reduced slightly further than when pitch was introduced in the magnesia alone. This further fall in strength was attributed to the introduction of larger cracks in the matrix which brought about the non-bonding of the graphite to the oxide. Similarly, the relative elastic modulus fell because of these cracks, in addition to the fact that graphite itself has a lower modulus than the magnesia.

When the amount of graphite was doubled, from 10 ^{w}/o to 20 ^{w}/o, the strength increased slightly, while the modulus remained almost the same. On increasing the graphite content to 30 ^{w}/o (50 ^{v}/o), the strength of the composite doubled, but the modulus essentially remained the same. This increase in strength was attributed to the increased keying effect of the graphite in the composite. The effect of graphite content on some of the physical properties of the magnesia-graphite composites is discussed fully in Sections 5.5.3 through to 5.5.6 and summarized in Figures 5.5.6(i)-(iv).

(ii) Fired composites of a fixed magnesia/graphite ratio and n-value did not show a significant strength increase with increasing pitch content. Fired composites bonded with the resin mixture, however, showed lower strength at low resin contents than those bonded with pitch at equal amounts of binder in the green state. The low strength with the resin bonded composites was almost certainly due to low carbon yield from the resin, as shown in Figure 5.5.7(i)(b). The reasons for the low carbon yield from the resin are discussed in Section 5.5.7.

However, the strength rise, for a given carbon content interval, Figure 5.5.7(i)(b), in composites containing the resin mixture was higher than those containing pitch. When the ratio of the resin mixture (PR67 + P41) was increased in favour of P41, the strength increased from 0.7 to 1.6 MPa. for the same level of binder (5 $^{w}/o$) in the composite. This latter strength is equal to that obtained from composites "bonded" with a similar amount of pitch.

(iii) Composites containing the same amount of graphite, but of different types, did not show significant differences in strength, with typical values of about 2 MPa at n = 0.3 and about 1 MPa at n = 1.0. Similarly, there were little differences in moduli of composites containing different types of graphite. These results are discussed in Section 5.5.8.

(iv) It has been shown in this work that when a metal, such as aluminium or silicon, is added to a composite of a fixed magnesia/graphite ratio bonded with pitch, the strength of the composite is double over that of the same composite without a metal additive after firing in a non-oxidizing atmosphere at 1500°C. This increase in strength is thought to be due to increased interlocking of the matrix provided for by the fibrous nature of the nitride phases, both of aluminium and silicon, formed during the firing of such composites in a nitrogen-rich atmosphere.

When the metal content was increased in the composite, the strength also increased proportionately, but there was little difference in strength between composites containing aluminium and silicon in the raw state, as shown in Figure 5.5.10(iii).

7.1.7 During the packing and strength measurement tests, the largest grain size magnesia fraction, defined as D, equation (1) Section 4.1.2, was kept constant at D = 3.35 mm. When D was reduced in the composites, the strength increased. For instance, a composite containing 80 parts MgO, 20 parts graphite A and 5 parts pitch had strength values of 1.6, 2.9 and 3.5 MPa for D- values of 3350 μm, 600 μm and 250 μm respectively, as discussed in Section 5.5.11.

7.1.8 The results obtained from slag attack tests at 1500°C and 1650°C carried out on graphite-containing magnesia composites, indicated that the slag was shown not to penetrate through an area occupied by graphite, as expected. Some of the micrographs show that the graphite flakes are in contact with both the slag and the reduced iron; but this may not be the real situation at test temperatures and therefore the apparent contacts of the slag and iron with the flakes may be a result of contraction of the phases involved during cooling.

Finally, there was less slag penetration at higher n-values than at lower n-values, because at high n-values the composite contains large quantities of coarse magnesia grains which cannot easily be corroded and dissolved by the slag, while graphite is not affected by the slag under non-oxidizing atmosphere as was the case here.

7.2 Future Work

7.2.1 In this work it has been shown that different graphites oxidize differently at the same heating rate, temperature and oxidizing conditions. It would, perhaps, be beneficial to carry out systematic investigations of the kinetics of oxidation of natural flake graphites used in the refractories industry with a view to establishing the effect of impurity content and type and the flake size on the oxidation of graphites. Furthermore, it would be useful to establish whether there is a correlation between specific surface areas of the graphites and coke binders used in the refractories industry and their oxidation rates. These experiments may help in establishing the most influential parameters in the oxidation of graphite, and work can therefore be directed towards reducing dependency on these parameters.

7.2.2 More work towards development of aspect ratio measurement techniques of natural flake graphite is needed, particularly development of techniques that can be used in routine characterization of graphite in terms of its aspect ratio.

7.2.3 In the packing experiments carried out in this work, it has been shown that the porosity increase of composites after firing was due to the bulk volume increase of the composites on firing. What has not been established in this work is, how different size fractions of the same graphite would affect the packing characteristics, volume change and other physical properties after firing. Several investigations can be carried out to establish the influence of flake size on porosity, coefficients of thermal expansion and thermal conductivity, strength, work of fracture, etc.

7.2.4 (i) Further to the suggested proposals in Item No. 3 above, work of fracture experiments should include the influence of type of binder and graphite on work of fracture. Furthermore, hot modulus of rupture determination of composites containing varying amounts of binder and graphite would be of great importance for practical purposes.

(ii) An experiment which might be of industrial importance would be to fire the specimens containing a binder at the required temperature and then, impregnate the specimens at the binder liquid temperature, possibly under vacuum, and refire the specimens at the same temperature, then determine porosity, elastic modulus, hot and room temperature strength. This can be extended further by determining the fracture toughness, K_{IC}, for each cycle of impregnation .

(iii) The addition of metals, for instance aluminium, silicon and magnesium, are said to hinder the oxidation of the carbon phase in the refractory composite at working temperatures. The logical experiments would be to study the kinetics of oxidation of graphite-containing composites with varying quantities of metallic additives at various temperatures in varying oxidizing atmospheres, such as CO, CO_2, air, oxygen, etc. Also mechanical properties could be determined again as part of the experiment.

7.2.5 In Chapter 6, Section 6.2.1, several slag resistance mechanisms obtained from the literature are listed and it is not clear at present which of the mechanisms are responsible for the high slag resistance of the magnesia graphite composites. It is very important to study these mechanisms because it is the high slag attack resistance, together with high thermal shock resistance, which make these refractory composites superior to the oxide refractories.

One of the study techniques which might help in understanding the slag resistance of the magnesia-graphite refractory composites is hot stage microscopy. To reduce the number of variables, synthetic slags may be used. The study may involve putting various types of slags on graphite flakes in an inert, neutral and semi-oxidizing (CO, CO_2) atmosphere and examine the reactions between graphite and the slag. The second part of the experiment would be to use composites containing varying amounts of graphite and, again, study the reactions at temperature. Finally, to investigate whether different types of graphite react differently to the same type of slag, atmosphere, etc., composites containing different types of graphite can be used. Hot stage microscopy studies have been suggested here because of the difficulties involved in interpreting the microstructure after the specimen has been cooled. Quenching of these composites has the disadvantage of possible oxidation of the carbon phase as well as the possibility of the graphite flakes shrinking away from the matrix during quenching and then their position at temperature cannot be ascertained.

REFERENCES

1. Fitzgerald, F., Refractories Journal, Sept./Oct., 1983, p. 6.
2. Marukawa, K., Hiroki, N. and Shirota, Y., Taikabutsu Overseas, Vol. 5, No. 1, March 1985, p. 28.
3. Wilshire, B., Homer, D. and Cooke, N.L., Technological and Economic Trends in Steel Industry, p. 129-179, Monographs in Materials Technology by Pineridge Press, Swansea, UK.
4. Jackson, B. and Webster, R., Iron and Steel International, April 1981, p. 67.
5. White, J., High Temperature Oxides, Volume 5-I, p. 82 139, 1970, Ed. by A.M. Alper, Academic Press.
6. Taylor, M.I., Ford, W.F. and White, J., Trans. Brit. Ceram. Soc., 68, 1969, p. 173.
7. Ryshkewitch, E., Oxide Ceramics, Academic Press, 1960, p. 283.
8. Artelt, P., Refractories Journal, May/June, 1981, p. 10.
9. Cooper, C.F., Chemistry and Industry, 18th Sept. 1982, p. 679.
10. Mikami, H.M. and Martinet, J.R., Refractories Journal, Vol. 6, Nov./Dec., 1980.
11. Fitchett, A.M. and Wilshire, B., Trans. Brit. Ceram. Soc., Vol. 83(2), 1984, p. 59.
12. Nacamu, R.L. and Lalama, S.J., Refractories Journal, July/Aug., 1982, p. 9.
13. Kingery, W.D., Introduction to Ceramics, 2nd Ed., John Wiley and Son, 1976, p. 791.
14. Hayashi, T., Reprint of the First International Conference on Refractories, Japan, Nov. 15-18, 1983, p. 5-50.

15. Chesters, J.H., Refractories for Iron and Steelmaking, Metals Society, 1974, p. 172.

16. Gilpin, W.C., Refractories Journal, June 1963, p. 214.

17. Ainscow, W.S., Refractories Journal, May/June 1984, p. 6.

18. Pettifer, L., 'IM' Refractories Survey, 1981, p. 131.

19. Rand, B. and McEnaney, B., Carbon Binders for Refractories from Pitch and Resin, Part 1, Trans. Brit. Ceram. soc. vol. 84(5) P157 1985

20. Lemon, P.H.R.B., Trans. and Journal of Brit. Ceram. Soc., Vol. 84, (3), 1985, p. 77-112.

21. Kremer, H.A., Chemistry and Industry, 18 Sept. 1982, p. 702.

22. Brunnauer, S., Emmett P.H. and Teller, E., J. Amer. Chem. Soc., 60, 1938, p. 309.

23. McCellan, A.L. and Harnsberger, H.F., J. Coll. Interface Sci., 23, 1967, p. 577.

24. Micrometrics Instrument Corporation - Micrometrics User Manual for FlowSorb 2300, 31st Oct. 1983; Micrometrics Instrument Corporation, 5680 Goshen Springs Road, Norcross, Georgia 30093, USA.

25. Heindl, R.A. and Mohler, N.F., J. Amer. Ceram. Soc., 38(3), 1955, p. 89-94.

26. Thomas, J.M., Chemistry and Physics of Carbon, Vol. 1 , 1965, p. 35, 134, 156. Ed. P.L. Walker, JR. and P.A. Thrower, publ. by Marcel Dekker INC. N.Y.

27. McEnaney, B. and Rand, B., Carbon Binders from Polymeric Resins and Pitch, Part II, in press.

28. White, J., High Temperature Oxides, Vol.5-1, 1970, p. 77-139.

29. Carniglia, S.C., Boyer, W.H. and Neely, J.E., Ceramics in Severe Environments, Vol. 5, 1971, p. 57-86.

30. Ryshkewitch, E., Oxide Ceramics, 1960, p. 275-317, accademic Press

31. Nightingale, R.E., Fundamentals of Refractory Compounds, Ed., Hausner, H.H. and Bowman, M.G., Plenum Press, N.Y., 1968, p. 203.

32. Kelly, B.T., Physics of Graphite, Applied Science Publishers, Inc., Englewood, New Jersey 09631, USA, 1981, p. 197-200.

33. Kelly, B.T., ibid, p. 62-146.

34. Hennig, G.R., Chemistry and Physics of Carbon, Vol. 2, 1966, p. 29., ed. P.L. Walker, Jr. and P.A. Thrower, publ. Marcel Dekker, INC. N.Y.

35. Fitzer, E. and Heym, M., High Temperatures - High Pressures, Vol. 10, 1978, p. 29-66.

36. Hutcheon J.M. , Modern Aspects of Graphite Technology, ed. Blackman L.C.F. P.2., Academic Press, London and N.Y., 1970.

37. Cooper, C.F., Trans. Brit. Ceram. Soc., 84(2), 1985, p. 39-76.

38. Wilson, C.M., Department of Ceramics, Glasses and Polymers, Sheffield University (Private communication).

39. Herdan, G., Small Particle Statistics, Second Ed., Publ. Butterworths, 1960, p.

40. Amelinck , S., Delavignette, P. and Heerschap, M., Chemistry and Physics of Carbon, Vol. 1, 1965, p. 1, ed. P.L Walker and P.A. Thrower, publ. Marcel Dekker INC. N.Y.

41. Nielsen, L.E., Predicting the Properties of Mixtures, Published by Marcel Dekker, Inc., 1978.

42. White, W.E. and Walton, S.F., J. Amer. Ceram. Soc., 20, 1937, p.155.

43. Elmes, A.W. and Francis, M., Trans. Brit. Ceram. Soc., 45, 1946, p. 323.

44. Skola, V., Feuerfest, 6, 1930, p. 81.

45. Hugill, H.R. and Westman, A.E.R., J. Amer. Ceram. Soc., 13, 1930, p. 767.

46. Andreasen, A.H.M., Kolloid Z., 50, 1930, p. 217.

47. Furnas, C.C., Ind. and Eng. Chem., 23, 1931, p. 1052.

48. Talbot, A.N. and Richart, F.E., University of Illinois, Eng. Exp. Bull. No. 1, 1918.

49. Mong, L.E. and Adelman, D.M., J. Amer. Ceram. Soc., 41, 1958, p. 267.

50. Fuller, W.D. and Thompson, S.E., Proc. Amer. Soc., Civil Eng., 33, 1907, p. 222.

51. Hughan, R., Refractories Journal, June 1961, p. 166.

52. Landy, R.A., Darroudi, T. and Hughes, R.H., Industrial Heating, April 1982, p. 27.

53. Kingery, W.D., Introduction to Ceramics, 2nd Ed., John Wiley and Son, Inc., 1976, p. 817.

54. Davidge, R.W., Mechanical Behaviour of Ceramics, Cambridge University Press, 1979.

55. Kingery, W.D., J. Amer. Ceram. Soc., 38, 1955, p. 3.

56. Hasselman, D.P.H., Bulletin Amer. Ceram. Soc., Vol. 49, No. 12, 1970, p. 1033.

57. Hasselman, D.P.H., Journal of Amer. Ceram. Soc., Vol. 52, No. 11, Nov. 1969, p. 600.

58. Orowan, E., Fracture and Strength of Solids, Rep. Prog. Physics, 12, 1949, p. 185.

59. Davidge, R.W., Mechanical Behaviour of Ceramics, Cambridge University Press, 1979, p. 26.

60. Griffith, A.A., Philosophical Trans. of the Royal Soc. of London, A221, 1921, p. 165.

61. Davidge, R.W. and Tappin, G., J. Mater. Sci., Vol. 3, 1968, p. 165-173.

62. Nakayama, J., J. Amer. Ceram. Soc., 48(11), 1965, p. 583.

63. Tattersall, H.G. and Tappin, G., J. of Material Sci., 1(3), 1966, p. 296-301.

64. Voigt, W., Lehrbuch der Kristall. Physik, Leipzig, 1928, p. 739.

65. Reuss, A., Z. Angew Math. Mech., 9, 1929, p. 49.

66. Wachtman, J.B., Elastic Deformation of Ceramics and Other Refractory Materials, Mechanical and Thermal Properties of Ceramics, Ed., J.B. Watchman, NBS Special, p139, 1969.

67. Knudsen, F.P., J. Amer. Ceram. Soc., 45(8), 1962, p. 94.

68. Spriggs, R.M., ibid, 44(12), 1961, p. 628.

69. Spriggs, R.M., ibid, 45(8), 1962, p. 454.

70. Hashin, Z. and Shrikman, S., J. Mech. Phys. Solids, 11, 1963, p. 127.

71. Creyke, W.E.C., Sainsbury, I.E.J. and Morrel, R., Design with Non-ductile Materials, Applied Science Publishers, 1982, p. 76.

72. Dean, G.D. and Read, B.E., The Determination of Dynamic Properties of Polymers, Pub. Adam Hilger Ltd., 1978, p. 157.

73. Filipczynski, L., Pawlowski, Z. and Wehr, J., Ultrasonic Methods of Testing Materials, Pub. Butterworths, 1966, p. 64-91.

74. Ibid, p. 21.

75. Dean, G.D. and Lockett, F.J., ASTM Special Technical Publications, S21, 1973, p. 326-46.

76. Rand, B. and McEananey, B., Carbon Binders for Refractories from Pitch and Resins, Part 1, Trans., Brit., Ceram. Vol. 84(5), P157, 1985

77. Boley, B.A. and Weiner, J.H., Theory of Thermal Stress, John Wiley and Son, Inc., N.Y., 1960.

78. Paul, B., Trans. the Metallurgical Society of AIME, 218(2), 1960, p. 36.

79. Kelly, B.T., Physics of Graphite, Applied Science Publishers, 1981, p. 381, 102.

80. Kingery, W.D., Introduction to Ceramics, 2nd Ed., 1976, p. 777.

81. Knudsen, F.P., J. Amer. Ceram. Soc., 42, 1959, p. 377.

82. Mrozowski, S., Proc. 1st and 2nd Conf. on Carbon, Univ. of Buffalo Press, Buffalo N.Y.,

83. Watanabe, A., Takahashi, M. and Matsuki, T., Reprint of the First International Conference on Refractories, Japan, Nov. 15-18, 1983, p. 125.

84. Yamaguchi, A., Taikabutsu Overseas, Vol. 4, No. 3. Sept. 1984, p. 14.

85. Mori, M., Inoue, H. and Ochiai, T., Progress in Nitrogen Ceramics, Applied Science Series, No. 65, Ed. by F.L. Riley, 1983, p.

86. Schweitz, K.A., Knoch, H. and Lipp, A., ibid, p. 245.

87. Fundamentals of Refractory Compounds, ed. Hausner, H, and Bowmanan, M.G., Plenum Press, N.Y., 1968, p. 217.

88. Lalama, S.J. and Nacamu, R.L., Refractories Journal, 4/1982

89. Kingery, W.D., Introduction to Ceramics, 2nd Ed., Publ. by John Wiley and Sons, Inc., p. 211.

90. Budworth, D.W., Introduction to Ceramics, Pergamon Press, 1970, p. 124.

91. Cooper, A.R., Ceramic Engineering and Science Proceedings, Vol. 2, Part 11-12, 1981, p. 1063.

92. Cholerton, J.F.E. and Charlton, W., Proc. Brit. Ceram. Soc., 14, 1969, p. 59-78.

93. Leonard, R.J. and Herron, R.H., J. Amer. Ceram. Soc., 55(1), 1972, p. 1-6.

94. Betts, W.D., Trans. and Journal of Brit. Ceram. Soc., Vol. 74, 1975, p. 85.

95. Metz, P., Stahl und Eisen, 74(1), 1954, p. 10-24.

96. Cooper, C.F., Refractories Journal, 6/1980, Nov./Dec., p. 11.

97. Barthel, H., and Pascal, I., Ber. Dt. Keram. Ges., 40(6), 1963, p. 373-384.

98. Barthel, H., Stahl und Eisen, 86(2), 1966, p. 81-88.

99. Robinson, P.C., Refractories Journal, 42(6), 1966, p. 218.

100. Gans, W., Knacke, O. and Marouf, E., Archiv. Eisenhüttenwesen, 39(9), 1968, p. 669-672.

101. Pickering, G.D. and Batchelor, J.D., Bull. Amer. Ceram. Soc., 50(7), 1972, p. 163-170.

102. Landy, R.A. and Brezny, B., Trans. Brit. Ceram. Soc., 71(6), 1972, p. 163-170.

103. Barthel, H. and Kaltner, E., Reprint of the First International Conference on Refractories, Nov. 15-18, 1983, Tokyo, Japan, p. 91.

104. McGee, T.D., Ceramic Engineering and Science Proceedings, Vol. 2, Part.11-12, 1981, p. 1141-55.

105. Eichler, B. and Owen, A.J., Trans. Brit. Ceram. Soc., 59, 1960, p. 149.

106. Oeters, F. and Neuer, B., Arch. Eisenh., 14, 1973, p. 443.

107. Trömel, G., Obst, K.H., Görl, E. and Stradtmann, J., J. Tonind. Ztg. Keram. Rdsch., 90, 1966, p. 193.

108. Cooper, A.R. and Kingery, W.D., J. Amer. Ceram. Soc., 47(1), 1964, p. 37-43.

109. Safdar, M., Frischat, G.H. and Hennicke, H.W., Ber. Dtsch. Keram. Ges., 51(10), 1974, p. 291-4.

110. ASTM Designation C768-73, 1980 Annual Book of ASTM Stamdards, Part 17, PP200-2, Americal Society for Testing and Materials, Philadelphia, Pa.

111. Grigsby, C.E., J. Amer. Ceram. Soc., 12, 1929, p. 241.

APPENDICES

APPENDIX 2.3.3i(b)

Determination of powder densities of the starting materials was carried out as described in Section 2.3.3. To show how the measurements were carried out on the starting materials, one set of measurements on magnesia is indicated below; four sets of measurements were carried out on each sample.

Weight of dry bottle (including stopper) = 21.7084 g

Weight of bottle + sample = 31.6969

Weight of sample = 9.9885

Weight of Bottle + sample + xylene = 50.3384

Weight of xylene = 18.6415

Density of xylene at 22°C = 0.8434 g/cc

hence volume of xylene = 22.1082 cc

∴ volume of sample (25-22.1082) = 2.8972 cc

∴ density of MgO = 3.4476 g/cc

APPENDIX 3.2.2(i)

1(a) Calculation of the aspect ratio of a graphite flake using a shadowing technique

The diagram below is a schematic representation of a graphite flake, in an evaporating chamber, lying flat on a glass slide which in turn is sitting on a moveable stage. The evaporating source is fixed, but by raising or lowering the stage, the angle θ can be changed. It is important that there should be no lateral movements of any of the three operands, source, flake or slide, and stage.

The thickness, h, has been exaggerated to show how the calculation was attempted.

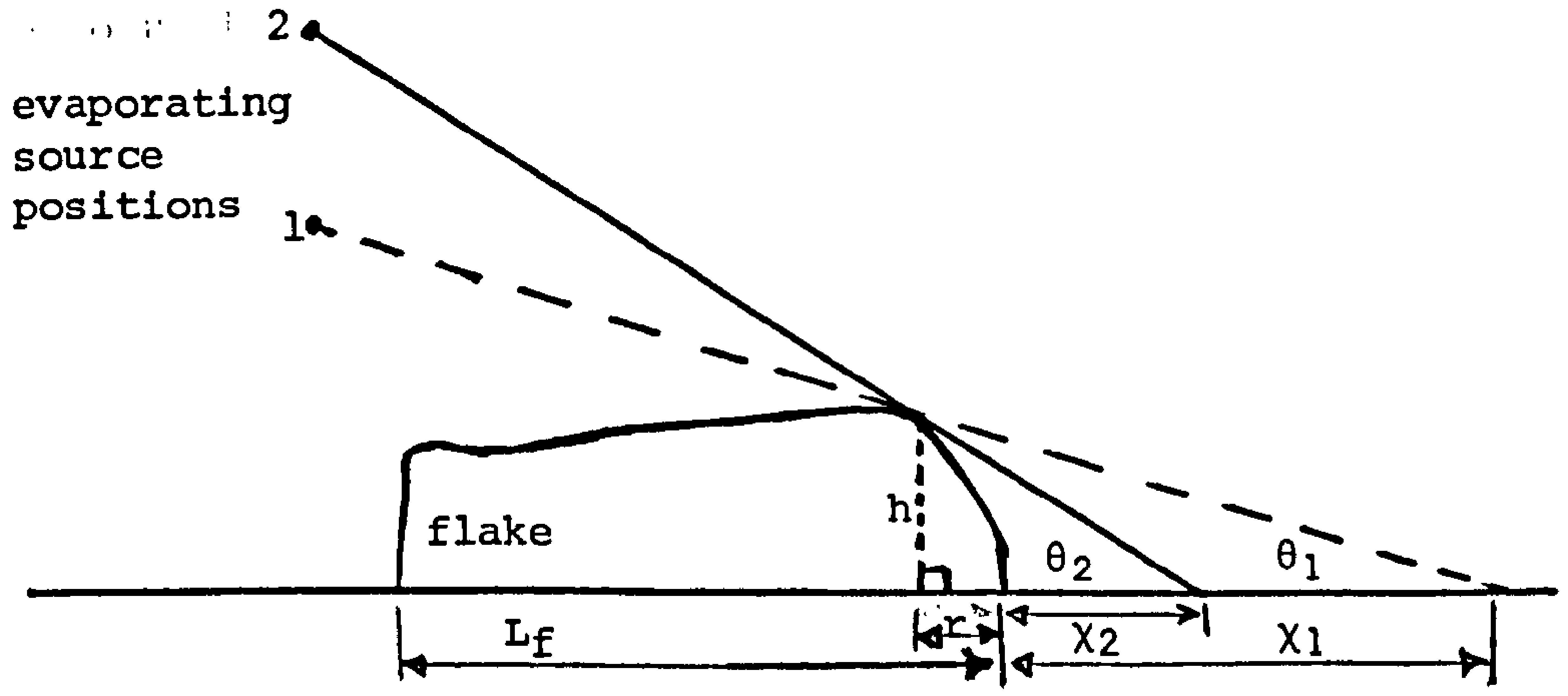

L_f = length of flake, h = height of flake = thickness of flake. r is a variable which depends on the regularity of the thickness of the flake and also surface roughness at the point of contact with the evaporated metal. If the surface at the contact point is smooth and the flake is regular, then r will coincide with the end of the flake; therefore r = o. Similarly, r = o if the debris of the flake is at either end of the flake. Other situations will give a finite value of r. This could have been one way of trying to estimate surface roughness of the flakes. χ_1 and χ_2 are lengths of shadows from the end of the flake making andles θ_1 and θ_2 with the horizontal respectively.

The thickness of the flake could be determined as below:-

$$\text{Tan } \theta_2 = \frac{h}{\chi_2 + r} \quad (2) \quad \text{and} \quad \text{Tan } \theta_1 = \frac{h}{\chi_1 + r} \quad (1)$$

From (2) $r = \frac{h - \chi_2 \tan \theta_2}{\tan \theta_2}$ and from (1) $r = \frac{h - \chi_1 \tan \theta_1}{\tan \theta_1}$

$$\therefore \quad \frac{h - \chi_2 \tan \theta_2}{\tan \theta_2} = \frac{h - \chi_1 \tan \theta_1}{\theta_1}$$

Rearranging this $h = (\chi_1 - \chi_2) \frac{\tan \theta_1 \tan \theta_2}{\tan \theta_2 - \tan \theta_1}$.

suppose $\theta_1 = 5°$ and $\theta_2 = 10°$, then $h = (\chi_1 - \chi_2)0.174$. Therefore, knowing θ_1 and θ_2 and by measuring the corresponding lengths of the resulting shadows after evaporating the metal, the thickness of the flake could have been determined. Further its length and breadth could as well have been measured at the same time as shadow lengths were being measured.

APPENDIX 3.3.2

Equations which may be used to change number distributions to weight distributions of particles (spherical particles) derived by Herdan[39]

The normal distribution of particle size is given by

$Y = \frac{1}{\sigma_n \sqrt{2\pi}} \exp\left[- \frac{(\chi-\bar{\chi})^2}{2\sigma_n^2} \right]$; where Y = probability density - probability means limiting frequency of occurrence of an observation falling within any given interval variate. σ_n is the standard deviation, χ is the diameter of the particle and $\bar{\chi}$ is the arithmetic mean. The number of particles or number distribution with a diameter between χ_1 and χ_2 is given by

$$n_i = \frac{\Sigma n_i}{\sigma_n \sqrt{2\pi}} \int_{\chi_1}^{\chi_2} \left(\exp\left[- \frac{(\chi-\bar{\chi})^2}{2\sigma_n^2} \right] \right) dx$$

Σn_i is the total number of particles measured, while the distribution by weight is given by

$$w_i = \rho \, \alpha_v \frac{\Sigma n_i \chi_i^{-3}}{\sigma_n \sqrt{2\pi}} \int_{\chi_1}^{\chi_2} \left(\exp\left[- \frac{(\chi-\bar{\chi})^2}{2\sigma_n^2} \right] \right) dx$$

where ρ is the density of the material, χ_i is the diameter of the particles and α_v is the volume shape factor.

If the dispersion of size fractions of a material is attained by comminution, the distribution appears to be governed very often by the log normal law. Pulverized silica, granite, calcite, limestone, quartz, alumina, clay etc., give size distributions which can be satisfactorily fitted by the logarithmic form of the normal law[39]. Again through derivations, the log-normal distribution of the number of particles between χ_1 and χ_2 is given by

$$n_i = \frac{\Sigma n_i}{\log\sigma_g \sqrt{2\pi}} \int_{\chi_1/\log\sigma_g}^{\chi_2/\log\sigma_g} \left(\exp\left[- \left\{ \frac{(\log\chi - \log\chi_g)^2}{2 \log^2\sigma_g} \right\} \right] \right) d \log x$$

Similarly, the weight distributions or the weight fraction between χ_1 and χ_2 is given by

$$w_i = \frac{\rho\ \alpha_v\ \Sigma\ n_i\ \chi_i^{\ 3}}{\log\sigma_g\ \sqrt{2\pi}} \int_{\chi_1/\log\sigma_g'}^{\chi_2/\log\sigma_g'} \left\{ \exp \left| - \frac{(\log X - \log X_g')^2}{2\ \log^2\sigma_g'} \right| \right\} d\ \log x$$

where χ_g' is the weight geometric mean and σ_g' is the geometric standard deviation.

APPENDIX 3.3.2(a)

Changing number distributions to weight percent distributions.

Figures 3.3.1(iii)(a) and 3.3.1(iii)(b) show that the aspect ratio (length/thickness) for all the graphites is a constant. Then

$$L \propto T, \quad \text{where } L = \text{length and } T = \text{thickness}$$

i.e.,

$$L = kT \tag{1}$$

using the assumptions described in Section 3.3.2, that the flakes may be considered as discs and that the bulk density of the flakes is a constant in all sieve cuts for the sample, then weight distributions of the flakes may be calculated as follows:-

Projected area of a disc with diameter L is given as

$$\pi\left(\frac{L}{2}\right)^2 = \frac{\pi}{4} L^2 . \tag{2}$$

$$\therefore \qquad \text{volume of disc} = \frac{\pi}{4} L^2.T \tag{3}$$

substituting the value of L from equation (1) into equation (3) then volume of disc is given as

$$V_{disc} = \frac{\pi}{4} k^2 T^3 \tag{4}$$

Hence weight of a single flake can be calculated

i.e.

$$w_f = V_{disc}\, d_B \tag{5}$$

where V_{disc} is volume of disc and d_B is the bulk density of the flake and w_f is the weight of flake.

Then the weight of flakes in a given thickness interval may be obtained by the summation of the weights of flakes of a given thickness up to the upper limit of thickness in the interval, i.e., the total weight of flakes in thickness interval I is

$$\sum_{i=1}^{i=n_I} w_{fi} ,$$

where n_I is the total number of flakes up to interval I, and w_{fi} is the weight of the ith flake in the interval.

Then the weight fraction of the flakes in this thickness interval can be obtained by knowing the total weight of all the flakes measured in all thickness intervals in this sieve cut, given as:

$$\sum_{i=1}^{i=N_T} w_{fi} ,$$

where N_T = total number of flakes measured in all thickness intervals.

Then the weight fraction in the given interval is:

$$\frac{\sum\limits_{i=n_{min}}^{i=n_I} w_{fi}}{\sum\limits_{i=1}^{i=N_T} w_{fi}} \qquad (6)$$

where n_{min} is the starting flake number in the given interval.

From equation (5) above, $w_f = V_{disc} \cdot d_B$, then $w_{fi} = V_{disci} \times d_{Bi}$

$$\therefore \qquad w_f = \frac{\pi}{4} k^2 T^3 . d_B$$

Then

$$\frac{\sum\limits_{i=n_{min}}^{i=n_I} w_{fi}}{\sum\limits_{i=1}^{i=N_T} w_{fi}} = \frac{\sum\limits_{i=n_{min}}^{i=n_I} n_i \ \pi/4 \ k^2 T_i{}^3 . d_{Bi}}{\sum\limits_{i=1}^{i=N_T} n_i \ \pi/4 \ k^2 T_i{}^3 d_{Bi}}$$

However, $\frac{\pi}{4} k^2 d_B$ is a constant in both the numerator and denominator of the above expression.

$\therefore$ Fraction by weight of flakes in the chosen interval

$$I = \frac{\sum\limits_{i=n_{min}}^{i=n_I} n_i \ T_i{}^3}{\sum\limits_{i=1}^{i=N_T} n_i \ T_i{}^3} \qquad (7)$$

Then these weight fractions can be used to determine weight distributions of that particular sieve cut by multiplying the weight percent retained in the sieve cut being dealt with, e.g., if the weight percent retained on -60+100 B.S.S. mesh sieve is W_1, then the weight distributions in each thickness interval of the flakes whose thicknesses have been determined, can be determined by:

$$\text{weight distribution} = \frac{\sum_{i=I}^{i=i+I} n_i \, T_i^3}{\sum_{i=1}^{i=T} n_i \, T_i^3} \times W_1 \qquad (8)$$

Similarly the weight distributions can be obtained using the same procedure if length values are known, wherever there is T in expression (8) it is replaced by L.

APPENDIX 4.2.1(i)

Determination of the required amounts in various sieve cuts to obtain an efficiently packed mixture of different grain size magnesia fractions as predicted by Andreasen's[46] equation:

$$y = 100\left(\frac{d}{D}\right)^{n}$$

where y is the (volume) weight fraction of material of diameter, d, in a mixture of a material with maximum grain size D and n is a parameter used to vary the proportion of the coarse fraction to a fine fraction of the material in the mixture.

The example shown below illustrates the calculations of the amounts of magnesia grain size fractions required in each sieve cut when n = 0.3 to 0.5 and for D = 3.35 mm.

TABLE 1(a)

Mesh No.	Aperture in µm (d)	$(d)^{0.3}$	y (%)	$(d)^{0.4}$	y (%)	$(d)^{0.5}$	y (%)
5	3350	11.416	100.00	25.705	100.00	57.879	100.00
7	2400	10.329	90.48	22.495	87.51	48.90	84.60
25	600	6.815	59.69	12.920	50.26	24.495	42.32
60	250	5.241	45.91	9.103	35.41	15.811	27.32
100	150	4.496	39.38	7.421	28.87	12.247	21.16
200	75	3.652	31.99	5.624	21.88	8.660	14.96

From the above table the amount required in each sieve cut is the difference of the percentages between the two sieves involved; e.g., -5+7 sieve cut would be 100-90.48 = 9.52 ^{W}/o for n = 0.3. Therefore the percentages required in all the six sieve cuts indicated in the above table are given in Table 1(b) below including the n-values not shown above.

TABLE 1(b)

The Table below shows the amount of different grain size magnesia fractions in each sieve cut obtained by using Andreasen's equation $\left\{y = 100\left(\frac{d}{D}\right)^{n}\right\}$

	Weight percent of magnesia grain size							
n-value sieve cut	0.3	0.4	0.5	0.6	0.7	0.8	0.9	1.0
-5+7	9.52	12.50	15.36	18.14	20.82	23.42	25.93	28.36
-7+25	30.79	37.25	42.32	46.23	49.18	51.32	52.80	54.33
-25+60	13.78	15.00	15.00	14.56	13.74	12.72	11.60	9.85
-60+100	6.53	6.50	6.16	5.56	4.89	4.21	3.56	2.98
-100+200	7.39	6.88	6.20	5.28	4.37	3.54	2.84	2.24
-200	31.99	21.87	14.96	10.23	7.00	4.79	3.27	2.24
Totals	100.00	100.00	100.00	100.00	100.00	100.00	100.00	100.00

From the tables above the percentage of magnesia grains required in each sieve range for n = 0.3 to n = 1.0 are given.

APPENDIX 4.2.1(ii)

Calculations of two size combination of magnesia fractions using Hugill's[5] method

---

Mixture 1

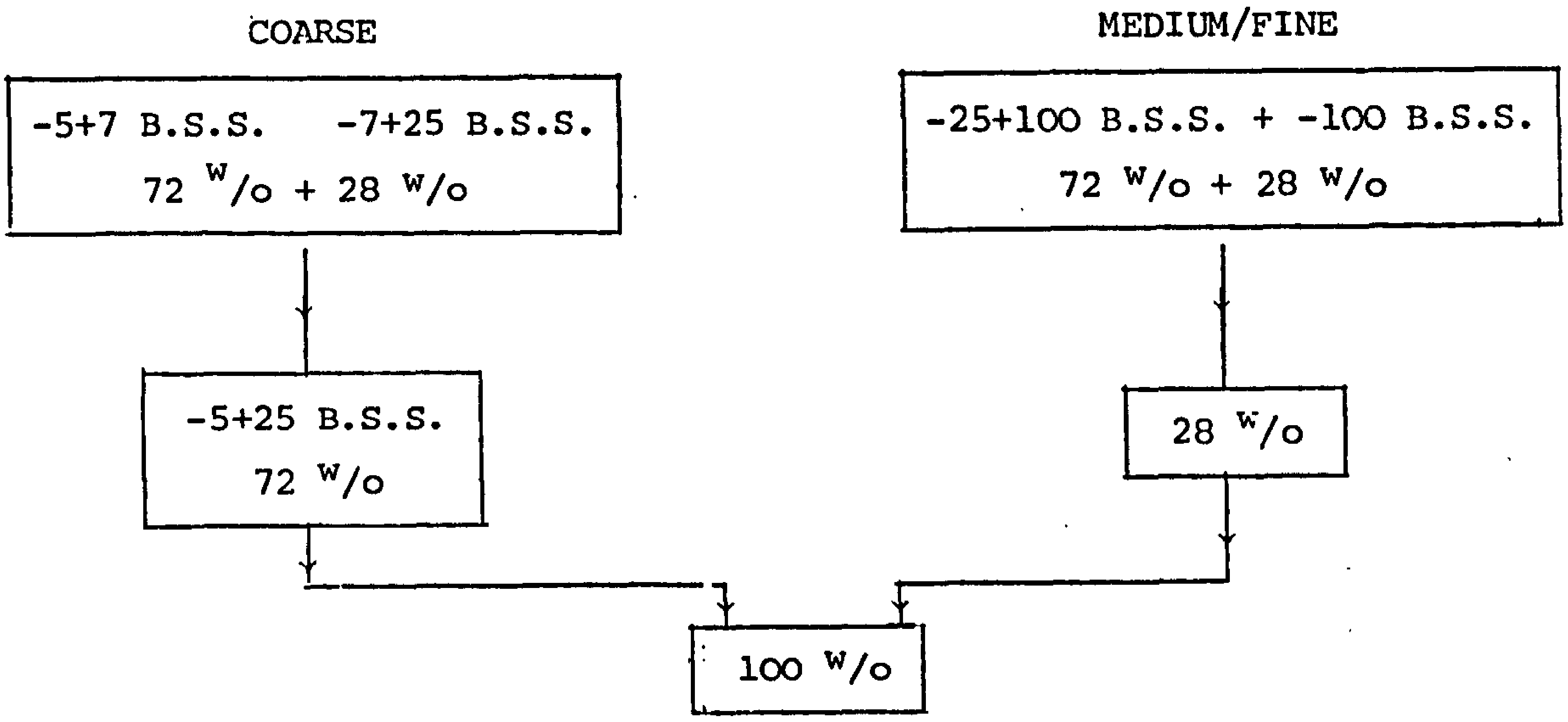

Mixture 2

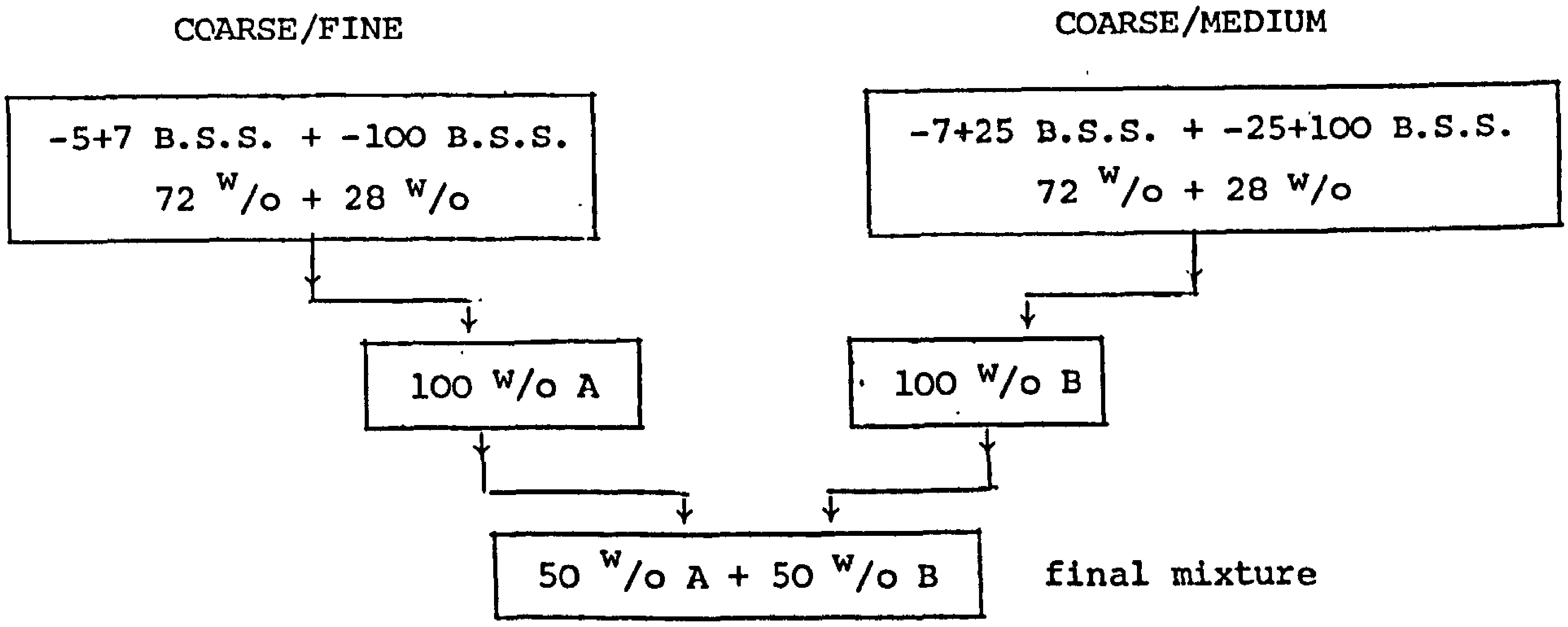

Mixture 3

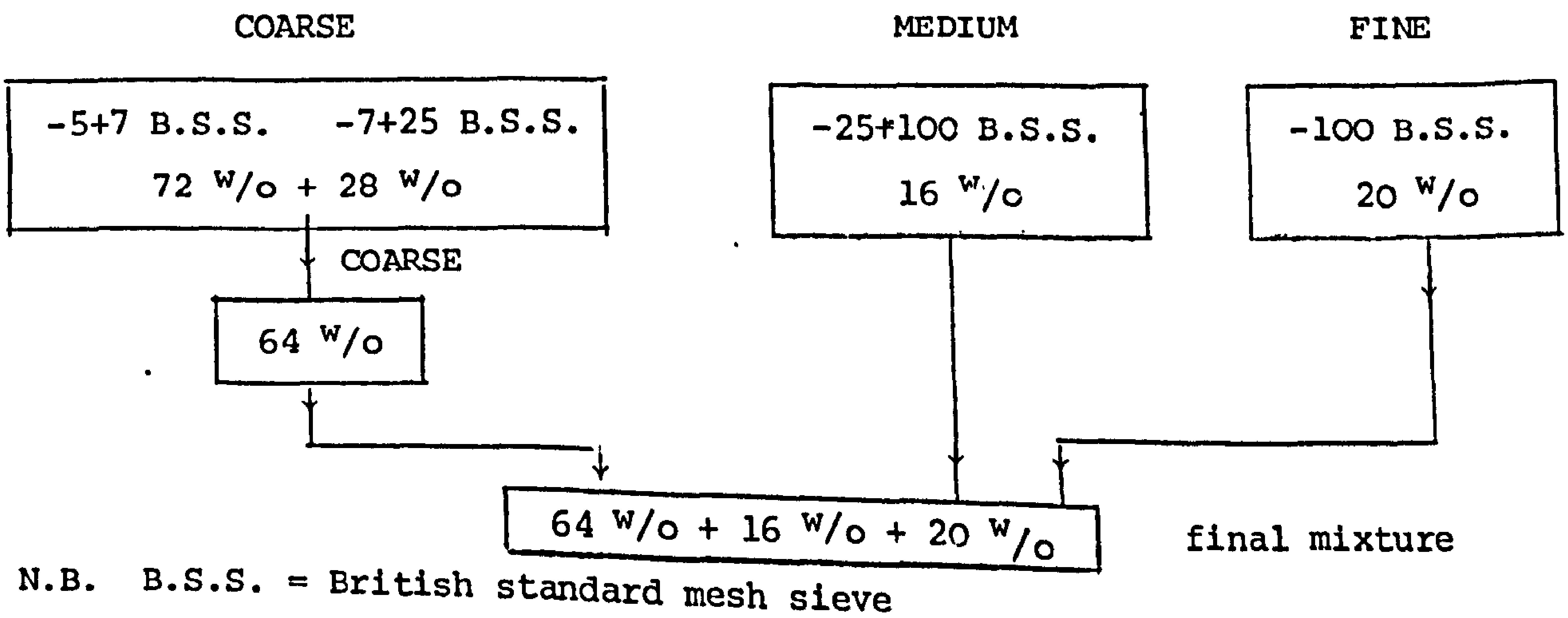

N.B. B.S.S. = British standard mesh sieve

APPENDIX 4.2.2(i)

An example of introducing graphite in a mixture of different grain size fractions using Method 1

First of all, the sieve analyses of graphite C are normalized to 20 $^{w}/o$ because only this amount of graphite is to substitute an equal amount of magnesia. Therefore the normalized analyses of graphite C are as follows:

TABLE 1(a)

Sieve cut	$^{w}/o$	MgO grain size mixture before introducing graphite at n = 0.3 $^{w}/o$
-5+7	-	9.52
-7+25	0.78	30.79
-25+60	6.71	13.78
-60+100	5.01	6.53
-100+200	3.93	7.39
-200	3.57	31.99
Total	20 $^{w}/o$	100.00

Now using Table 1(b) in Appendix 4.2.1(i) the amount of graphite is substituted into the magnesia for equal amounts of magnesia as shown in Table 1(b) below for n = 0.3; i.e. 80 $^{w}/o$ MgO + 20 $^{w}/o$ Graphite C

TABLE 1(b)

Sieve cut	$^{w}/o$ MgO	$^{w}/o$ Graphite C	Total
-5+7	9.52	-	9.52
-7+25	30.01	0.78	30.79
-25+60	7.07	6.71	13.78
-60+100	1.52	5.01	6.53
-100+200	3.46	3.93	7.39
-200	28.42	3.57	31.99
Total	80.00	20.00	100.00

APPENDIX 4.2.2(ii)

Method 2 of introducing graphite, as described in Section 4.2.2(ii), involved the replacement of all the magnesia grain fractions passing through 100 B.S.S. From Table 1(b) of Appendix 4.2.1(i), it can be seen that the amount of fines (-100 B.S.S.) decreases with increasing n-value. Therefore the amount of graphite added decreases with increasing n-value. In this method, the magnesia grain size fractions as shown in Table 1(b) of Appendix 4.2.1(i) were used as indicated but the total weight percent of magnesia fractions in the sieve cuts -100+200 and -200 B.S.S. were replaced by the equivalent amount of graphite in each n-value. Therefore using Table 1(b) of Appendix 4.2.1(i), the amount of magnesia replaced by graphite is 31.99 $^{w}/o$ + 7.39 = 39.38 $^{w}/o$ at n = 0.3 and 21.87 + 6.88 = 28.75 at n = 0.4 etc.

APPENDIX 4.2.2(iii)

This Appendix describes how the graphite was added to different grain size magnesia fraction mixture using Method 3 described in Section 4.2.2(iii).

This procedure did not involve any replacement of one material by another. Therefore the weight fractions of magnesia in each sieve cut for each n-value as given in Table 1(b) of Appendix 4.2.1(i) were used. For example, if a mixture of 80 parts of magnesia and 20 parts of graphite were to be mixed to obtain a batch sample of 50 g, then 40 g (80 $^w/o$) of magnesia mixture containing the different grain size fractions for a given n-value was obtained using Table 1(b) of Appendix 4.2.1(i) and then the 10 g component of graphite containing all the size distributions of graphite flakes as shown in Table 1(a) of Appendix 4.2.2(i), for example, was all added to the magnesia mixture. The Table below illustrates the procedure.

TABLE (iii)

n = 0.3, Graphite C to be added to MgO mixture

Sieve cut	MgO $^w/o$	MgO Weight Fraction (g)	Graphite C $^w/o$	Graphite C Weight Fraction (g)	MgO + graphite mixture weight fraction (g)
-5+7	9.52	3.81	-	-	3.81
-7+25	30.79	12.32	3.90	0.39	12.71
-25+60	13.78	5.51	33.60	3.36	8.87
-60+100	6.53	2.61	25.00	2.50	5.11
-100+200	7.39	2.96	19.70	1.97	4.93
-200	31.99	12.80	17.80	1.78	14.58
Totals	100.00	40.00	100.00	10.00	50.00

APPENDIX 4.4.3(i)

The derivation of a relationship between % change in bulk volume of specimens after firing and the % change in pore volume of specimens after firing.

From Section 4.2.5, % total porosity (% P) is given as:

$$\% \; P = \left(1 - \frac{D_B}{D_T}\right) \times 100$$

where D_B = bulk density and D_T is true density. This expression is equal to:

$$\% \; P = \left(1 - \frac{V_T}{V_B}\right) \times 100$$

where V_T is true volume and V_B is the bulk volume of the specimen. However, $PV_B = V_B - V_T$ and P is the pore fraction. The pore volume $= V_B - V_T$.

It can be deduced from above that the bulk volume of a specimen is equal to its true volume plus its pore volume, i.e.,

$$V_B = V_T + V_P$$

where V_P is the pore volume.

Then the change in bulk volume, ΔV_B, of a specimen after firing, is given as

$$\Delta V_B = V_{TF} + V_{PF} - V_{TG} - V_{PG} \qquad (1)$$

where V_{TF} is the true volume of the fired specimen;
V_{PF} is the pore volume of the fired specimen;
V_{TG} is the true volume of the green specimen; and
V_{PG} is the pore volume of the green specimen.

$$\text{porosity fraction} = \frac{V_P}{V_B} = P \qquad (2)$$

Now, assuming that true volume of the specimen does not change after firing, i.e. no evolution of gases, no oxidation of the graphite, etc., then

$$V_{TF} = V_{TG}$$

Then from equation (1)

$$\Delta V_B = V_{PF} - V_{PG} \tag{3}$$

i.e. change in bulk volume (ΔV_B) is equal to change in pore volume (ΔV_P) after firing.

But

$$\% \, \Delta V = \frac{\Delta V_B}{V_{BG}} \times 100$$

$$\therefore \quad \% \, \Delta V = \left(\frac{V_{PF} - V_{PG}}{V_{BG}} \right) 100$$

and from equation (2)

$$\% \, \Delta V = 100 \left(\frac{P_F \, V_{BF} - P_G \, V_{BG}}{V_{BG}} \right)$$

$$= \left(\frac{P_F \, V_{BF}}{V_{BG}} - P_G \right) 100 \, , \tag{4}$$

where V_{BG} and V_{BF} are green and fired bulk volumes and P_F and P_G are pore fractions, and by opening up the brackets in equation (4), the measured % porosity may be used, and the relationship can simply be stated as

$$\% \, \Delta V = P_f \frac{V_{BF}}{V_{BG}} - P_g \tag{5}$$

The terms P_f and P_g in equation (5) stand for % total fired and green porosity respectively.

Therefore $P_f \frac{V_{BF}}{V_{BG}} - P_g$ is the calculated change in bulk volume, if the porosity change in the specimen is entirely due to the bulk expansion.

N.B: (i) The change in volume indicated in this derivation is the volume per specimen.

(ii) $P_f = (100 \, P_F)\%$ and $P_g = (100 \, P_G)\%$

APPENDIX 5.2.1

Bend test measurements are affected by many factors and the equations used in determining Modulus of Rupture (MOR) have been derived using certain assumptions. Some of these assumptions, together with other factors that affect bend test strength, are outlined below:[71]

(a) Failure may occur from a defect within the test piece and not from the surface. The true fracture stress is then rather lower than that calculated.

(b) Failure may occur away from the loading point in three-point bending. Again the true fracture stress is lower than that calculated, but this error can be corrected if the position of the failure relative to the loading point is noted.

(c) The ratio of width b to height h of a rectangular section specimen may affect the results. Equations (9) and (10) assume a "thin" beam, but the stress distribution varies with geometry. A ratio of b:h of 2:1 is considered to be an optimum.

(d) The ratio of span to depth of specimen can affect the result. If the span is too small, shear stresses become significant and equations (9) and (10) above are no longer valid.

The greater the span, the better, but span may be limited by practicality. In any event, the ratio of the separation distance between the loading and support points (ℓ') to depth (h) for four-point or (ℓ) to (h) for three-point bending should exceed 4:1.

(e) The test jig should ideally be self-aligning for rectangular section specimens to allow for the top and bottom faces of the specimen not being flat and parallel. If this is not feasible, then accurate shaping of the test specimens is required, otherwise the strength will be underestimated. Round specimens pose fewer problems. In four-point bending, equal loading by each loading point is required.

(f) The loading and support points should not be sharp, or the local stress field induced around them may influence the result. A support or loading rod of 5-10 mm diameter is ideal. If possible, this rod should be free to rotate. The reason for this is, that with a fixed rod, frictional forces are produced as the specimen bends, and these forces apply a bending moment to the specimen which opposes that produced by the applied load. The result is that with fixed loading and support points, the fracture stress is overestimated by an amount depending on the coefficient of friction.

(g) The test results will depend on precisely how the test specimens have been prepared. Surface finish is most important because failure tends to occur from the surface, and particularly from the edges of the specimen. A wide variation in results could occur for different surface finishes. The important factor to note is that the surface and edge finish used in the test should model that which a component will possess in practice. Furthermore, the material for the test specimens should be prepared in the same way as that for the actual component.

(h) The test results may depend on the rate at which the load is applied to the test piece. This effect varies between materials; some are insensitive, some, such as glass, show a significant decrease of strength with decreasing loading rate. The ambient environment, particularly humidity, may also influence the result.

TABLES

TABLE 2.3.1(i)

Sieve analyses of the magnesia fractions and the graphites

		Weight Percent Material Retained					
Mesh Range (B.S.S.)		-5+7	-7+25	-25+60	-60+100	-100+200	-200
Size Range (in microns)		-3350-2400	-2400+600	-600+250	-250+150	-150+75	-75
Material	Type						
Magnesia A	-5+7	100	-	-	-	-	-
	-7+25	6.36	93.5	0.13	-	-	-
	-25	-	-	35.27	22.45	22.34	20.04
Ball-milled fines		-	-	-	7.93	18.27	73.79
Graphite	A	-	1.1	81.50	11.74	3.37	2.29
	B	-	-	0.40	30.11	68.00	1.50
	C	-	3.90	33.57	25.05	19.64	17.84
	D	-	0.09	42.51	53.57	3.00	0.85
(Malagasy graphite)	M	0.42	94.28	3.72	1.04	0.14	0.60

TABLE 2.3.1(ii)

The chemical analysis of the starting materials

	Graphites					Magnesia ($^W/o$)	
	Chemical analysis of graphite ashes (residue after oxidation) ($^W/o$)					Type	
Material	A	B	C	D	M	A	B
L.O.I. or Ash content	8.74	11.59	8.77	5.57	12.2		
Oxide							
SiO_2	50.1	54.6	47.6	55.90	42.0	0.46	0.59
TiO_2	1.48	1.00	0.86	0.41	0.83	0.02	0.03
Al_2O_3	18.22	14.56	18.88	10.27	40.50	0.18	0.21
Fe_2O_3	14.82	12.55	16.79	17.99	13.60	0.24	0.36
CaO	1.11	4.16	4.20	6.58	0.13	2.23	1.96
MgO	7.96	5.60	6.90	2.47	0.56	96.7	96.6
K_2O	3.89	2.42	2.21	3.03	0.90	0.02	0.02
Na_2O	0.72	2.81	0.80	0.74	0.05	-	-
P_2O_5	-	-	-	-	-		
Cr_2O_3	0.05	0.05	0.05	0.06		0.05	0.13
Mn_3O_4	0.09	0.12	0.38	0.45		0.04	0.035
ZrO_2	-	-	-	-		0.04	0.035
PbO	-	-	-	-			
BaO	-	-	-	-			
V_2O_5	-	-	-	-	0.01		
NiO	-	-	-	-	0.01		
CuO	-	-	-	-	0.02		
CaO/SiO_2 Molar ratio	0.02	0.08	0.09	0.13	0.003	5.17	3.57

These chemical analyses were carried out by the suppliers of the materials (see Section 3.1.2). Loss on ignition (L.O.I.) is used for the oxide materials and ash content for the graphites. The ash contents for graphites A,B,C and D were determined in this work.

TABLE 2.3.3(i)

Powder densities of the starting materials determined in this work. Theoretical densities are also shown where known.

Material		Powder Density x 10^3 kg/m^3	Standard Deviation x 10^3 kg/m^3	Theoretical density x 10^3 kg/m^3
Magnesia		3.44	0.03	3.58
Graphite:	A	2.22	0.02	
	B	2.25	0.01	
	C	2.22	0.02	2.26
	D	2.23	0.01	
	M	2.25	0.01	
Resins:	Cured resin P41	1.30	0.01	-
	Cured resin mixture (PR67:P41) (7.6 :1)	1.36		
	Coked resin P41	1.37	0.01	-
	Coked resin mixture (PR67:P41) (7.6 :1)	1.79		
	Raw pitch	1.33	0.01	-
	Coked pitch	2.03	0.01	-

The coking of the carbon binders was done in a neutral atmosphere at 1500°C.

The density values reported in this table are averages of four determinations.

TABLE 2.3.4(iii)

Specific surface areas (m^2/g) of graphites and binders determined by single-point adsorption method using FlowSorb 2300

Fraction Sample		Bulk Sample as-received	+25 mesh (> 600 µm)	-25+60 (600-250 µm)	-60+100 (250-150 µm)	-100+120 (150-75 µm)	-200 (< 75 µm)	Bulk sample as-received but ground (-200)
Graphite:	A	3.40	-	3.35	3.63	3.54	7.79	15.32
	B	1.81	-	-	1.67	1.49	-	2.57
	C	2.18	2.19	2.36	2.23	2.06	3.26	4.02
	D	1.43	-	1.54	1.20	1.51	2.44	11.14
	M	-	5.65	-	-	-	32.32	21.46
Binders:								
Coked pitch			0.45					13.36
Coked resin P41			1.30					13.90
Reference sample:								
Binder coke* A200 (1400°C)			1.35					3.98

* This sample was of known specific surface area (S.S.A.) in the unground state (with S.S.A. = 1.33 m^2/g). It was used as a standard.

TABLE 2.3.5(i)

X-ray analyses of magnesia fractions

2θ	D(Å)	I	Phase
-5+7 B.S.S. (3350-2400 μm) MgO fraction (Quality A)			
21.4	4.148	1	
21.65	4.101	1	
32.55	2.748	2	
33.45	2.676	1	
37.1	2.421	28	M
43.05	2.099	100	M
62.48	1.485	80	M
-7+25 B.S.S. (2400-600 μm) MgO fraction (Quality A)			
25.03	3.554	4	
32.05	3.790	1	
33.45	2.676	1	
37.1	2.421	23	M
43.1	2.097	100	M
62.45	1.486	76	M
-25 B.S.S. (< 600 μm) MgO fraction (Quality A)			
21.95	4.046	1	
32.55	2.748	1	
33.4	2.680	1	
37.1	2.421	23	M
43.12	2.096	100	M
62.4	1.487	76	M
69.1	1.358	2	
"Ball-milled" fines - MgO fractions (Quality B)			
21.4	4.148	1	
21.8	4.073	1	
32.6	2.744	1	
37.1	2.421	25	M
43.1	2.097	100	M
62.45	1.486	82	M

LEGENDS

M - MgO phase ; B.S.S. - British Standard mesh sieve

TABLE 2.3.5(ii)

2θ, d-values (Å) and relative intensities (I) of the four graphites as-received

A				B				C				D			
2θ	d (Å)	I	Phase	2θ	d (Å)	I	Phase	2θ	d (Å)	I	Phase	2θ	d (Å)	I	Phase
8.80	10.039	5		8.85	9.983	1		8.85	9.983	5		6.18	14.288	1	
12.35	7.160	1		12.30	7.189	2		12.50	7.075	1		7.12	12.404	1	
13.40	6.601	1		13.35	6.626	1		13.30	6.651	1		8.08	10.932	< 1	
17.57	5.040	1		17.75	4.992	< 1		18.75		< 1		13.45	6.577	1	
20.80	4.267	< 1		20.85	4.256	< 1		20.92	4.242	1		26.60	3.348	100	G
26.55	3.354	100	G	26.55	3.354	100	G	22.00	4.036	1		33.70	2.657	< 1	
35.70	2.513	1		35.50	2.526	< 1		26.60	3.348	100	G	38.33	2.346	1	
36.55	2.456	< 1		38.25	2.351	2		31.45	2.842	1		44.60	2.030	7	G
38.30	2.348	2		42.50	2.125	< 1	G	35.60	2.520	1		50.80	1.796	< 1	G
42.45	2.127	< 1	G	44.50	2.034	6	G	36.60	2.453	< 1		54.75	1.675	I8	G
44.55	2.032	7	G	52.70	1.735	1		38.30	2.348	1		59.98	1.541	< 1	
50.06	1.820	< 1		54.65	1.678	23	G	42.50	2.125	1	G	64.95	1.434	9	
54.65	1.678	25	G	59.80	1.548	< 1	G	44.55	2.032	6	G				
60.20	1.536	< 1	G	64.90	1.435	11		50.20	1.816	1					
64.90	1.435	20						54.70	1.676	25	G				
								60.00	1.540	1	G				
								64.95	1.434	11					

LEGEND: G - Graphite phase.

TABLE 2.3.5(iii)

2θ, d-values (Å) and relative intensities (I) of the ashes of the four graphites.

The ashes indicated here were obtained by oxidizing the graphites at 890°C

A				B				C				D			
2θ	d (Å)	I	Phase	2θ	d (Å)	I	Phase	2θ	d (Å)	I	Phase	2θ	d (Å)	I	Phase
8.85	9.983	54		8.85	9.983	54		8.81	10.023	30		13.66	6.476	5	
17.2	5.151	3		10.51	8.409	5		13.63	6.491	9		20.85	4.256	19	α-SiO_2
20.81	4.265	14	α-SiO_2	13.76	6.430	4		20.86	4.254	18	α-SiO_2	21.8	4.073	10	
23.7	3.751	4	Kyanite	20.82	4.263	13	Tridy.	21.65	4.101	15		23.5	3.782	8	
24.5	3.667	6	α-SiO_2	21.94	4.047	9	Tridy.	24.30	3.659	26		24.1	3.689	10	α-Fe_2O_3
26.67	3.339	100	α-SiO_2	23.60	3.766	7	Tridy.	26.60	3.348	100	α-SiO_2	25.18	3.533	7	
27.96	3.188	24	Kyanite	24.14	3.683	1		27.50	3.240	80		26.65	3.342	100	α-SiO_2
30.5	2.928	3		26.70	3.336	100	α-SiO_2	27.90	3.195	68		27.55	3.235	92	
31.10	2.873	4		27.94	3.190	98	Kyanite	31.13	2.870	36		27.9	3.195	50	Kyanite
33.25	2.692	16	α-Fe_2O_3	29.72	3.003	5	K_2O ?	33.25	2.692	67	α-Fe_2O_3	30.16	2.96	19	Kyanite
34.30	2.612	1	Kyanite	30.35	2.942	8	Kyanite	35.70	2.513	60	α-Fe_2O_3	33.2	2.696	20	α-Fe_2O_3
35.80	2.506	22	α-Fe_2O_3	33.15	2.700	14	α-Fe_2O_3 Kyanite	39.40	2.285	9	α-SiO_2	33.8	2.649	9	
36.55	2.456	5	α-SiO_2	35.15	2.551	14	Mn_3O_4 ?	41.00	2.199	12	α-Fe_2O_3	35.61	2.519	26	α-Fe_2O_3
39.50	2.279	3	α-SiO_2	35.96	2.495	11	Kyanite	41.70	2.164	7		38.65	2.327	3	Kyanite
40.95	2.202	3		36.70	2.446	6	Kyanite ?	42.47	2.126	10		39.5	2.279	4	
42.42	2.129	3	α-SiO_2	39.40	2.285	4	α-SiO_2	44.93	2.016	7		41.85	2.157	6	Kyanite ?
45.72	2.003	22	MgO ?	40.82	2.209	7	α-Fe_2O_3	49.61	1.836	18	α-Fe_2O_3	42.45	2.127	11	α-SiO_2
49.12	1.853	5		42.40	2.13	4		54.24	1.690	19	α-Fe_2O_3	45.8	1.979	3	α-SiO_2
50.13	1.818	4	α-SiO_2	45.41	1.995	9	Mn_3O_4	57.75	1.595	8		47.18	1.925	3	Kyanite ?
54.30	1.688	5	α-Fe_2O_3	49.45	1.841	5	α-Fe_2O_3	59.85	1.544	9	α-SiO_2	49.5	1.840	6	α-Fe_2O_3
54.92	1.670	5		50.06	1.820	7	α-SiO_2	62.60	1.483	16	α-Fe_2O_3	50.11	1.819	12	α-SiO_2

continued

TABLE 2.3.5(iii) (continued)

A				B				C				D			
2θ	d (Å)	I	Phase	2θ	d (Å)	I	Phase	2θ	d (Å)	I	Phase	2θ	d (Å)	I	Phase
57.85	1.592	2	Kyanite	54.08	1.694	5	α-Fe_2O_3	64.18	1.450	13	α-Fe_2O_3	54.15	1.692	3	α-Fe_2O_3
59.95	1.542	4	α-SiO_2	55.30	1.660	4	α-SiO_2	68.28	1.372	10	α-SiO_2	54.8	1.674	3	α-SiO_2
62.60	1.483	4	MgO or α-Fe_2O_3	59.92	1.542	6	α-SiO_2					56.5	1.627	10	
64.70	1.449	4	α-Fe_2O_3	62.42	1.486	4	α-Fe_2O_3					59.9	1.543	4	α-SiO_2
68.30	1.372	4	α-SiO_2	63.92	1.455	5	α-SiO_2					60.6	1.527	2	
				67.70	1.385	5						62.65	1.481	6	α-Fe_2O_3
				68.25	1.373	4	α-SiO_2					64.02	1.453	4	α-Fe_2O_3
												67.7	1.383	3	
												68.28	1.372	5	α-SiO_2

LEGENDS:

α-SiO_2 = α-Quartz; α-Fe_2O_3 = Hematite; Kyanite = $Al_2O_3.SiO_2$(sys. triclinic); Tridy = Tridymite (SiO_2)

TABLE 3.1.2

This table shows the elastic moduli and compliances of a single graphite crystal (After Kelly[32], p. 74)

Elastic Moduli (TPa)	Elastic Compliance x 10^{-12} M^2/N
$C_{11} = 1.06$ 0.02	$S_{11} = 0.98$ 0.03
$C_{12} = 0.18$ 0.02	$S_{12} = -0.16$ 0.06
$C_{13} = 0.015$ 0.005	$S_{13} = -0.33$ 0.08
$C_{33} = 0.0365$ 0.001	$S_{33} = 27.5$ 1.0
$C_{44} = 0.0045$	$S_{44} = 0.24 \times 10^{-10}$

TPa = Tera Pascal
= 10^{12} Pascals

TABLE 3.3(i)

This table shows the sieve analyses of the four graphites used in the aspect ratio measurements

Graphite Sample		A	B	C	D
B.S. Mesh sieve	Sieve Cut Range in µm	(${}^{W}/o$ retained)			
+30	> 500	7.76	-	7.82	1.00
-30+60	500-250	74.30	0.40	29.66	39.70
-60+100	250-150	12.00	30.11	25.05	56.12
-100+200	150-75	3.32	68.00	19.64	2.69
-200	< 75	2.62	1.50	17.84	0.50

TABLE 3.3.1(iii)(a)

Modes (most occurring) of thicknesses and lengths (all in microns) obtained from Figures 3.3.1(i)(a-d) and 3.3.1(ii)(a-d)

Graphite Sample	A		B		C		D	
Mesh Range	Thickness	Length	Thickness	Length	Thickness	Length	Thickness	Length
+30	25.30	963.00	-	-	37.59	1028.50	64.90	1028.50
-30+60	15.75	650.00	19.00	505.00	16.25	560.00	31.50	565.00
-60+100	12.25	405.00	13.25	345.00	9.38	385.00	22.63	435.00
-100+200	8.06	230.00	11.24	234.00	5.40	206.00	12.24	192.00
-200	3.90	22.50	4.98	29.50	3.30	32.00	5.07	111.00
*Slope (Aspect ratio)	44.54		34.38		26.97		15.51	

* From Figure 3.3.1(iii)(a) the slopes of the straight lines (length/thickness) were determined, and the slope for each graphite sample is equal to its aspect ratio.

TABLE 3.3.1(iii)(b)

Arithmetic means of thicknesses and lengths of total number of flakes measured in each sieve cut. The mean values are all in microns

Graphite Sample	A		B		C		D	
Mesh Range	Thickness	Length	Thickness	Length	Thickness	Length	Thickness	Length
+30	36.69	1004.52	-	-	45.77	1065.21	60.8	1058.98
-30+60	23.72	665.47	21.97	493.97	21.64	649.64	33.41	572.43
-60+100	14.62	407.36	15.95	322.55	12.51	389.45	23.75	414.90
-100+200	10.23	221.84	14.17	222.60	7.99	185.33	11.08	223.61
-200	5.46	31.60	6.93	40.61	4.00	44.23	9.44	104.18
*Slope (Aspect ratio)	33.70		30.60		23.80		17.72	

* From Figure 3.3.1(iii)(b) the slopes of the straight lines were determined and the slope for each graphite sample is equal to its aspect ratio (length/thickness).

TABLE 3.3.2

Weight distributions of Graphite A (see Section 3.3.2)

Thickness Size range (microns)	Wt.% distribution in each sieve cut +30	-30+60	-60+100	-100+200	-200	Total
0-5	0.00	0.00	0.01	0.02	0.15	0.17
5-10	0.00	0.09	0.23	0.19	0.76	1.28
10-15	0.00	0.69	0.82	0.46	0.94	2.92
15-20	0.07	1.53	1.73	0.86	0.77	4.96
20-25	0.19	2.36	1.94	0.34	2.62	4.82
25-30	0.16	2.21	0.84	0.36		3.55
30-35	0.27	2.42	1.03	1.09		4.78
35-40	0.49	3.38	1.44	3.32		5.30
40-45	0.20	3.13	2.32			5.65
45-50	0.27	10.23	0.00			10.50
50-55	0.72	0.00	1.69			2.41
55-60	0.00	2.69	12.00			2.69
60-65	0.25	3.05				3.30
65-70	0.84	3.80				4.64
70-75	0.73	10.32				11.06
75-80	1.27	0.00				1.27
80-85	1.56	7.38				8.93
85-90	0.00	9.02				9.02
90-95	0.73	0.00				0.73
95-100	7.75	12.00				12.00
		74.30				100.01

An illustration of how the weight distributions were obtained in each graphite sample after converting number distributions to weight distributions in any given thickness or length interval using the method described in Appendix 3.3.2(a).

TABLE 4.4.2(a)

Magnesia grain size mixtures only

Bulk density and porosity values determined from specimens prepared by using Andreasen's[46] method of combining different grain size fractions of magnesia. The largest grain size in the mixture is 3.35 mm

n-value	Green state Bulk Density x 10^3 kg/m^3	Green state % Porosity	Fired state Bulk Density x 10^3 kg/m^3	Fired state % Porosity
0.3	2.90	15.9	2.89	16.2
0.4	2.93	14.8	2.92	15.1
0.5	2.93	14.8	2.92	15.2
0.6	2.91	15.5	2.89	16.0
0.7	2.92	15.3	2.93	14.9
0.8	2.88	16.4	2.90	15.8
0.9	2.88	16.4	2.85	17.1
1.0	2.85	17.2	2.83	17.8

TABLE 4.4.2(b)

MgO grain size mixtures

Bulk density and porosity values determined from specimens prepared by using Hugill's method

Mixture No.	Green state Bulk Density x 10^3 kg/m^3	Green state % Porosity	Fired state Bulk Density x 10^3 kg/m^3	Fired state % Porosity
1	2.87	16.7	2.9	16.5
2	2.88	16.4	2.9	16.4
3	2.9	15.4	2.9	15.6

TABLE 5.3.3.1(b)

This table shows the weight percent losses of magnesia-graphite composite specimens, containing 80 parts magnesia + 20 parts graphite B + 5 parts pitch in the green state, after oxidizing the pitch and graphite at 485°C and 1300°C respectively in an oxidizing atmosphere. The batch from which these specimens were made was warm mixed in the mixer shown in Figure 5.3.2(i).

Sample No.	Wt. before firing	Wt. after removing the pitch (485°C)	Weight loss	$^{w}/_{o}$ loss	Weight after firing to 1300°C	Weight loss	$^{w}/_{o}$ loss	Total $^{w}/_{o}$ loss
1	50.0030	47.5800	2.4230	4.85	38.9849	-	-	-
2	50.0016	47.5017	2.4999	5.00	38.4765	-	-	-
3	49.9986	47.5171	2.4815	4.96	-	-	-	-
4	50.0040	47.5845	2.4195	4.84	-	-	-	-
5	50.0000	47.6243	2.3757	4.75	39.2179	8.3904	17.62	22.37
6	49.9915	47.4880	2.5040	5.01	38.5918	8.8912	18.73	23.74
7	49.9920	47.6430	2.3490	4.70	38.9275	8.6895	18.25	22.95
8	50.0059	47.6850	2.3210	4.64	39.1349	8.4739	17.80	22.44
9	50.0044	47.5175	2.4870	4.97	-	-	-	-
10	50.0297	47.6997	2.3300	4.66	39.5876	8.0833	16.96	21.62
11	50.0047	47.5762	2.4290	4.86	39.0442	8.5297	17.93	22.79
12	49.9977	47.5857	2.4120	4.82	-	-	-	-
13	50.0020	47.6777	2.3243	4.65	39.2580	8.3985	17.62	22.27
Average weight percent losses only				4.79 ±0.15			17.84 ±0.52	22.60 ±0.66
Expected total weight loss								21.60

N.B. Graphite B had an ash content of 11.59 $^{w}/_{o}$ (see Table 2.3.1(ii)).

TABLE 5.5.3

The table shows the sonic velocity measurements of discs made out of graphite samples only. Also the velocity measurements of magnesia with pitch are shown.

	Before Firing (Green)				After Firing (1500°C)			
Graphite	Bulk Density g/cc	Total Porosity	Sonic Velocity m/sec x 10^3	ρC_L^2 GPa	Bulk Density g/cc	Total Porosity	Sonic Velocity m/sec=C_L x 10^3	ρC_L^2 GPa
A	2.13	4.17	0.7	1.04	1.97	11.75	0.60	0.72
B	2.18	3.20	1.13	2.79	2.01	10.86	0.57	0.66
C	2.10	5.51	0.6	0.83	1.88	15.21	0.50	0.46
D	2.15	3.17	0.81	1.41	2.01	9.49	0.62	0.78
					100 $^{W}/o$ + 5 $^{W}/o$ Pitch			
				n-value				
				0.3	2.64	22.04	2.31	14.09
				0.5	2.66	21.50	2.16	12.41
				0.6	2.63	22.41	2.8	20.77
				0.7	2.64	21.95	2.65	18.54
				0.8	2.58	23.81	2.59	17.31
				0.9	2.58	23.72	2.34	14.13
				1.0	2.57	24.10	2.05	10.80

N.B. ρC_L^2 is the calculated relative elastic modulus (see Section 5.4.2).

TABLE 6.2.

Chemical Analysis of Slag 161R
(As determined by the supplier)

Sample dried at 110°C

	%		%
Silica (SiO_2) ...	20.7	Zinc Oxide (ZnO) ...	0.63
Titania (TiO_2) ...	1.36	Barium Oxide (BaO) ...	0.04
Alumina (Al_2O_3) ...	4.36	Strontia (SrO) ...	...
Ferric Oxide (Fe_2O_3) ...	23.0	Vanadium Pentoxide (V_2O_5) ...	...
Lime (CaO) ...	22.1	Cobalt Oxide (Co_3O_4) ...	...
Magnesia (MgO) ...	13.9	Nickel Oxide (NiO) ...	1.13
Potash (K_2O) ...	0.03	Cupric Oxide (CuO) ...	...
Soda (Na_2O) ...	0.09	Stannic Oxide (SnO_2) ...	...
Phosphorus Pentoxide (P_2O_5) ...	0.04	Boric Oxide (B_2O_3) ...	...
Chromium Sesquioxide (Cr_2O_3) ...	13.7	Lithia (Li_2O) ...	...
Manganic Oxide (Mn_3O_4) ...	3.47	Fluorine (F) ...	...
Zirconia (ZrO_2) ...	0.05		
Hafnia (HfO_2) ...	...		
Lead Monoxide (PbO) ...	0.05		

FIGURES

TYPICAL BOF SERVICE LINING

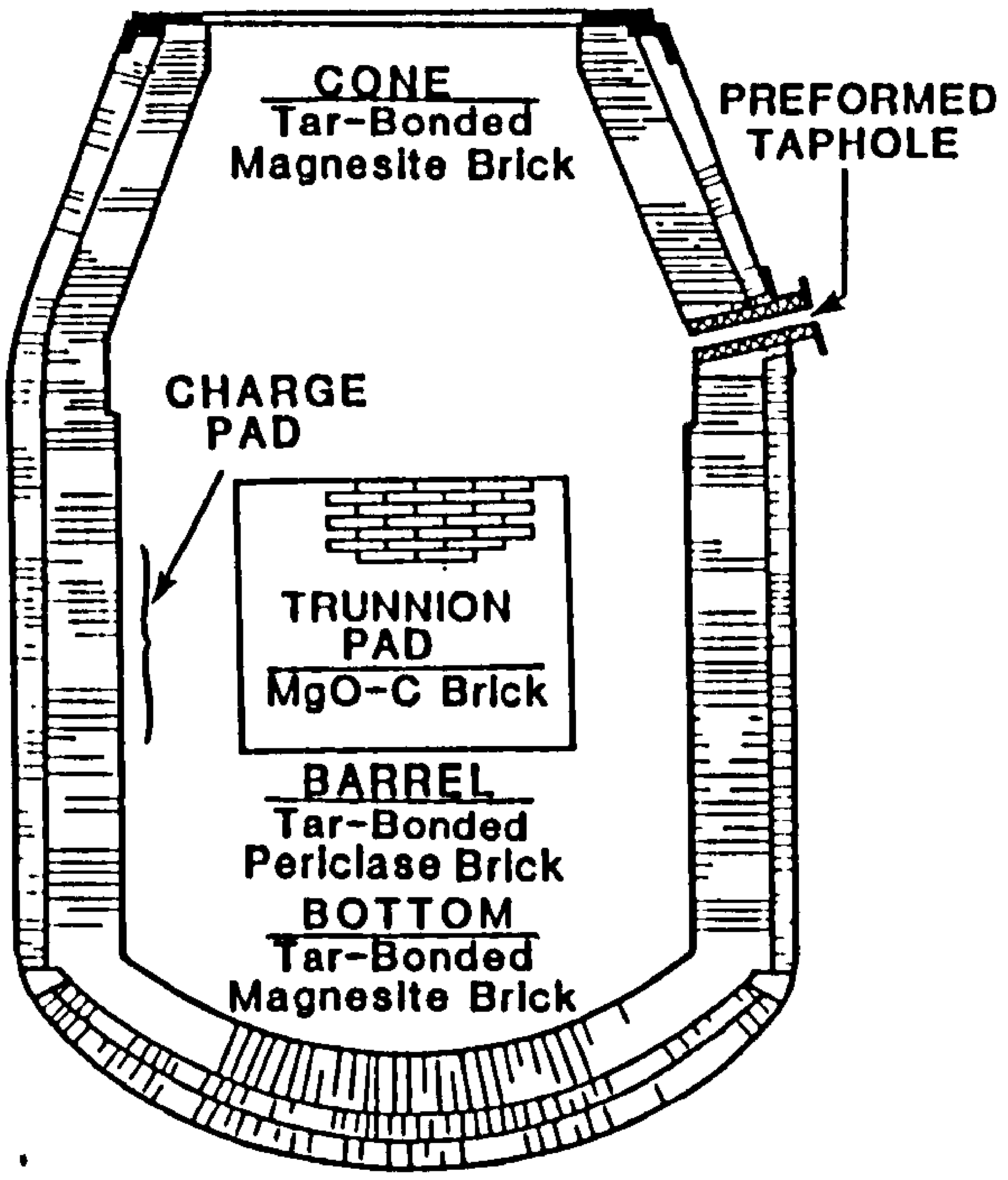

Fig. 1.5.1(a) showing current practices in the lining of BOF furnaces.[14]

PROPERTIES OF BOF BRICK

Type	Tempered Tar-Bonded Magnesite	Tempered Tar-Bonded Periclase	MgO-C	MgO-C	MgO-C	Burned, Tar-Impregnated
Residual Carbon Level,%	4-5	4-5	18-20	18-20	>20	2 0-2.5
Usual Application	Bottom;Cone	Barrel	Trunnion Pads	Trunnion Pads	Trunnion Pads	Charge Pad
Grain Type	Sintered	Sintered	Sintered	Sintered& Fused	Sintered	Sintered
Carbon Additive	Carbon Black	Carbon Black	Flake Graphite	Flake Graphite	Flake Graphite	·
Bond Type	Pitch	Pitch	Pitch	Resin	Resin	Ceramic
Chemical Analysis of Grain Component (ignited basis),%						
MgO	93.6	96.5	96.5	98.9	98 3	96 0
CaO	3 6	2.3	2.3	0.5	0.6	2 3
SiO_2	2.3	0.8	0 8	0.2	0.7	1 3
Residual Carbon,%	4.5	4 5	18.5	19.2	22.3	2.3
As-Received Bulk Density,g/cm^3	3.10	3.12	2.85	2.83	2.80	3.15
Coked Apparent Porosity,%	10.0	9.0	10.0	11.7	11.5	12 0
Modulus of Rupture,kg/cm^2						
As-received	105	112	112	128	138	134
Coked	60	63	24	41	36	—
At 1482°C	—	—	—	—	—	77

Table 1.5.1(a) showing various bricks being used in the BOF furnace and the Ω-BOP furnace[14] (see Figures 1(a) and 1(b)).

TYPICAL Q-BOP SERVICE LINING

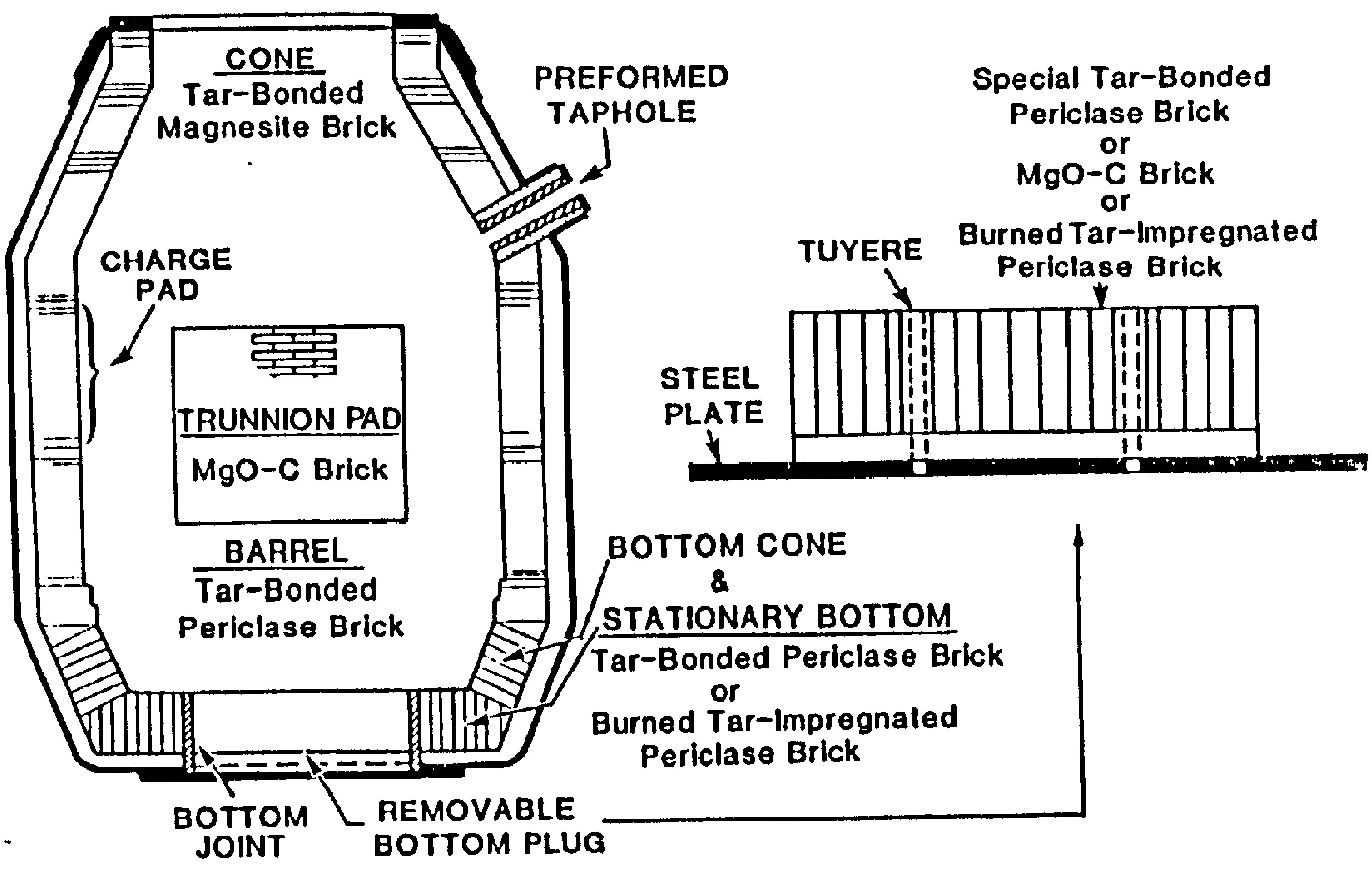

Fig. 1.5.1(b)

TYPICAL EAF HEARTH, SLAGLINE, AND SIDEWALL INSTALLATIONS.

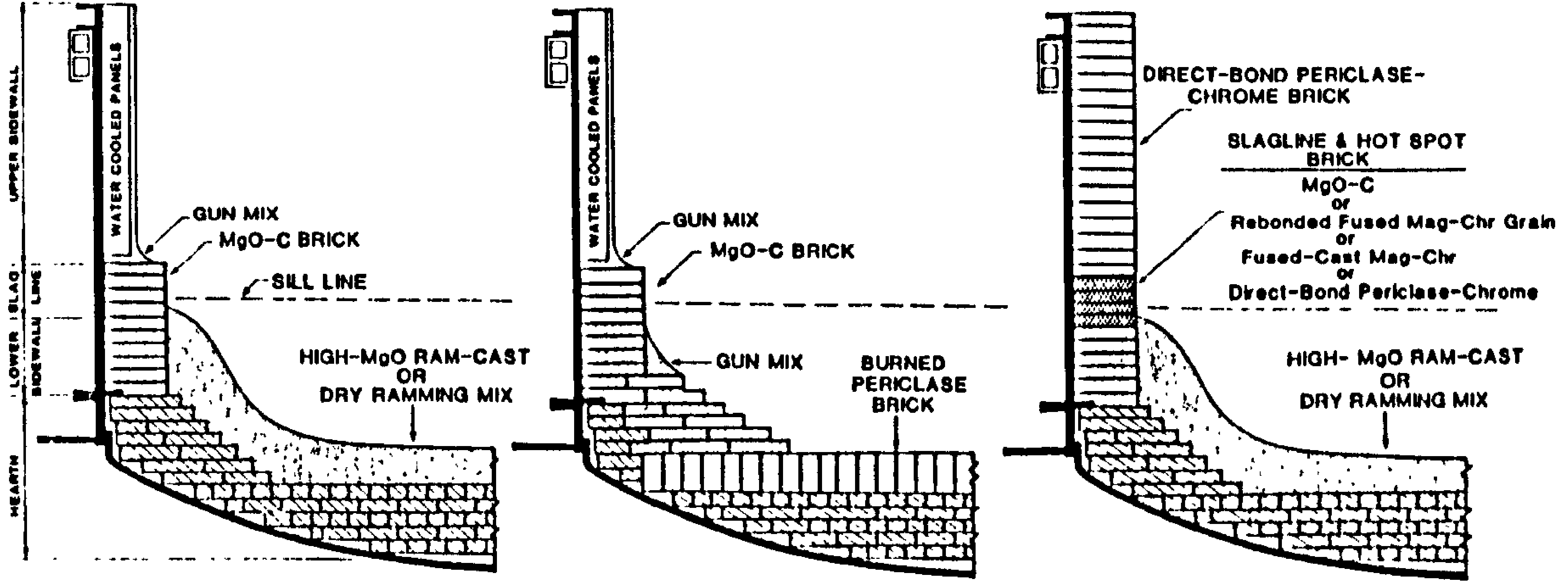

A. HP or UHP EAF with Watercooled Panels and Rammed or Cast Hearth

B. HP or UHP EAF with Watercooled Panels and Brick Hearth

C. EAF without Watercooled Panels or LP EAF with Rammed or Cast Hearth

Fig. 1.5.1(c)

PROPERTIES OF EAF SIDEWALL AND SLAGLINE BRICK

TYPE	Direct-Bond Periclase-Chrome	Direct-Bond Periclase-Chrome	Rebonded Fused Grain	MgO-C (Amorphous Graphite)	MgO-C (Flake Graphite)	MgO-C (Flake Graphite)
USUAL APPLICATION	Sidewall	Sidewall	Slagline	Slagline; hot spots	Slagline; hot spots	Slagline; hot spots
CHEMICAL ANALYSIS (IGNITED BASIS),%				(chemical analysis of grain component only)		
MgO	60.6	80.3	56.0	96.5	96.5	96.5
CaO	0.5	0.6	0.9	2.3	2.3	2.3
SiO_2	1.9	1.4	2.2	0.8	0.8	0.8
Cr_2O_3	16.5	7.8	19.9	—	—	—
RESIDUAL CARBON,%	—	—	—	7.8	12.5	18.5
AS-RECEIVED BULK DENSITY,g/cm³	3.12	3.00	3.34	3.03	2.93	2.85
APPARENT POROSITY,%	17.0	17.5	13.0	9.0 (coked)	9.7 (coked)	10.0 (coked)
MODULUS OF RUPTURE,kg/cm²						
As-Received	53	47	182	109	105	112
Coked	—	—	—	39	21	24
At 1482°C	42	23	59	—	—	—

Table 1.5.1(b) showing properties, chemical composition and areas of application of various bricks in the Electric Arc Furnace (EAF)[14]. (See also Fig. 1(c)).

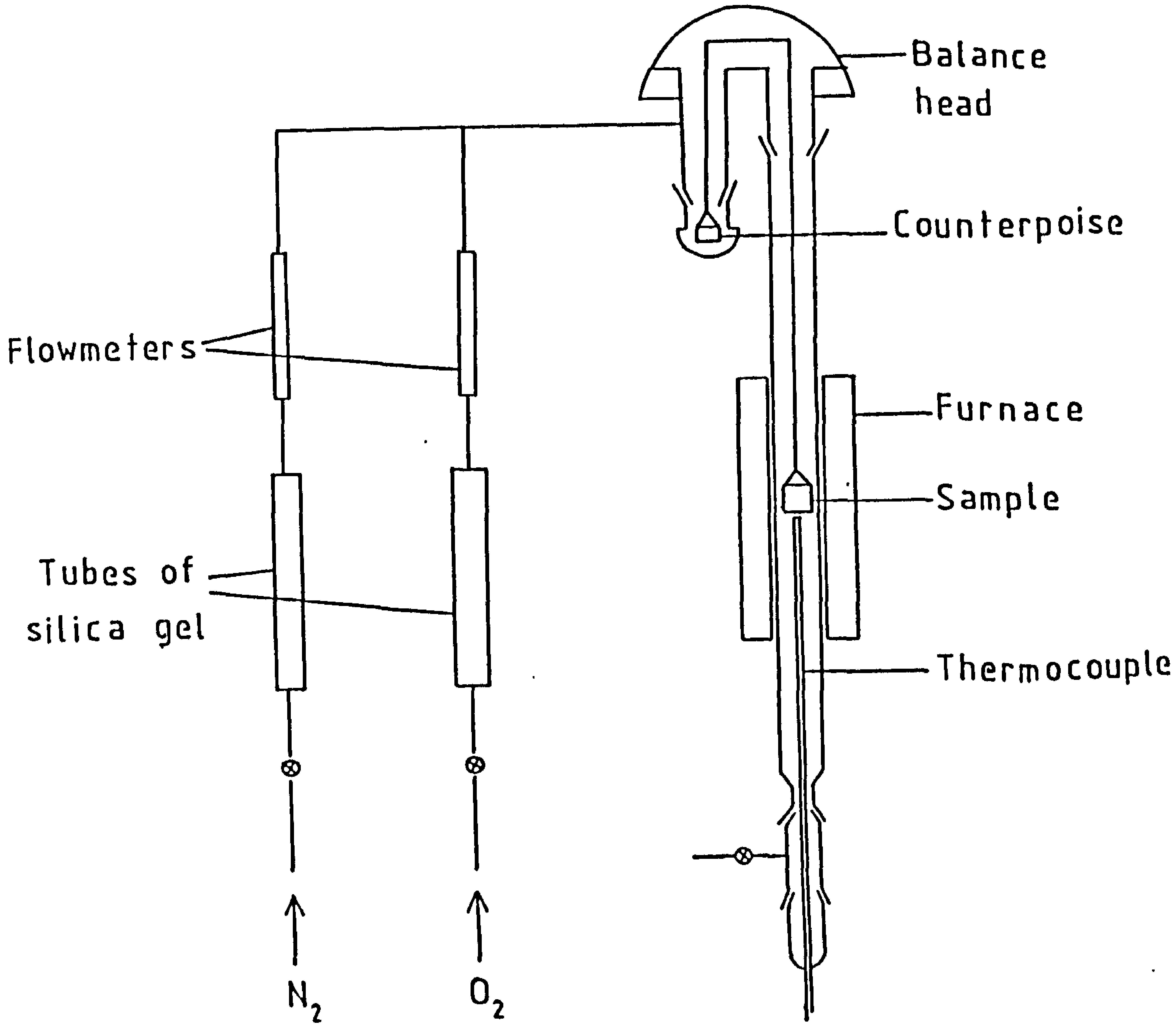

Fig. 2.3.2(i) Schematic diagram of a CI Electronics Mark 3 Microbalance used in thermogravimetric analysis.

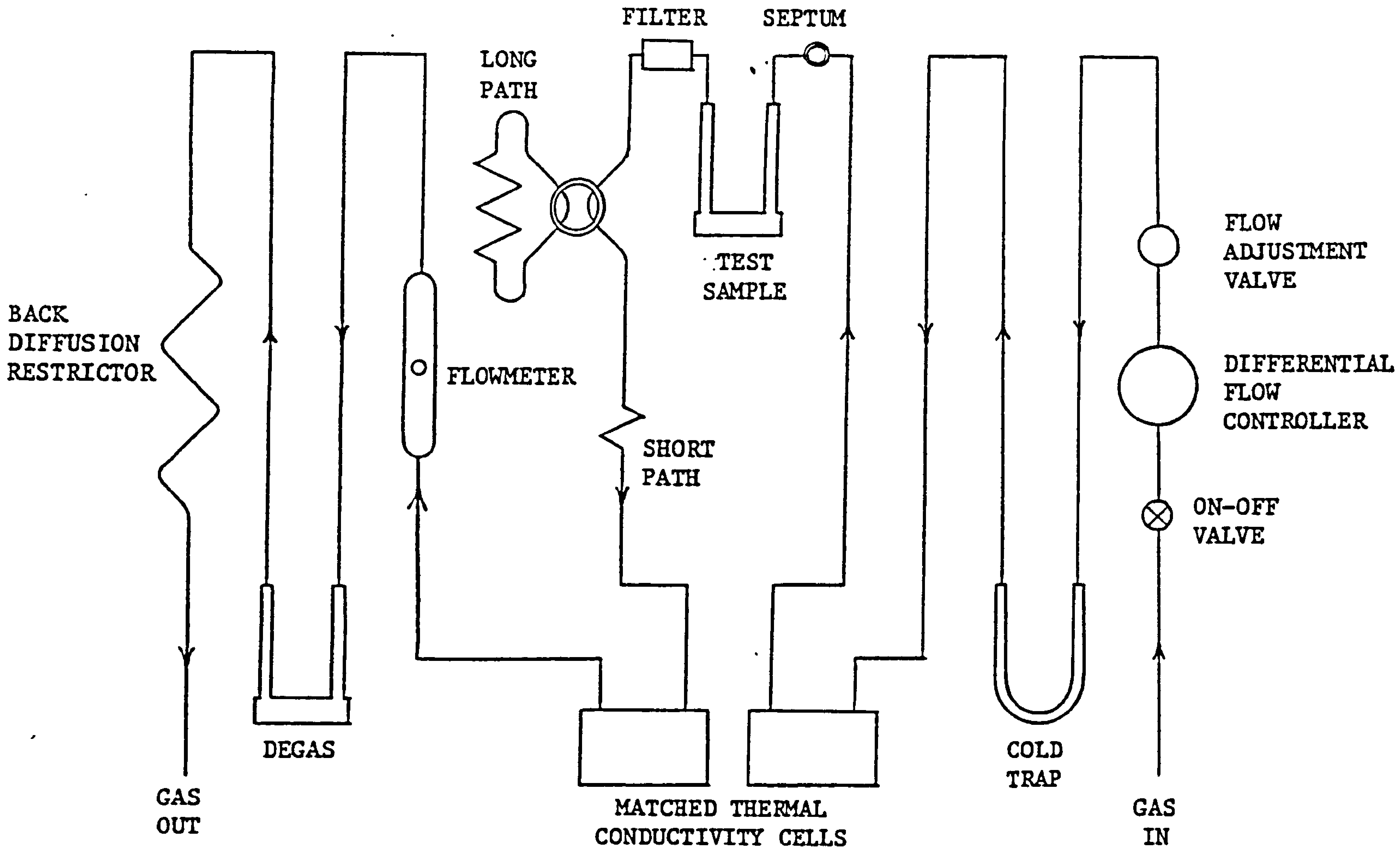

Fig. 2.3.4(ii) Schematic diagram of FlowSorb 2300 used in specific surface area determinations of the graphites and coked binders. (After Ref. 24).

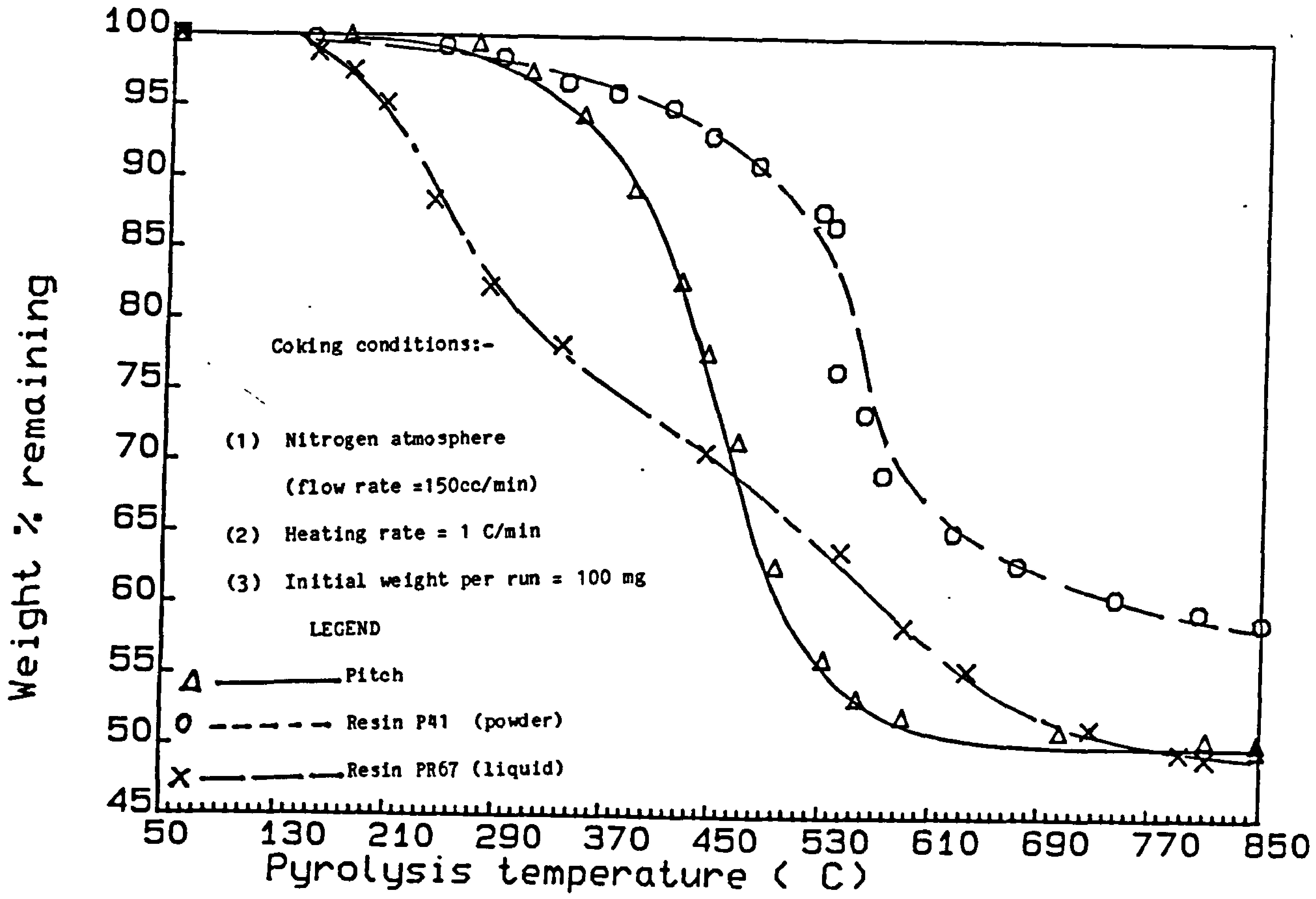

FIG. 2.4.4 :Wt.% remaining V's pyrolysis temperature of resins & pitch

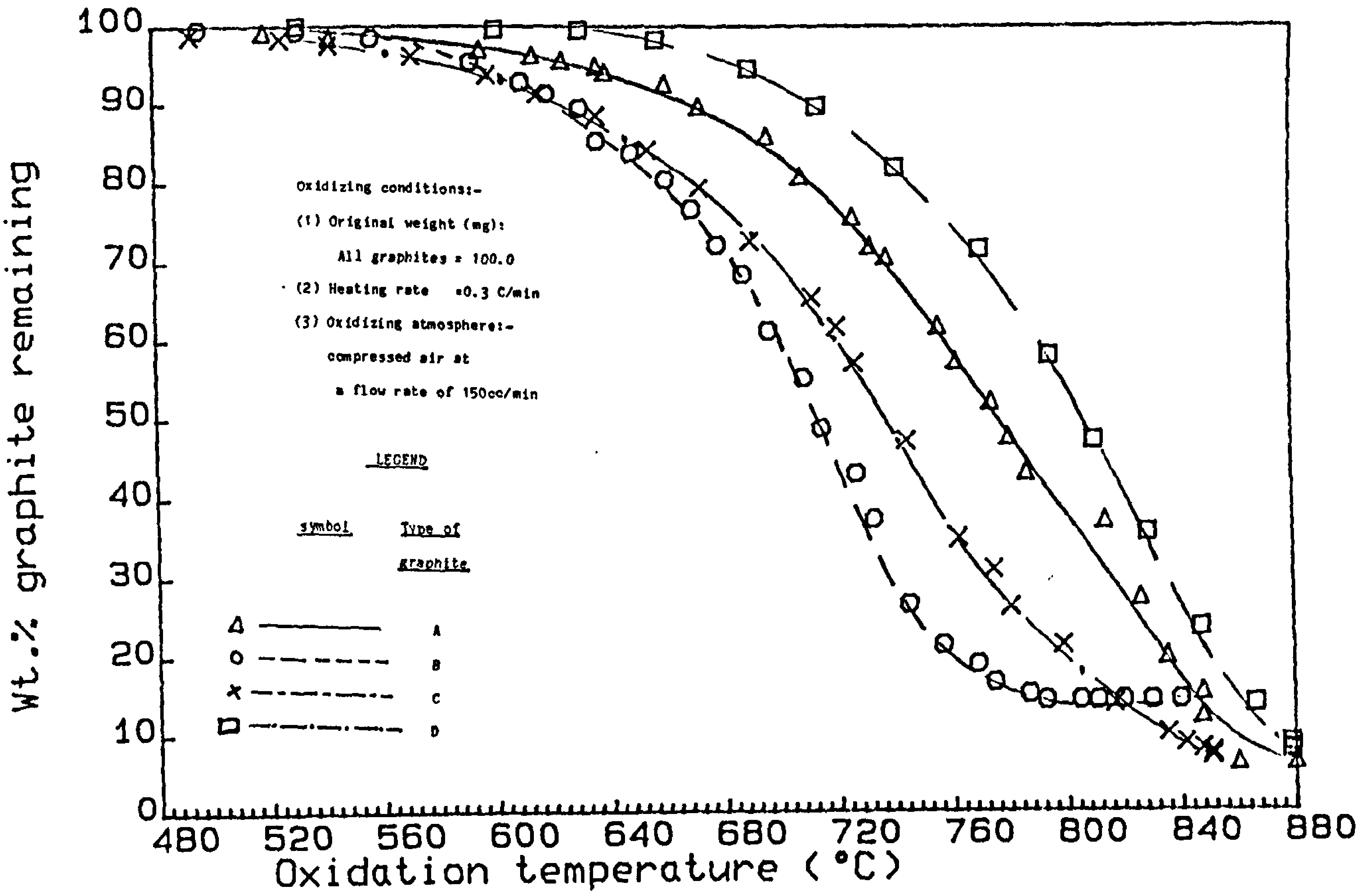

FIG. 2.4.5 (i):Wt.% graphite remaining V's oxidation temperature(°C)

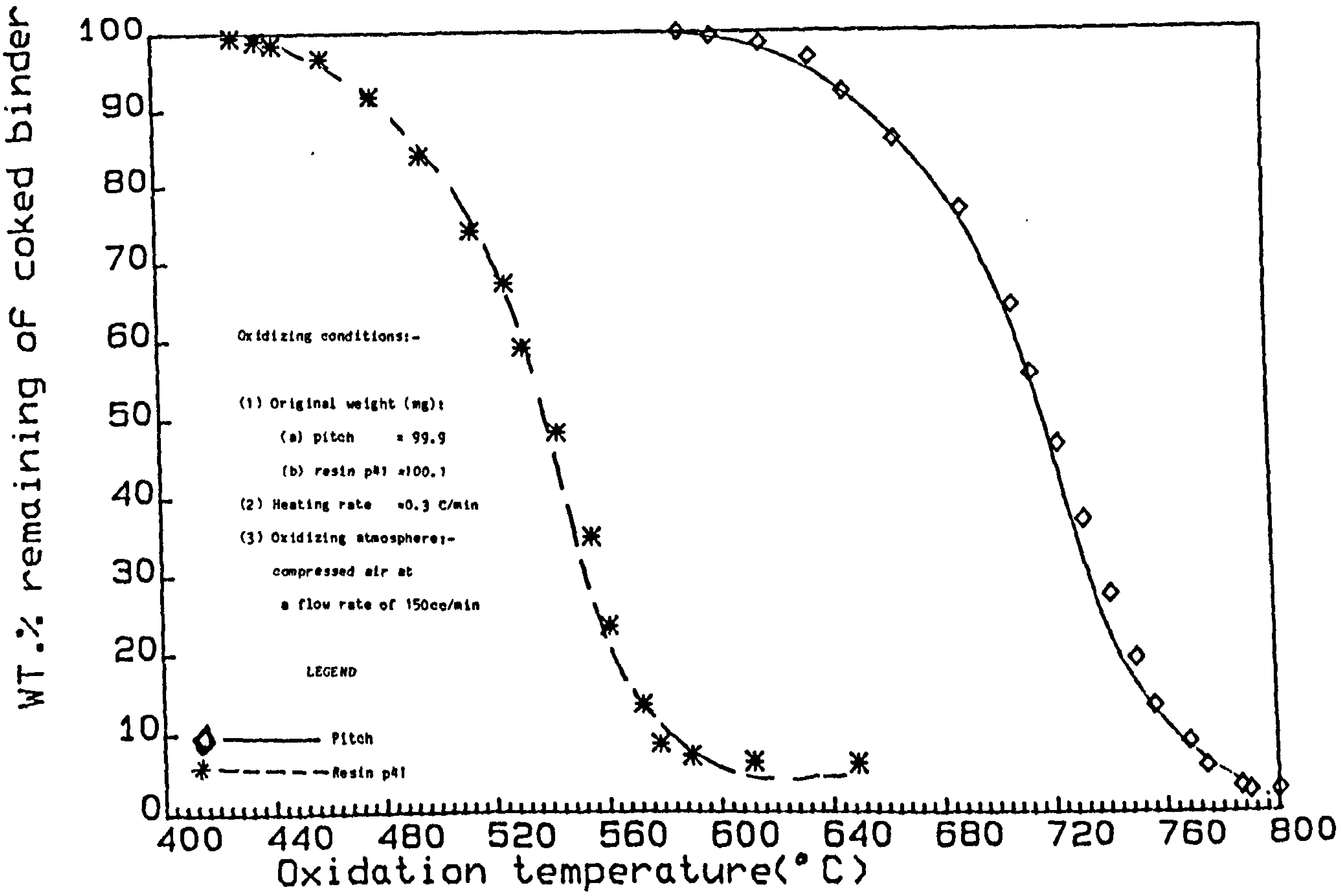

FIG. 2.4.5 (ii):Wt.% of coked binder remaining V's oxidtion temperature (°C)

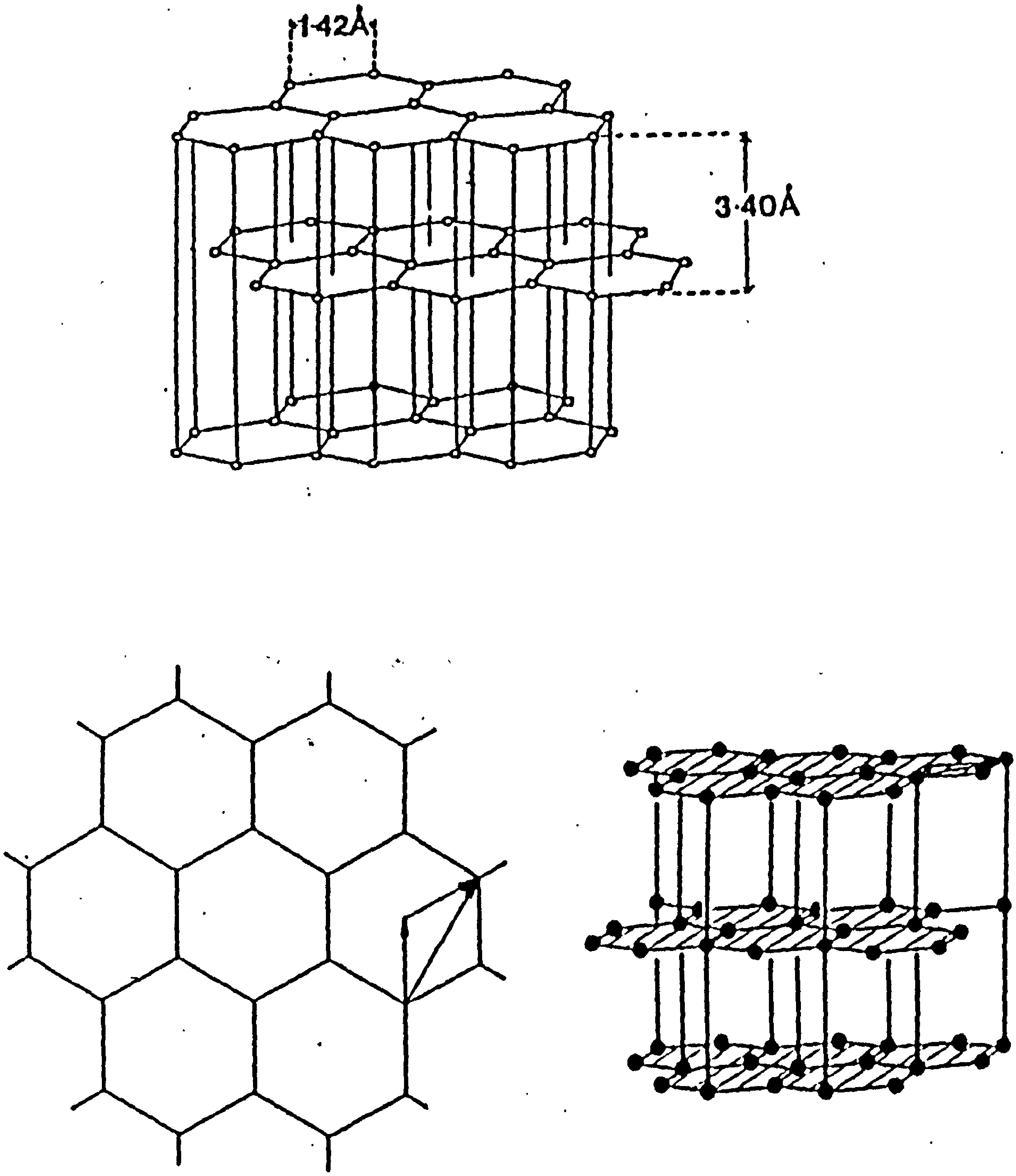

Fig. 3.1.2(a) The structure of single crystal graphite. (After Amelincky et al.[40]).

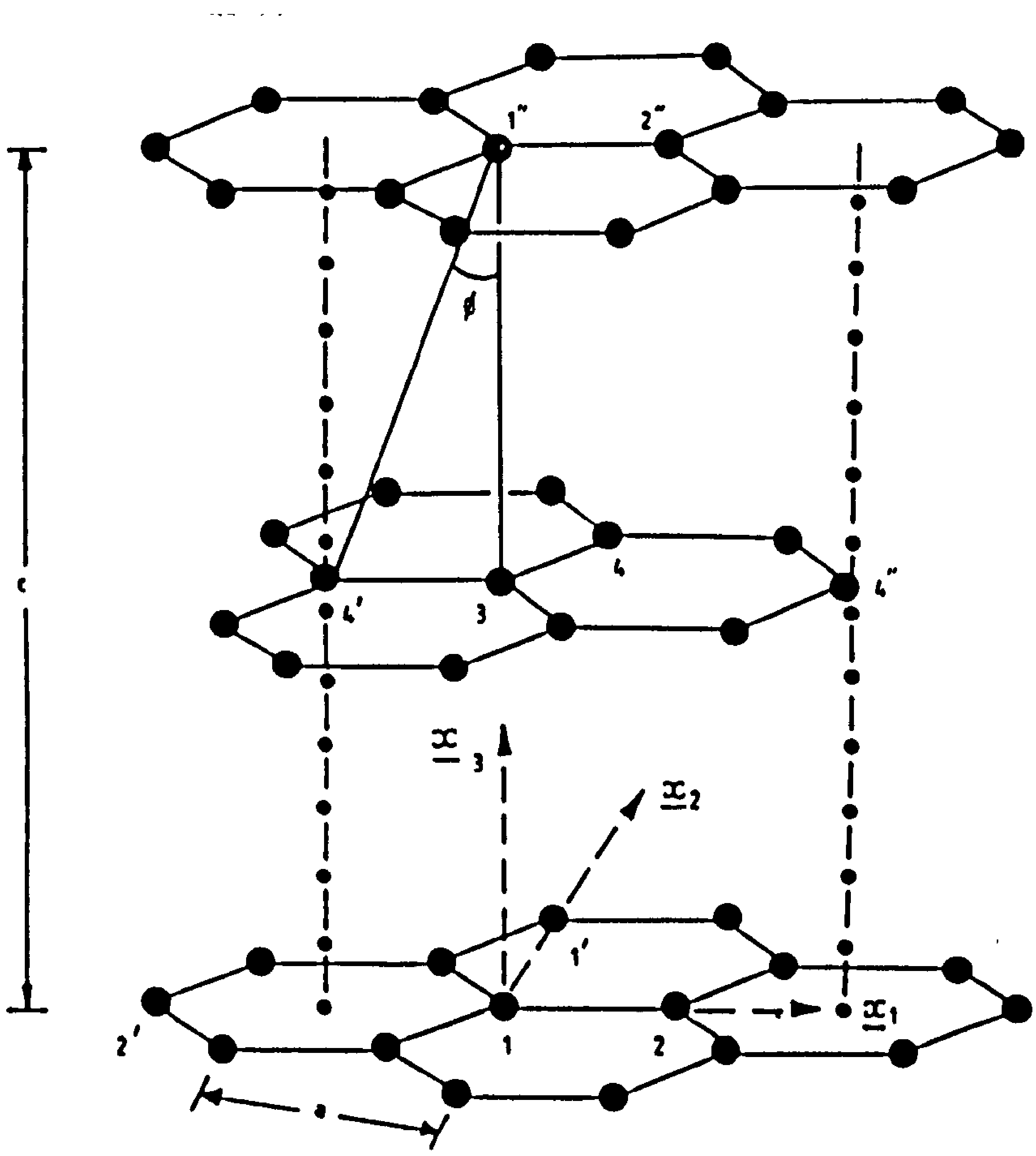

Fig. 3.1.2(b) showing the structure of single crystal graphite and the angle ϕ giving the direction, with the hexagonal axis, in which Young's modulus may be measured. (After Kelly[33]).

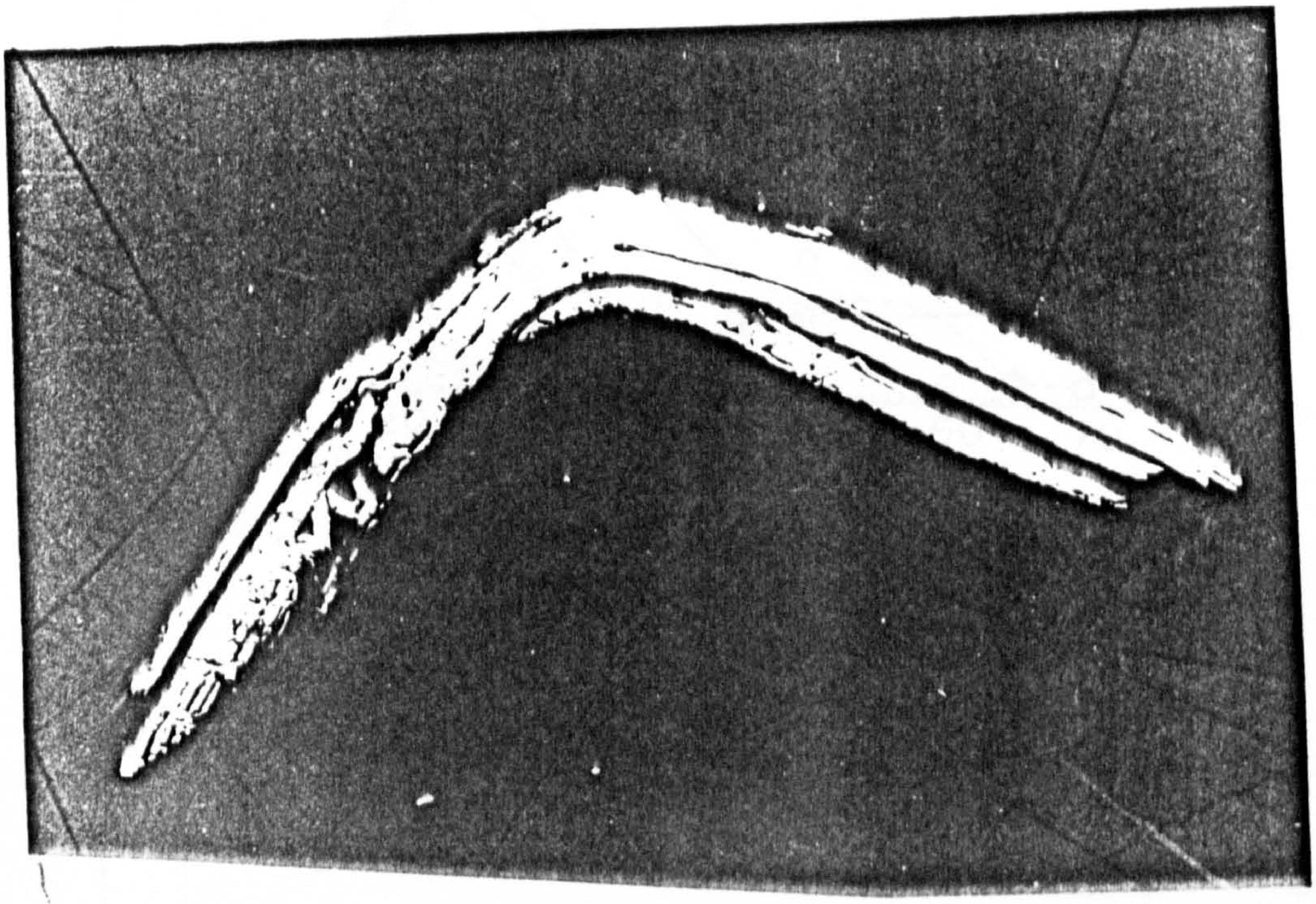

Fig. 3.1.2(c) Bent flake illustrating the flexibility of graphite. (After Cooper[37]).

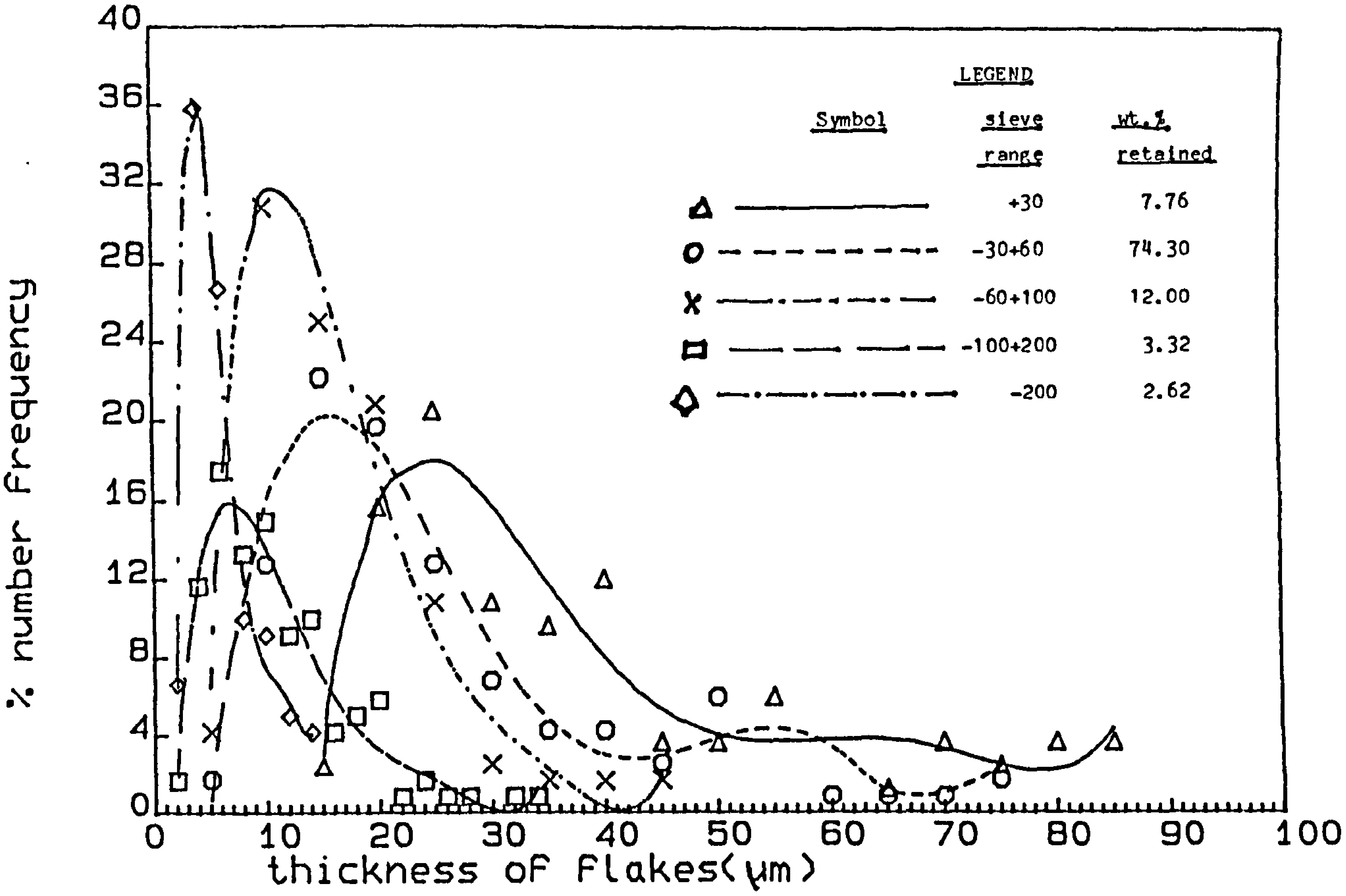

FIG. 3.3.1 i(a):% number Frequency V's thickness of Flakes(μm):GRAPHITE A

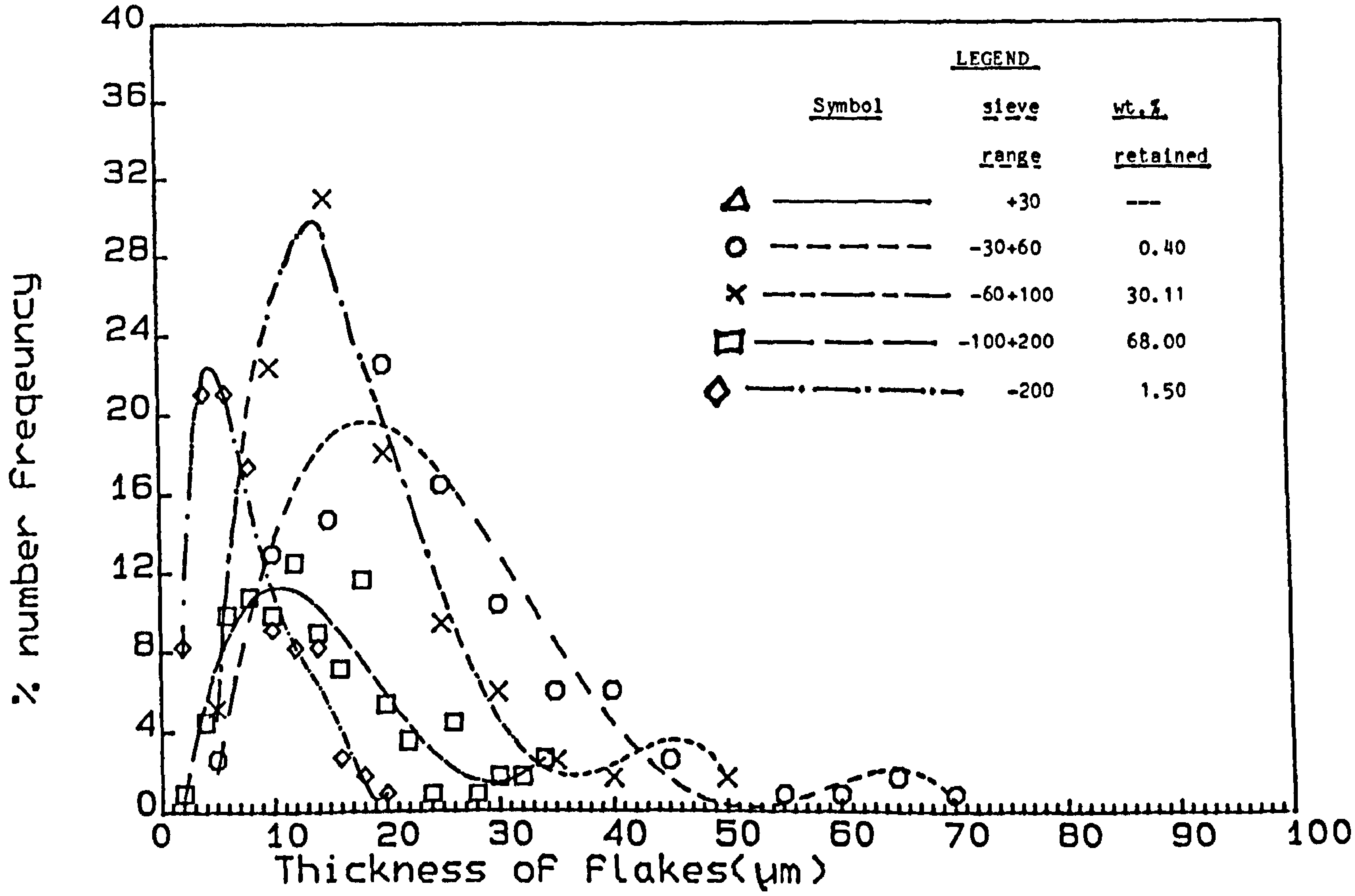

FIG. 3.3.1 i(b):% number Frequency V's thickness of Flakes(μm):GRAPHITE B

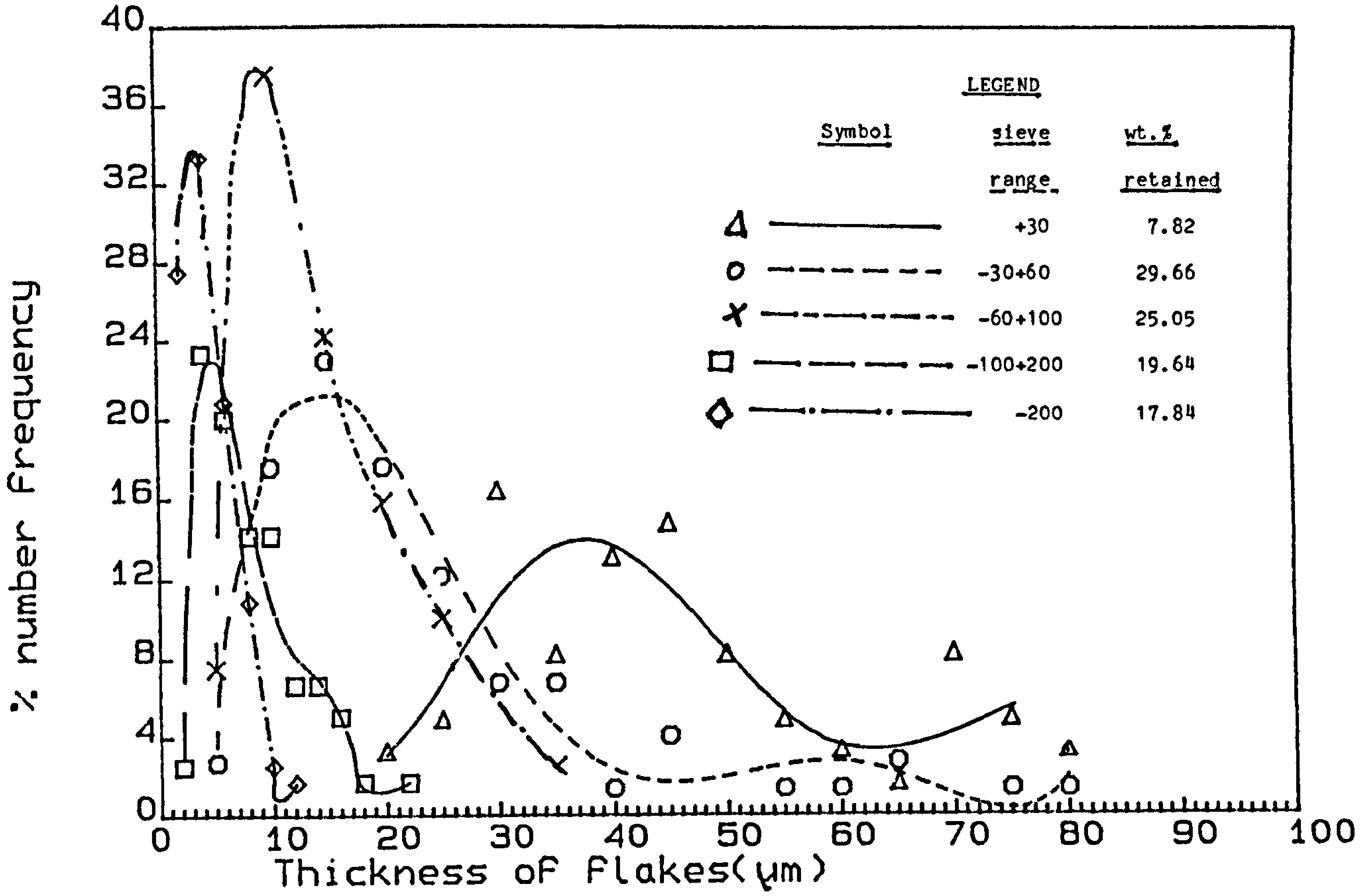

FIG. 3.3.1 i(c):% number frequency V's thickness of flakes(μm):GRAPHITE C

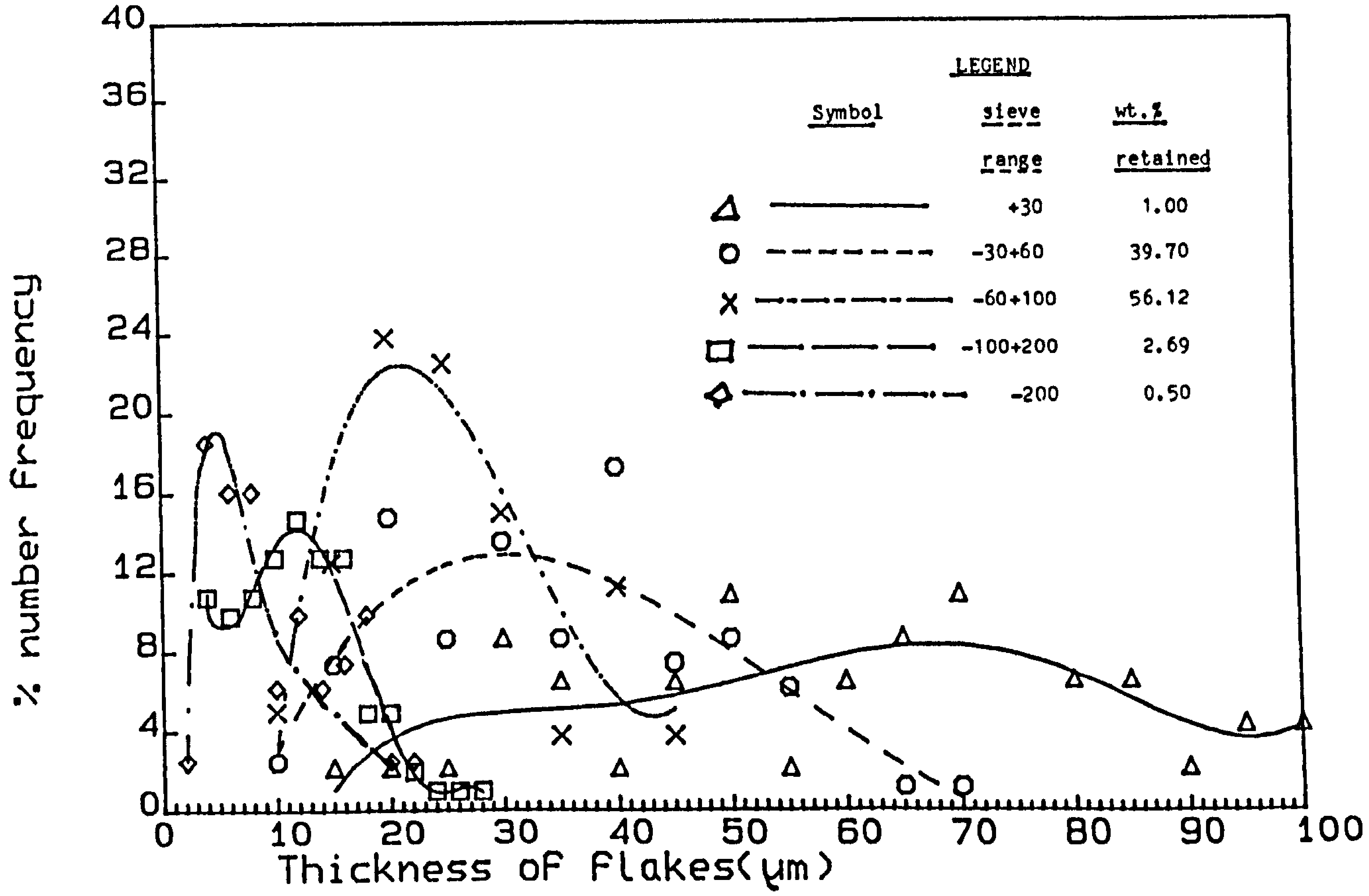

FIG. 3.3.1 i(d):% number frequency V's thickness of flakes(μm):GRAPHITE D

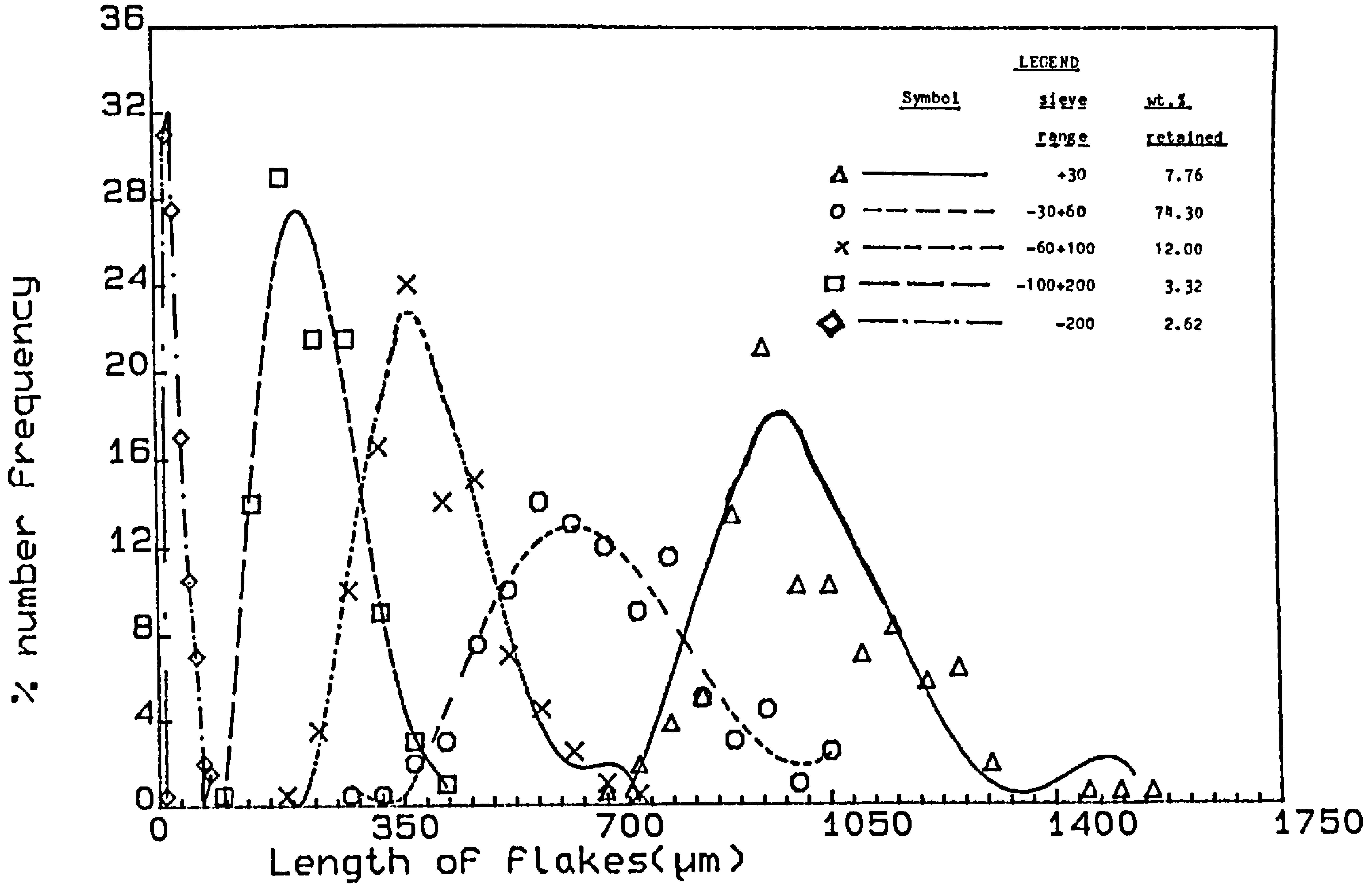

FIG. 3.3.1 ii(a):% number frequency V's length of flakes(µm):GRAPHITE A

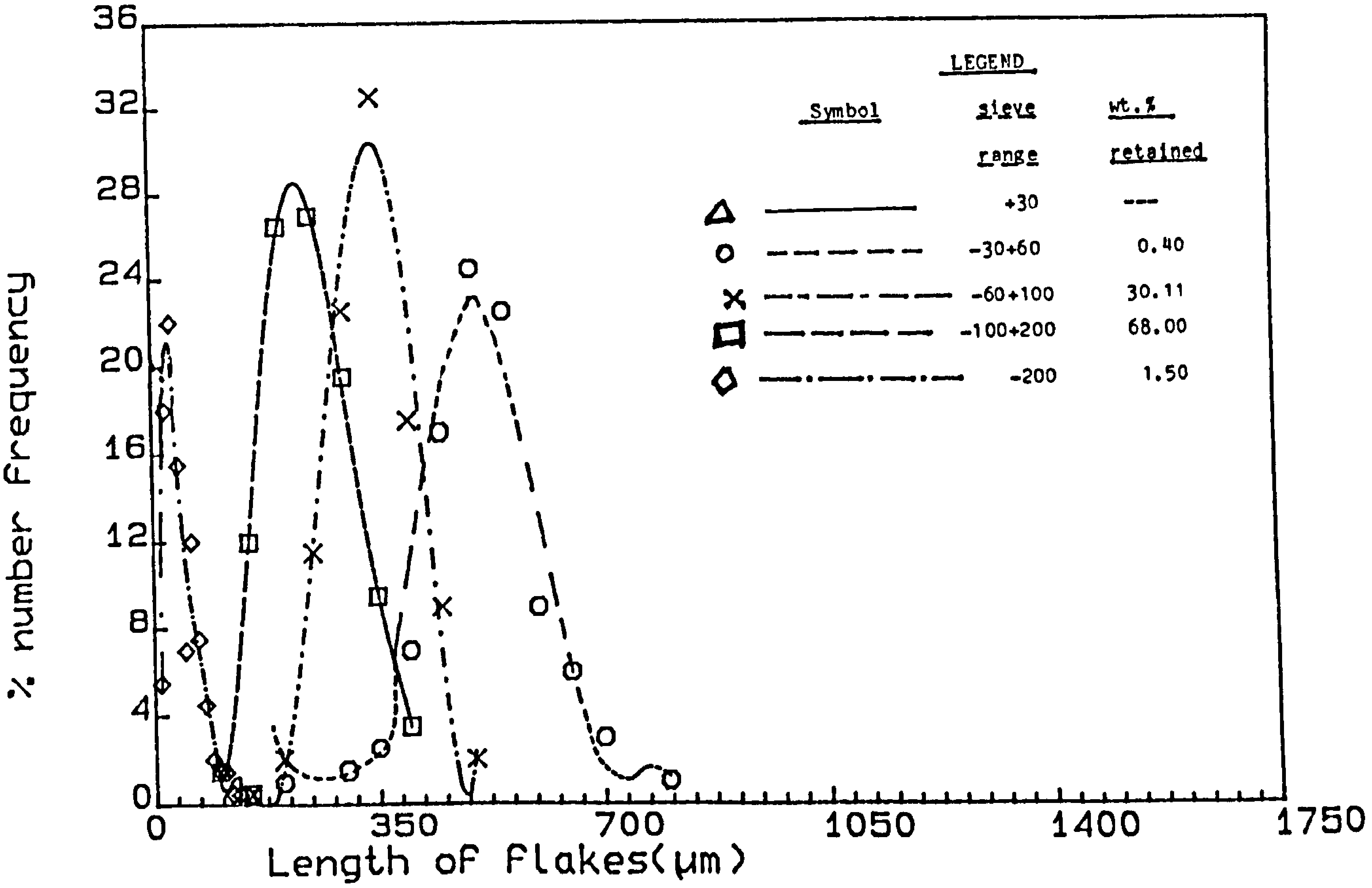

FIG. 3.3.1 ii(b):% number frequency V's flake length(µm):GRAPHITE B

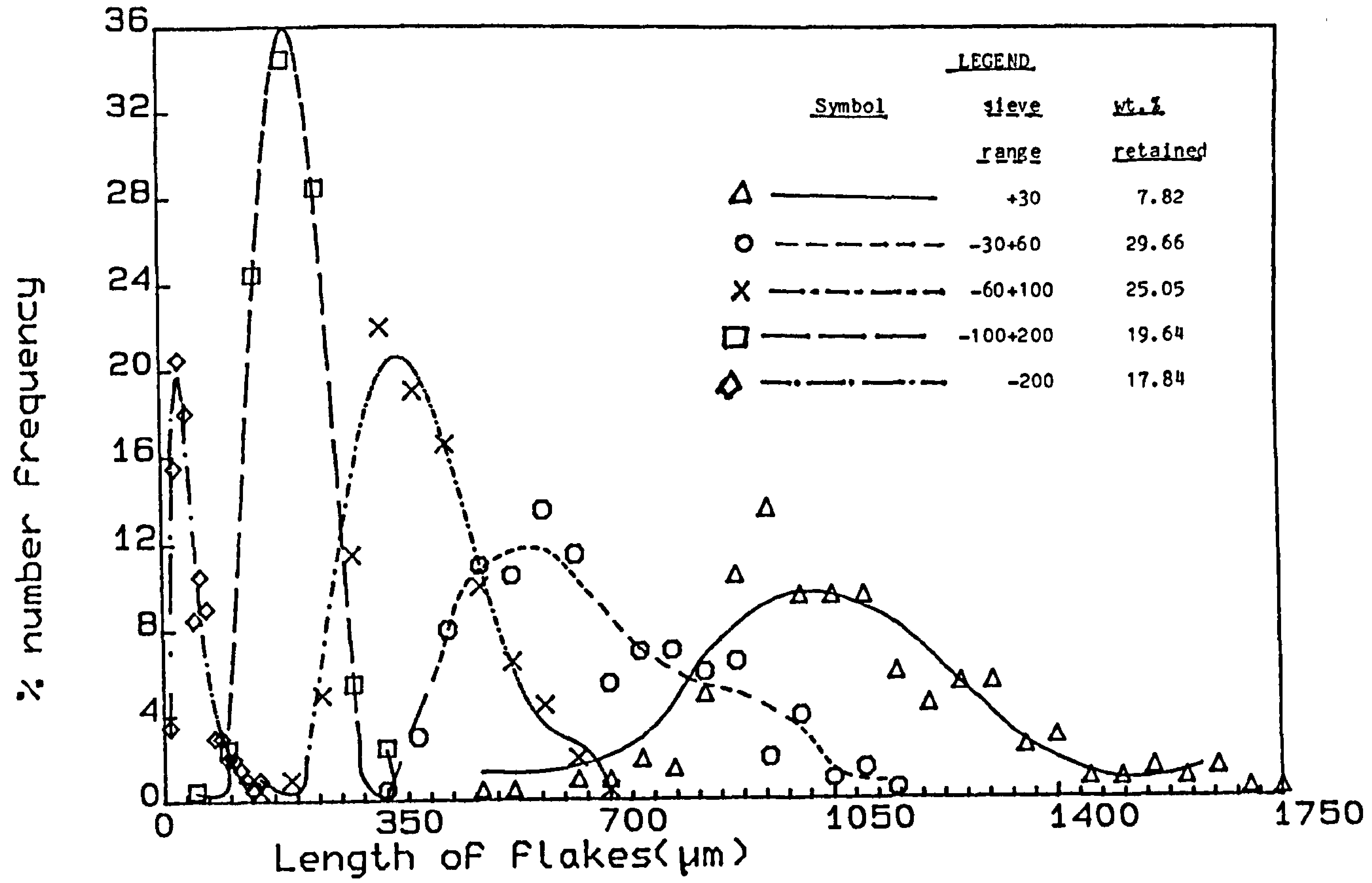

FIG. 3.3.1 ii(c):% number Frequency V's Flake Length(μm):GRAPHITE C

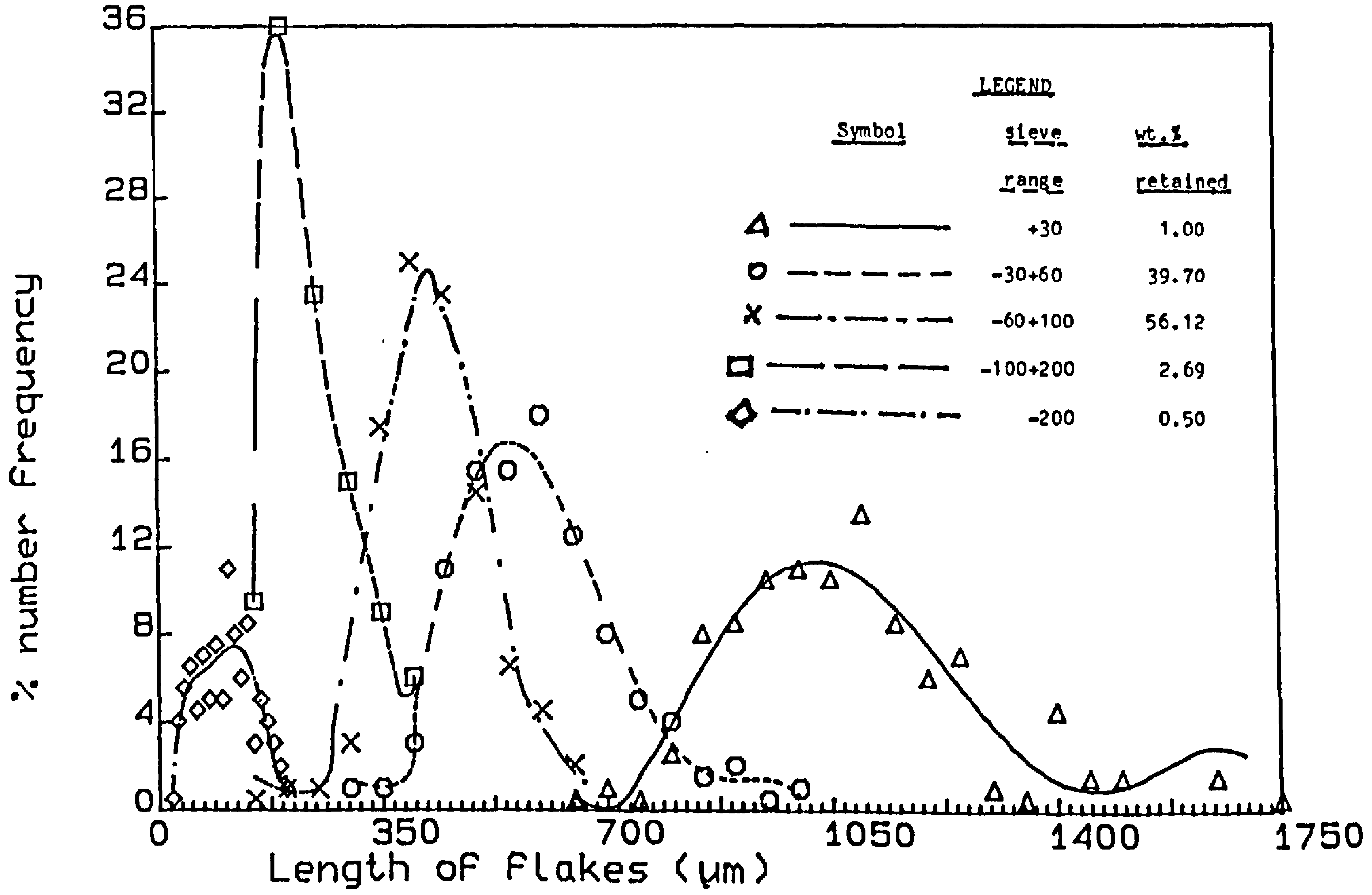

FIG. 3.3.1 ii(d):% number Frequency V's Flake Length(μm):Graphite D

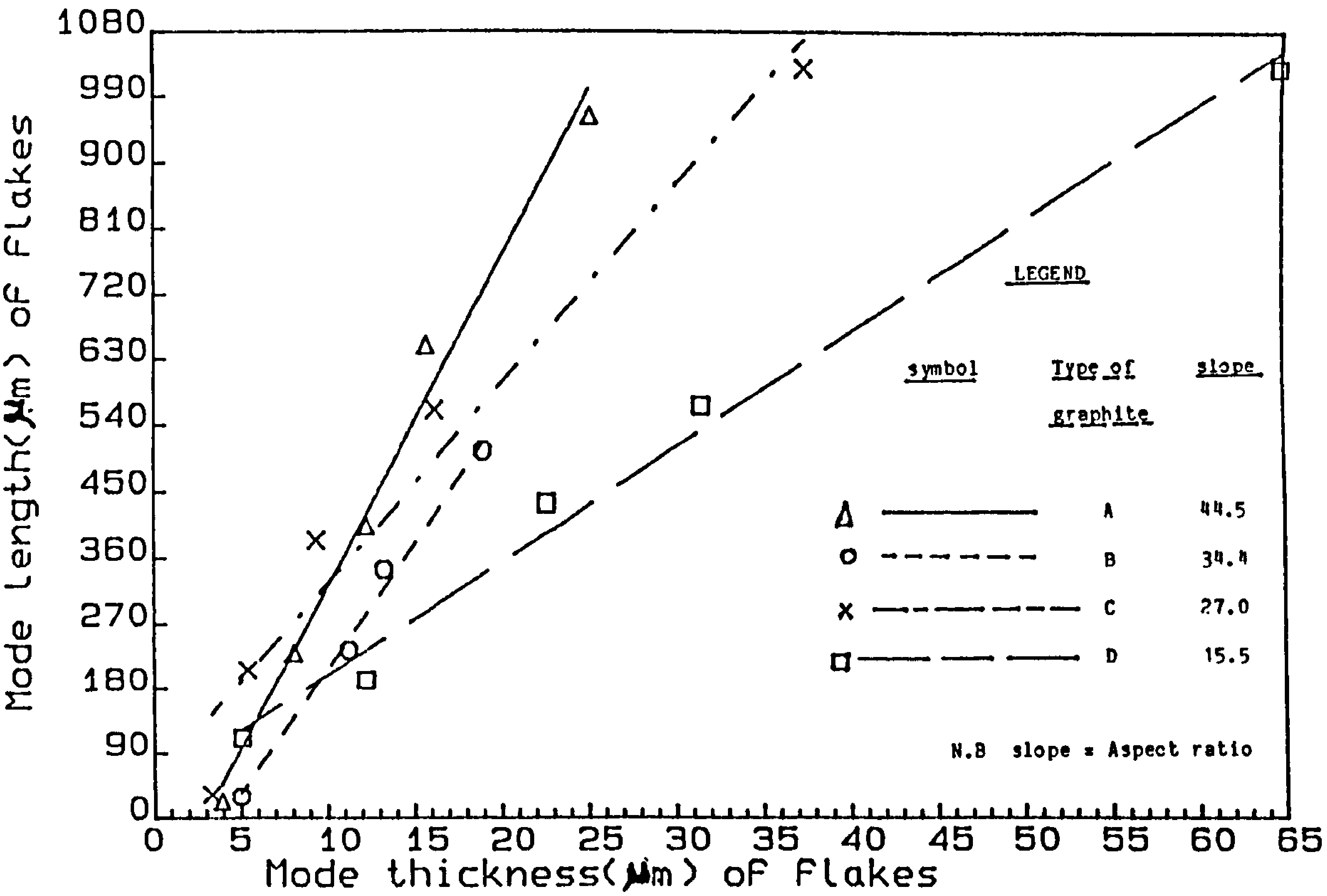

FIG 3.3.1 iii(a):Mode length of Flakes V's mode thickness of Flakes

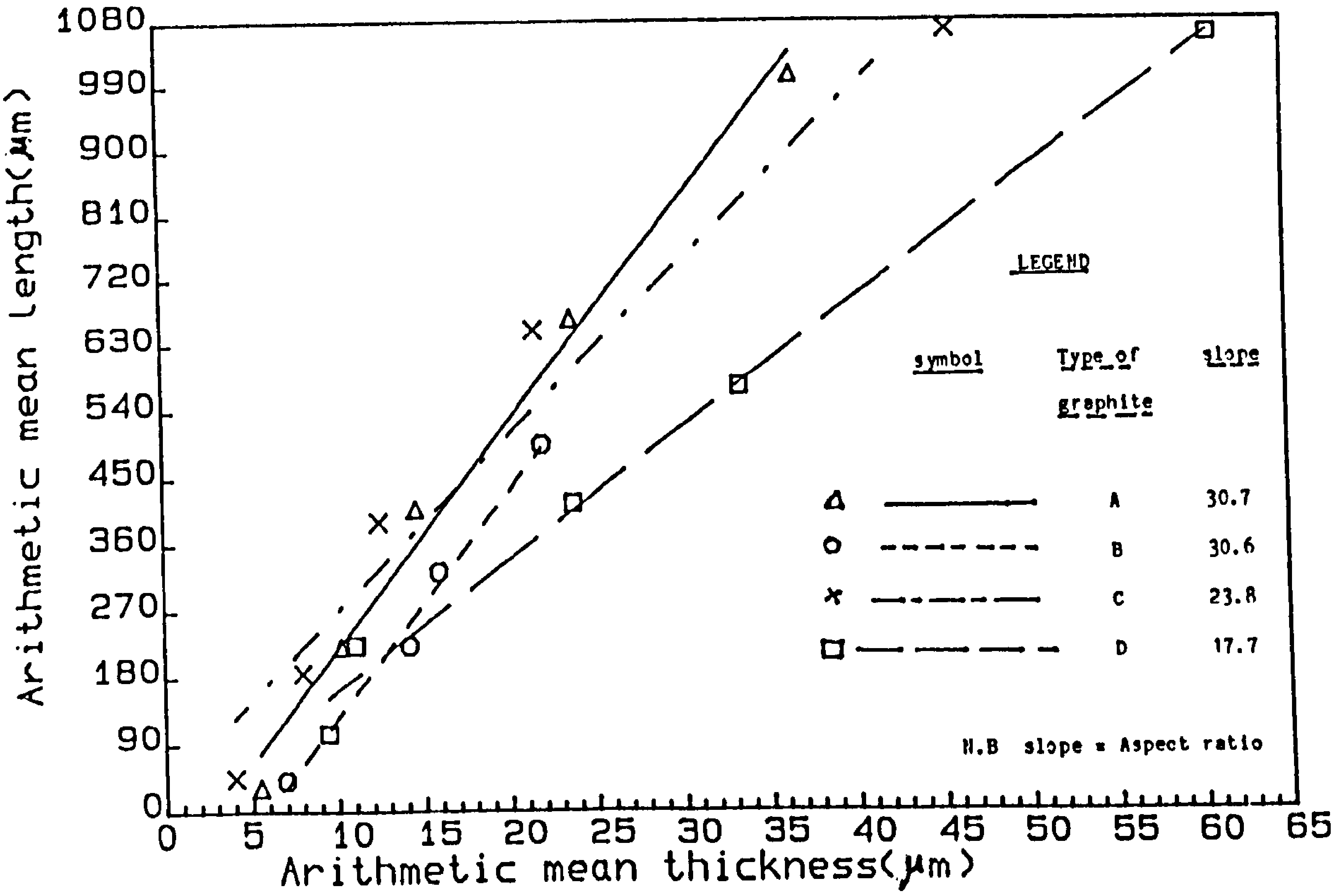

FIG. 3.3.1 iii(b):Arithmetic mean length of Flakes V's arith. mean thickness of Flakes

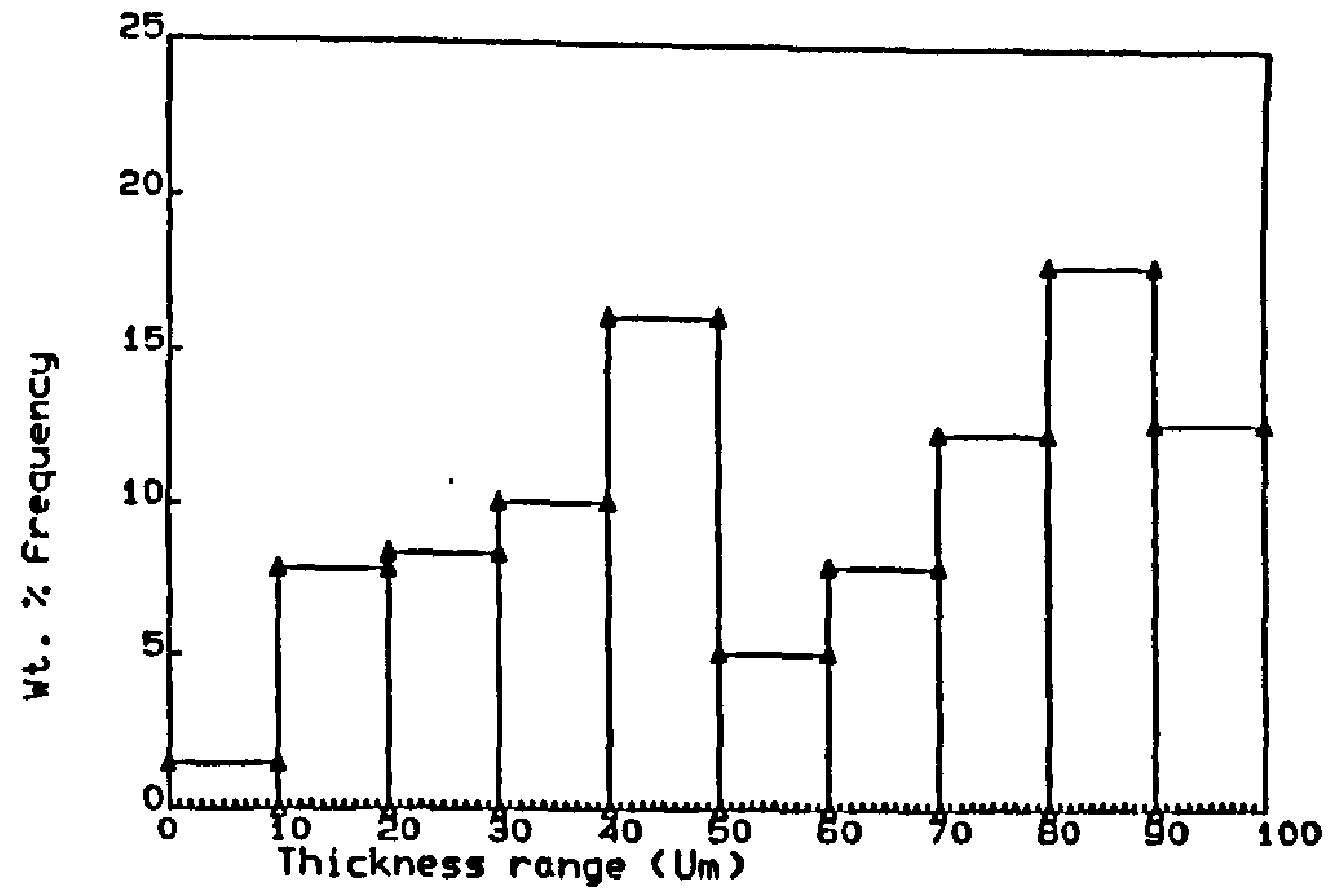

FIG. 3.3.2 1(a) :Flake thickness distributions of Graphite A

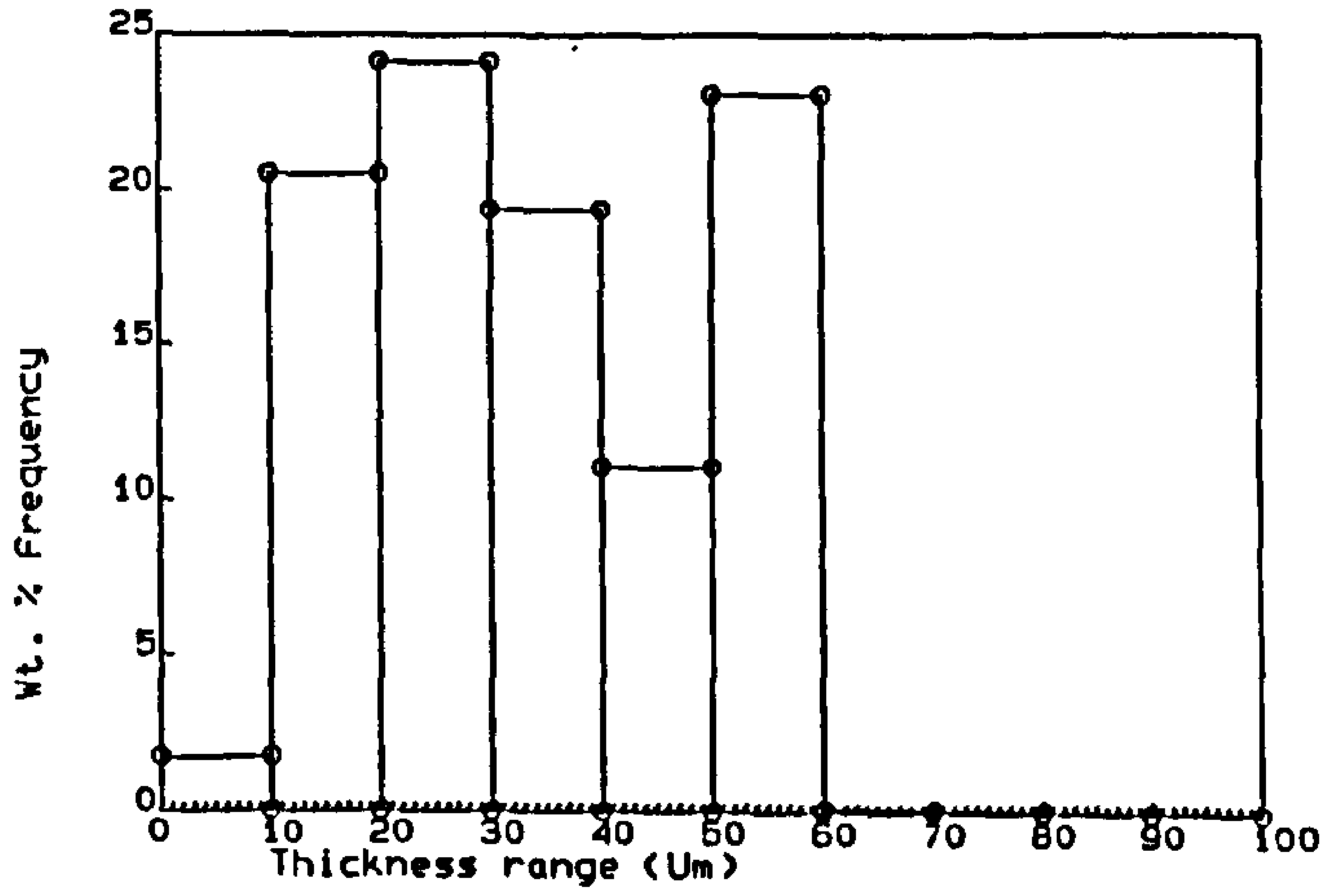

FIG. 3.3.2 1(b):Flake thickness distributions of Graphite B

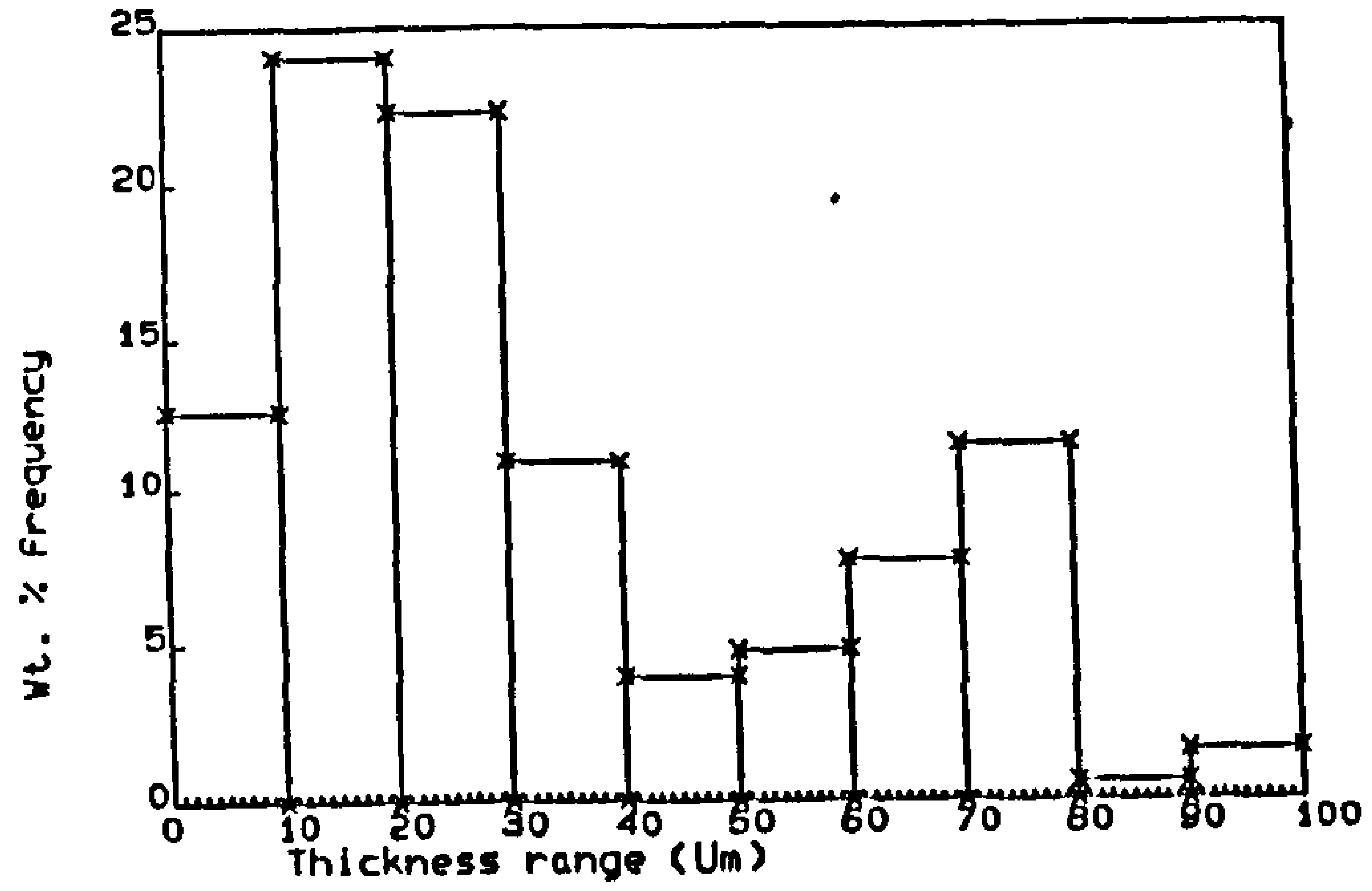

FIG. 3.3.2 1(c) :Flake thickness distributions of Graphite C

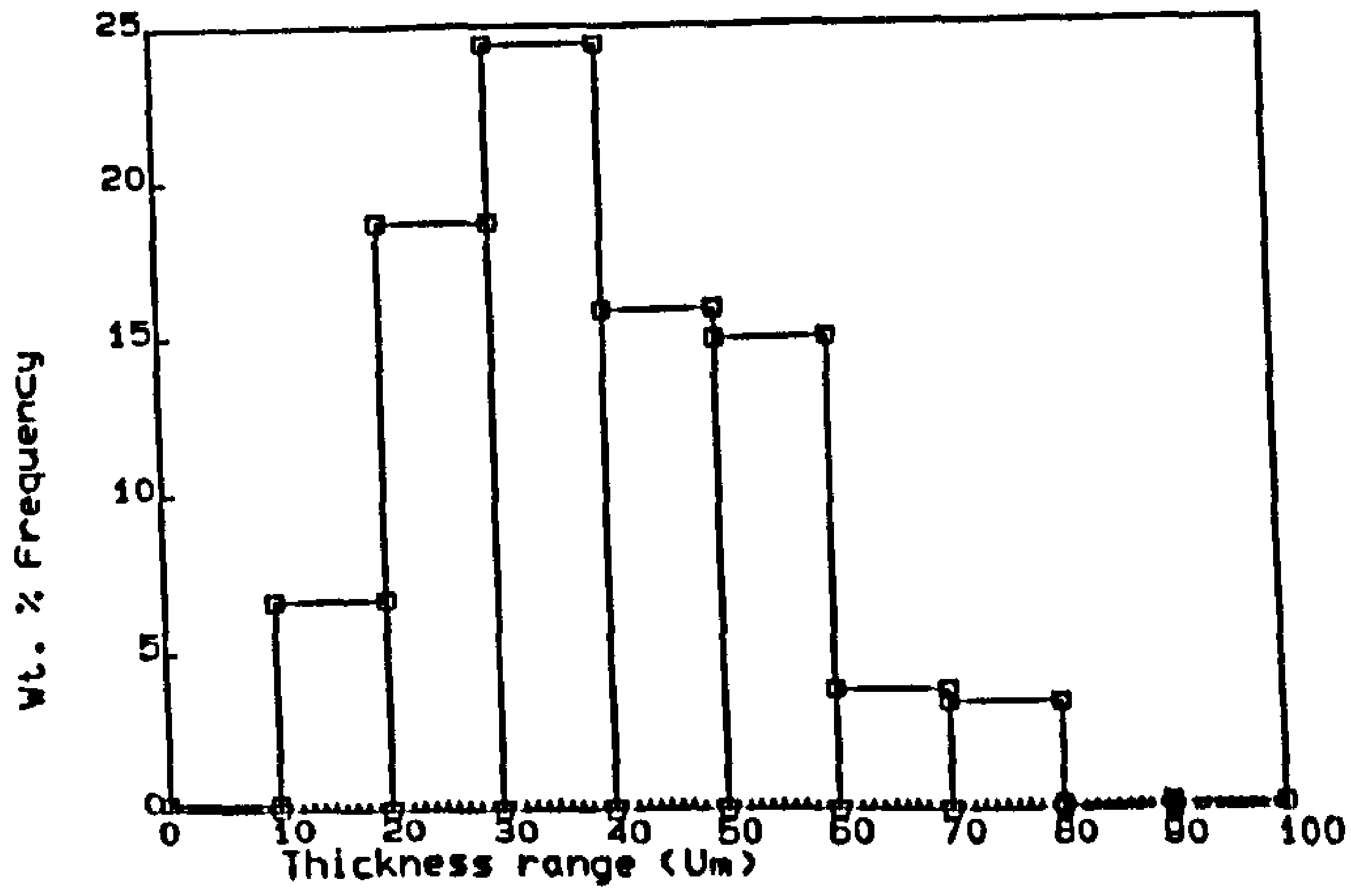

FIG. 3.3.2 1(d):Flake thickness distributions of Graphite D

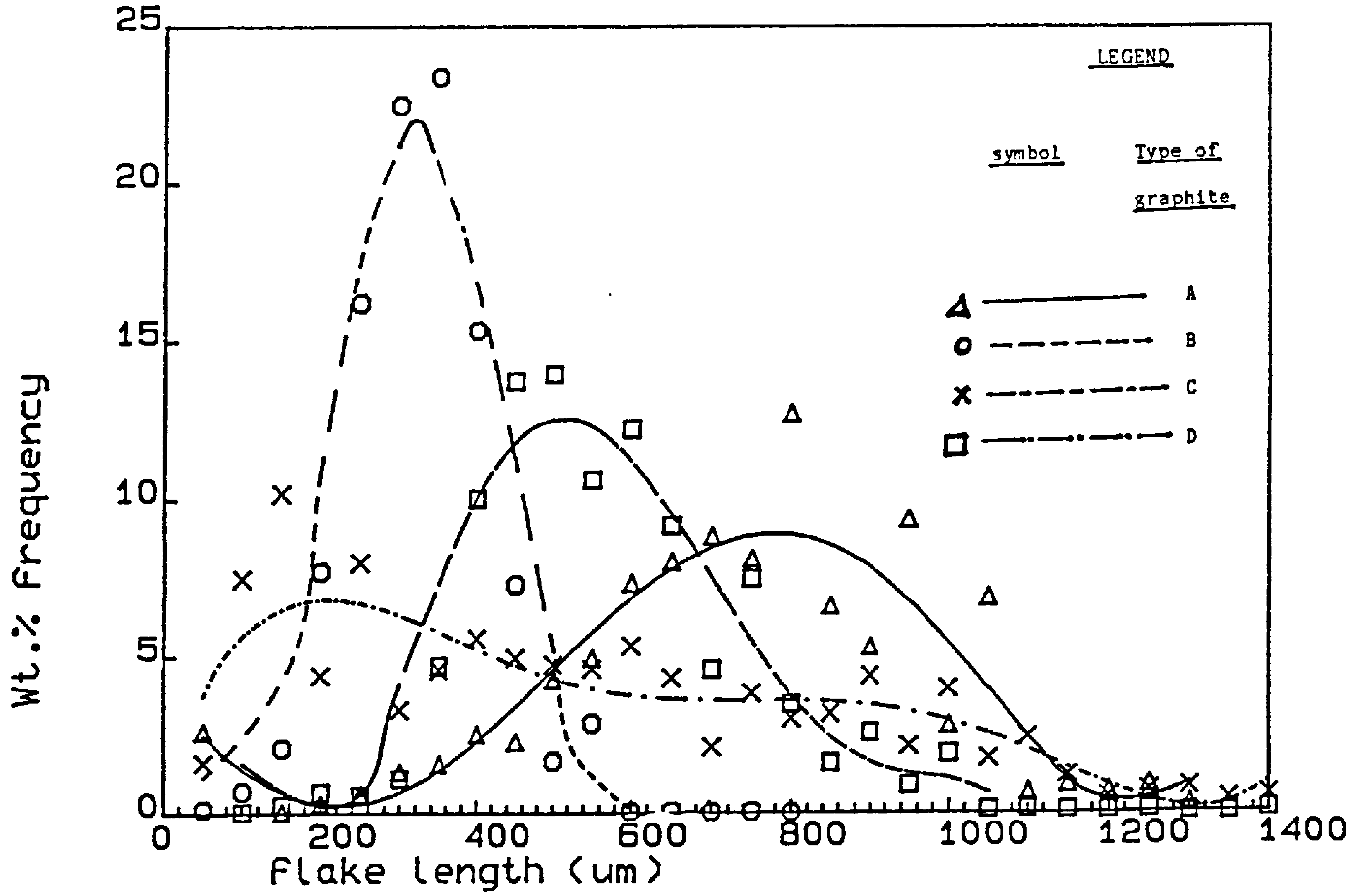

FIG. 3.3.2(ii): Wt. % Frequency V's length of graphite flakes

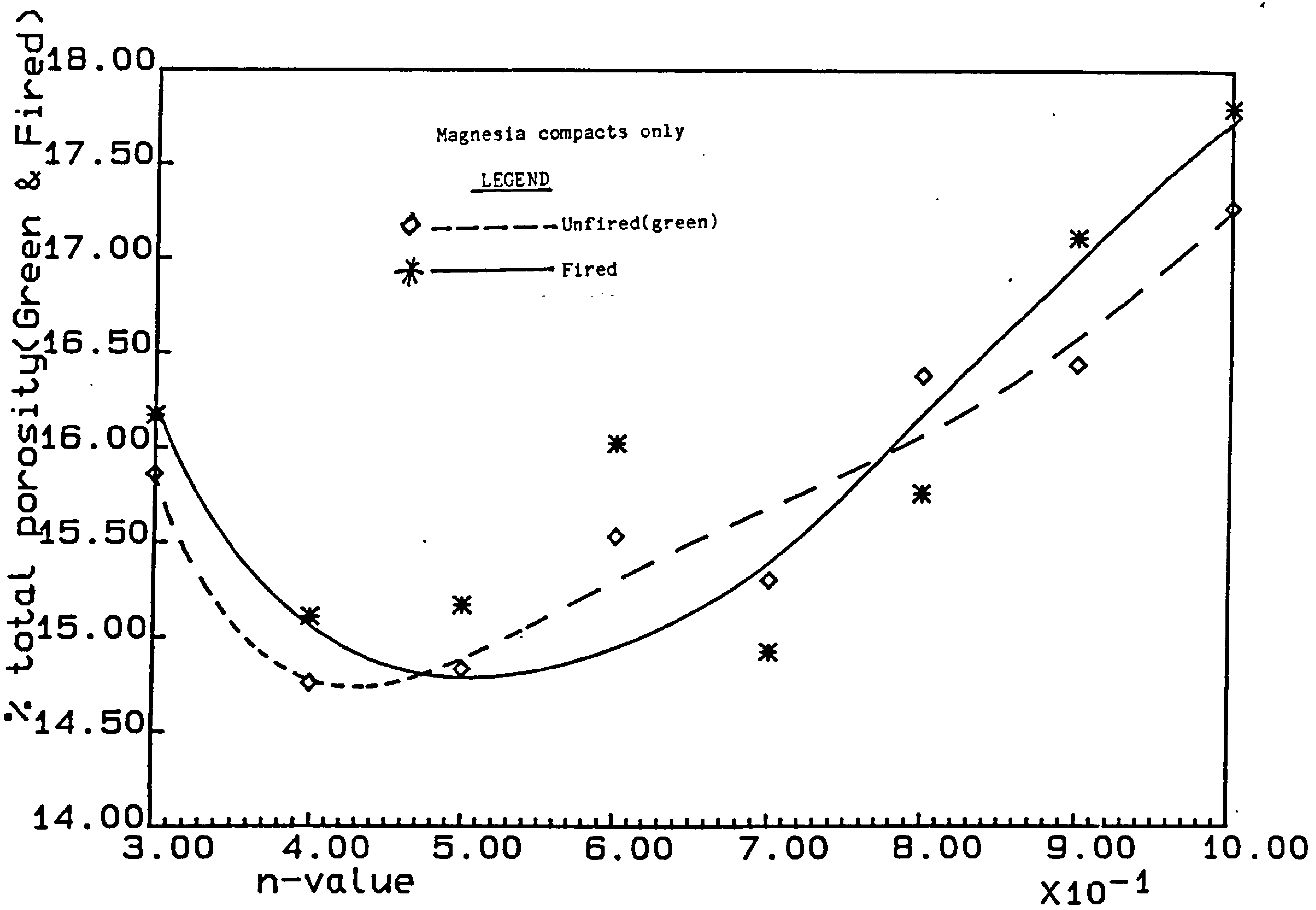

FIG. 4.4.2 :Green & Fired porosity of Mgo only V's n-value

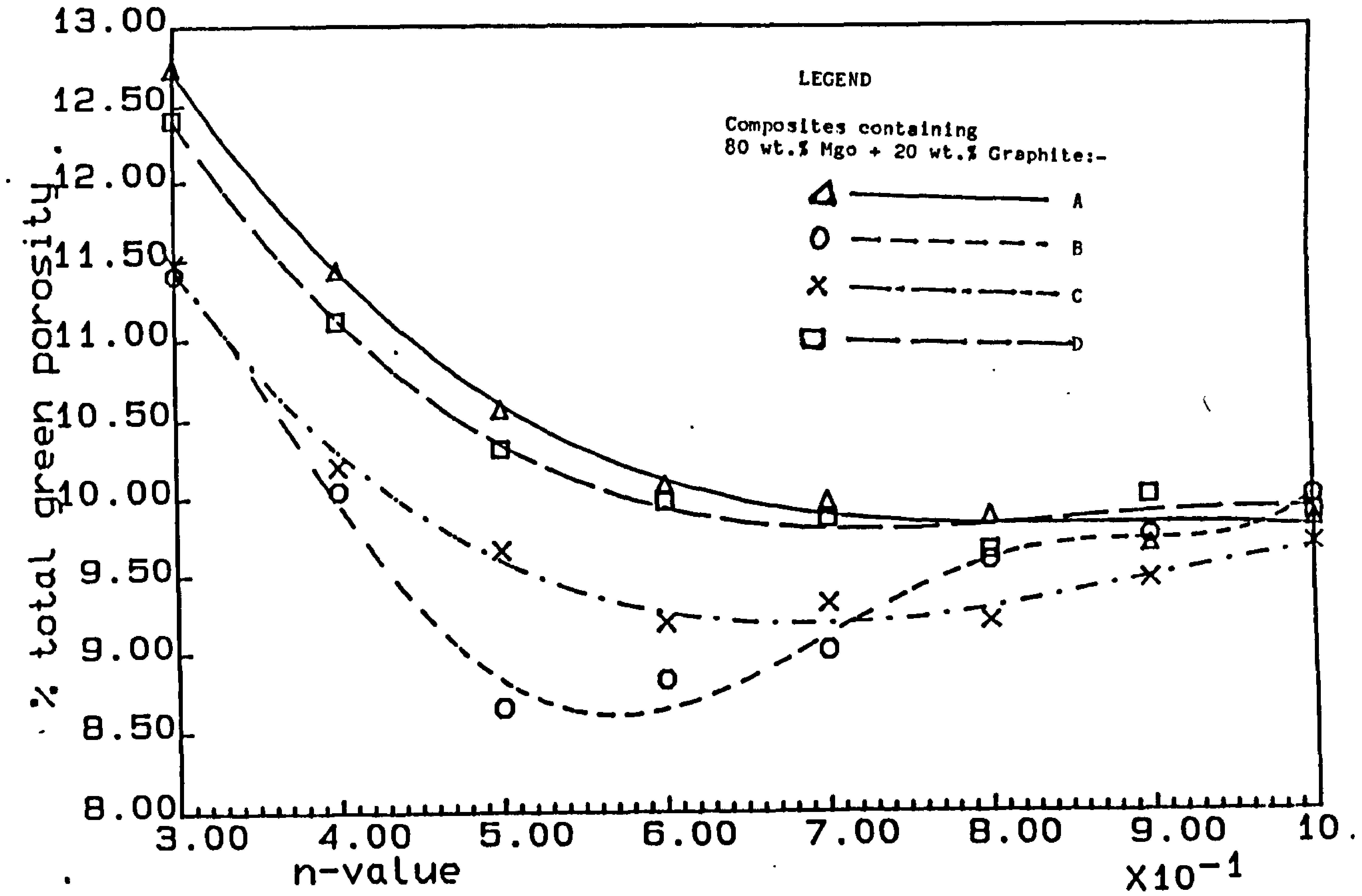

FIG. 4.4.3 i(a):Green porosity of composites V's n-value:METHOD 1

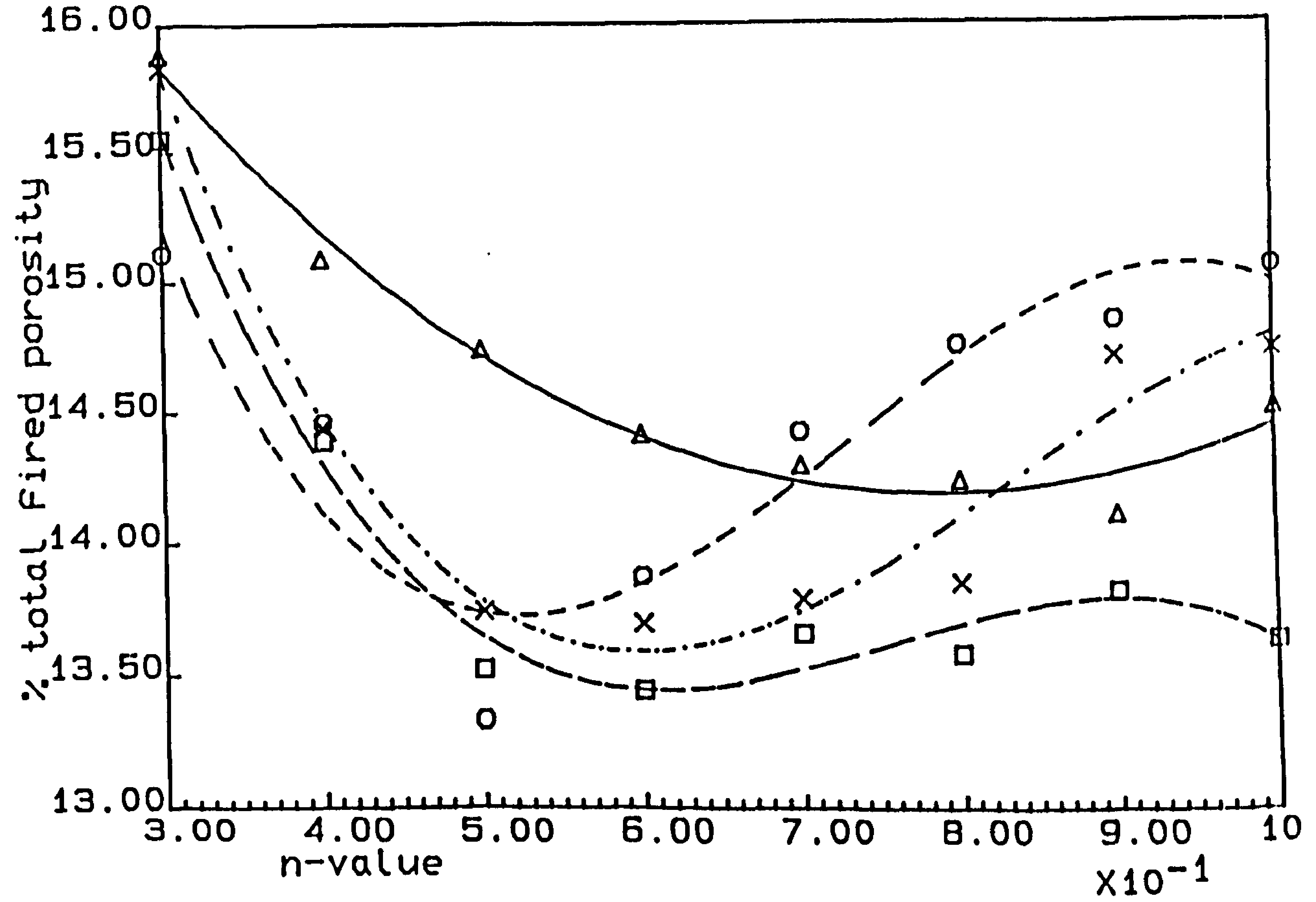

FIG. 4.4.3 i(b):Fired porosity of composites V's n-value:METHOD 1

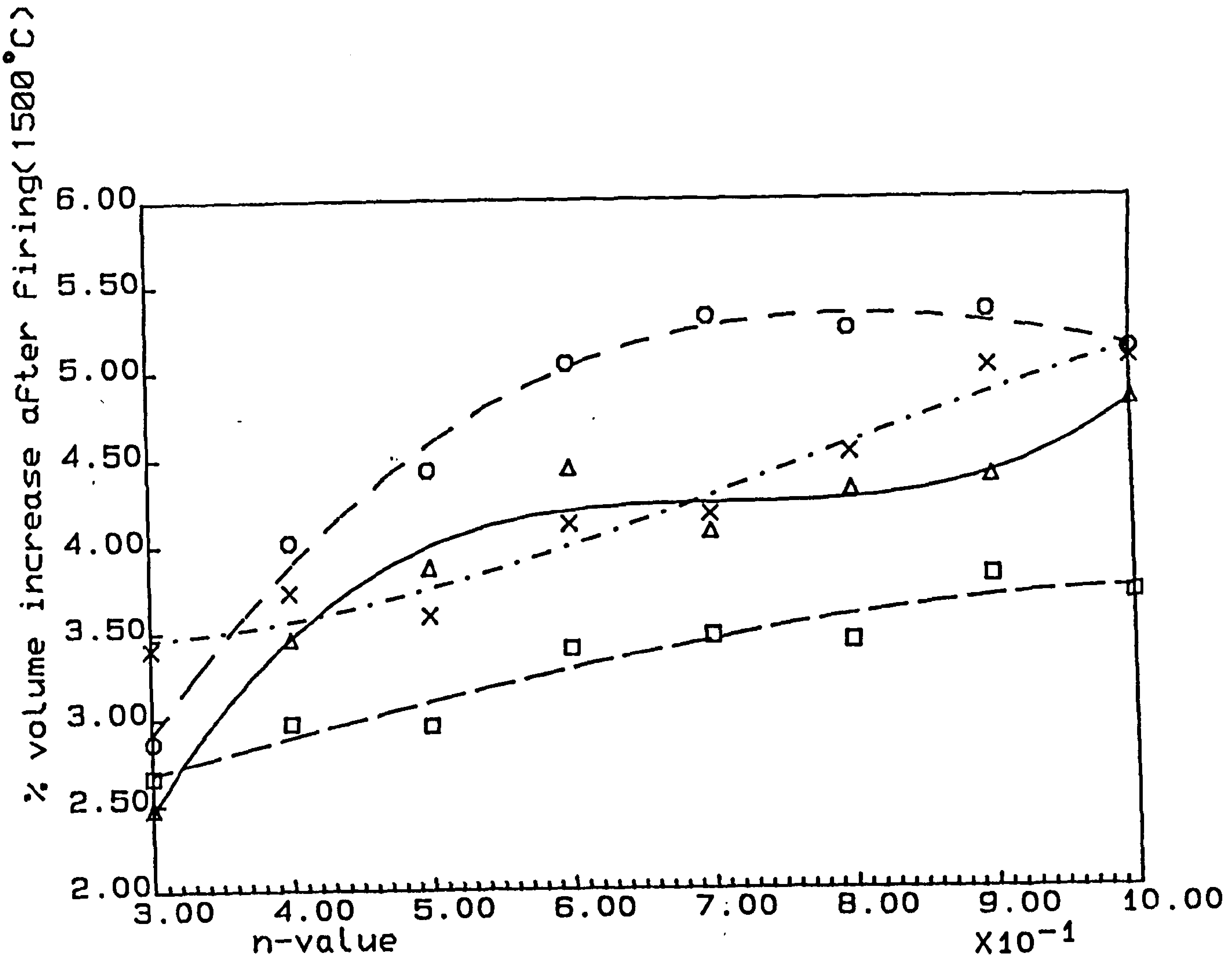

FIG. 4.4.3i(c):% volume increase V's n-value:METHOD 1

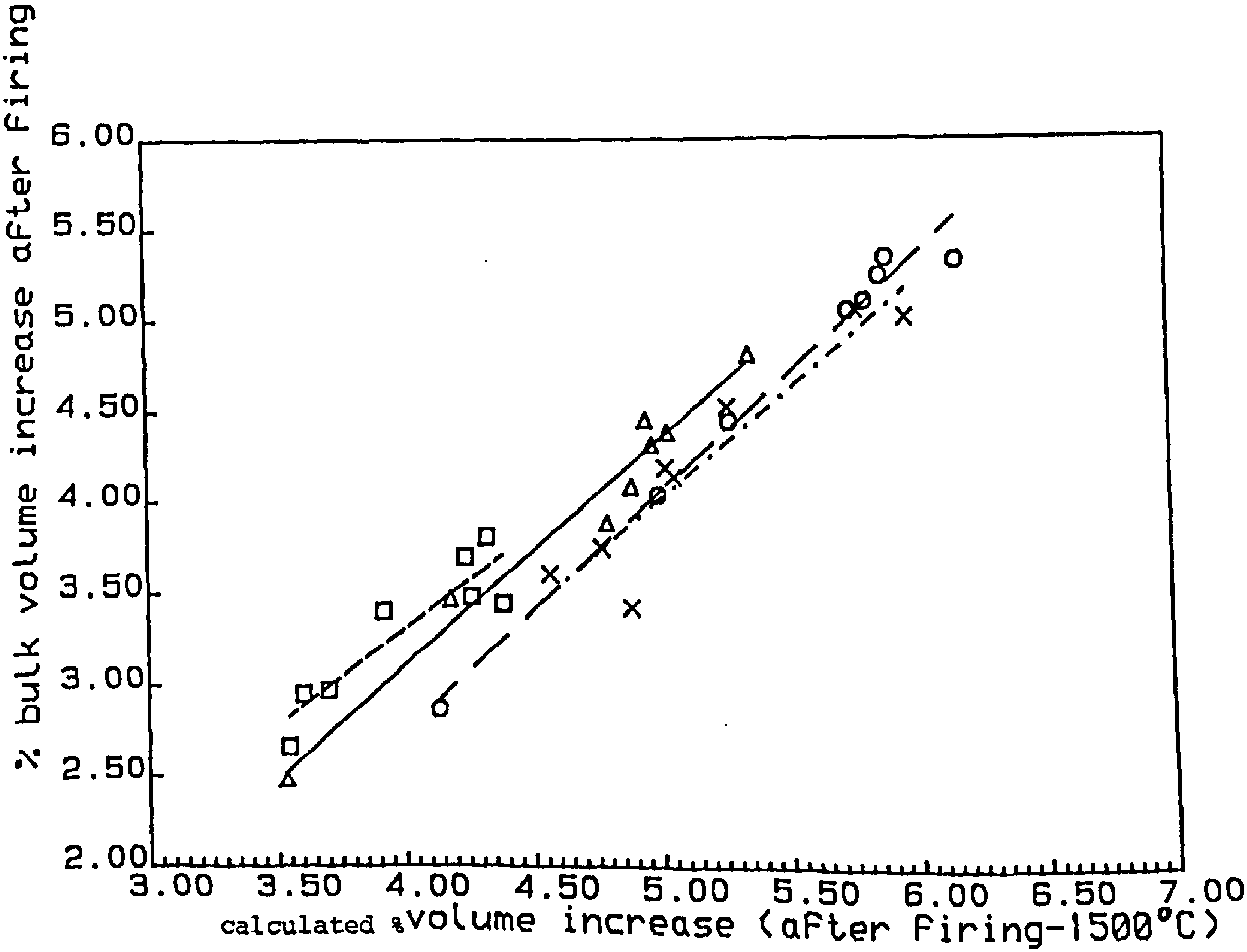

FIG. 4.4.3 i(d):% bulk volume increase V's Calculated % volume increase:METHOD 1

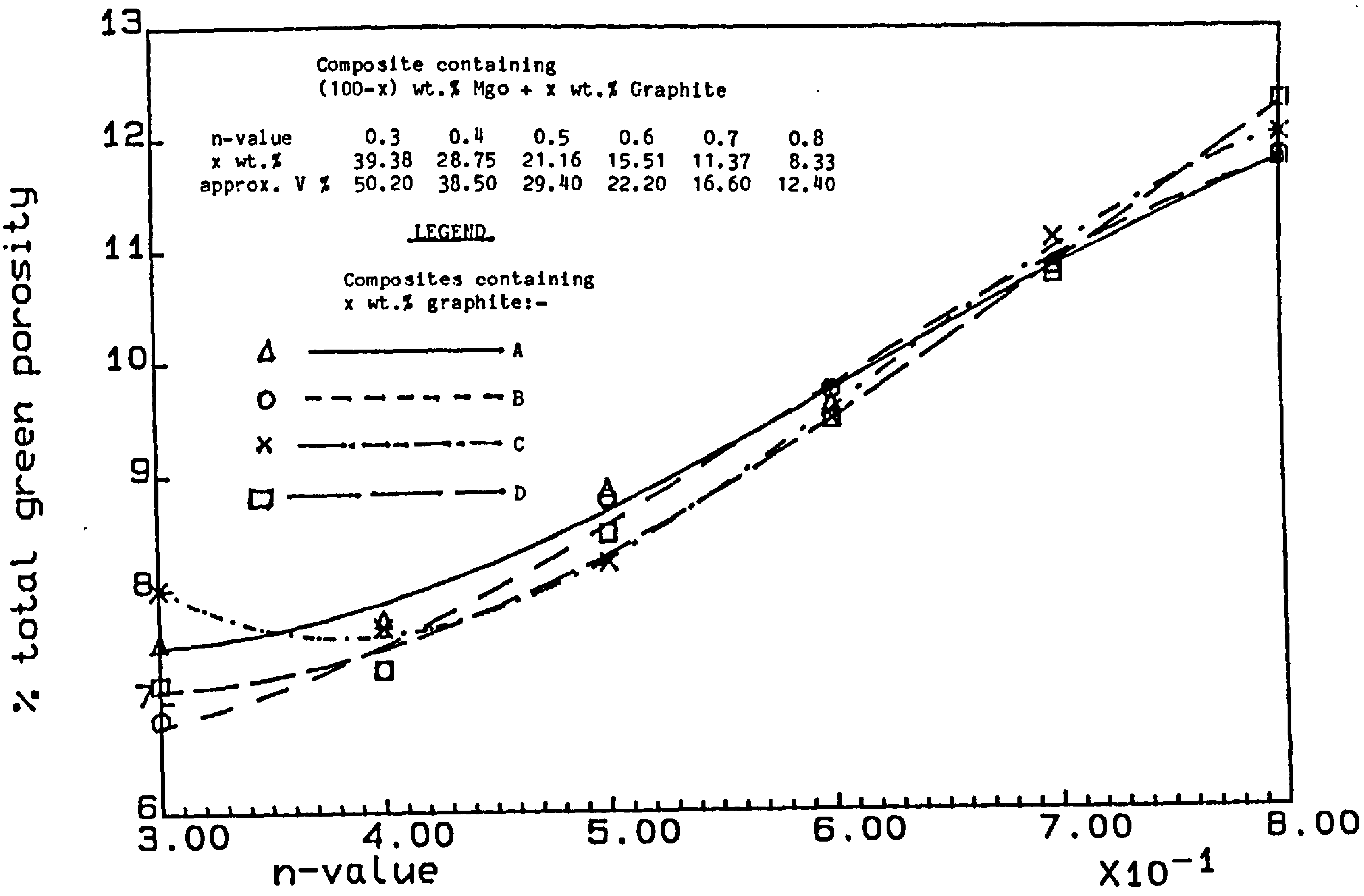

FIG. 4.4.3 ii(a):Green porosity of composites V's n-value:METHOD 2

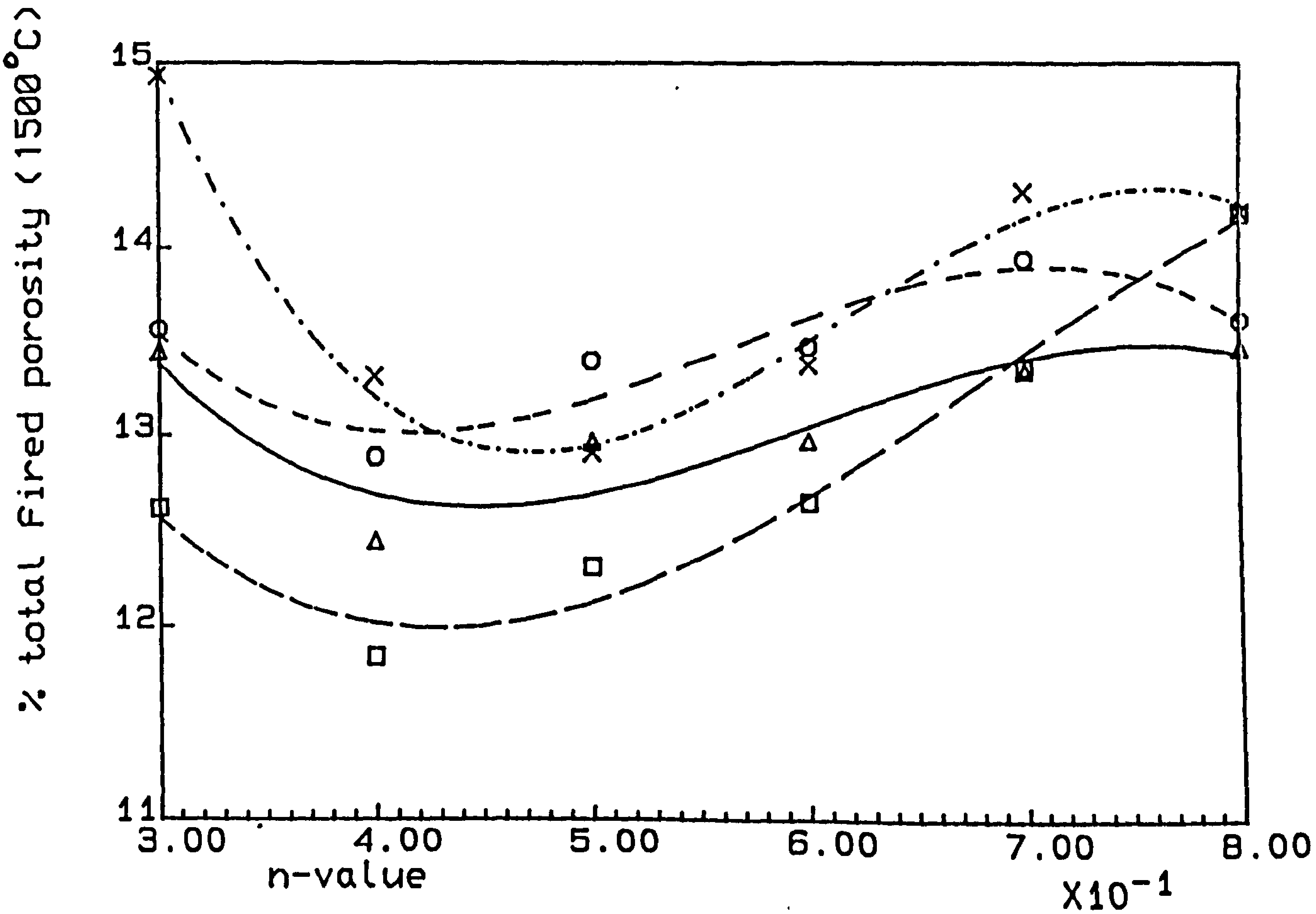

FIG. 4.4.3 ii(b):% fired porosity of composites V's n-value:METHOD 2

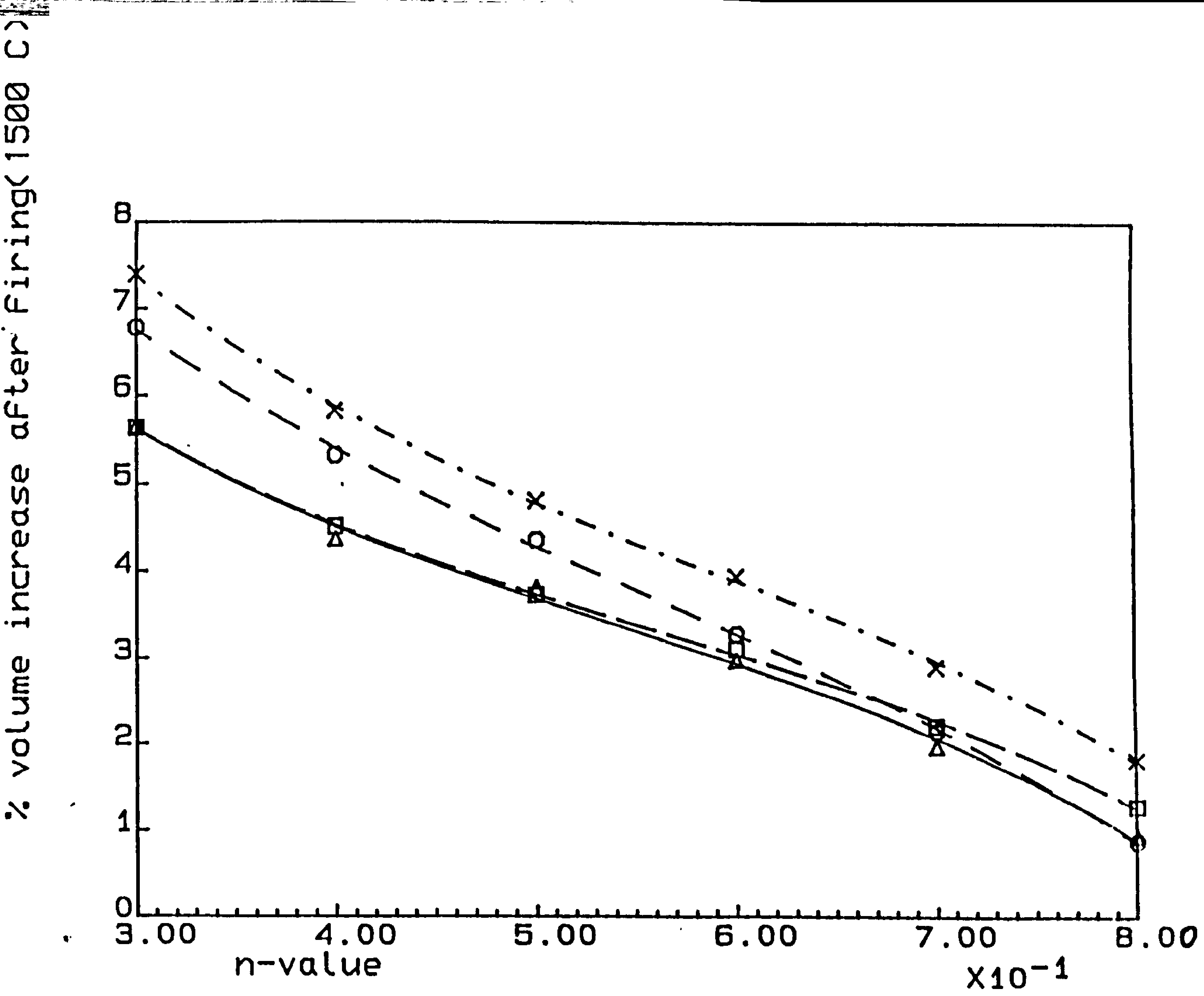

FIG. 4.4.3 ii(c):% volume increase of composites V's n-value:METHOD 2

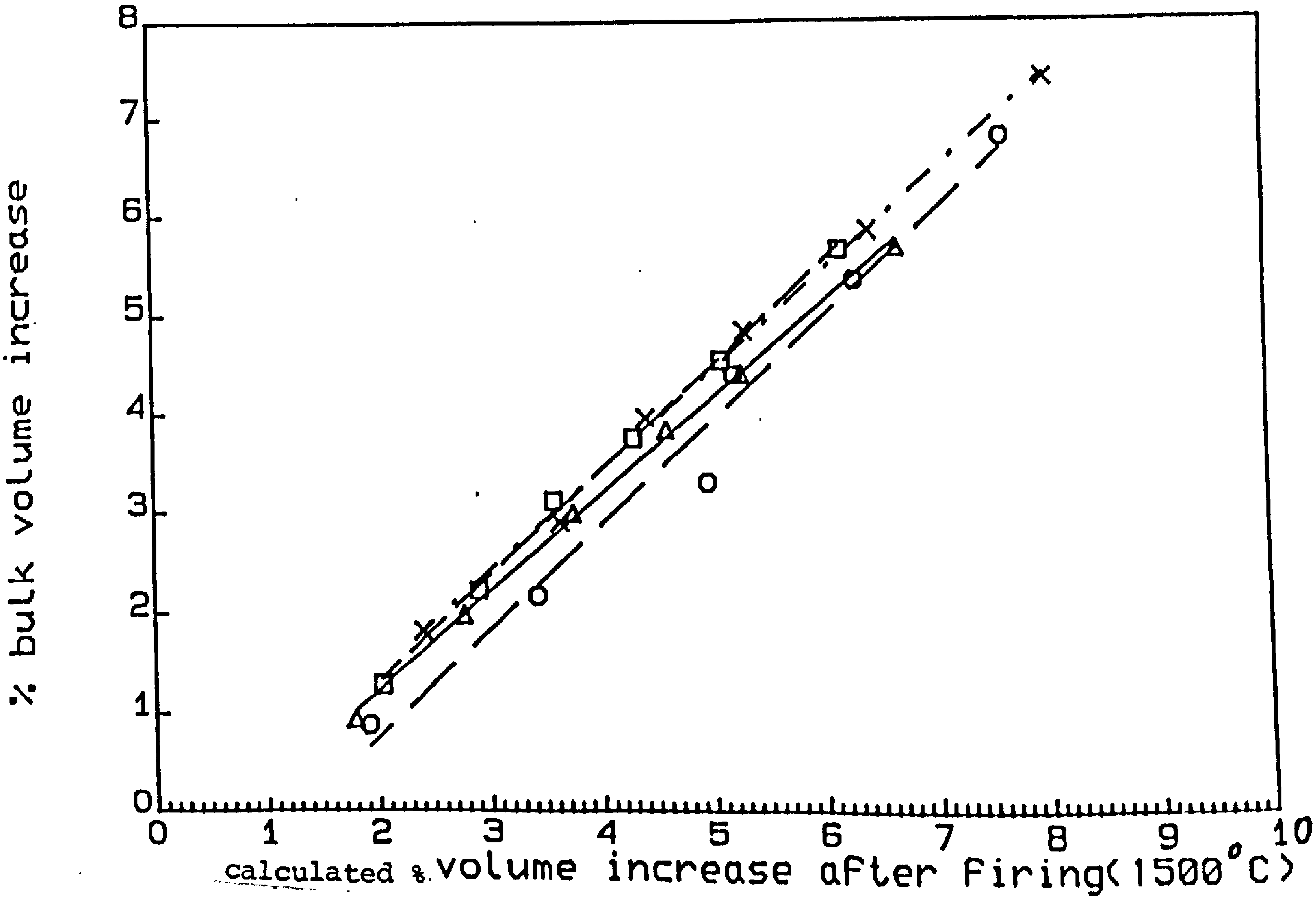

FIG. 4.4.3 ii(d):% bulk volume increase V's Calculated % volume increase:METHOD 2

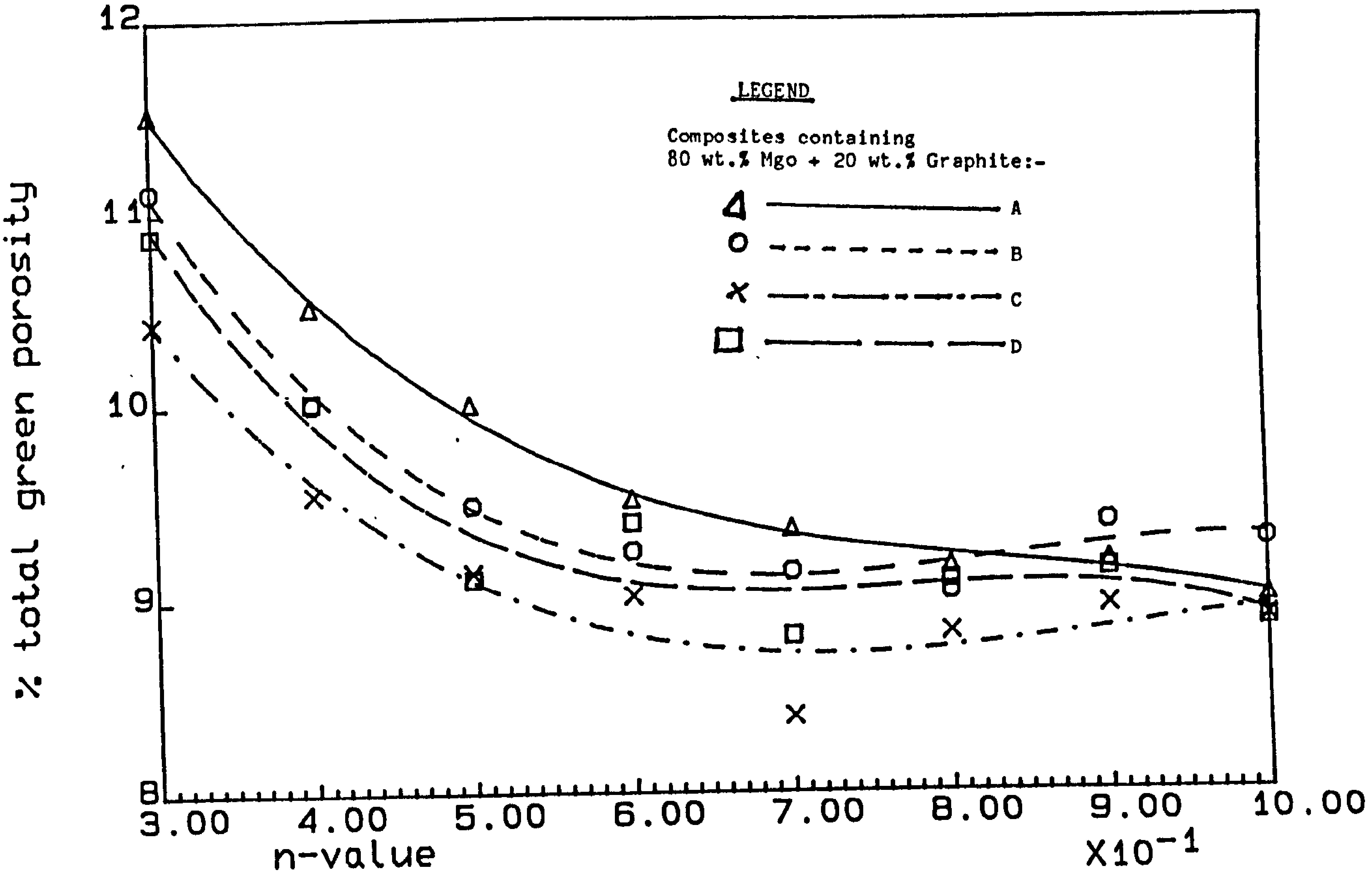

FIG. 4.4.3 iii(a):% total green porosity of composites V's n-value:METHOD 3

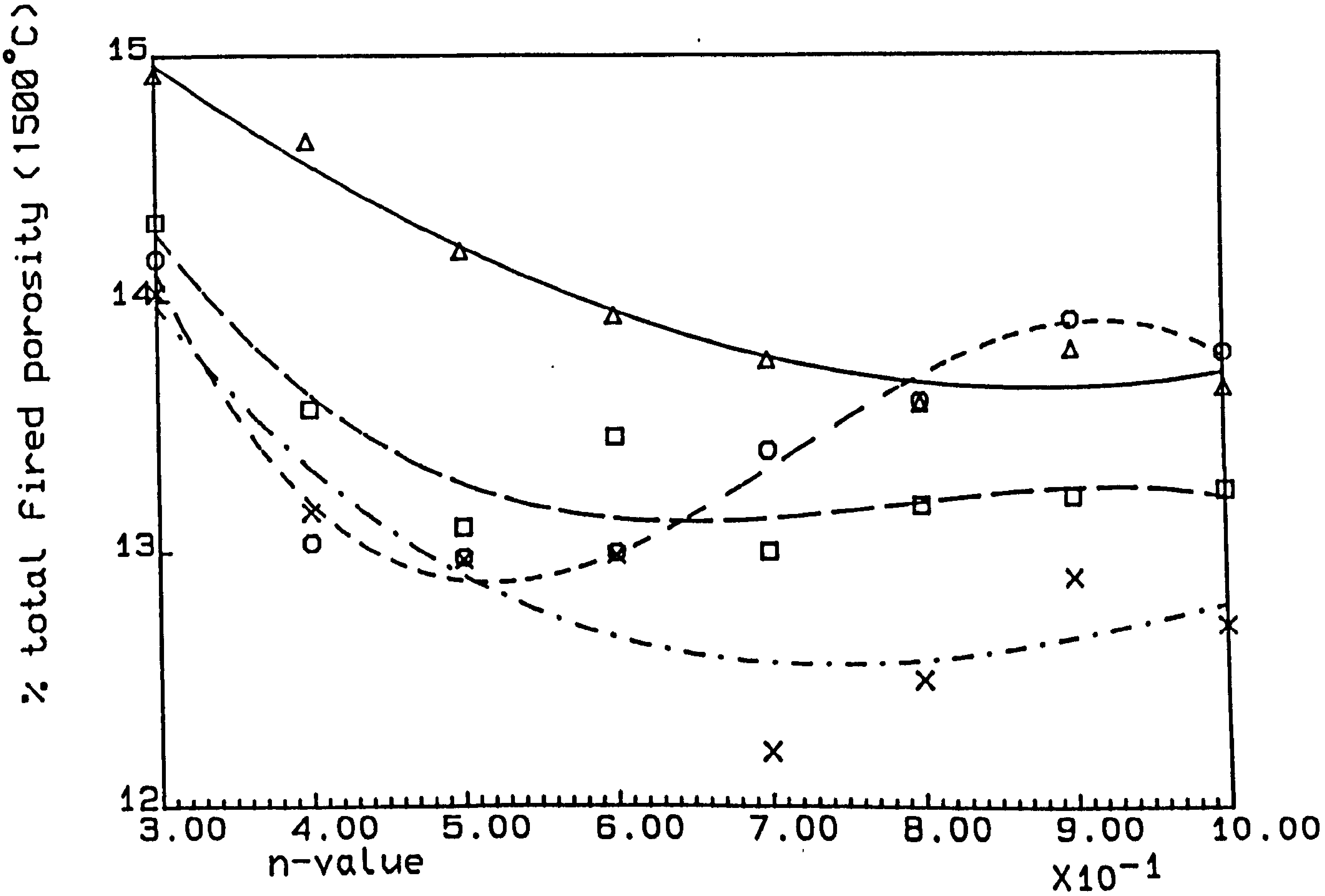

FIG. 4.4.3 iii(b):% total fired porosity of composites V's n-value:METHOD 3

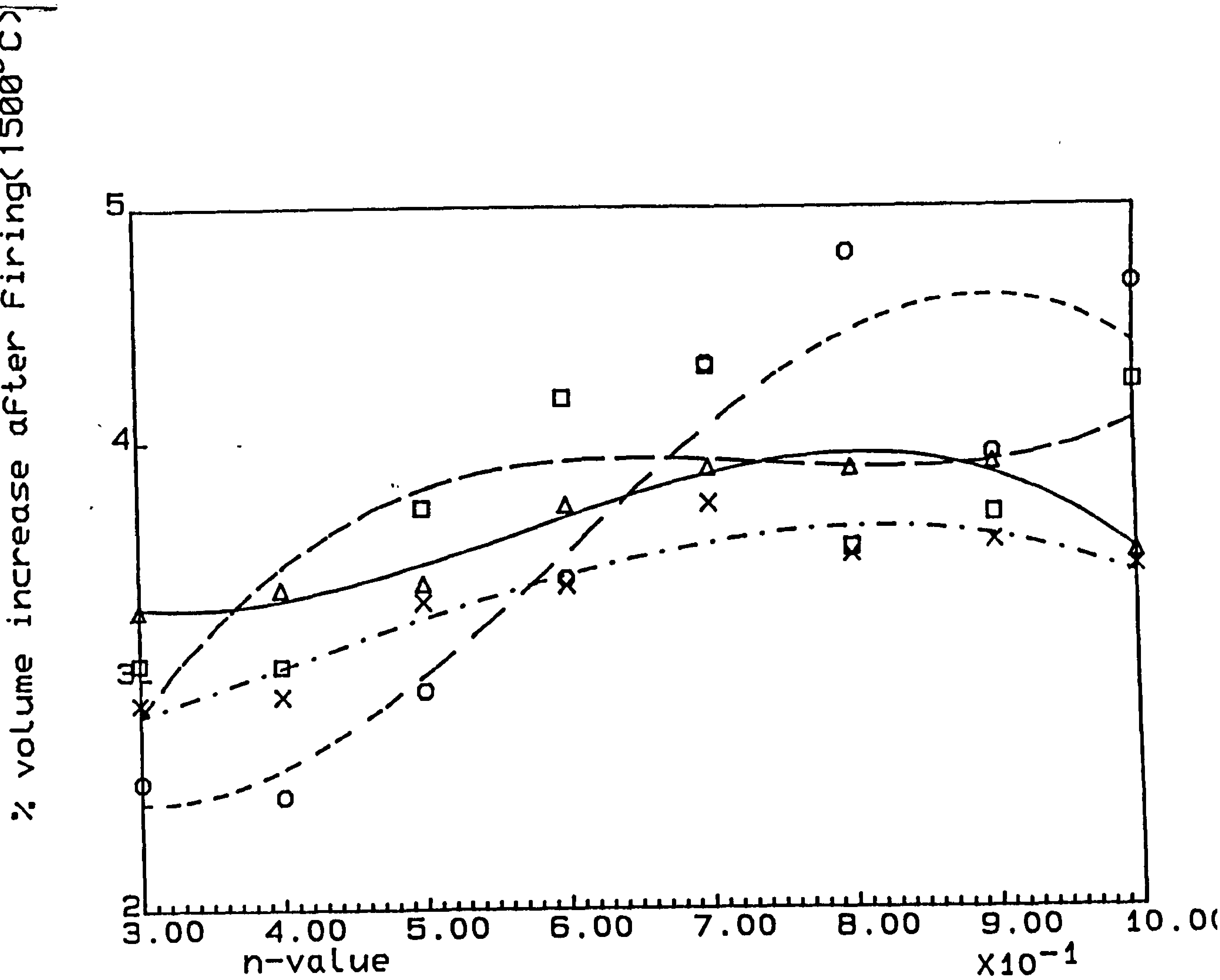

FIG. 4.4.3 iii(c):% volume increase of composites V's n-value:METHOD 3

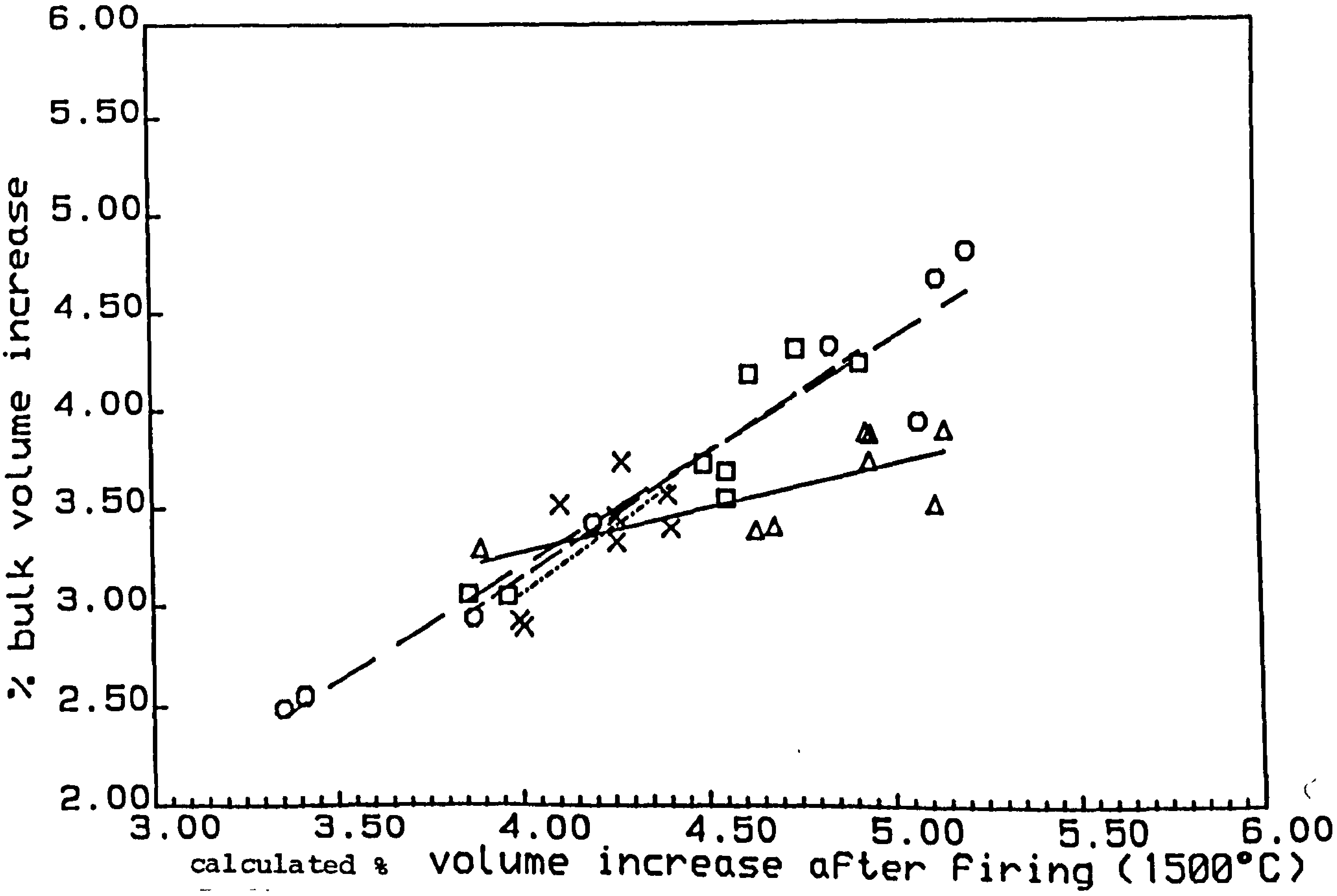

FIG. 4.4.3 iii(d):% bulk volume increase V's Calculated % volume increase:METHOD 3

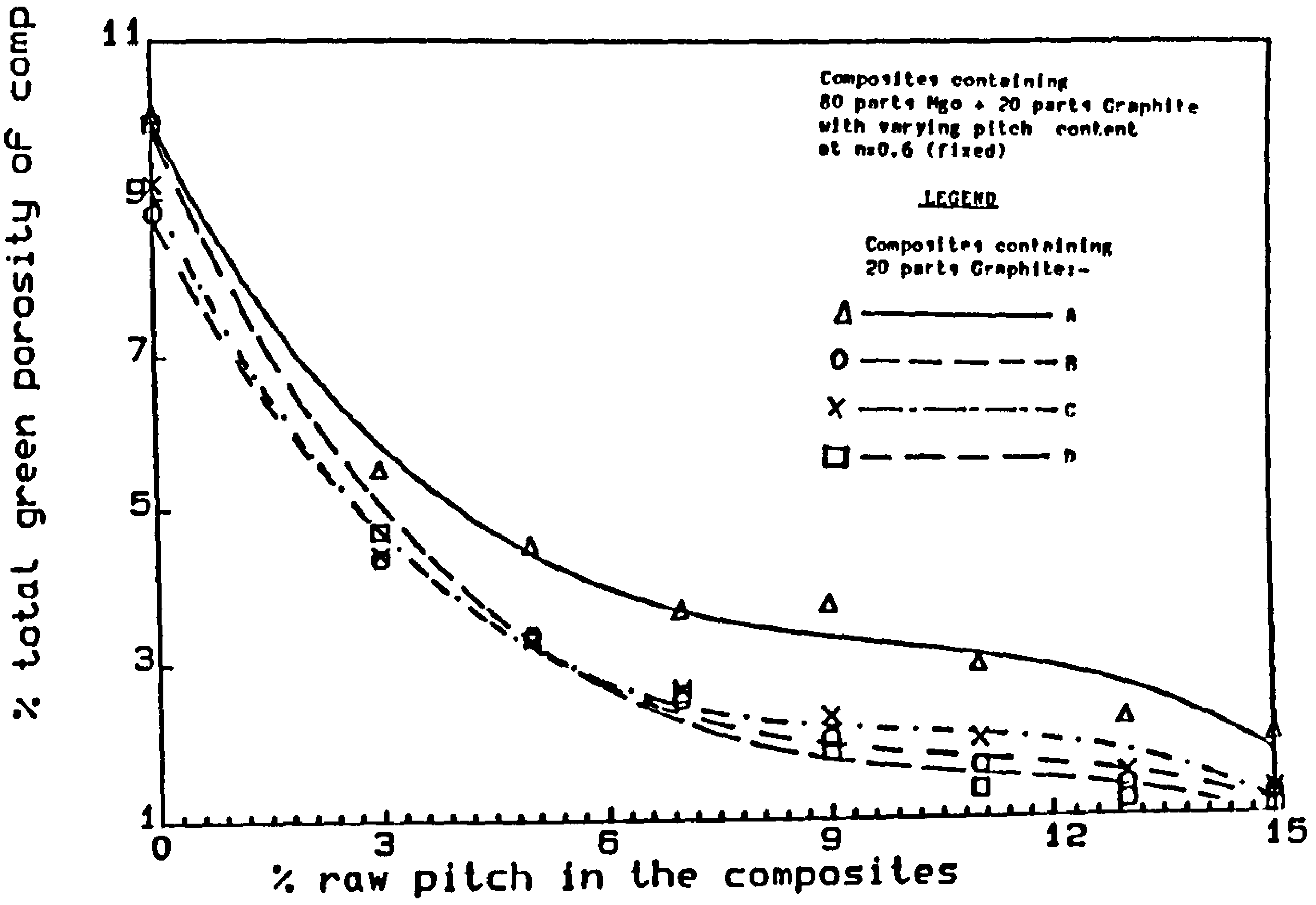

FIG. 4.4.4 i(a): % total green porosity V's % raw pitch in the composites

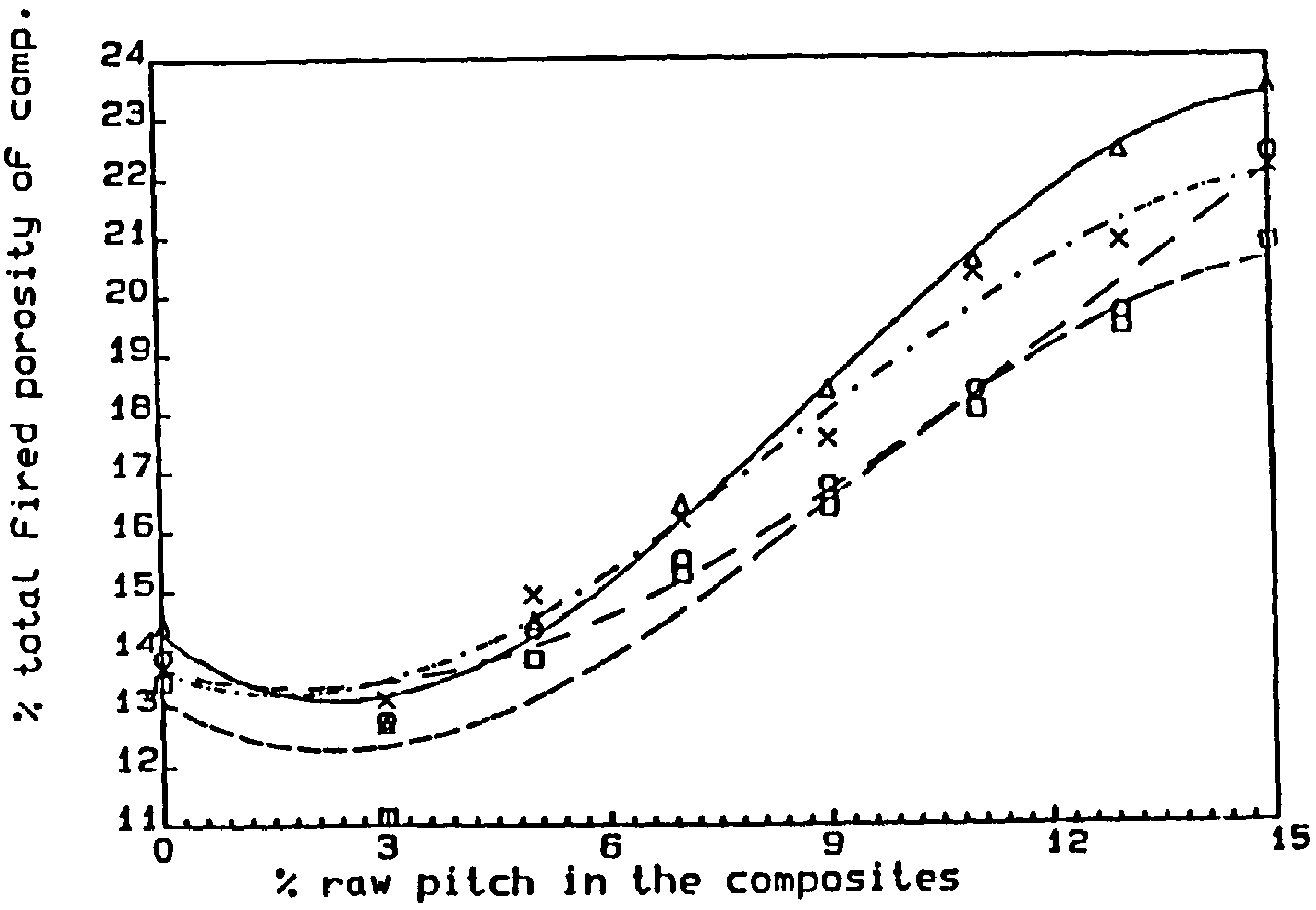

FIG. 4.4.4 i(b): % total fired porosity V's % raw pitch in the composites

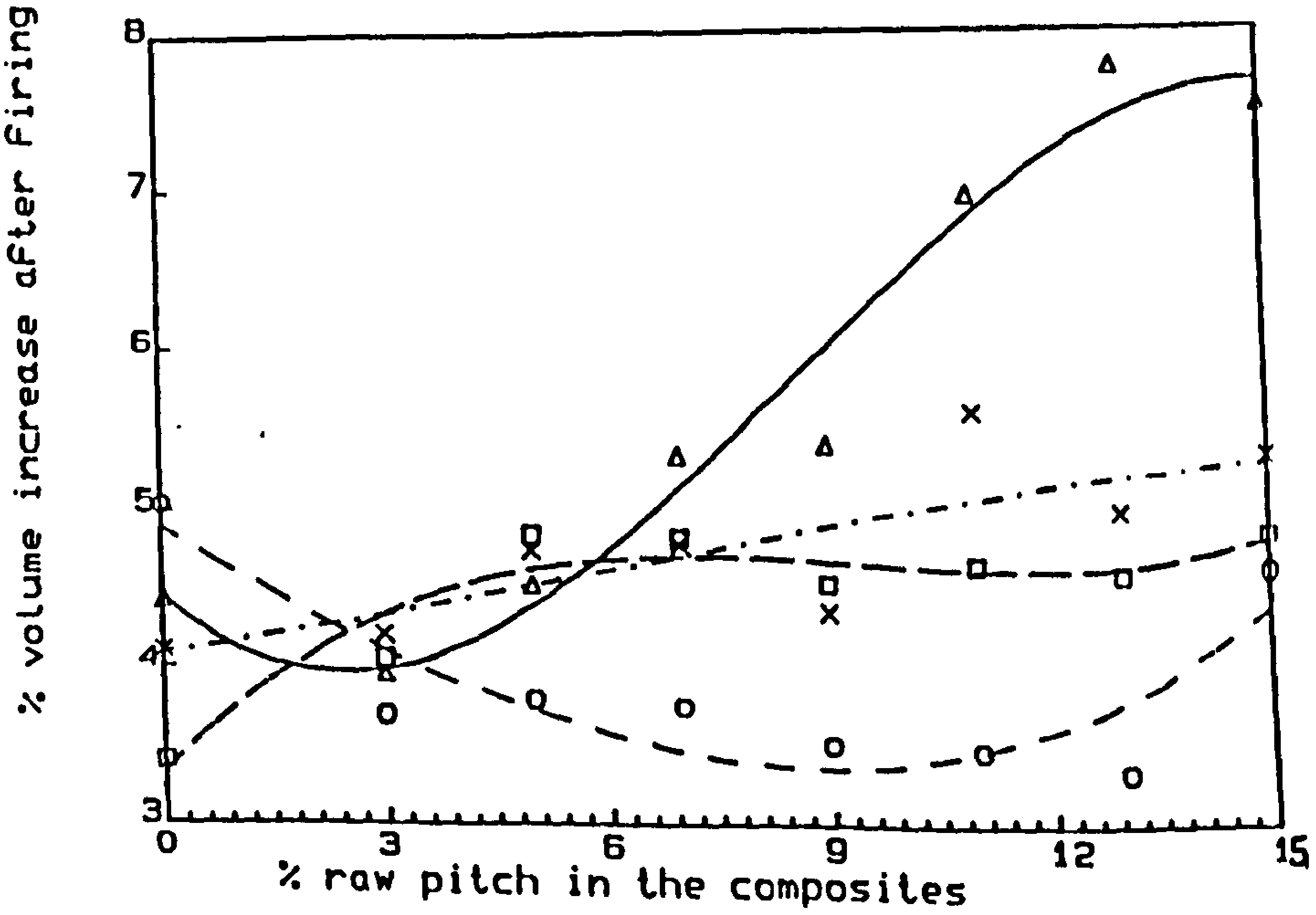

FIG. 4.4.4 i(c):% volume increase V's % raw pitch in the composites

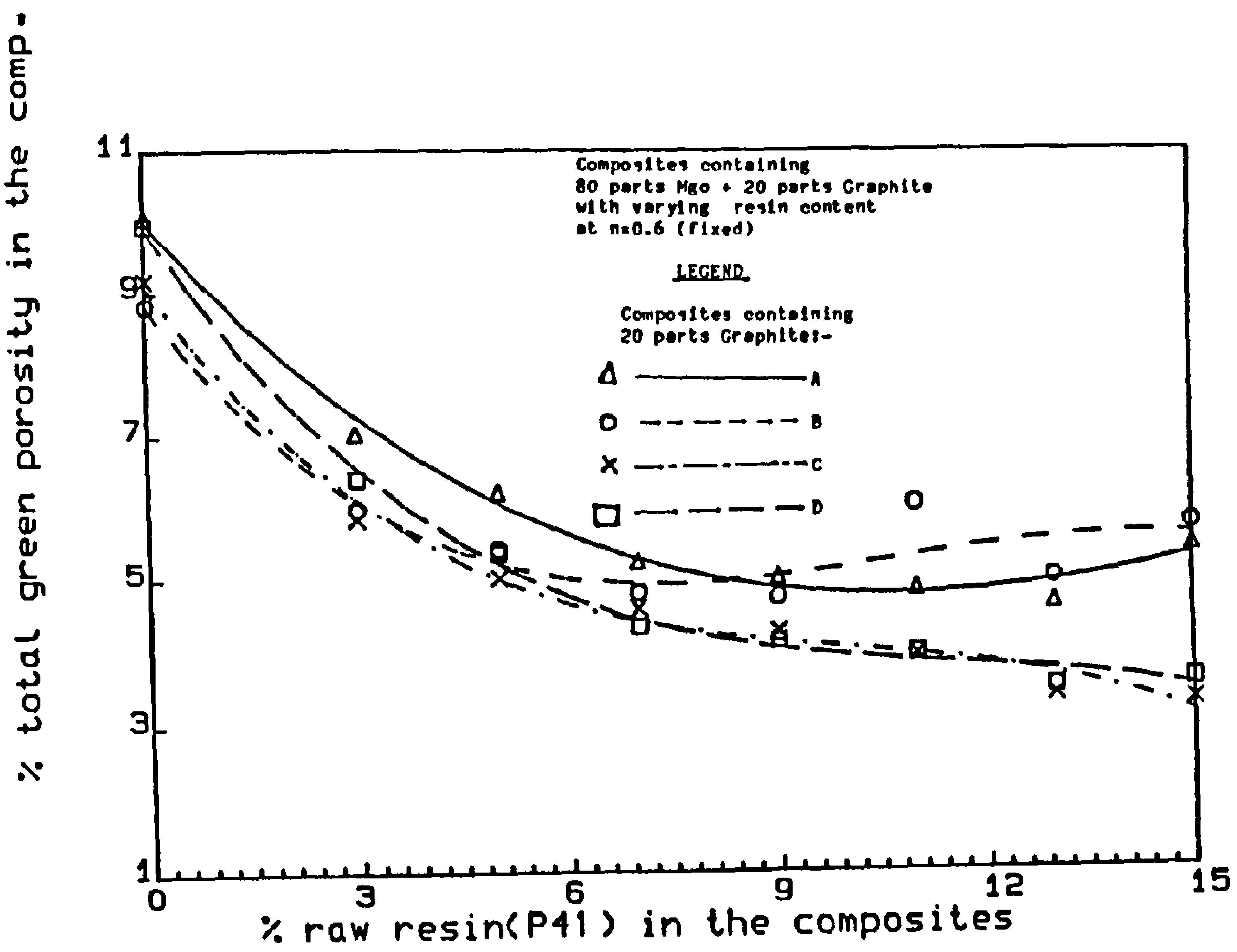

FIG. 4.4.4 ii(a):% total green porosity V's % raw resin(P41) in the composites

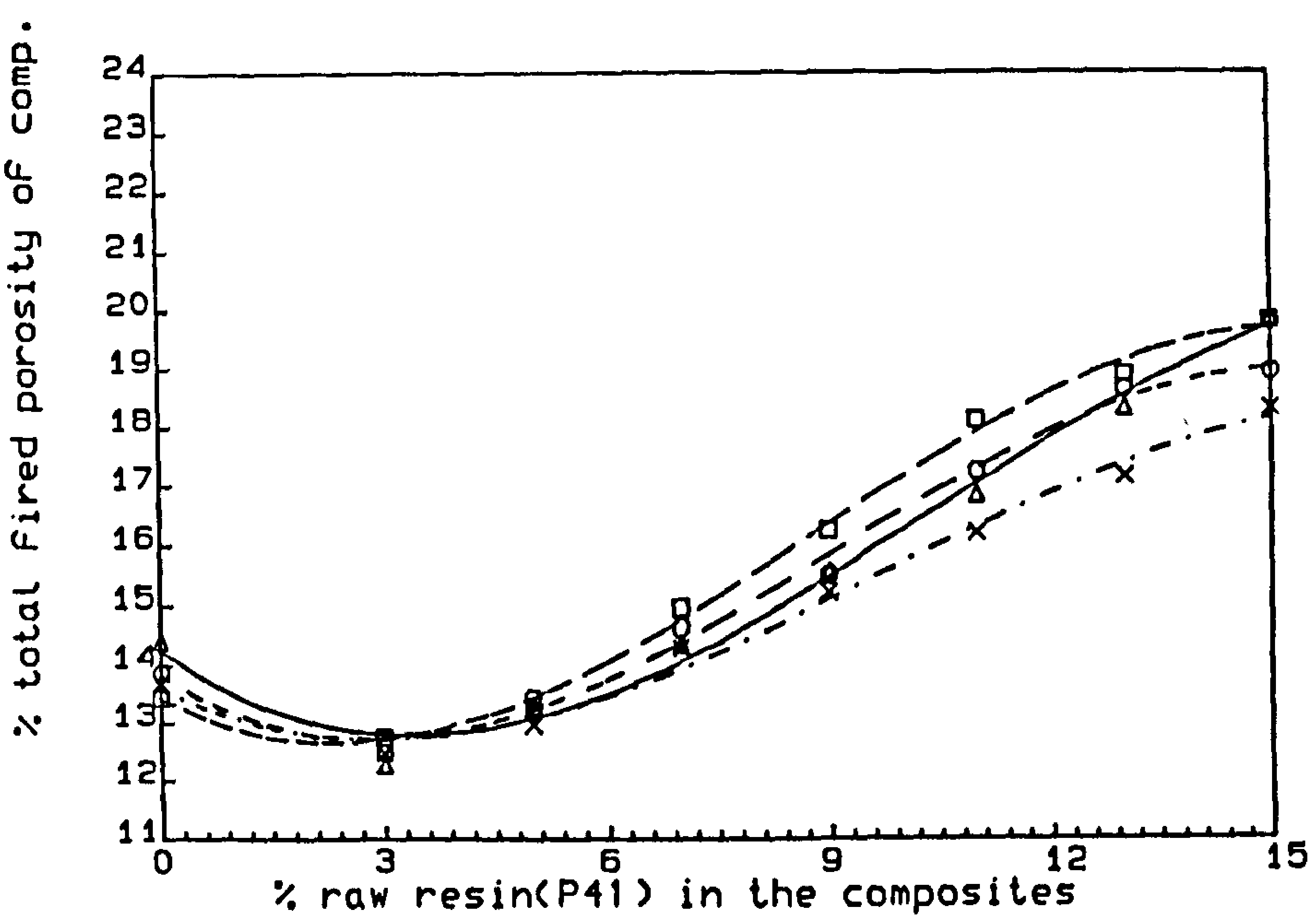

FIG. 4.4.4 ii(b):% total fired porosity V's % raw resin in the composites

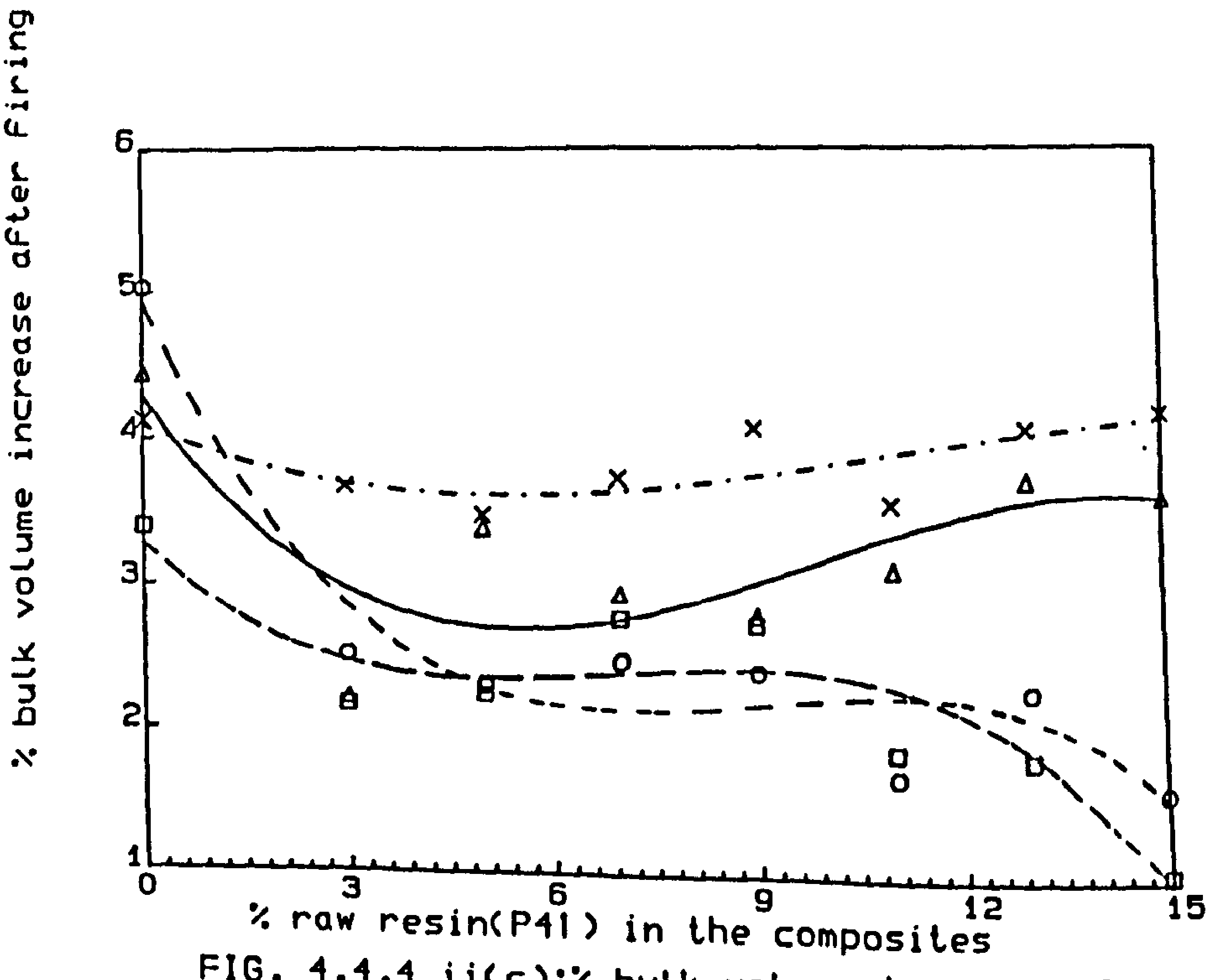

FIG. 4.4.4 ii(c):% bulk volume increase V's % raw resin(P41) in the composites

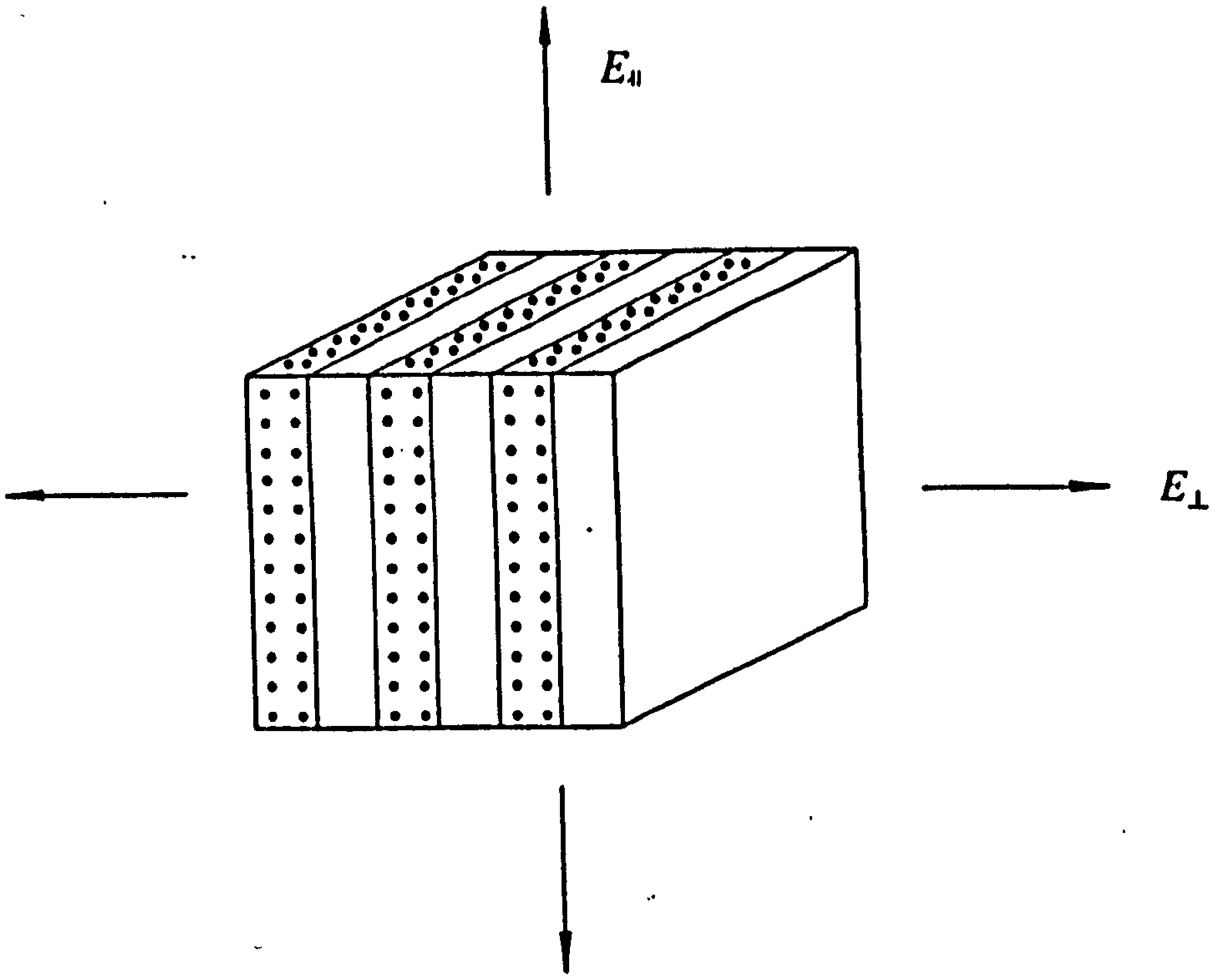

Fig. 5.1.1(b) Material of sandwich-type structure, indicating orientations parallel and perpendicular to the slabs. (After Davidge[59]).
$E_{\parallel}$ = elastic modulus parallel, and
$E_{\perp}$ = elastic modulus perpendicular.

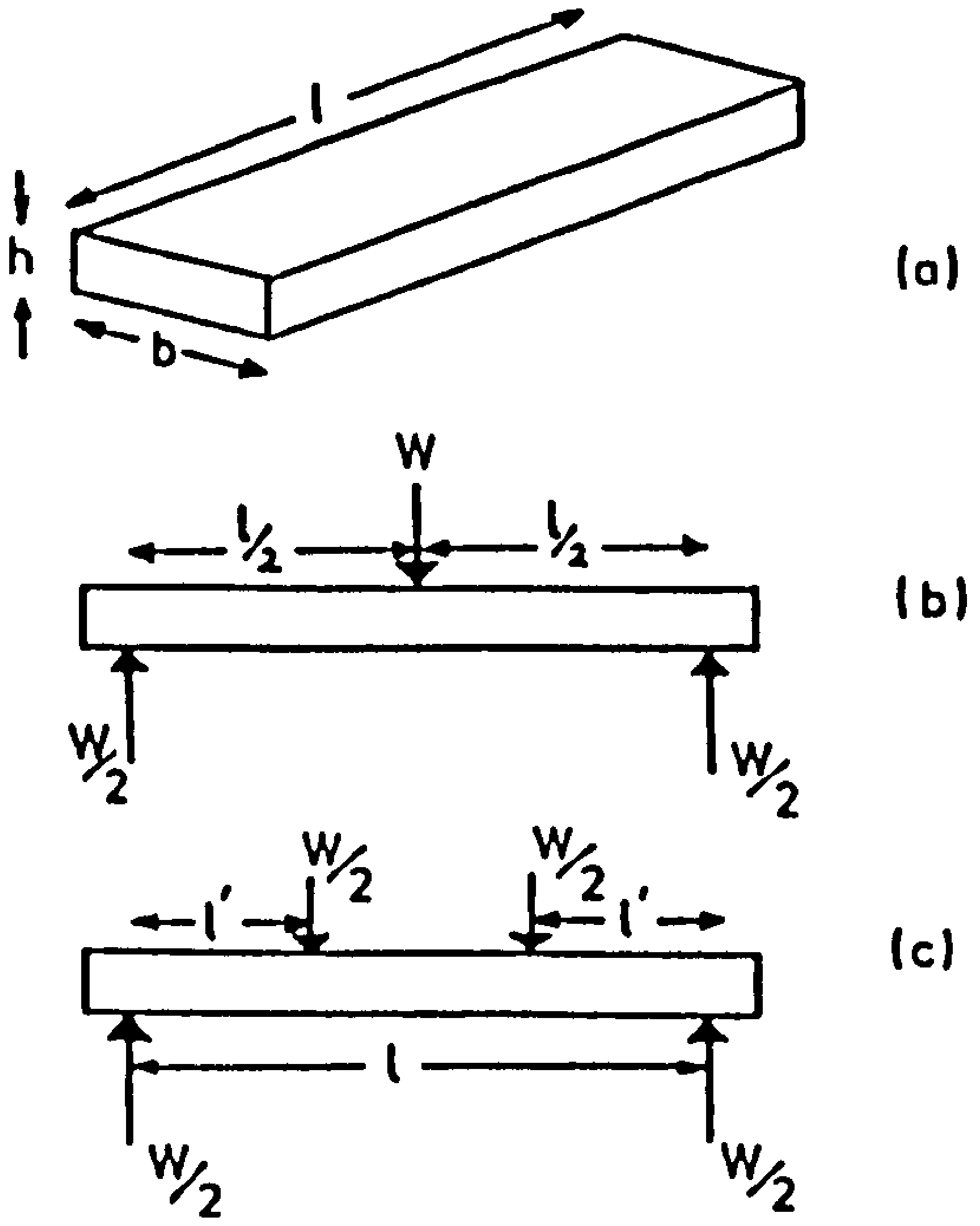

Fig. 5.2.1 Three- and four-point bend test geometries, (b) and (c) respectively, with associated symbols for dimensions (see (a)). (Ref. 71).

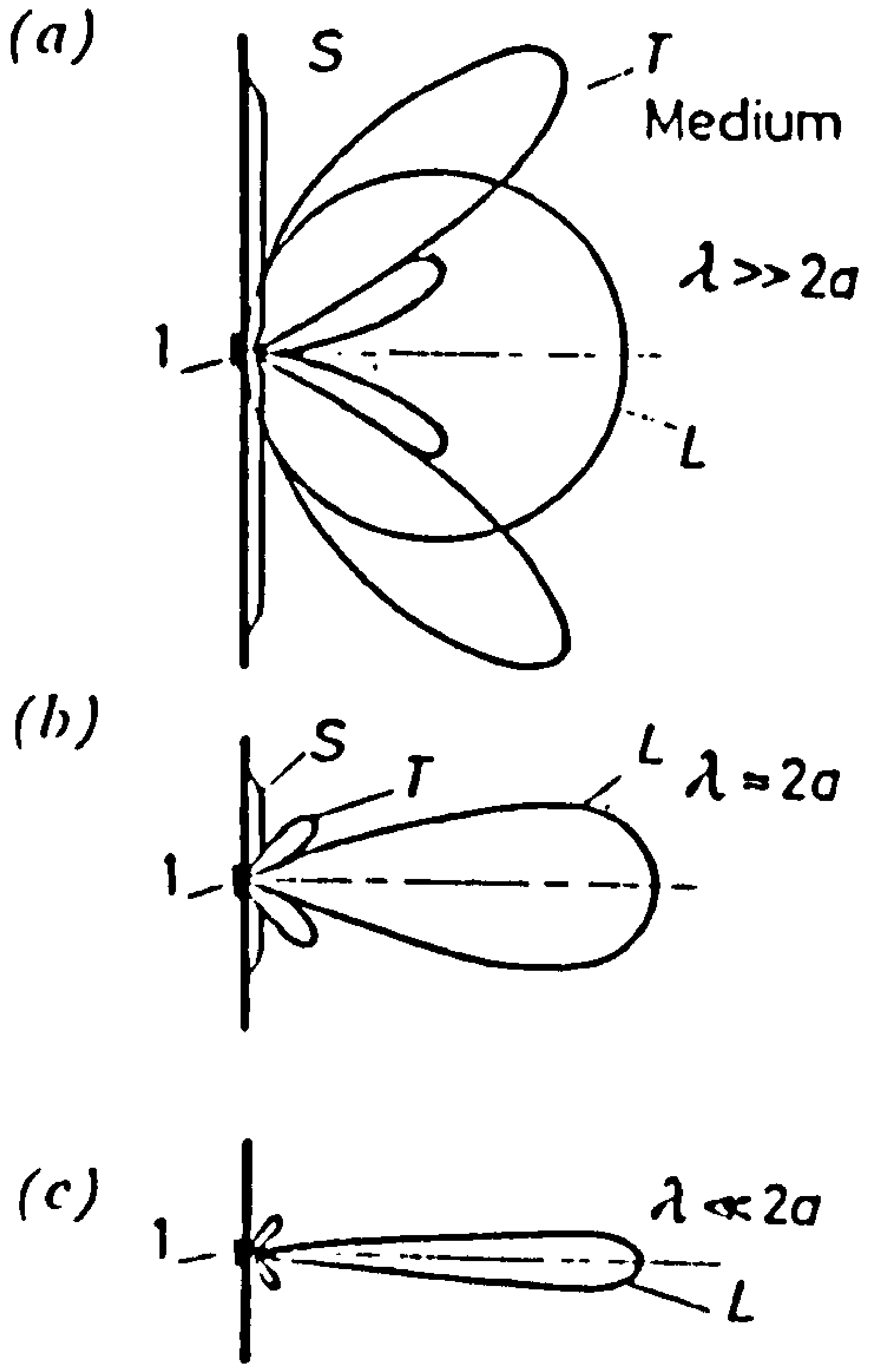

Fig. 5.2.2(b) Directional characteristics of a longitudinal wave transducer, having a diameter 2a, in a solid. L = longitudinal waves, T = transverse waves, S = surface waves, 1 = transducer. (Ref. 74).

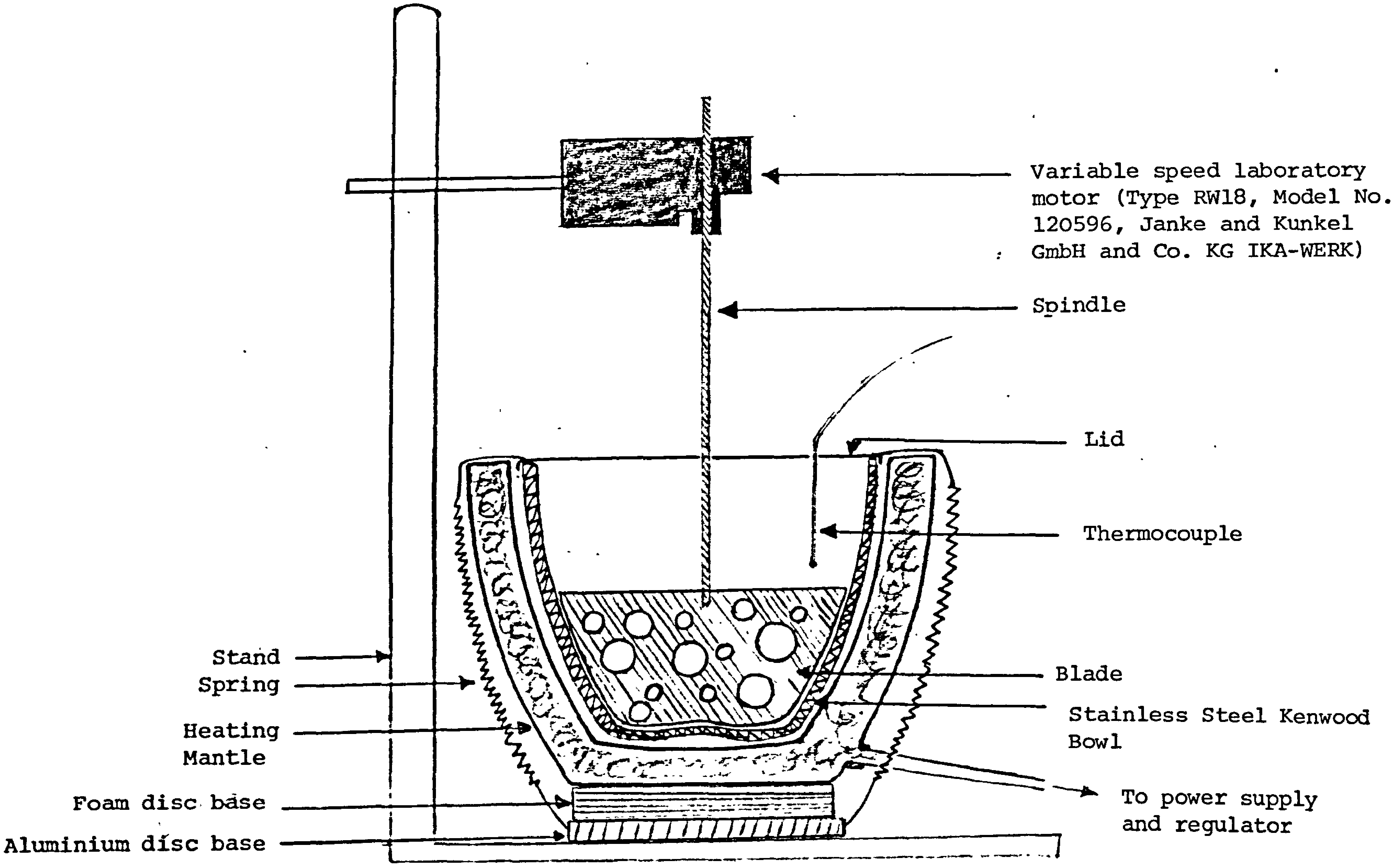

Fig. 5.3.2(i) Cross-section of the warm mixing apparatus used in mixing binder-containing composites.

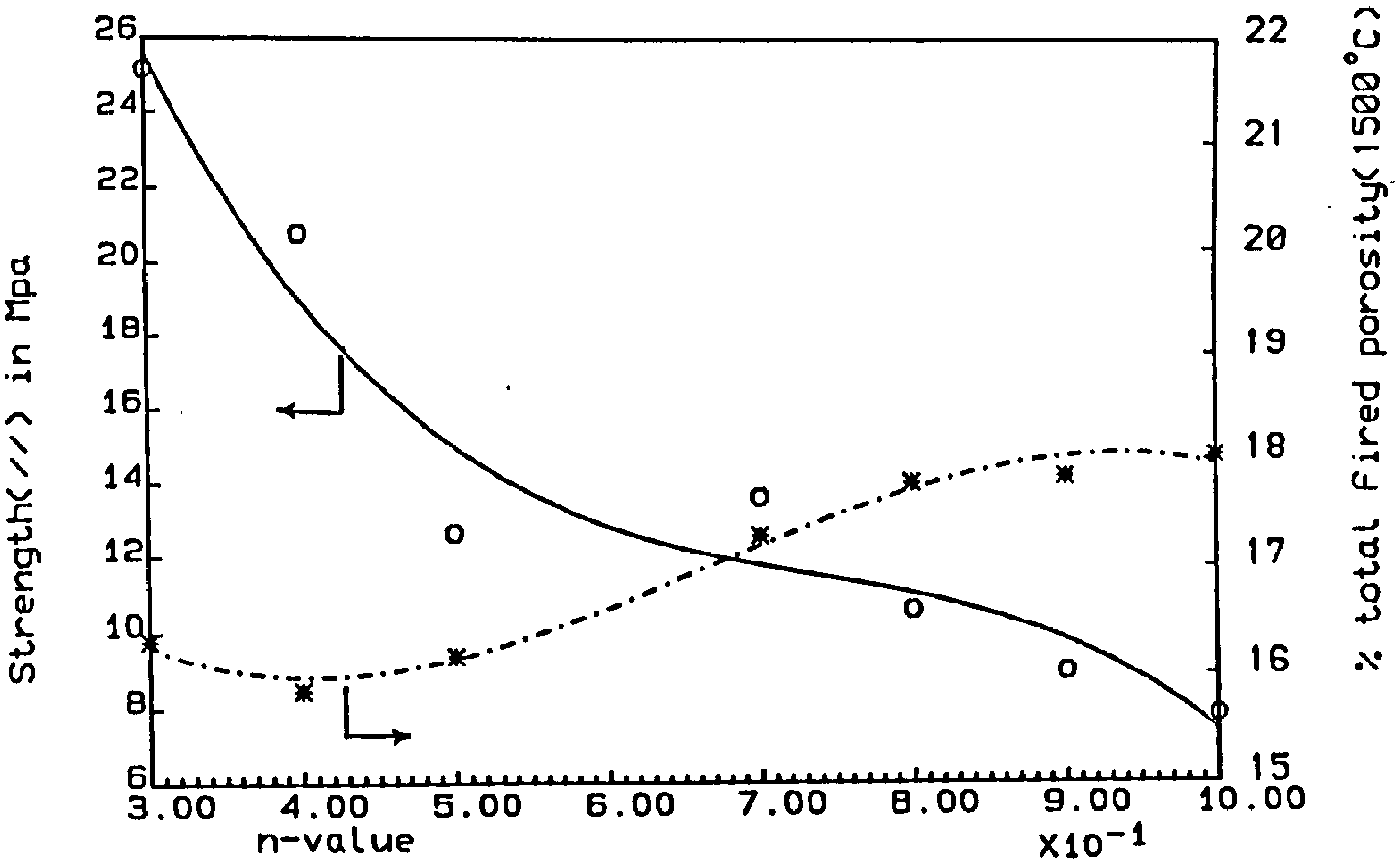

FIG. 5.5.1(a):Strength & porosity V's n-value (Fired Mgo only)

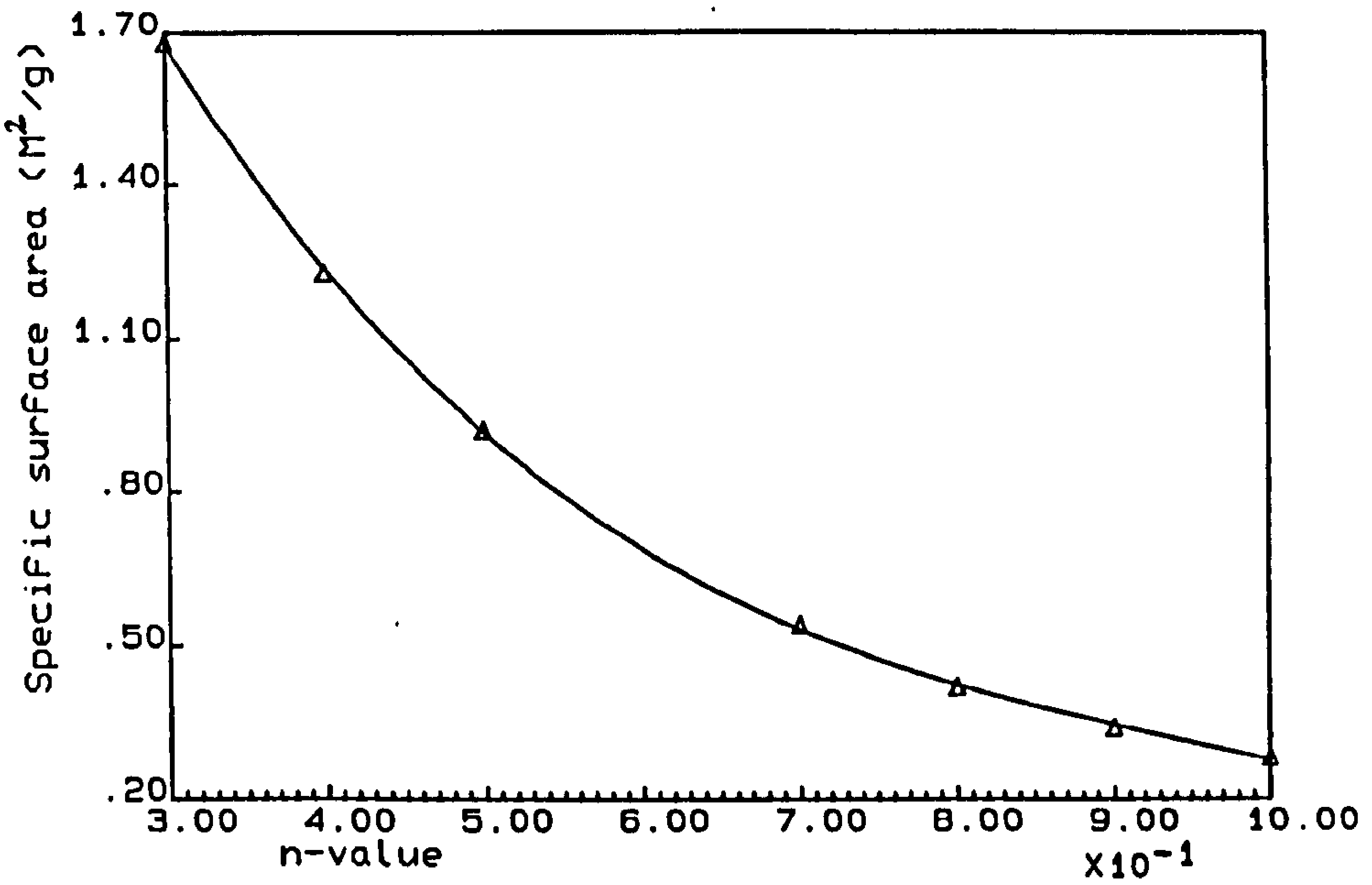

FIG. 5.5.1(b) :Specific surface area V's n-value of Mgo grain size mixtures only.

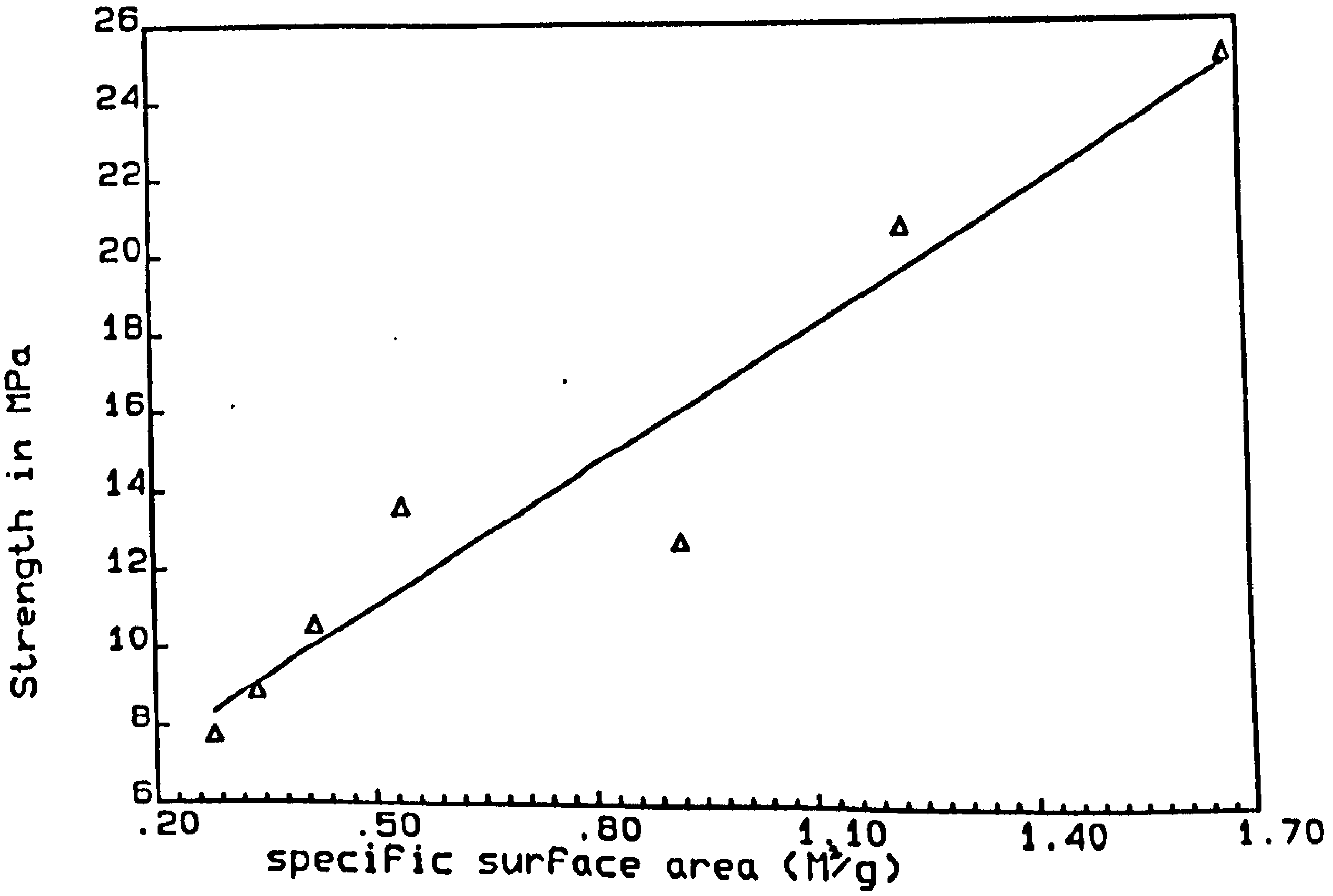

FIG. 5.5.1(c): Strength V's specific surface area of Mgo grain size mixtures only.

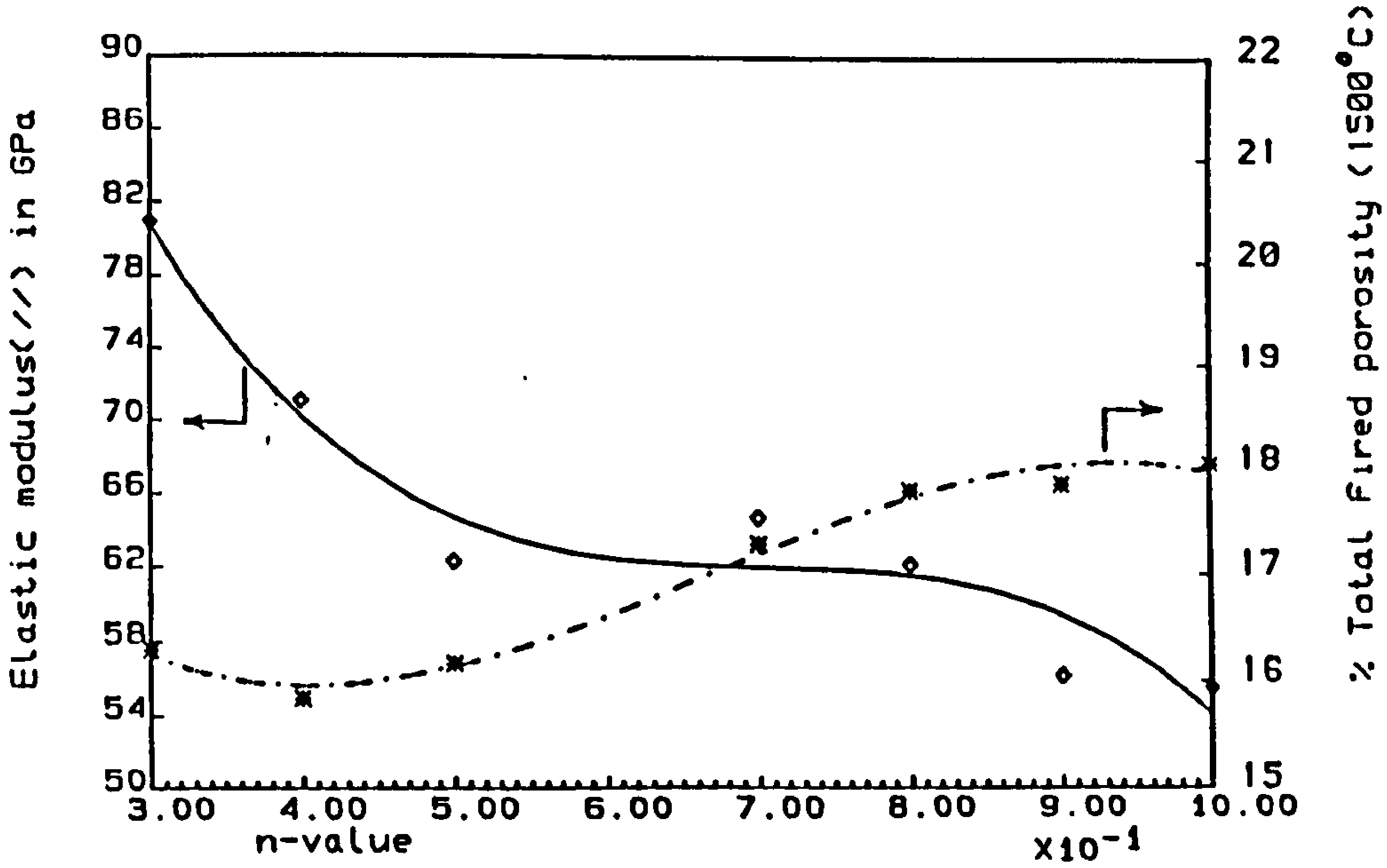

FIG. 5.5.1(d): Elastic modulus & porosity V's n-value (Fired Mgo only)

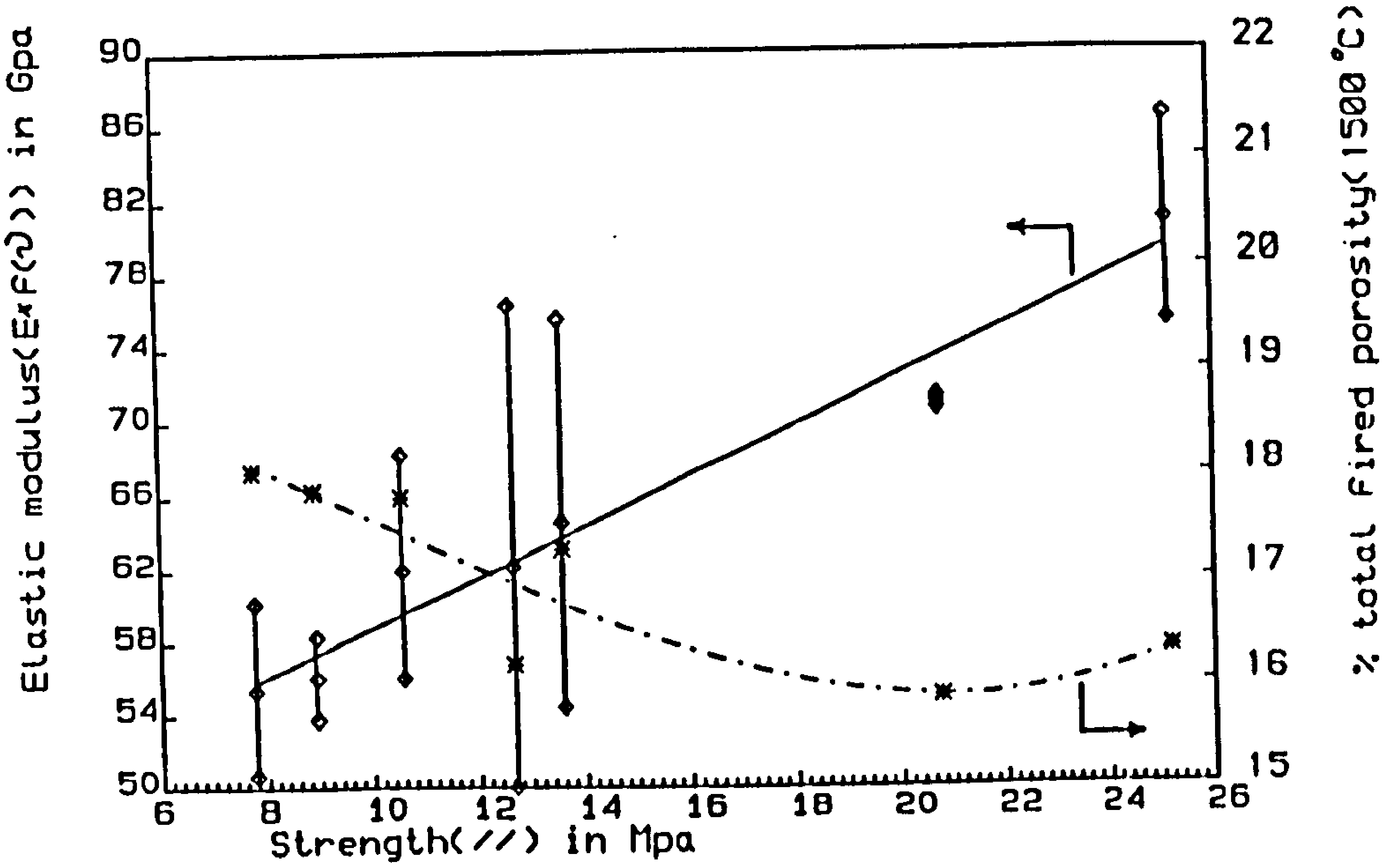

FIG. 5.5.1(e):Elastic modulus(//) & porosity V's Strength(//) of Fired Mgo only

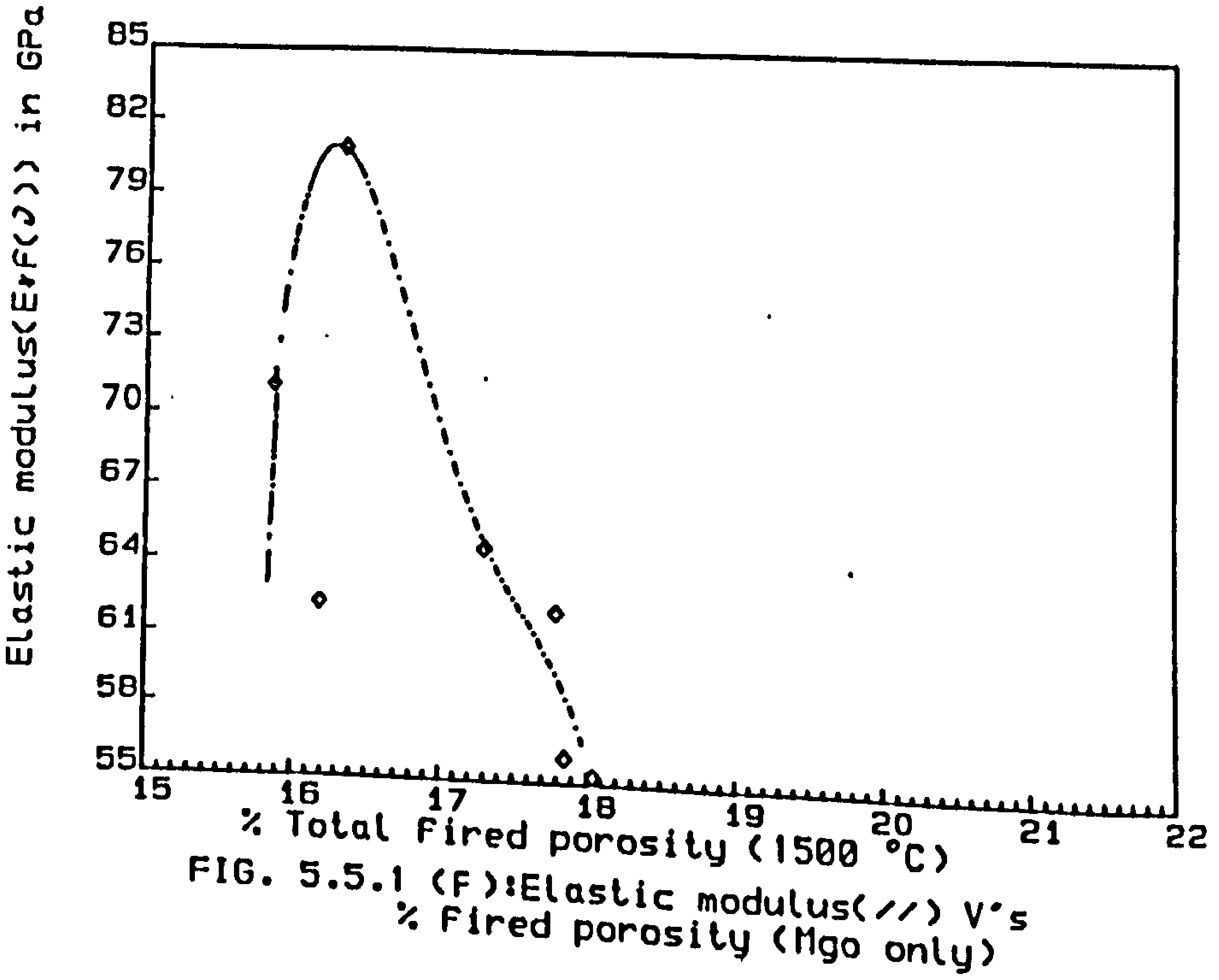

FIG. 5.5.1 (F):Elastic modulus(//) V's % Fired porosity (Mgo only)

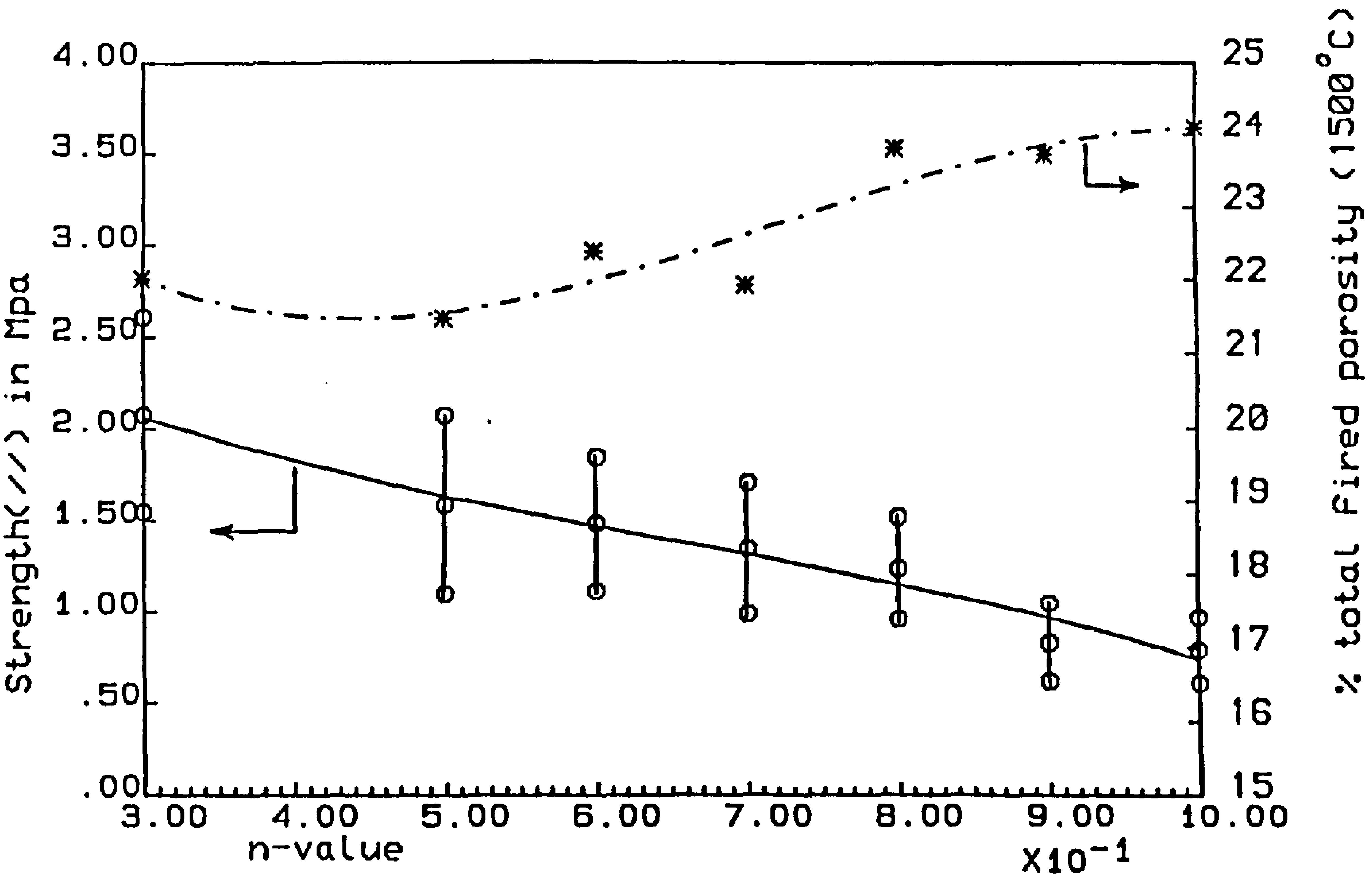

FIG. 5.5.2(a):Strength & porosity V's n-value (Fired Mgo+5% pitch)

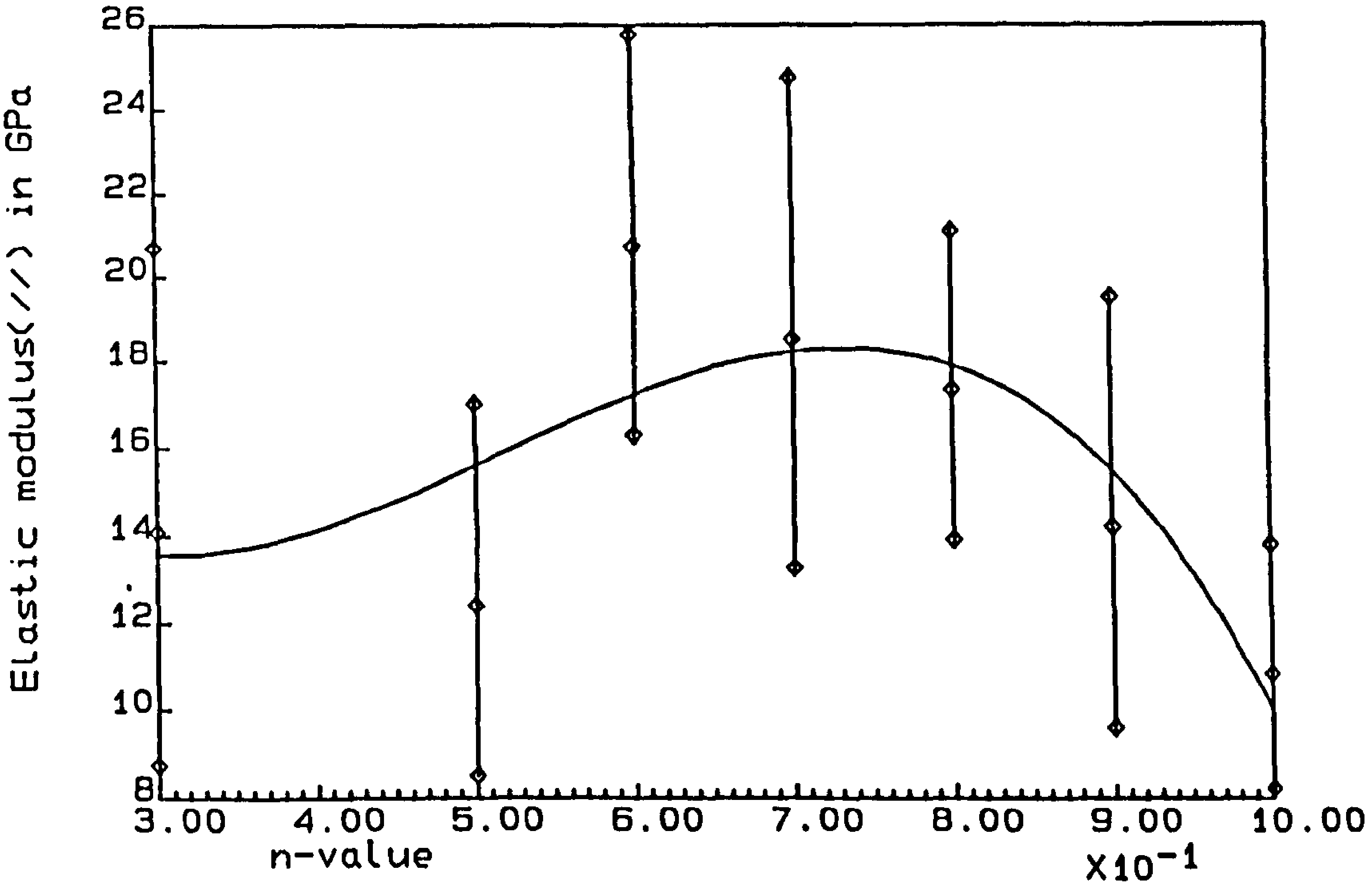

FIG. 5.5.2 (b): Relative elastic modulus V's n-value (Mgo + pitch only)

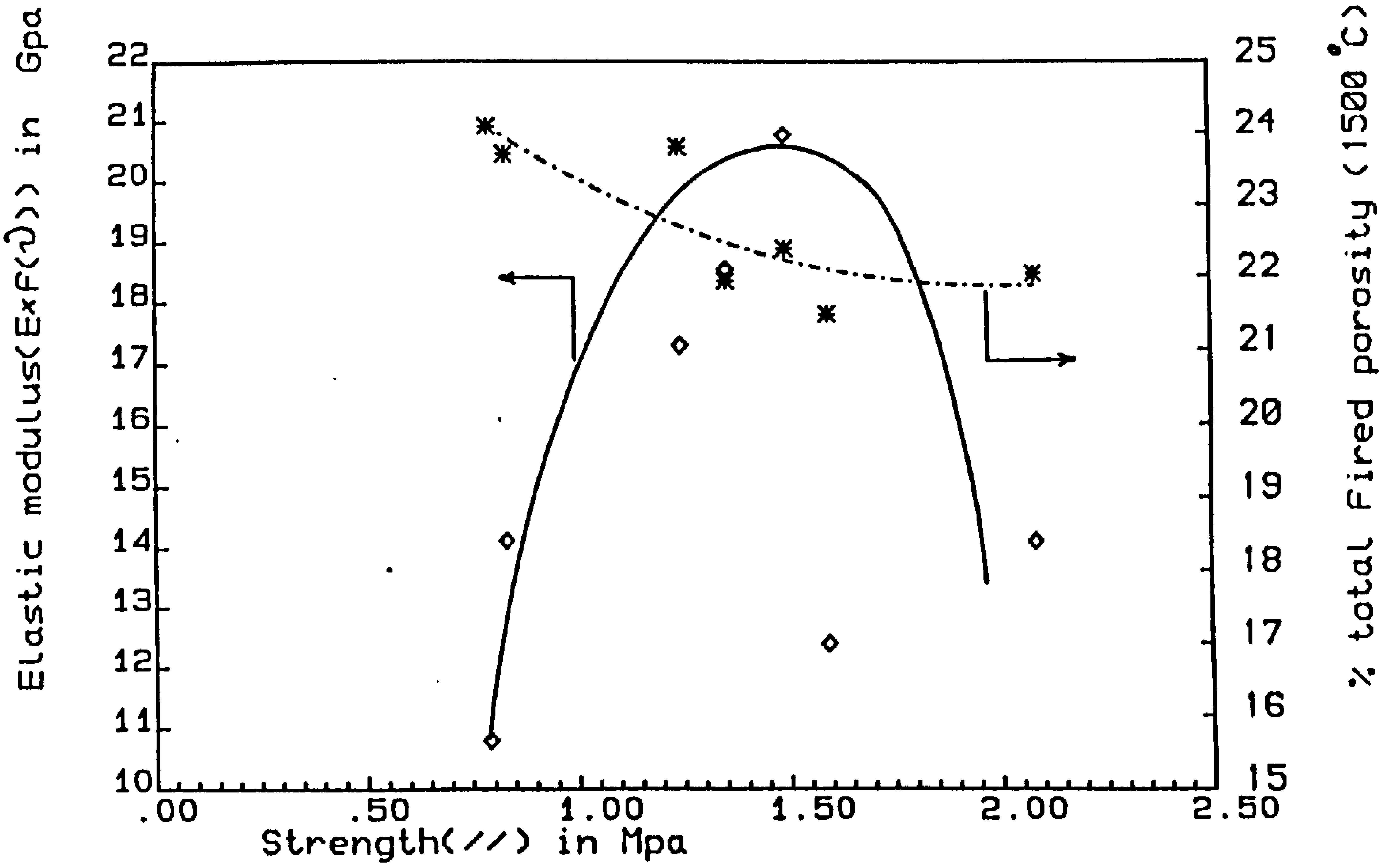

FIG. 5.5.2(c):Elastic modulus & porosity
V's strength (Fired Mgo+5% pitch)

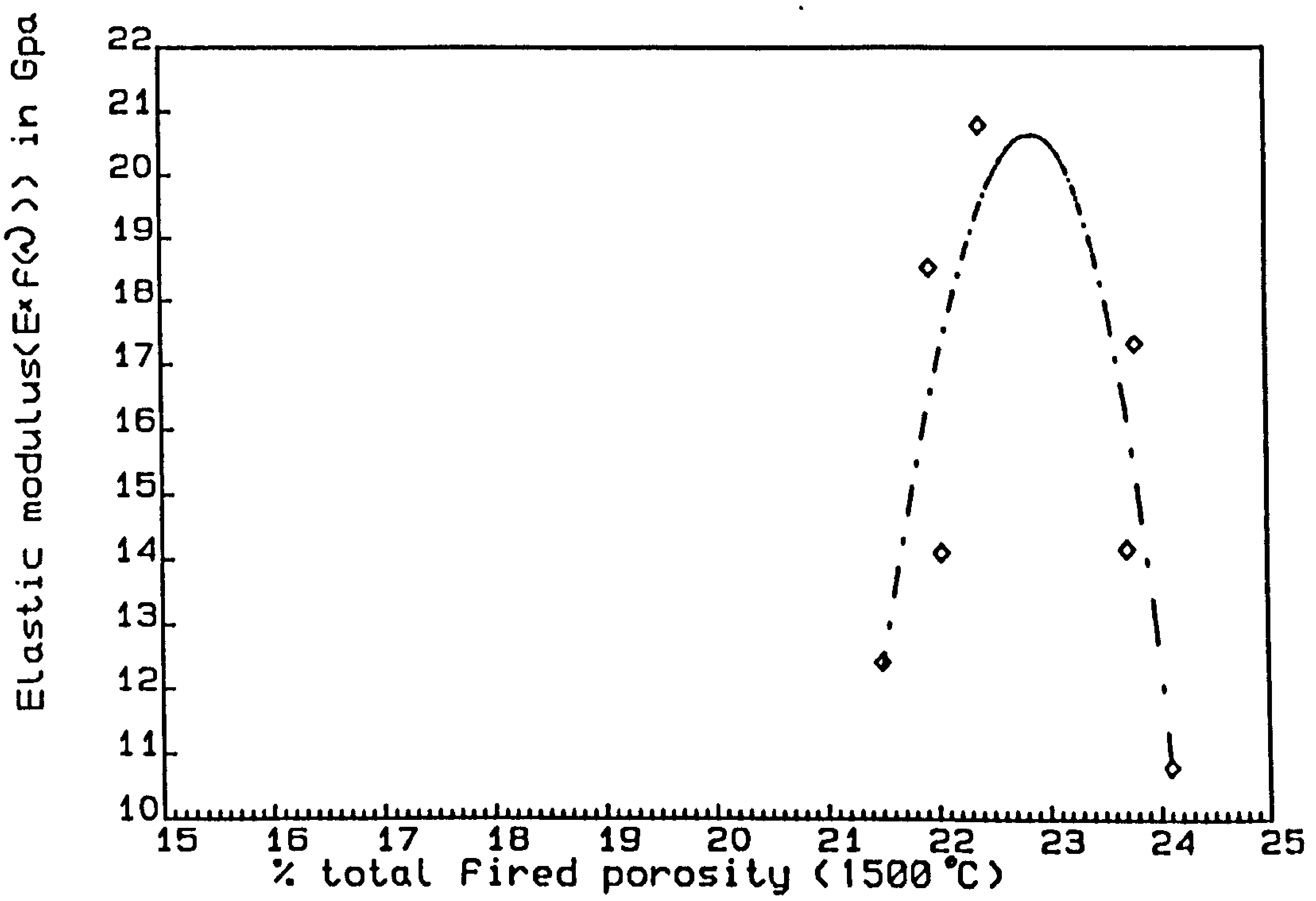

FIG. 5.5.2(d):Elastic modulus(//) V's
% total porosity (Fired Mgo+5% pitch)

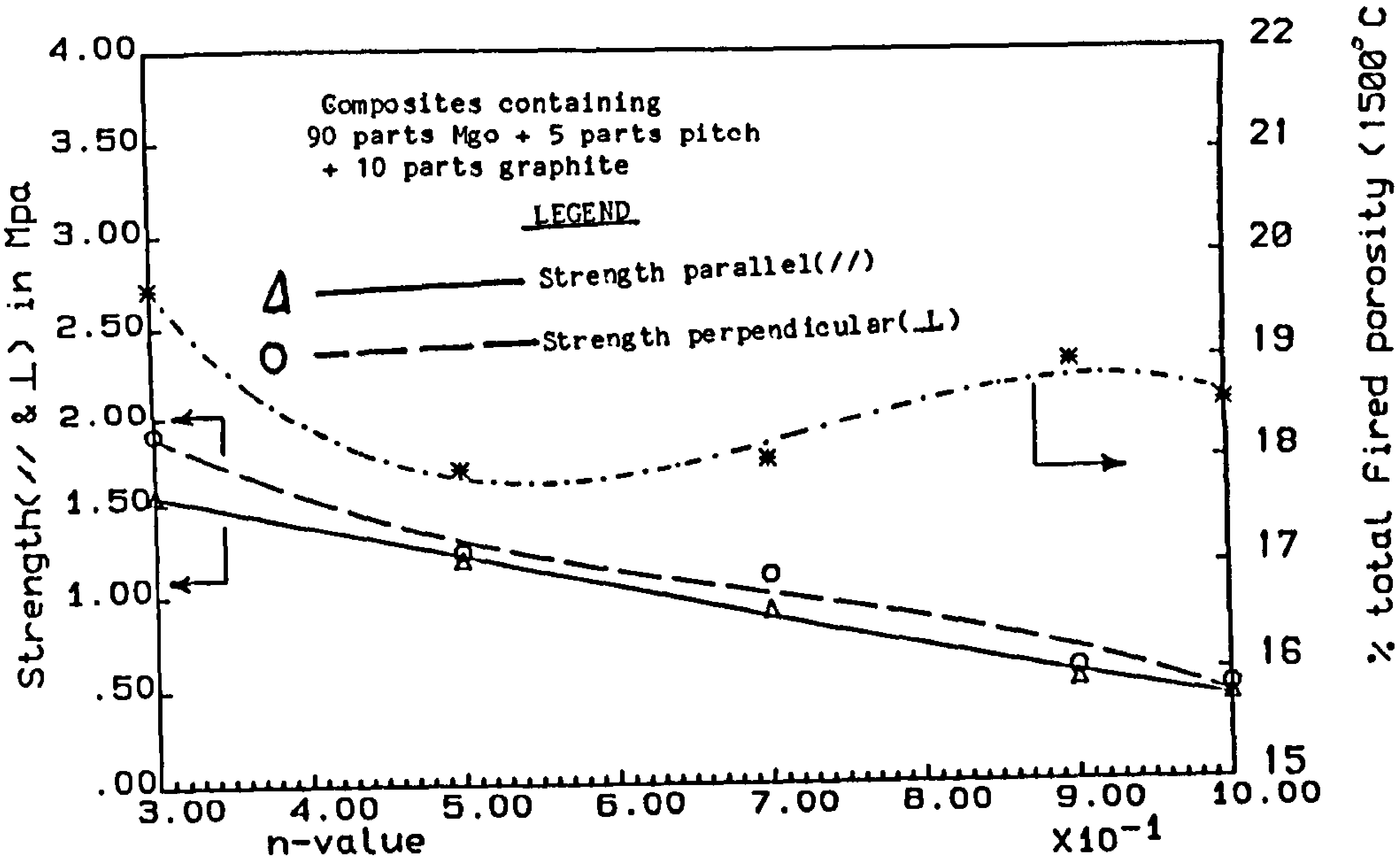

FIG. 5.5.3 i(a):/Strength & porosity V's n-value(Comp. with 10% graphite A)

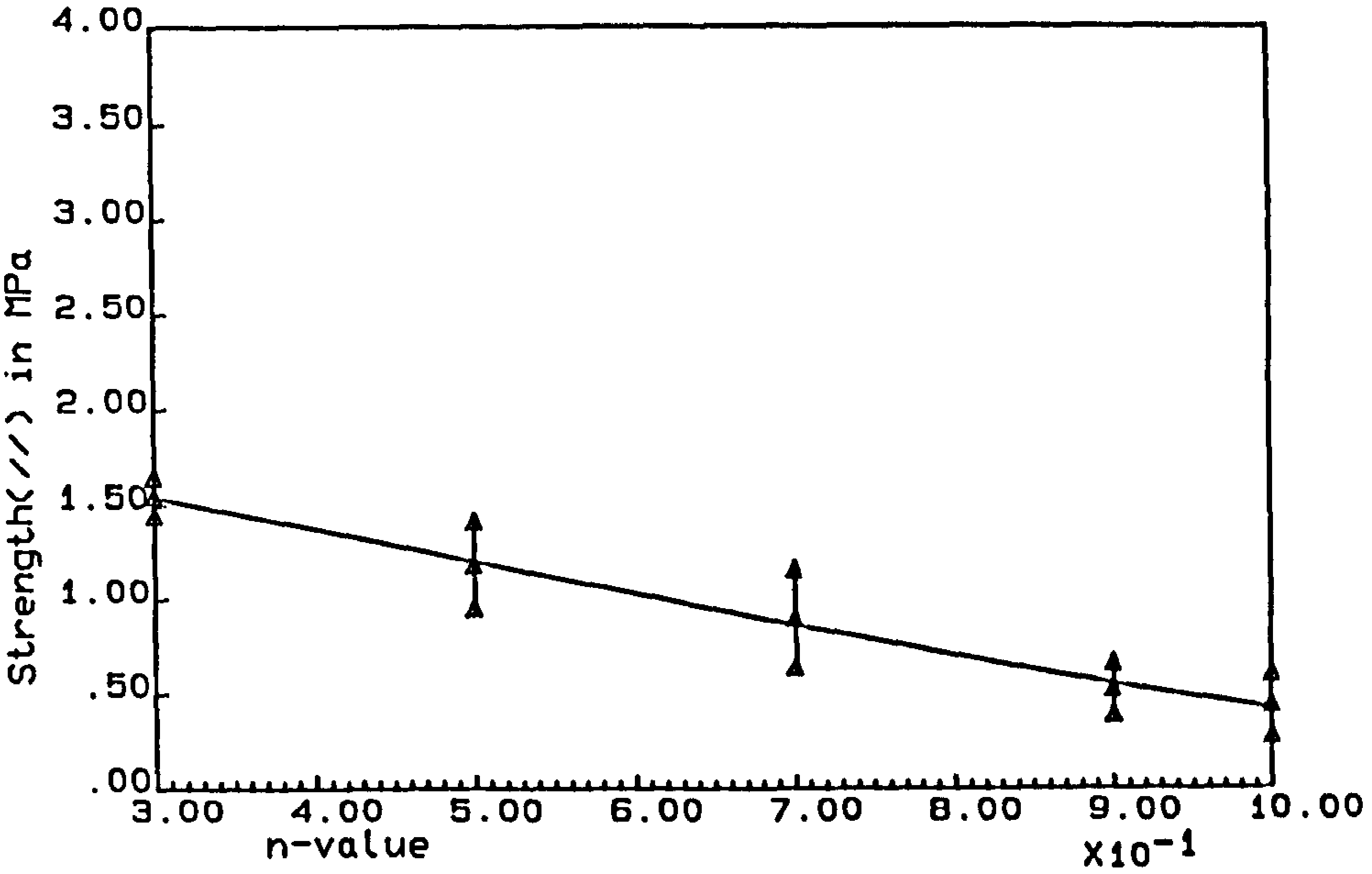

FIG. 5.5.3 i(b):Strength(//) V's n-value (Comp. with 10% graphite A)

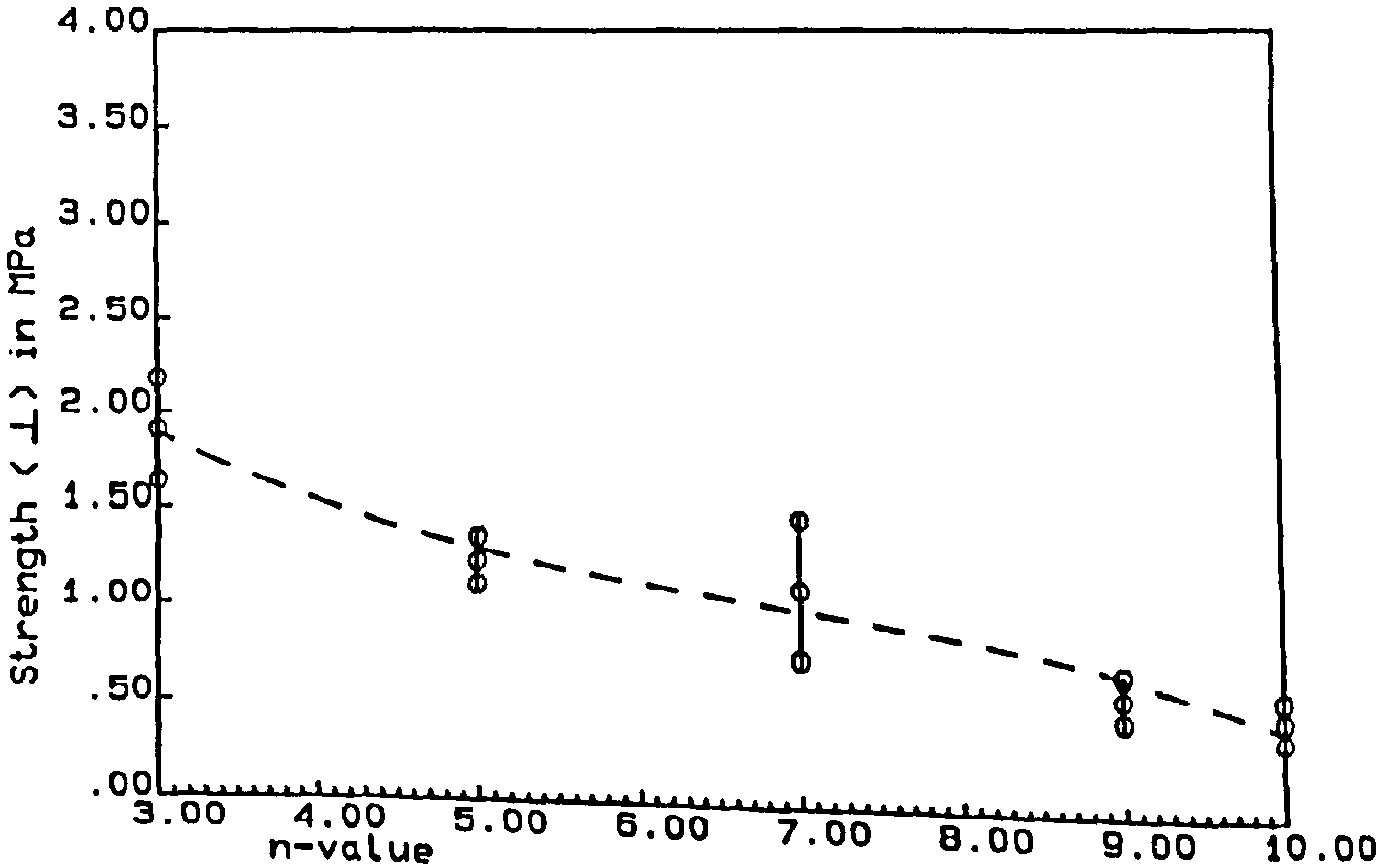

FIG. 5.5.3 i(c):Strength(⊥) V's n-value (Comp. with 10% graphite A)

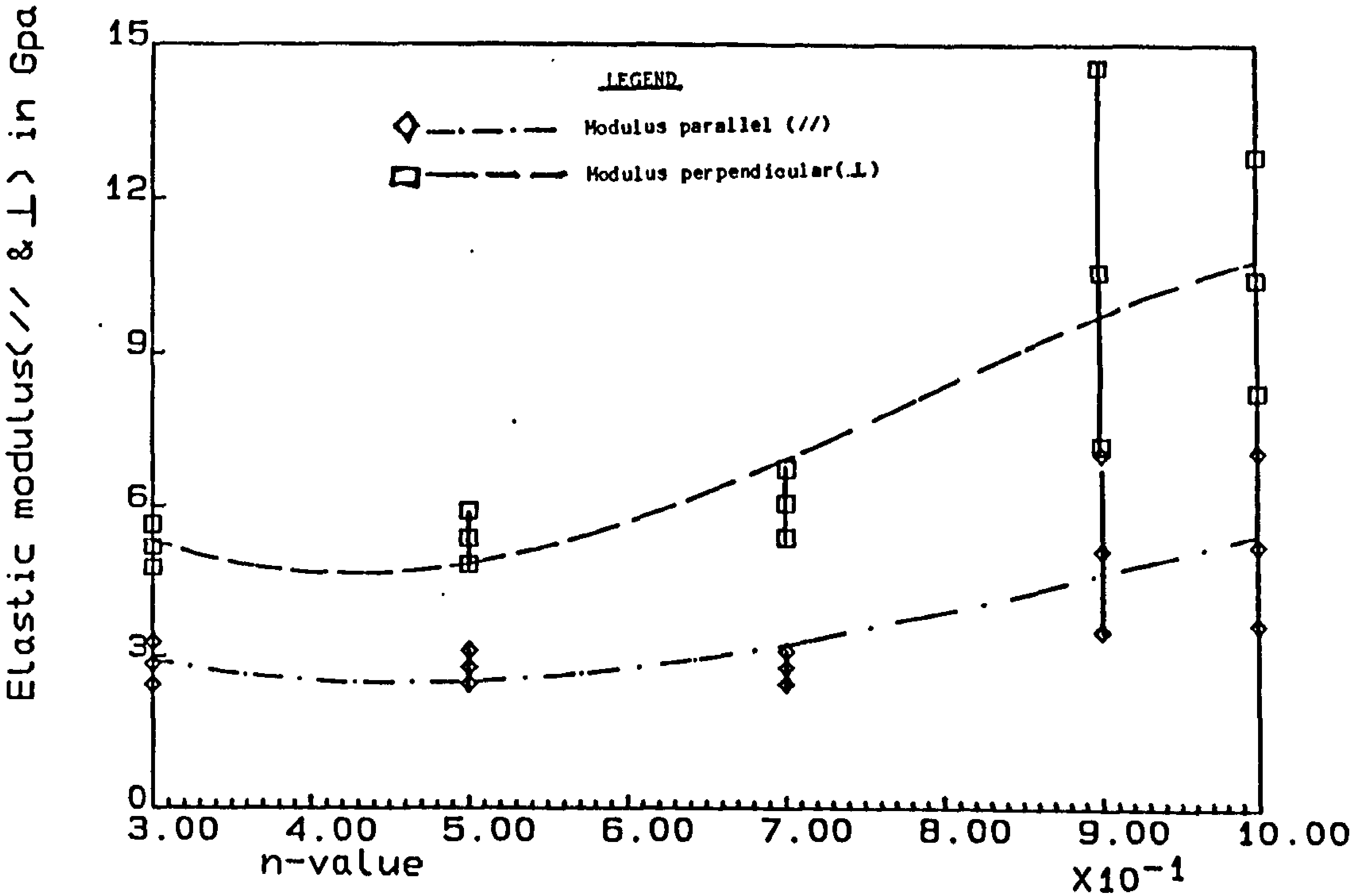

FIG. 5.5.3 ii(a):Ealstic modulus(ExF(ϑ))
V's n-value (Comp. with 10% graphite A)

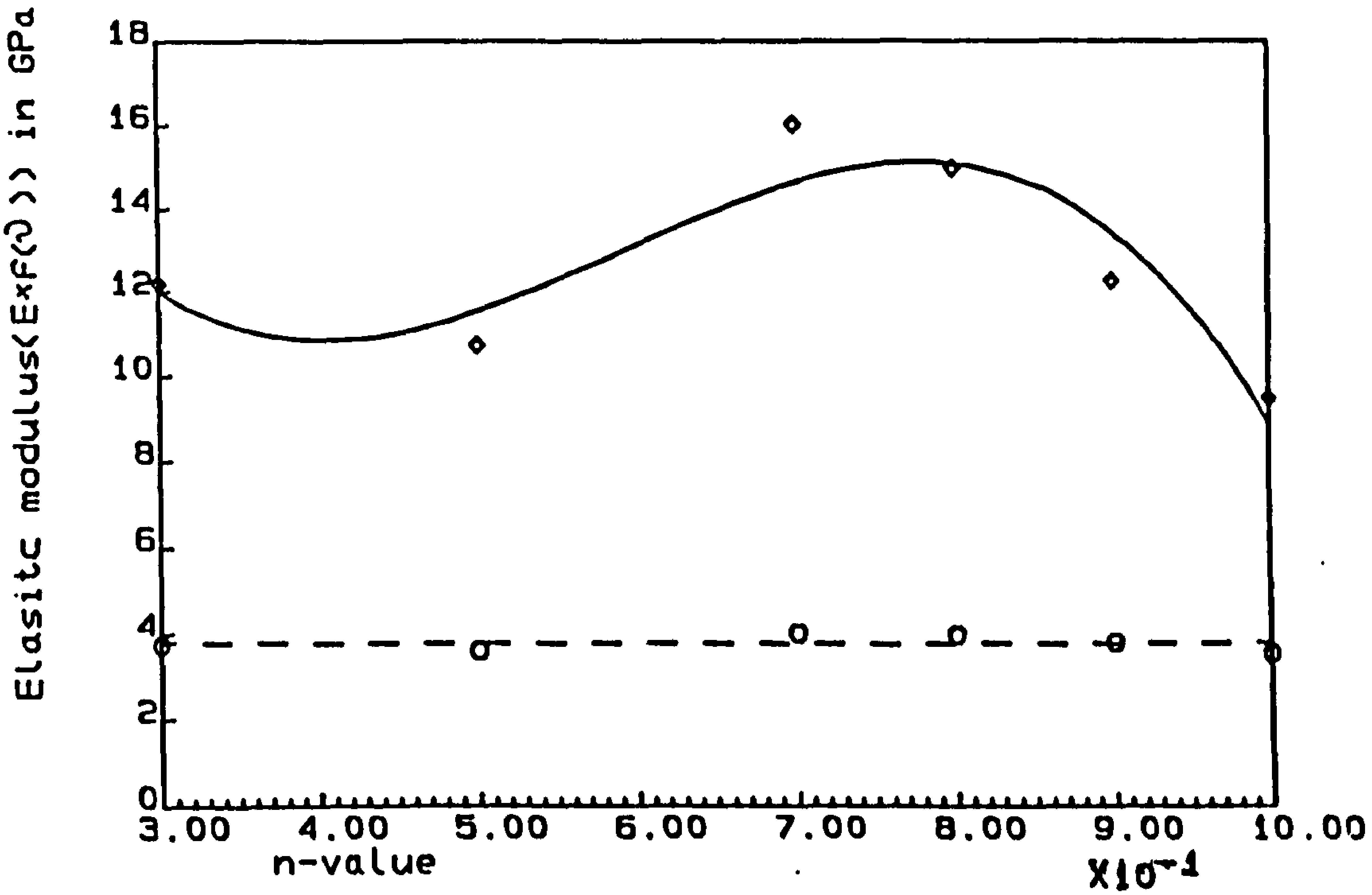

FIG. 5.5.3 ii(b):Elastic modulus (calculated)
V's n-value

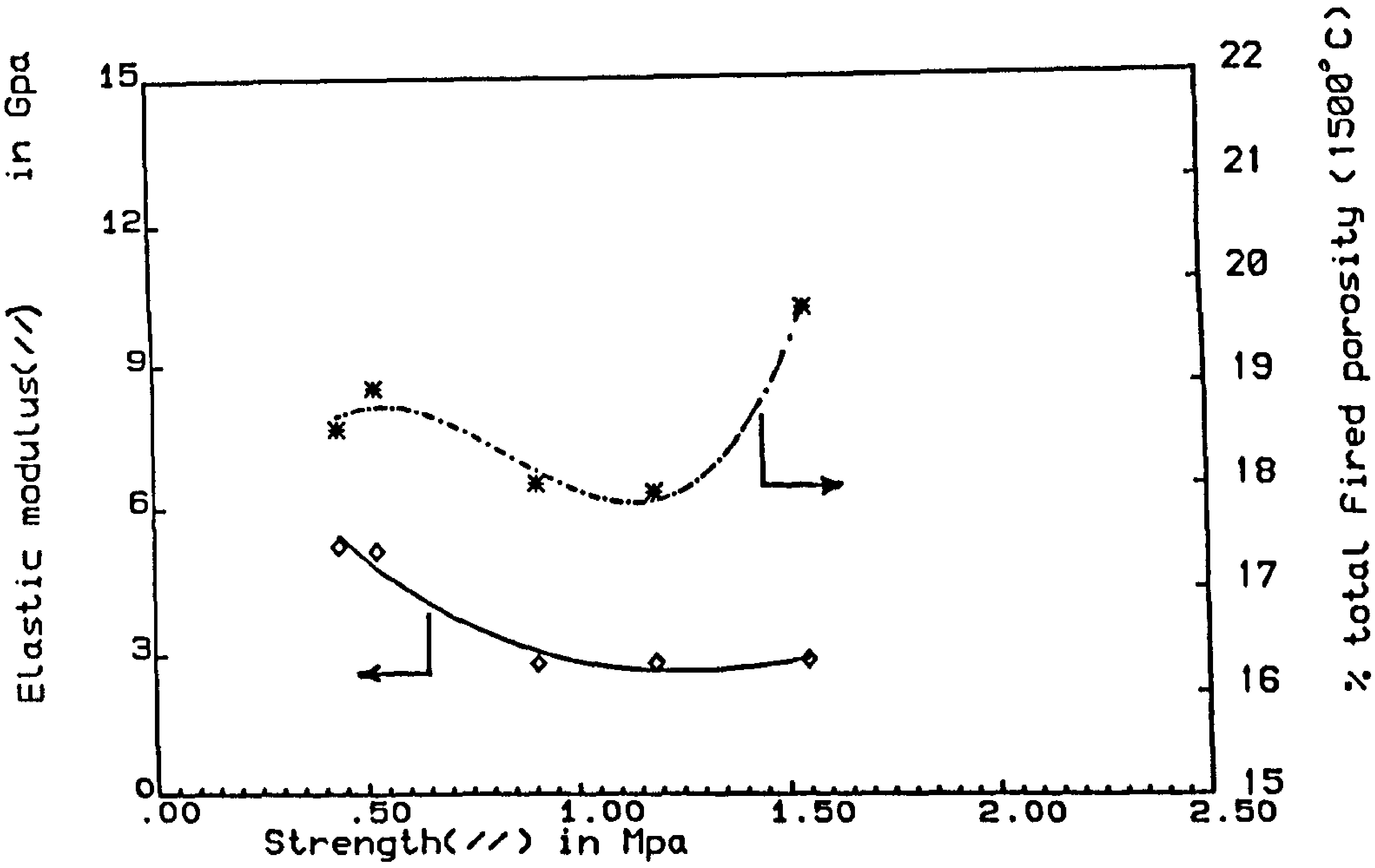

FIG. 5.5.3 iii(a):elastic modulus & porosity
V's strength (Comp. with 10% graphite A)

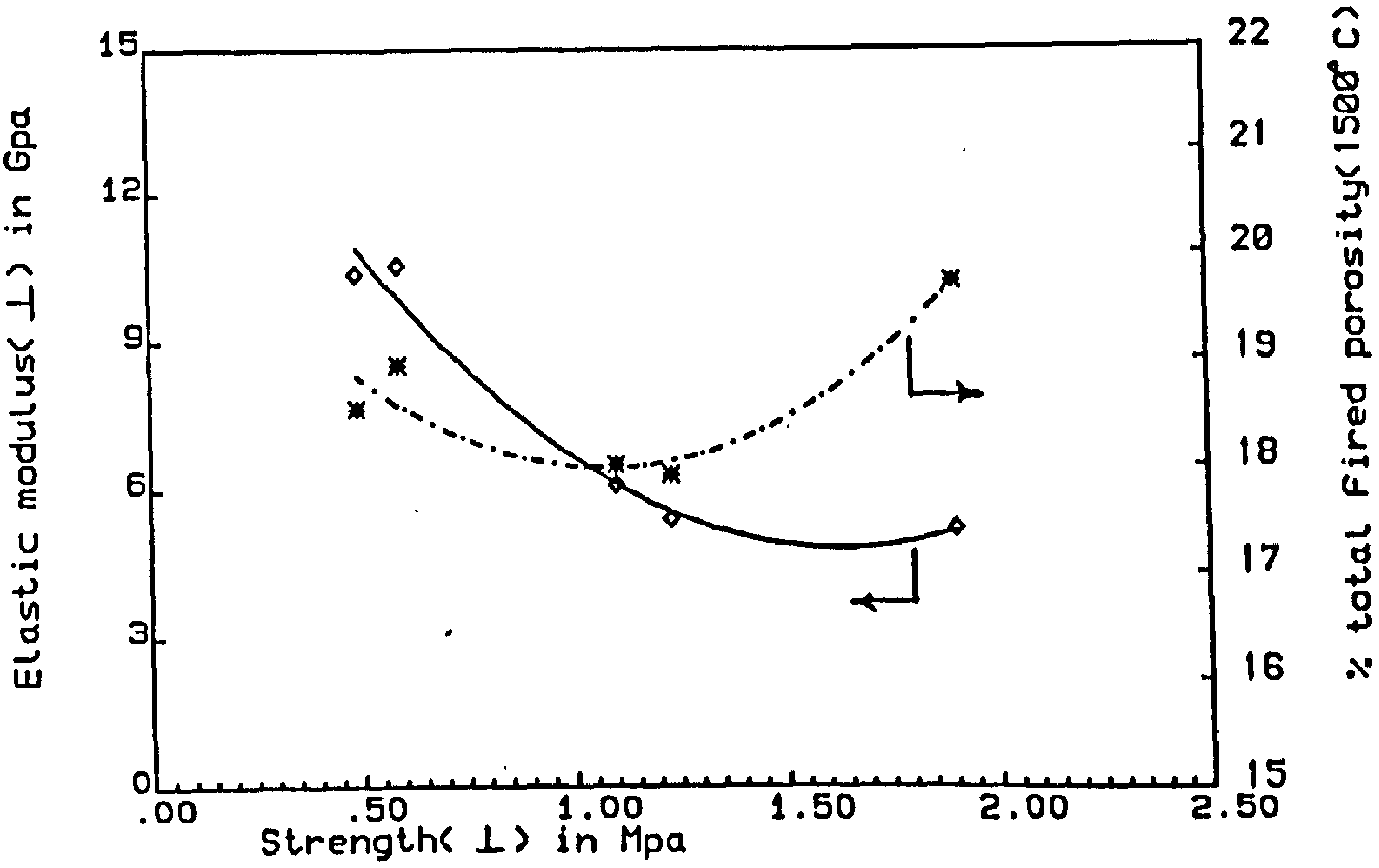

FIG. 5.5.3 iii(b):elastic modulus & porosity
V's strength (Comp. with 10% graphite A)

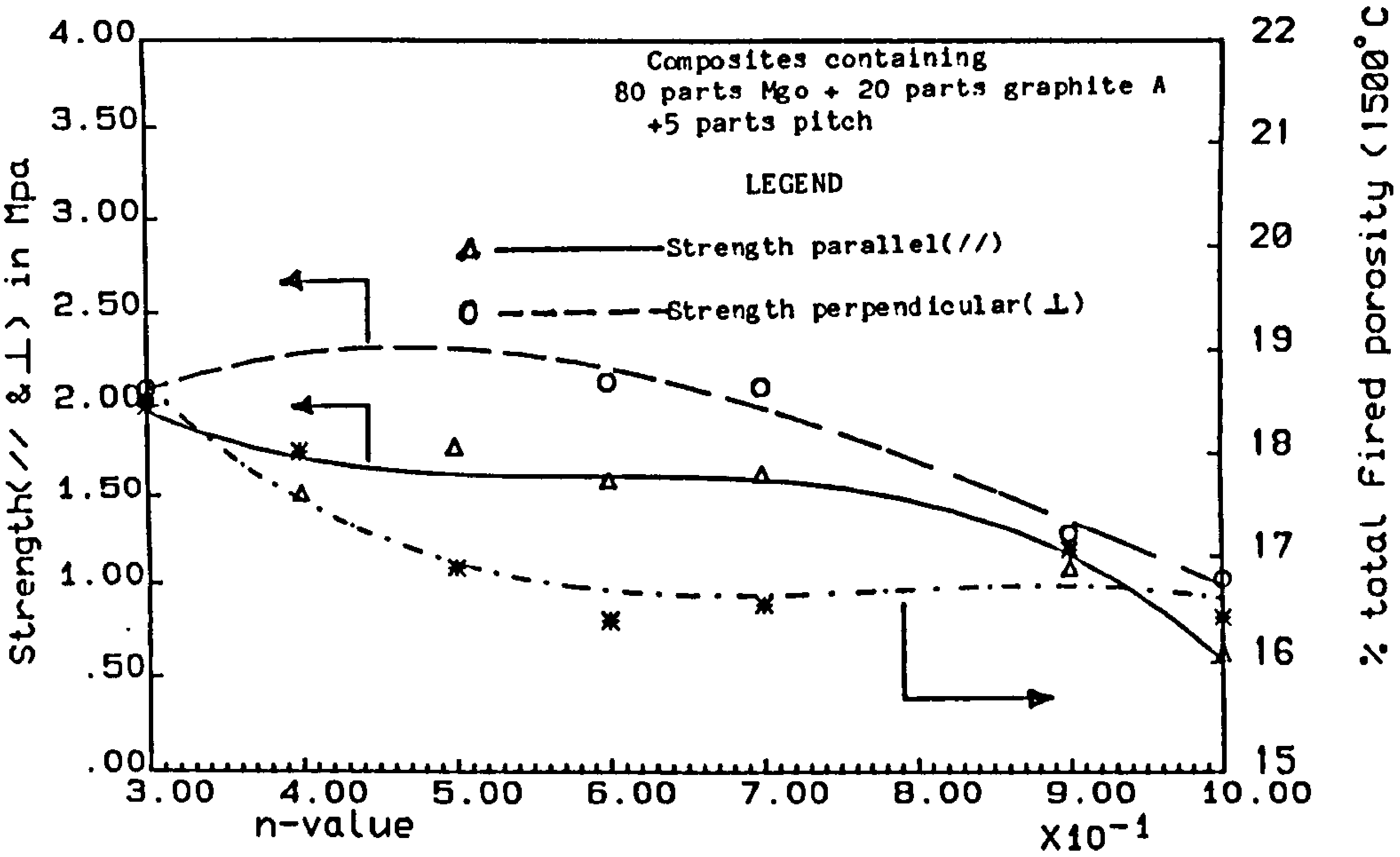

FIG. 5.5.4 i(a):Strength & porosity V's n-vaue (Comp.with 20% graphite A)

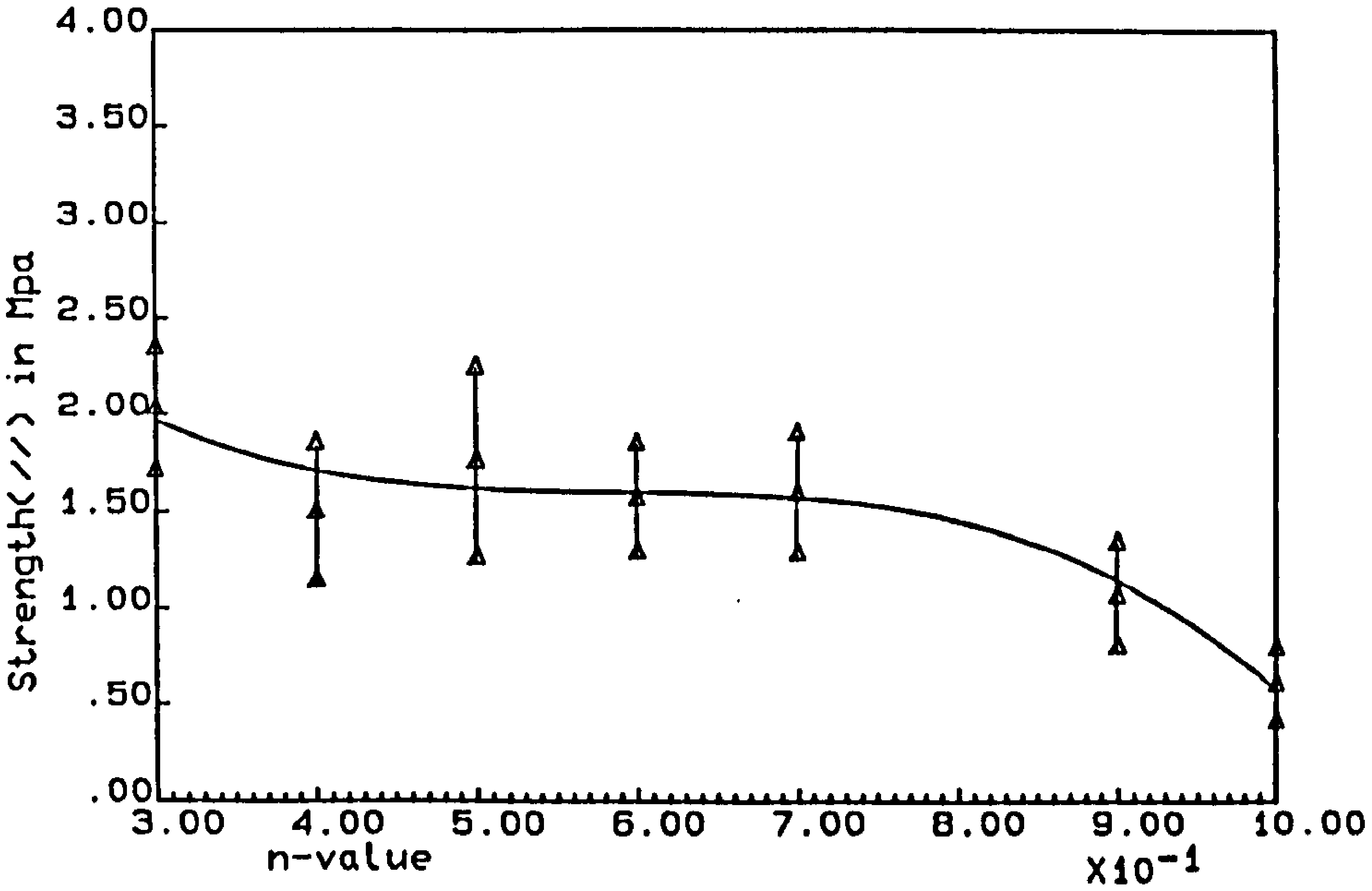

FIG. 5.5.4 i(b):Strength(//) V's n-value (Comp. with 20% graphite A

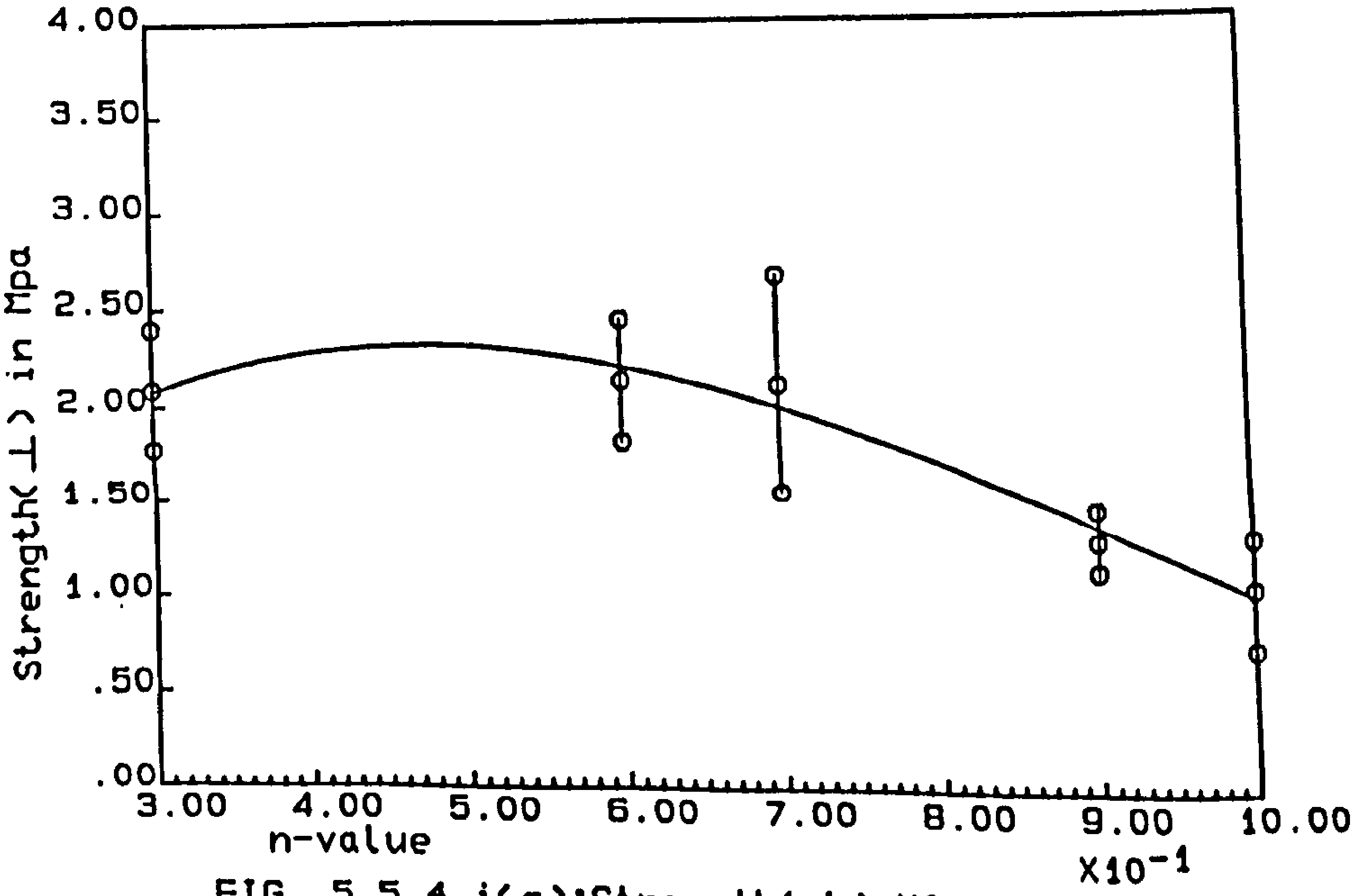

FIG. 5.5.4 i(c):Strength(⊥) V's n-value (Comp. with 20% graphite A)

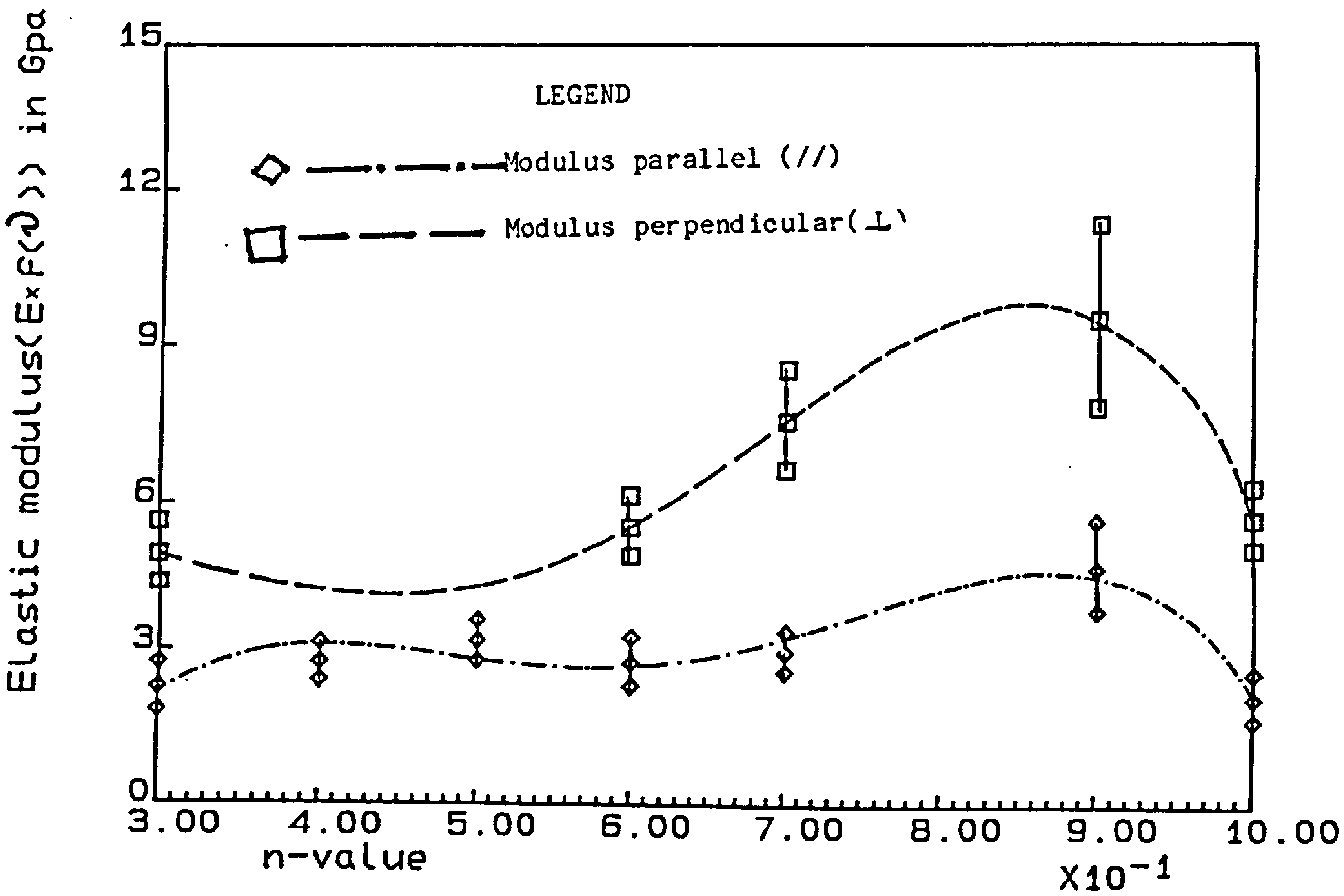

FIG. 5.5.4(ii):Elastic modulus V's n-value
(Comp. with 20% graphite A)

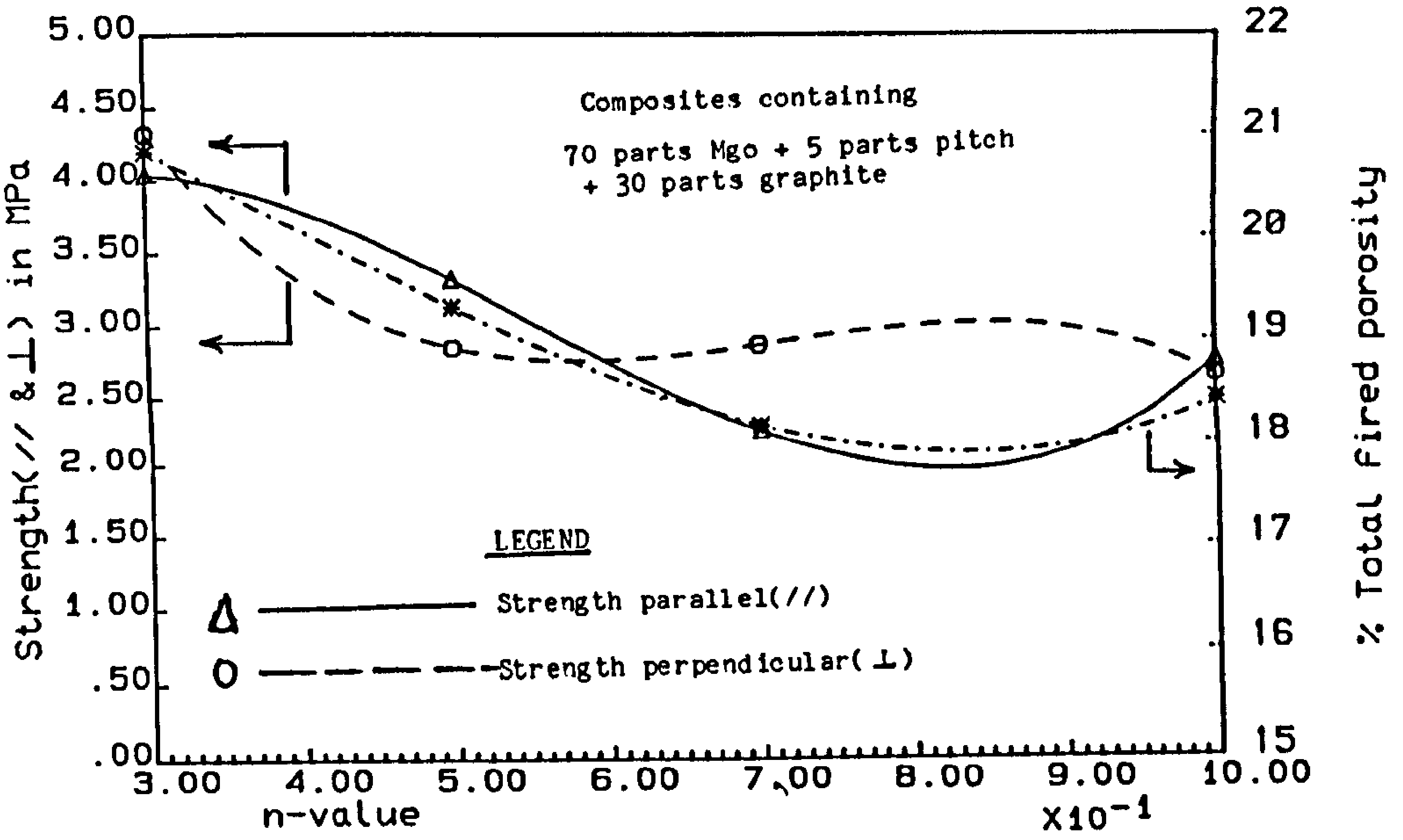

FIG. 5.5.5 i(a):Strength & porosity V's n-value (Comp. with 30% graphite A)

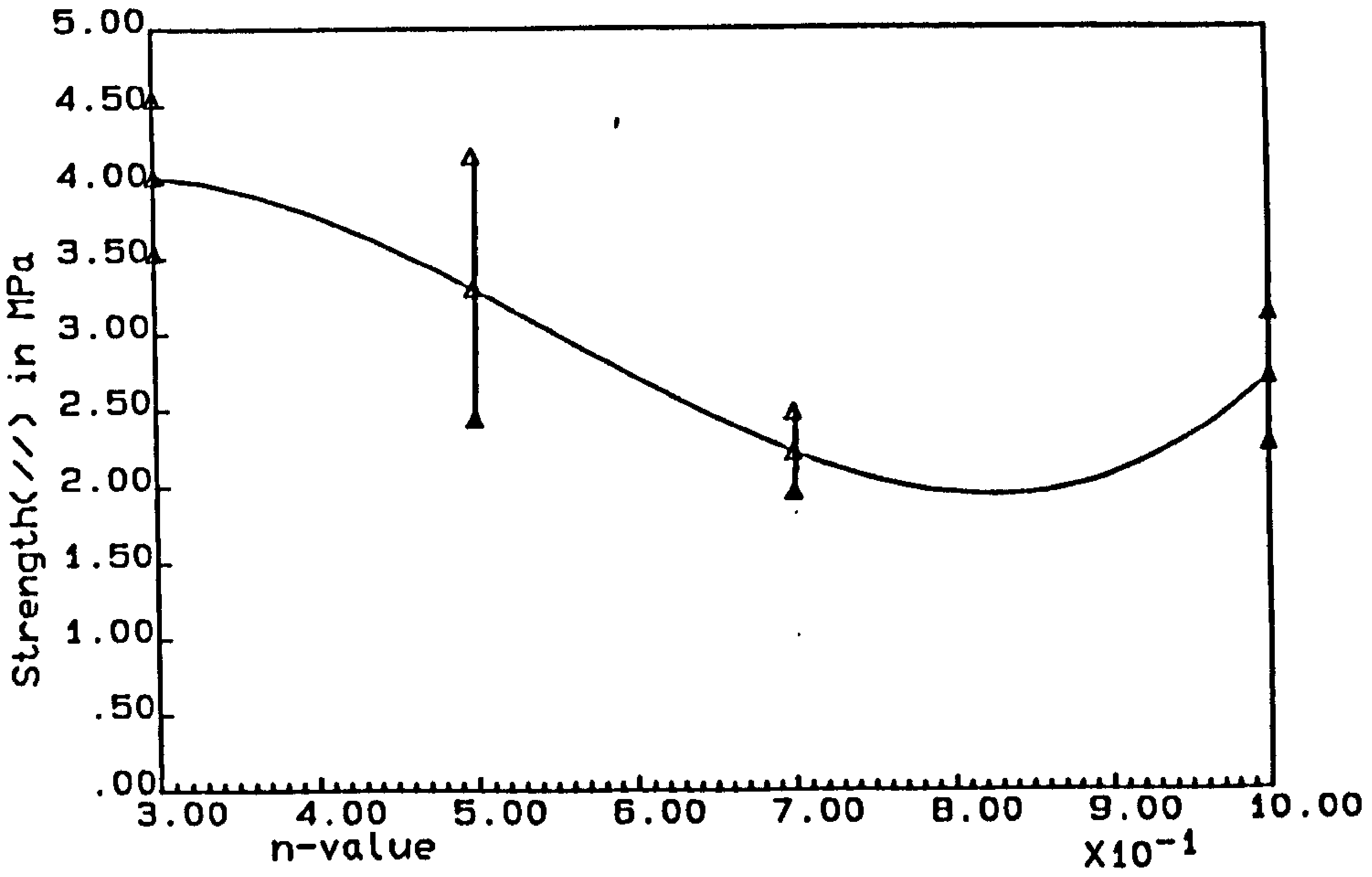

FIG. 5.5.5 i(b):Strength V's n-value (comp. with 30% graphite A)

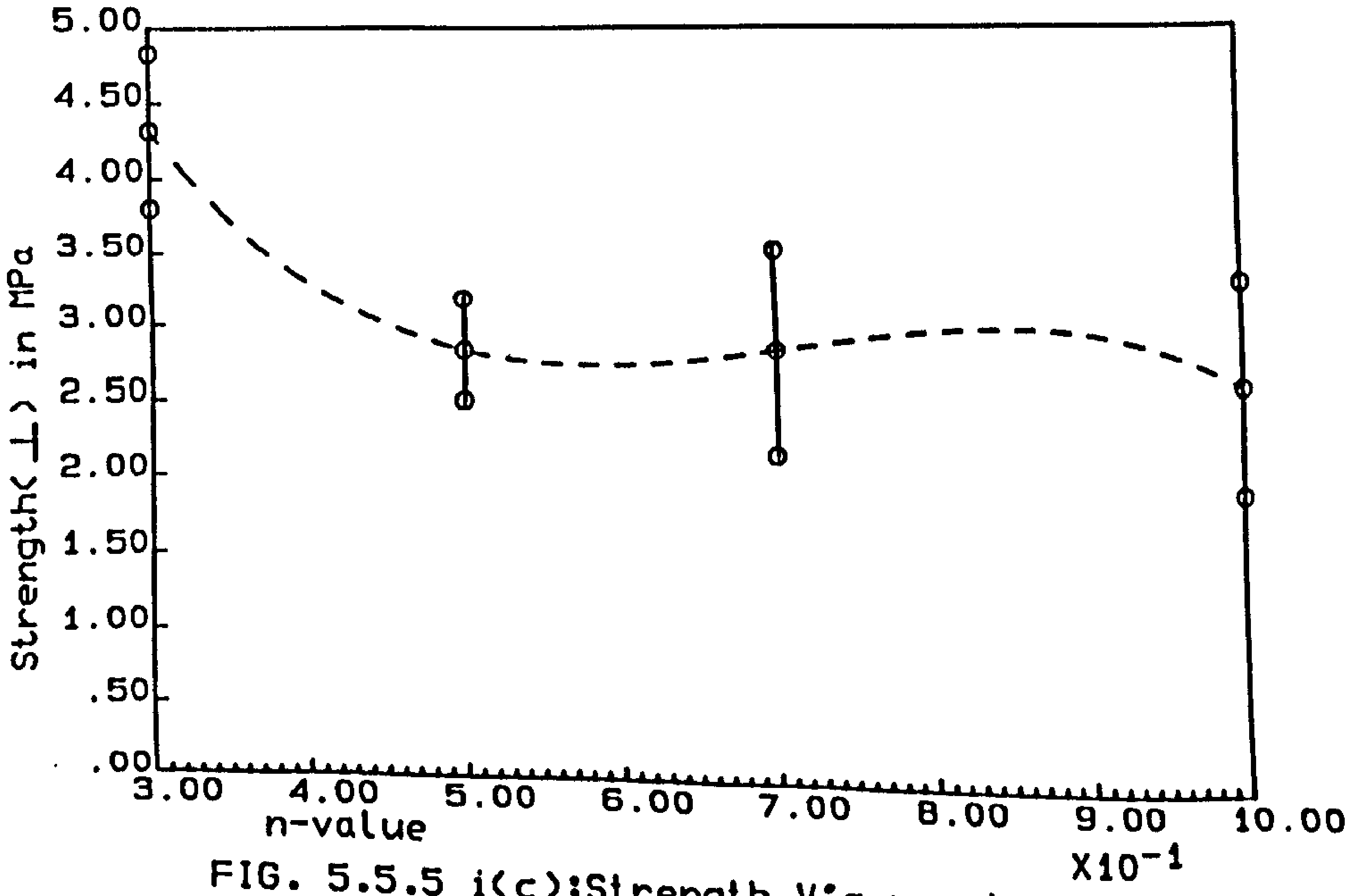

FIG. 5.5.5 i(c):Strength V's n-value (Comp. with 30% graphite A)

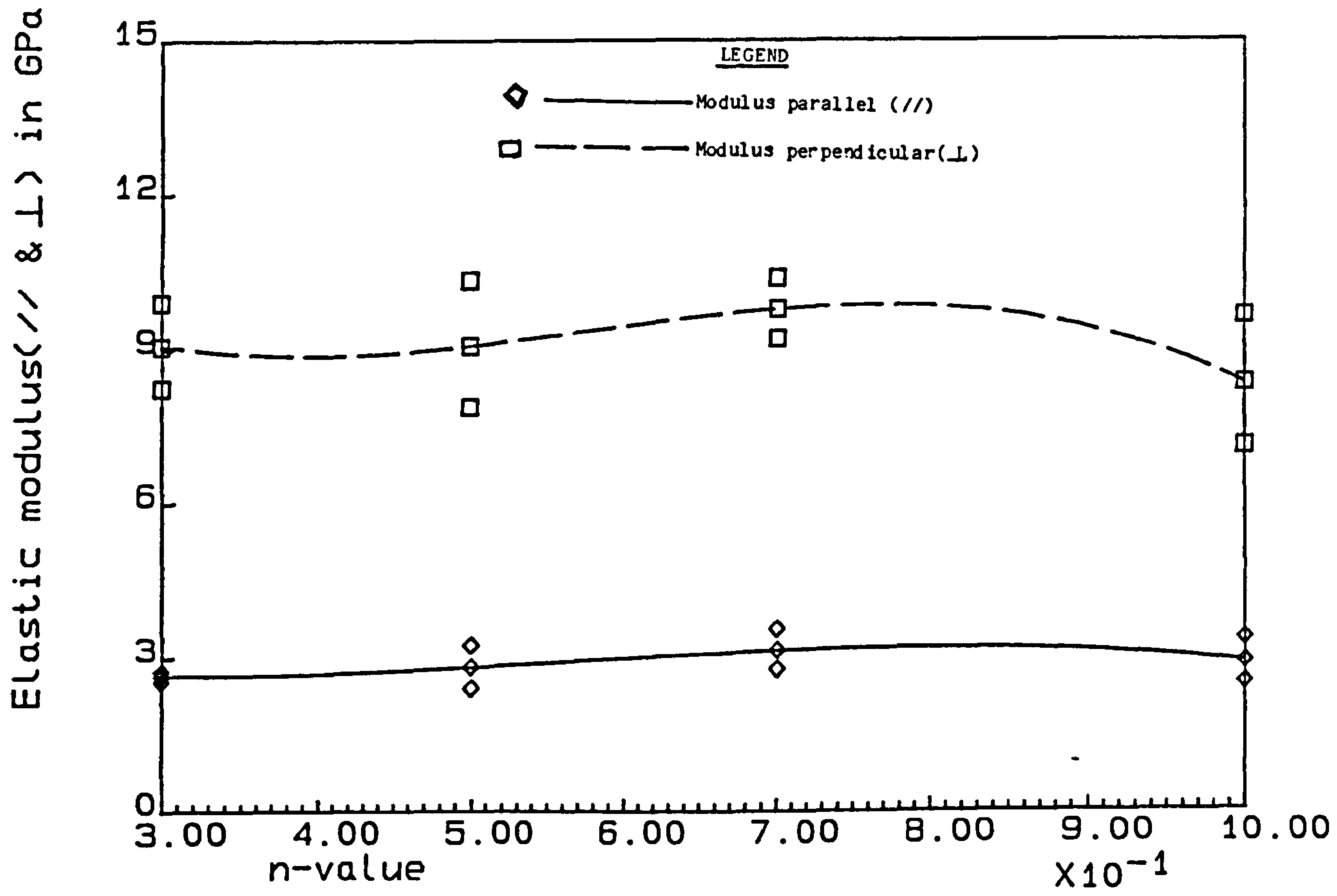

FIG. 5.5.5 ii : Elastic modulus V's
n-value (Comp. with 30% graphite A)

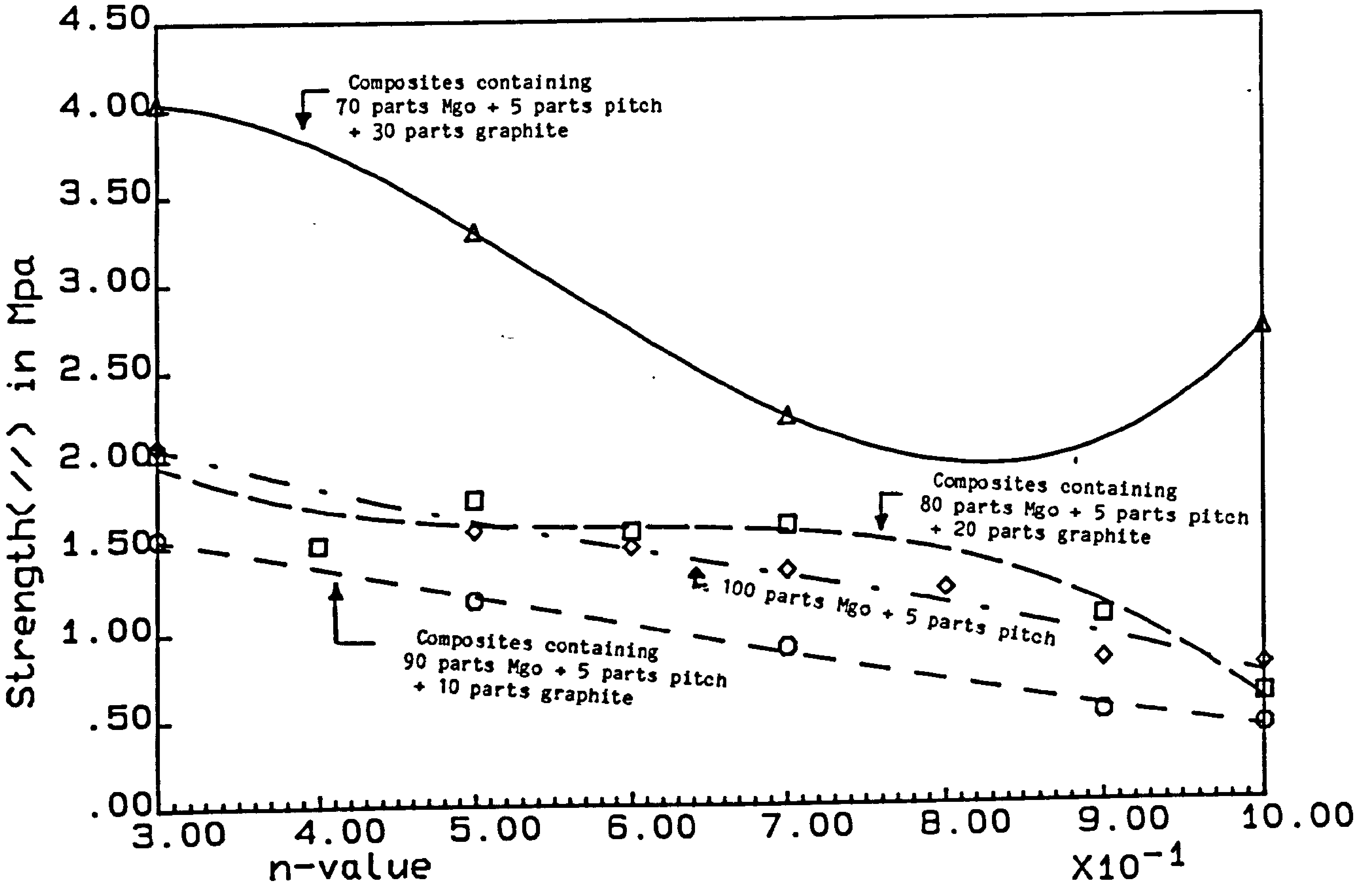

FIG. 5.5.6(i):Strength V's n-value comp. with varying graphite content

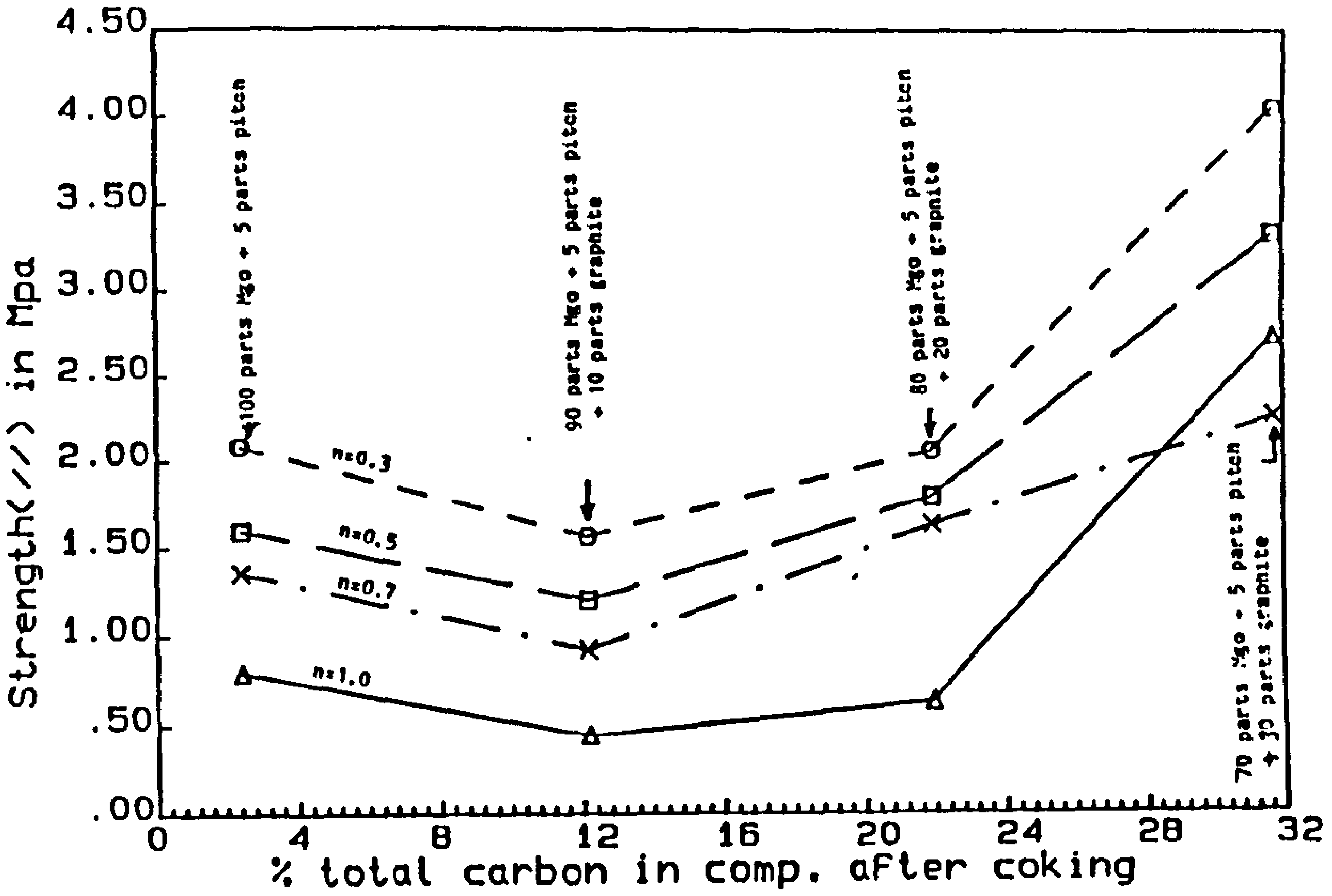

FIG. 5.5.6(ii):Strength V's % carbon content.
comp. of Y%Mgo+x% graphite A+5% pitch

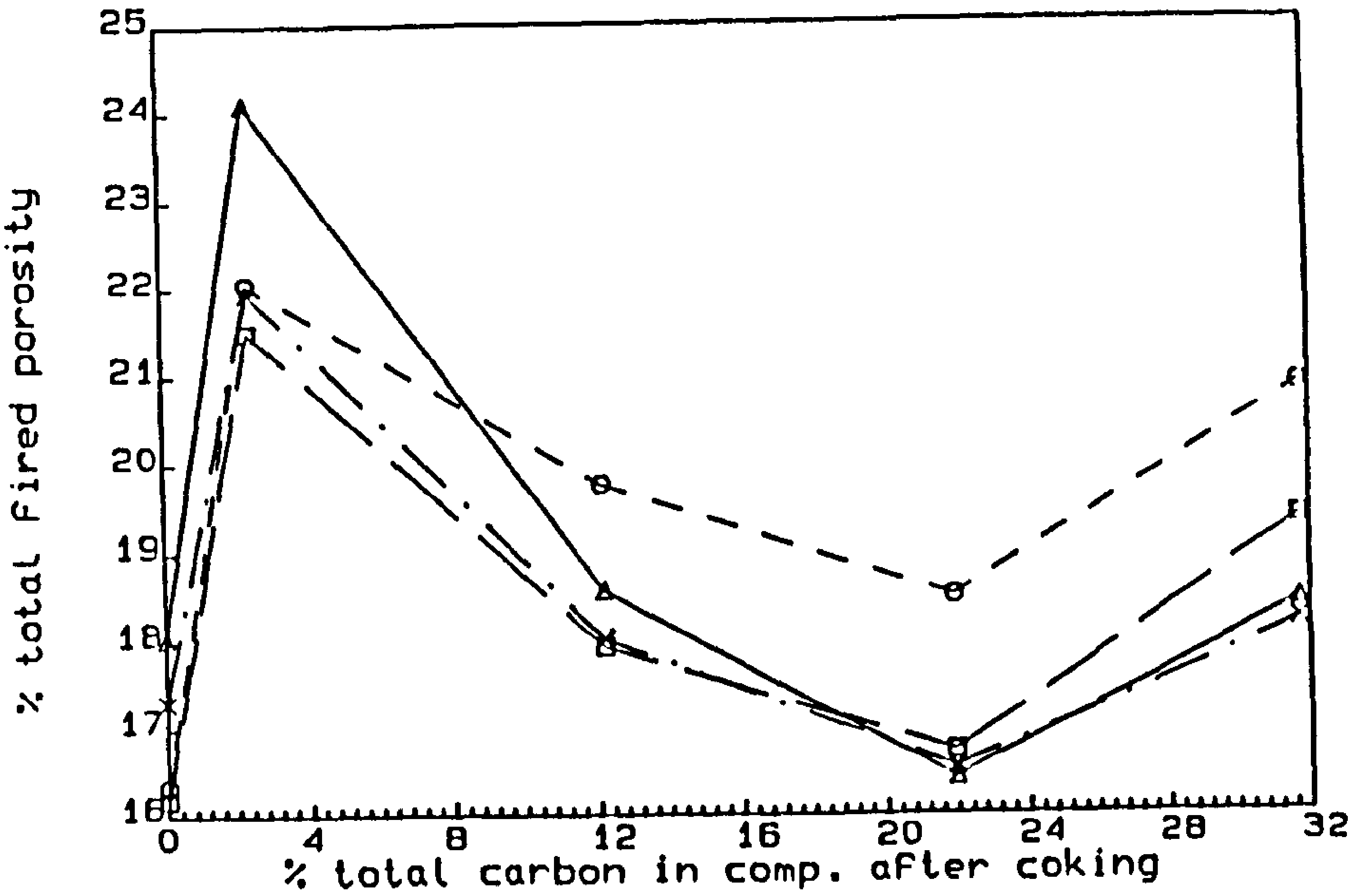

FIG. 5.5.6(iii):% porosity V's % carbon content
comp. of Y%Mgo+x% graphite A+5% pitch

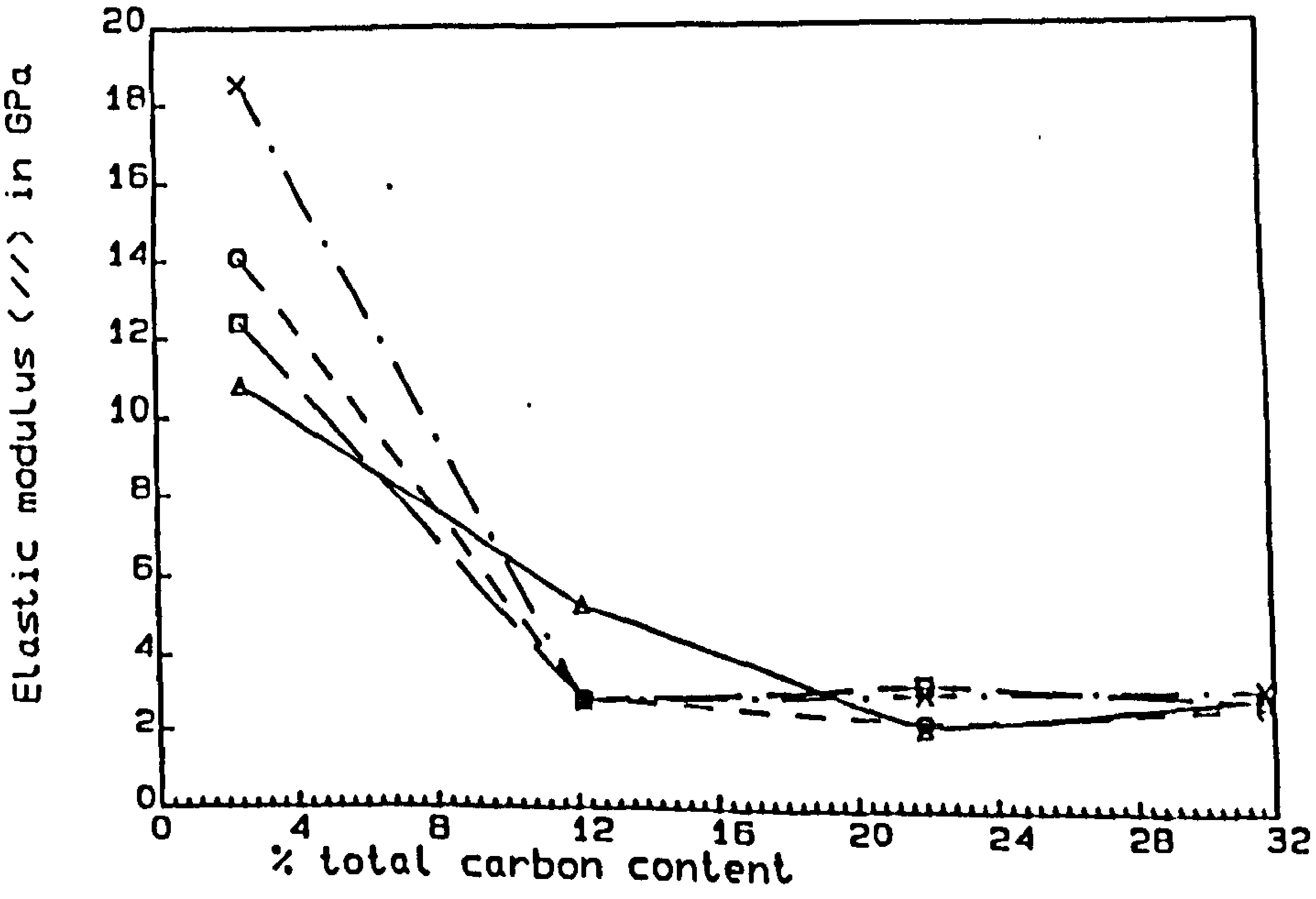

FIG.5.5.6 iv :Elastic modulus V's
% Total carbon content

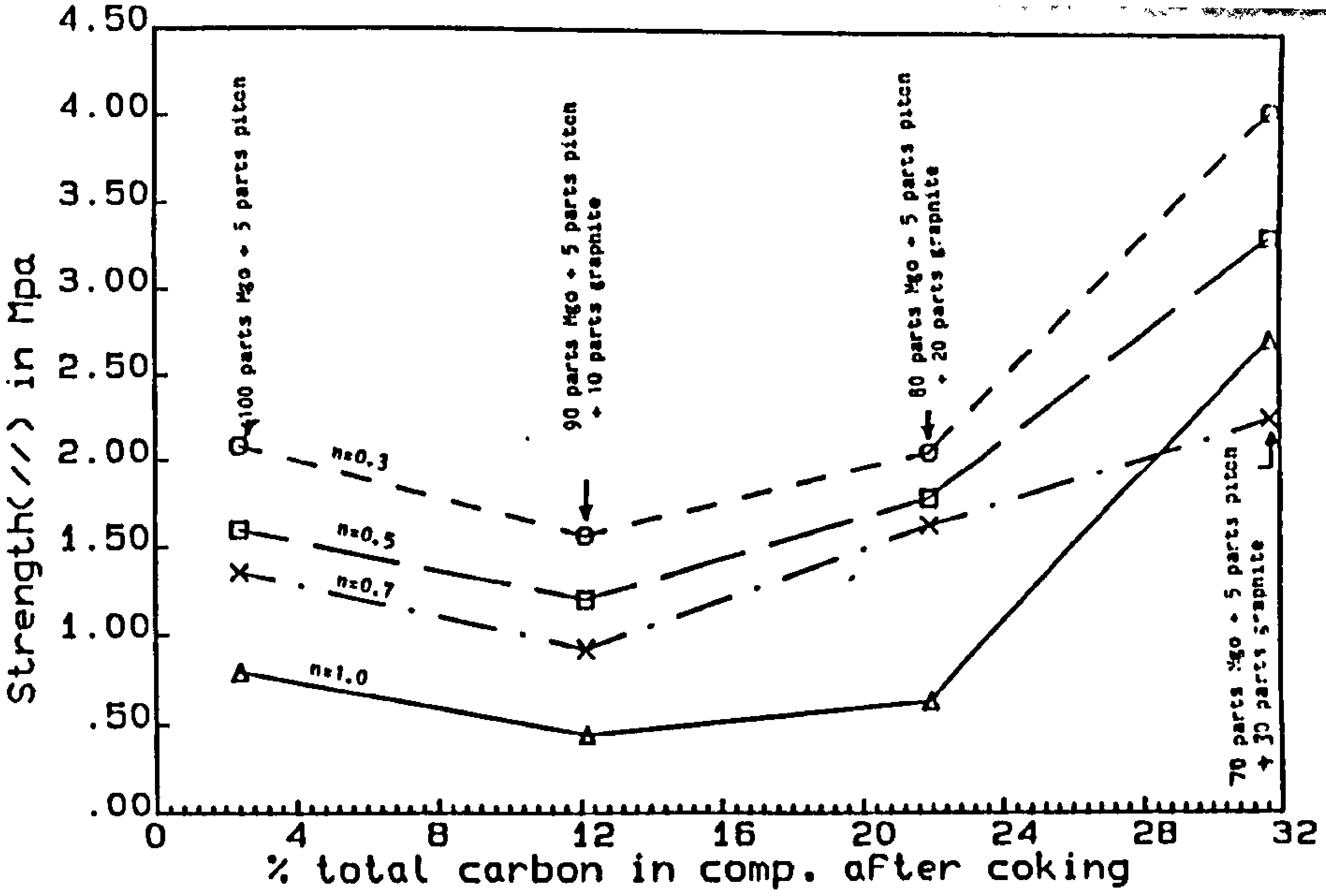

FIG. 5.5.6(ii):Strength V's % carbon content. comp. of Y%Mgo+x% graphite A+5% pitch

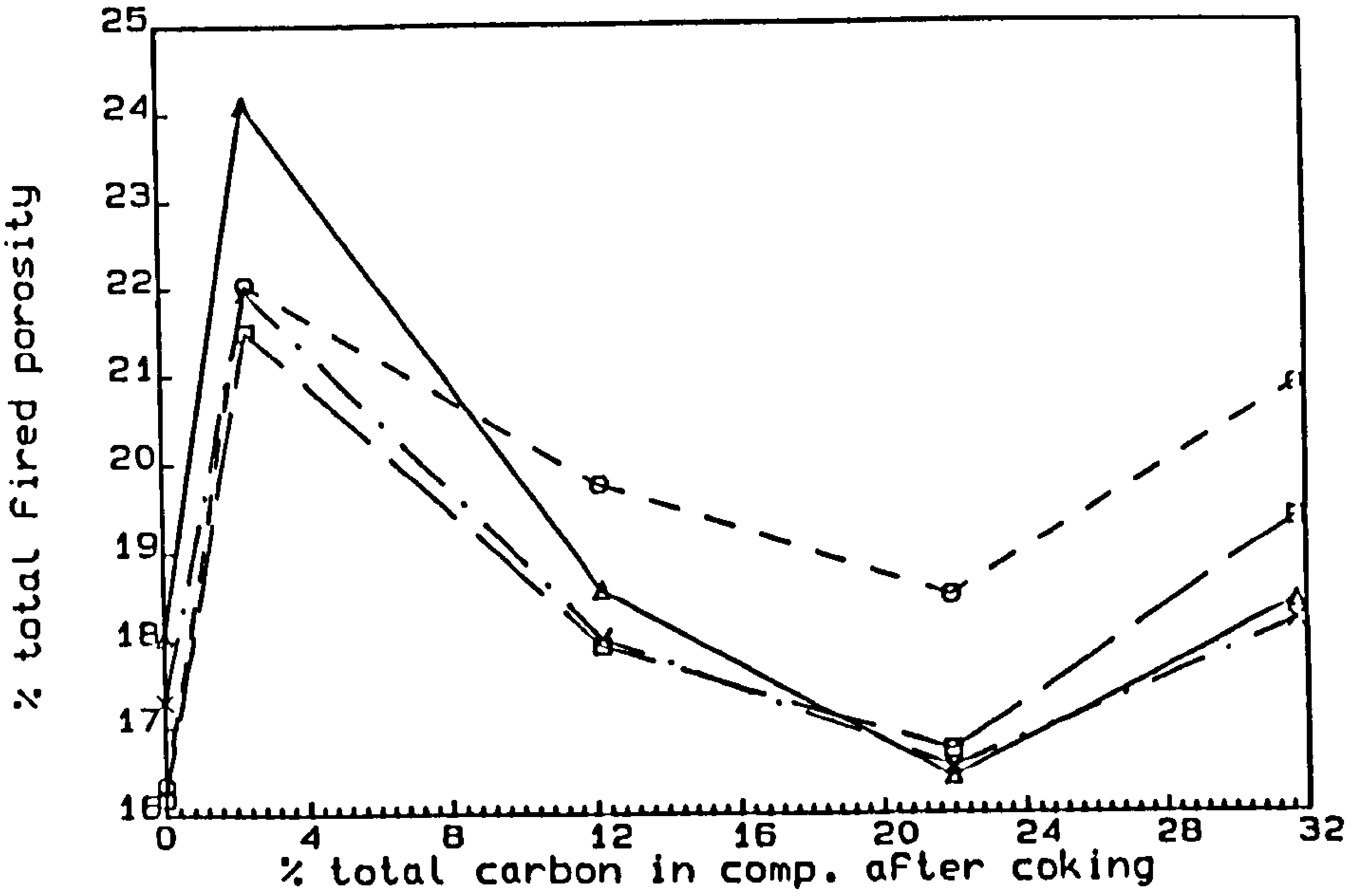

FIG. 5.5.6(iii):% porosity V's % carbon content comp. of Y%Mgo+x% graphite A+5% pitch

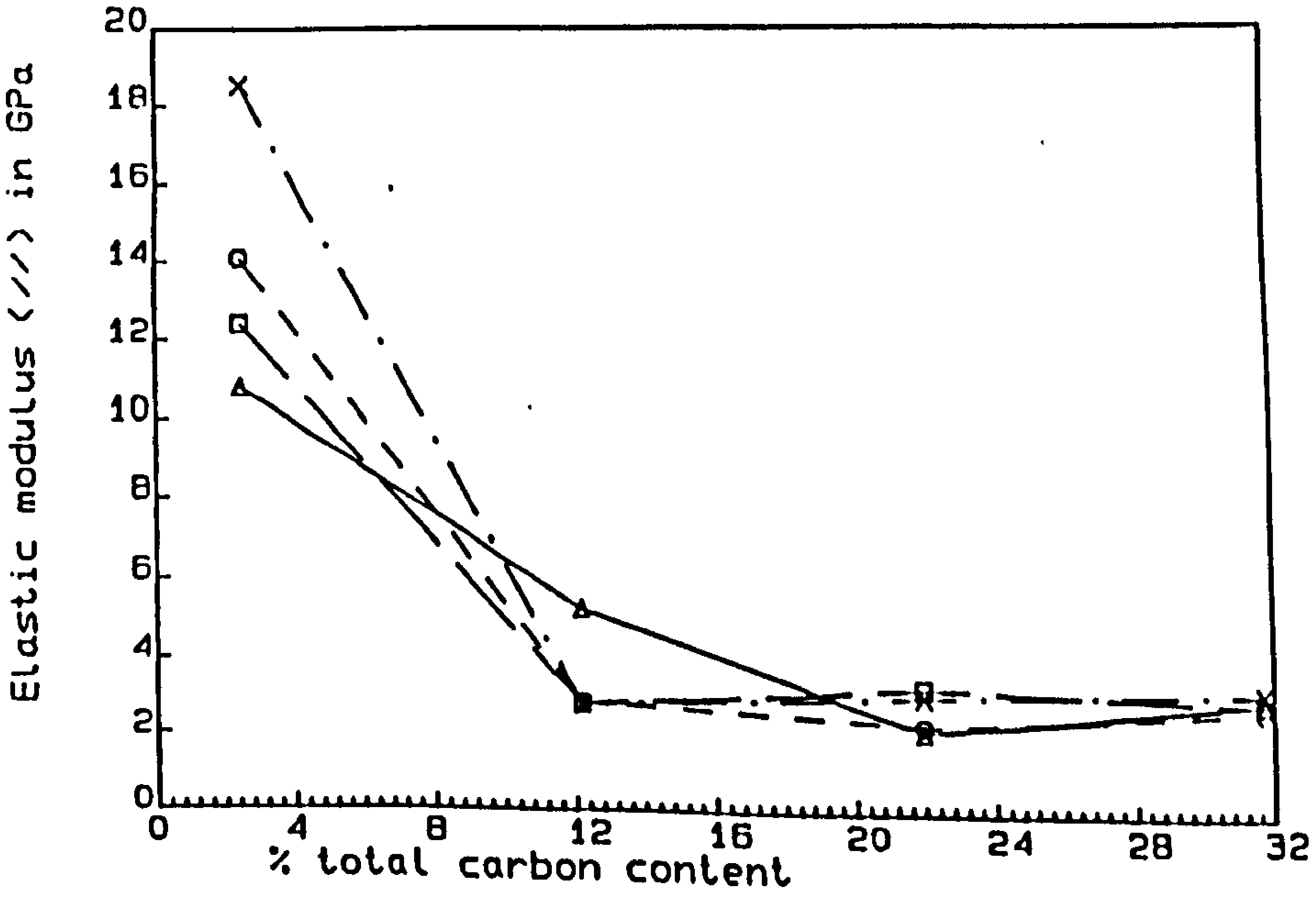

FIG.5.5.6 iv :Elastic modulus V's % Total carbon content

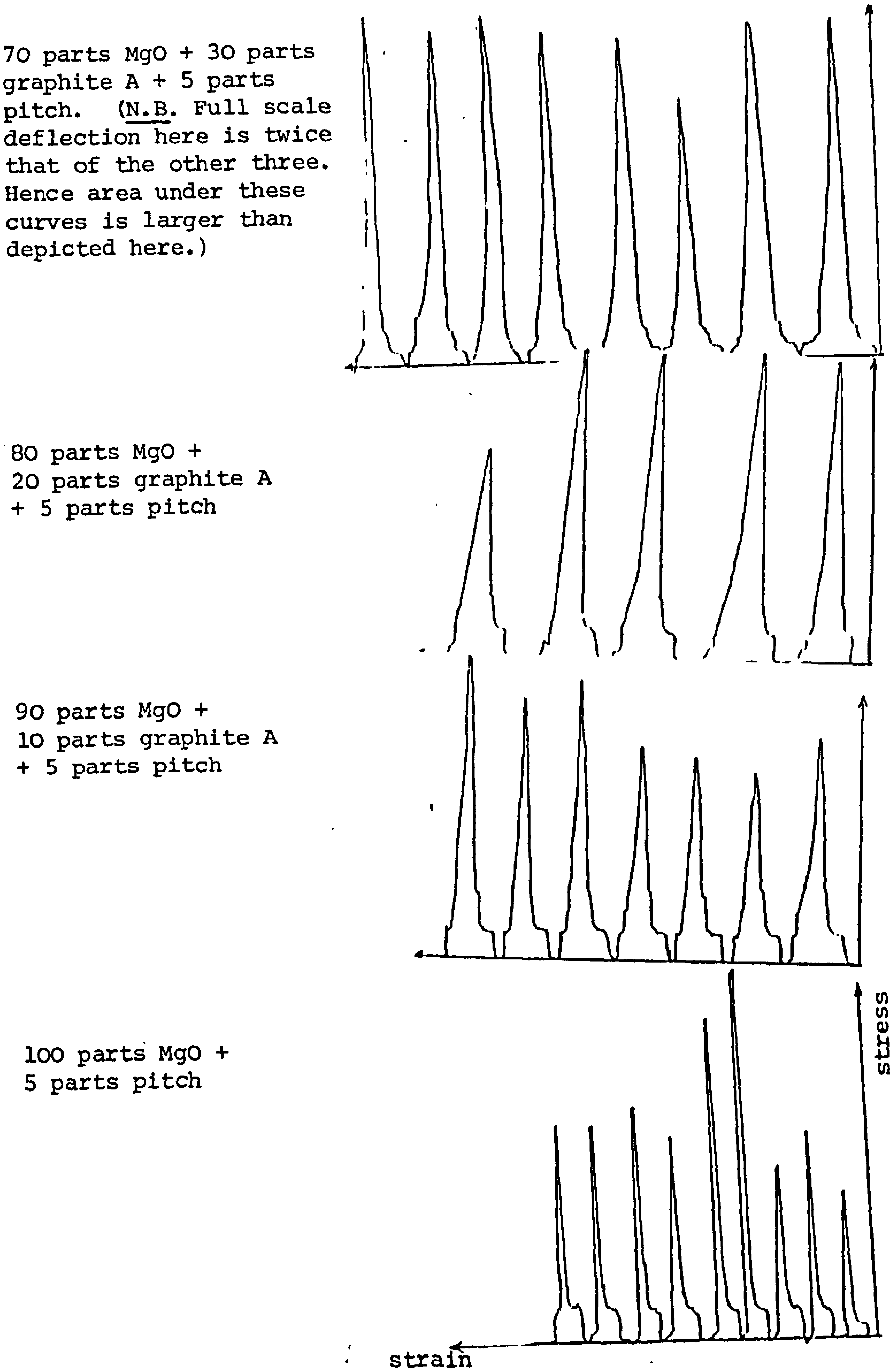

Figure 5.5.6(v)(a) Traces of stress-strain curves of test specimens obtained during testing. Composites containing varying amounts of graphite at a fixed n-value of 0.3 and pitch content (~ 5 $^{w}/_{o}$ pitch). n = 0.3.

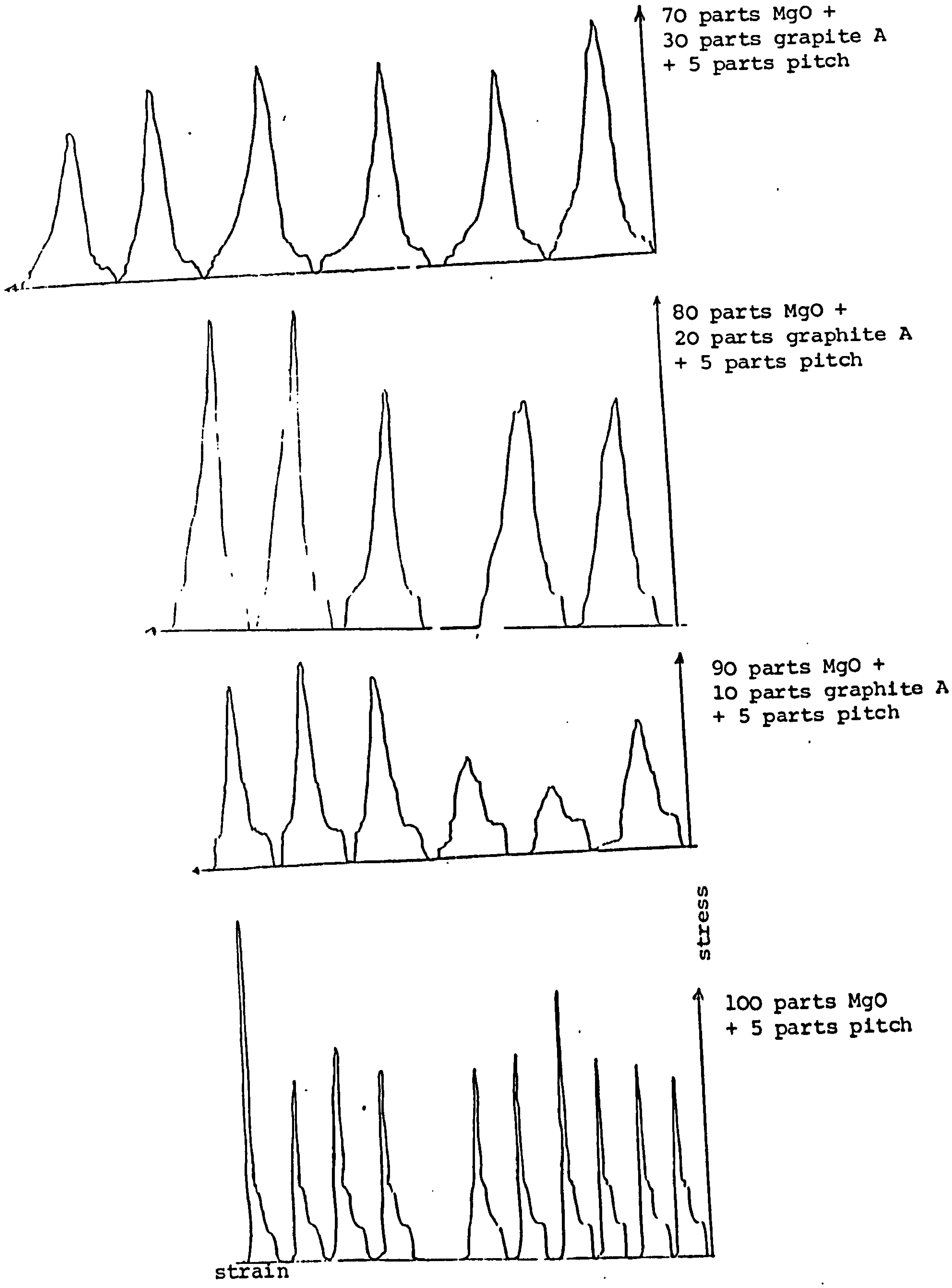

Figure 5.5.6(v)(b) Traces of stress-strain curves of test specimens obtained during testing. Composites containing varying amounts of graphite at a fixed n-value of 0.7 and pitch (~ 5 $^{w}/_{o}$ pitch). The full scale deflection is the same for the bottom three (10 kg) and the topmost is 20 kg (not shown here). n = 0.7.

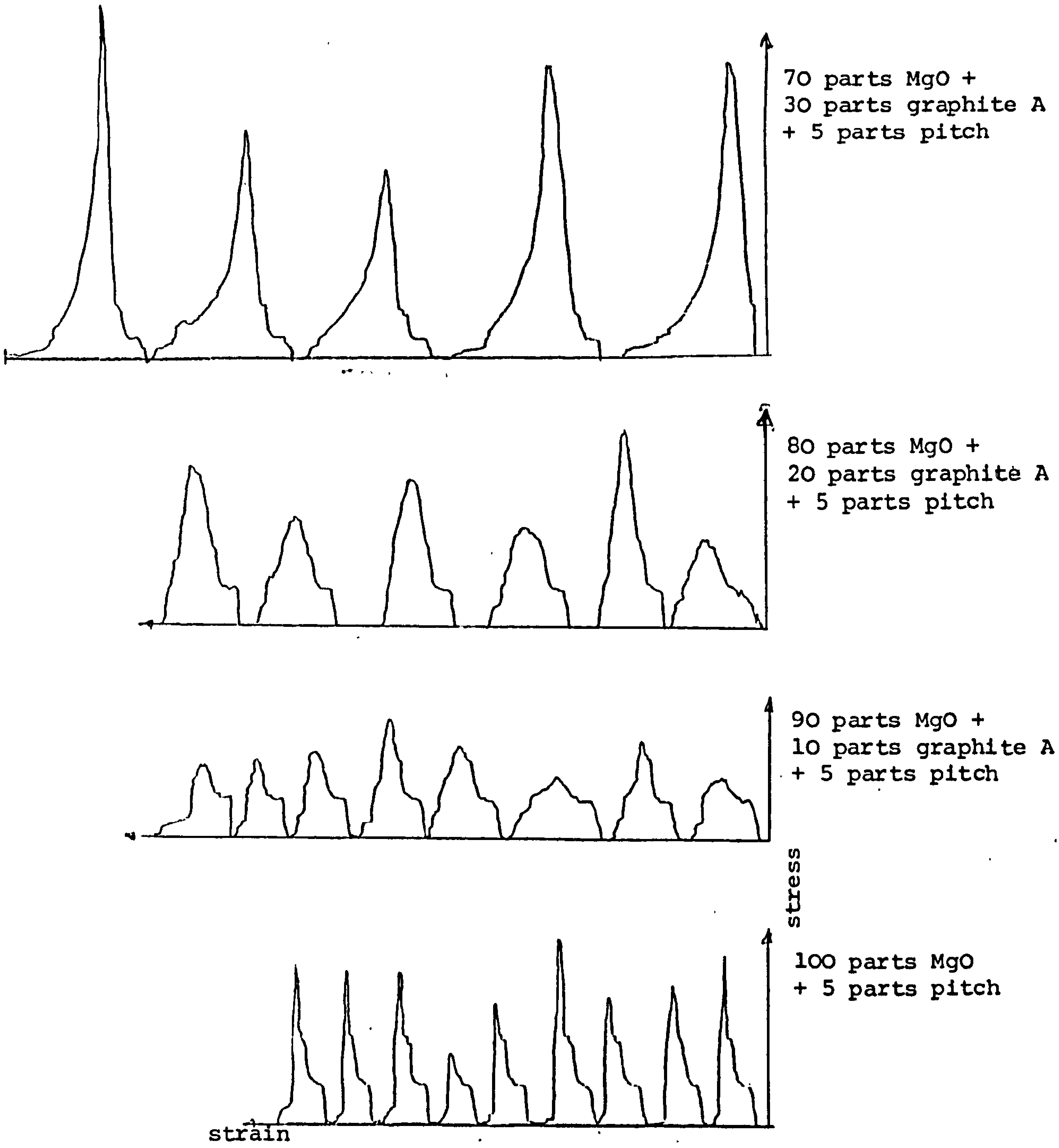

Figure 5.5.6(v)(c) Traces of stress-strain curves of test specimens obtained during testing. Composites containing varying amounts of graphite at a fixed n-value of 1.0 and pitch ~ 5 ^{w}/o. The full scale deflection is the same for the bottom three, 10 kg, and the topmost is 20 kg. Hence the area under the curves of composites containing ~ 30 ^{w}/o graphite is much larger than is depicted in the traces. $n = 1.0$.

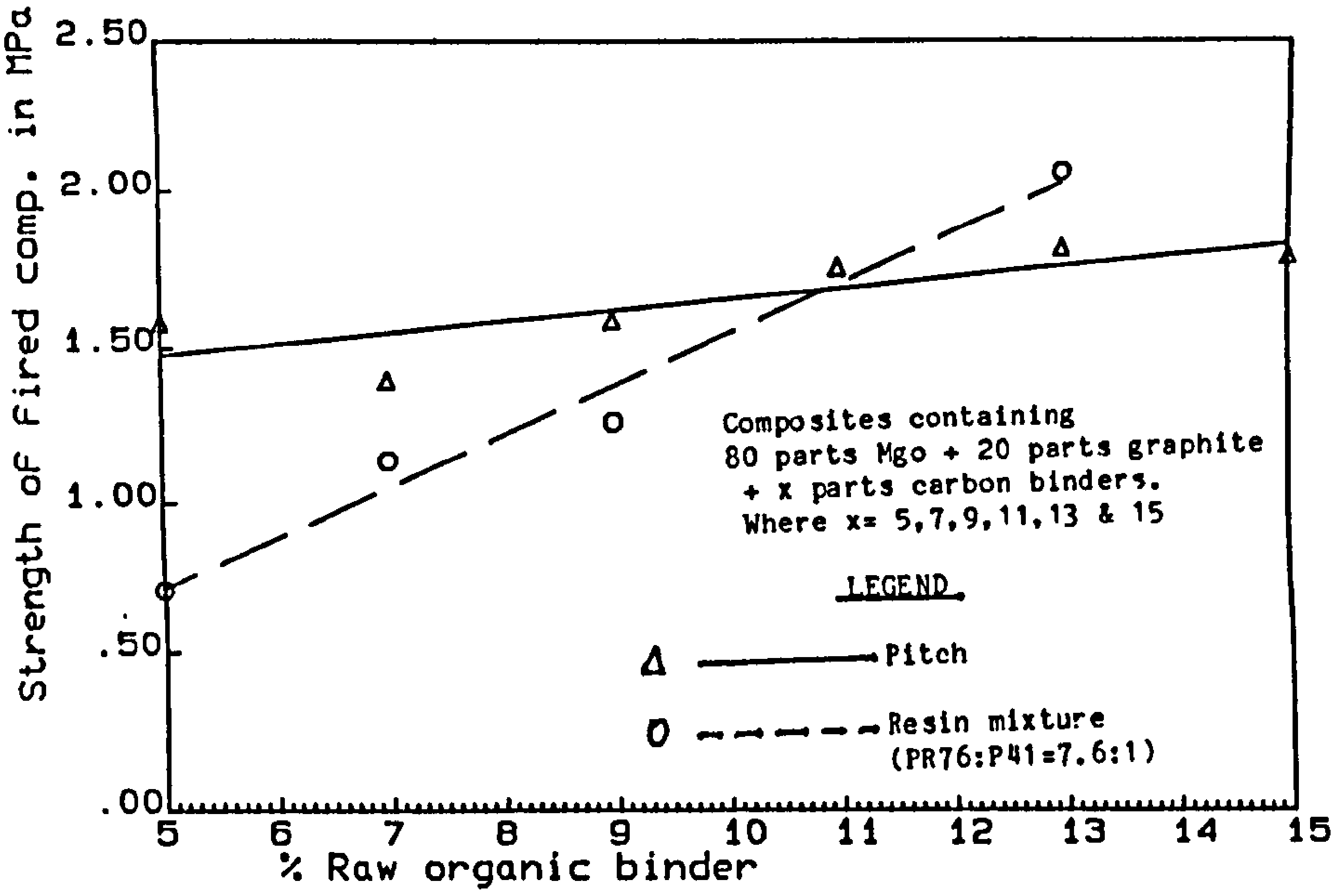

FIG. 5.5.7 i(a):Strength of comp. V's Raw pitch & Resin(Comp. 80%Mgo+20% A)

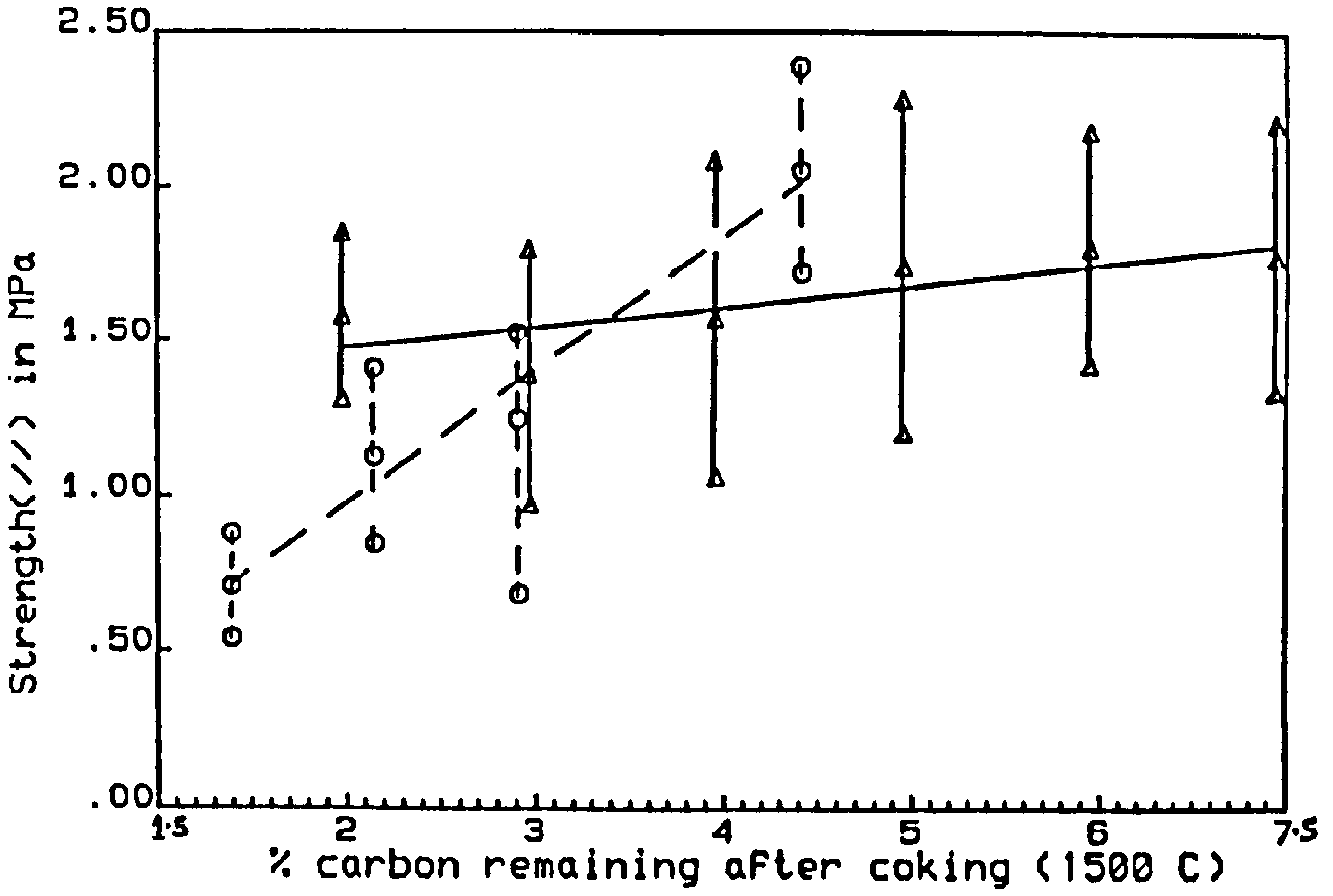

FIG. 5.5.7 i(b):Strength V's % residual carbon from pitch& resin after coking

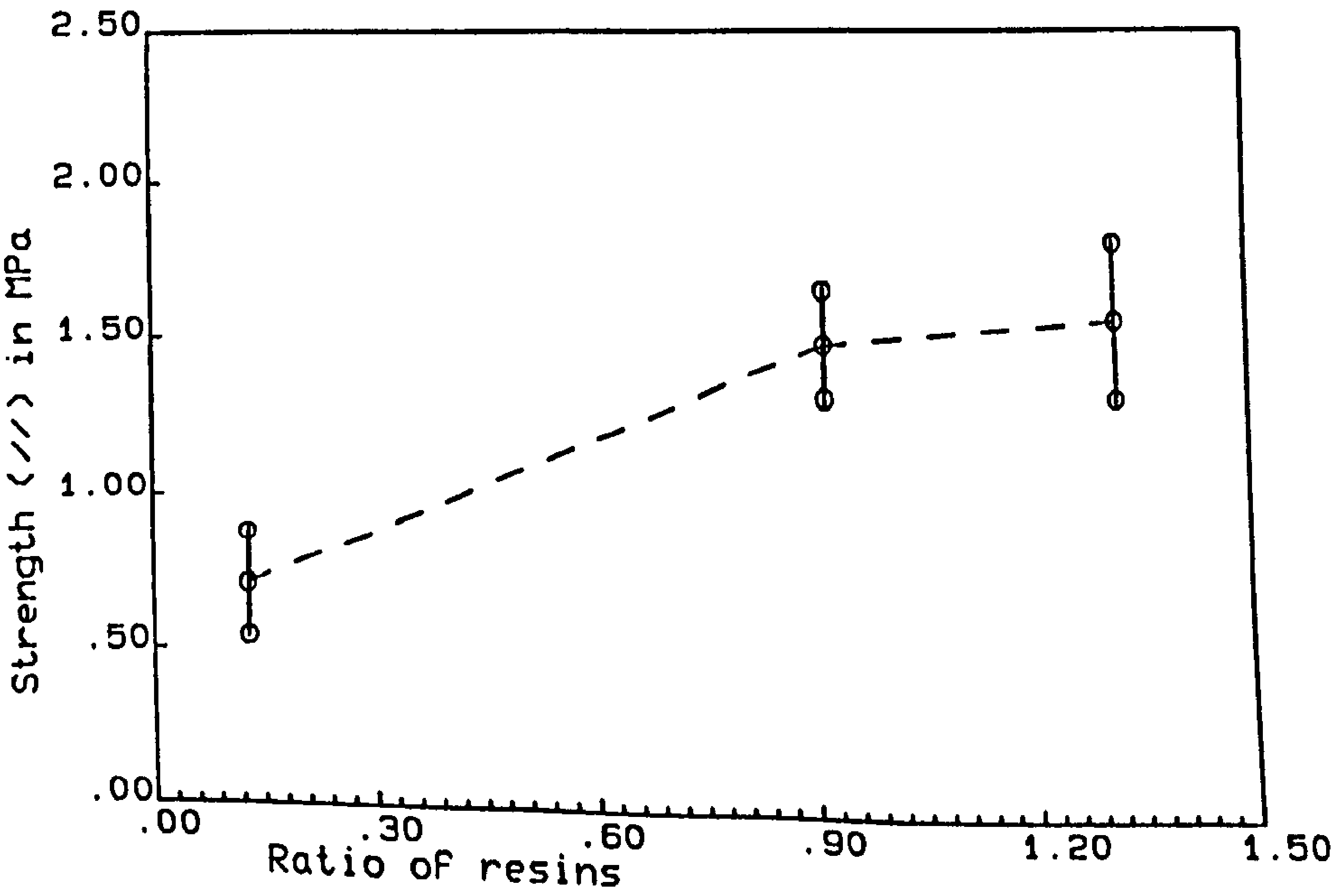

FIG. 5.5.7 i(c): Strength V's ratio of resin mixtures(P41/PR67)

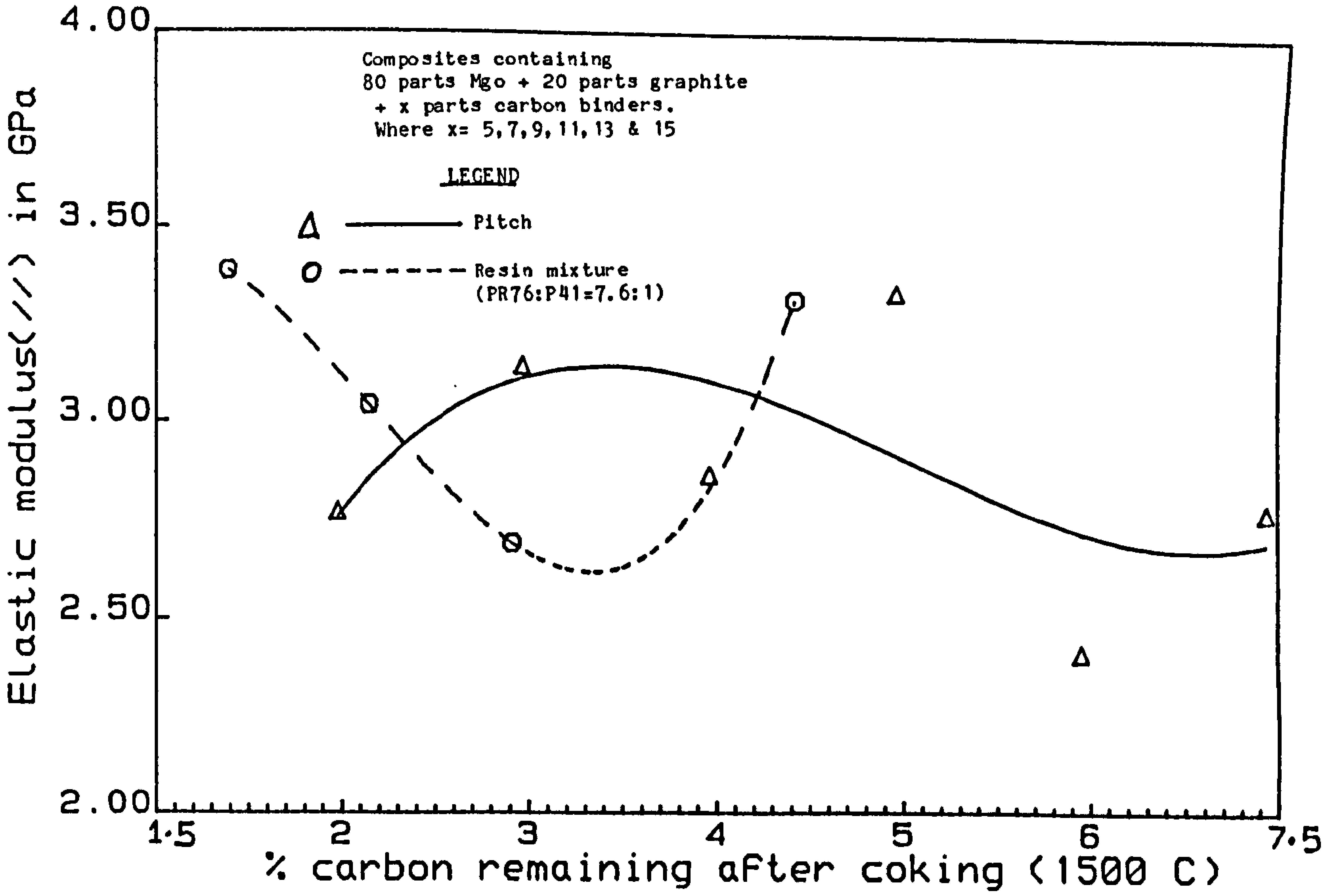

FIG. 5.5.7 i(d):Elastic V's % carbon
from pitch & resin after coking

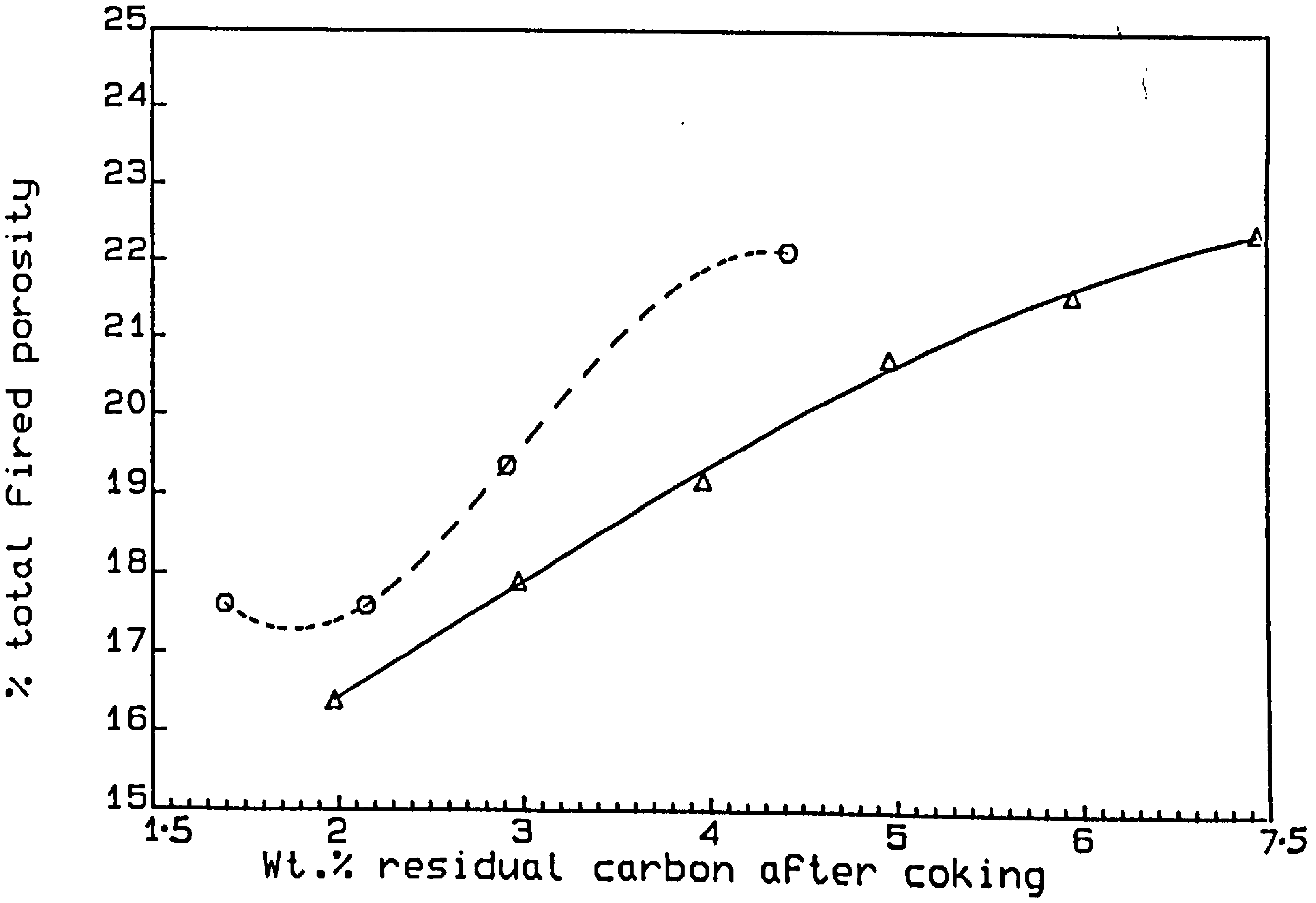

FIG. 5.5.7 ii : % total fired porosity V's
Wt.% residual carbon from binders

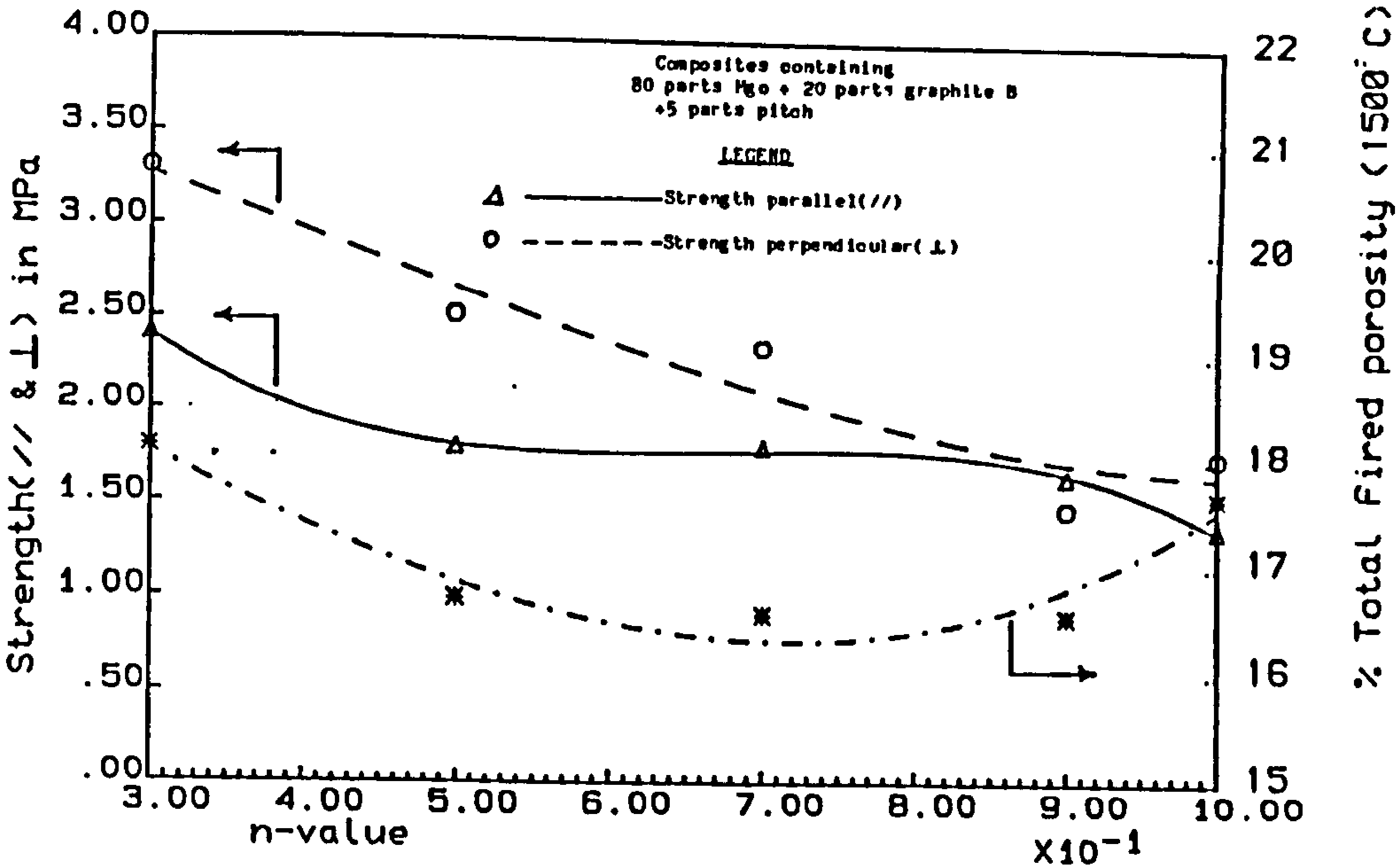

FIG. 5.5.8 i(a):Strength & porosity V's n-value (Comp. with 20% graphite B)

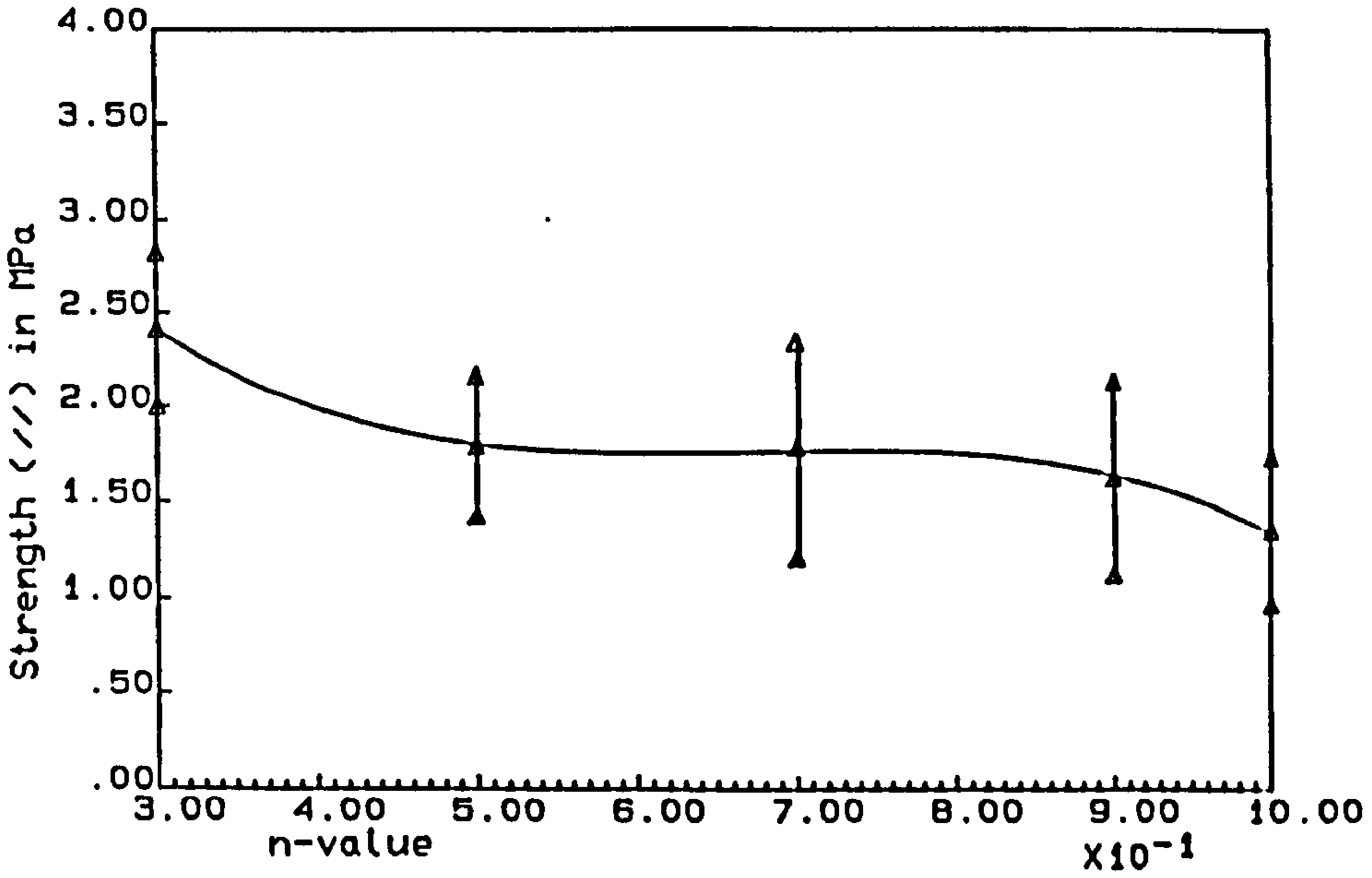

FIG. 5.5.8 i(b):Strength V's n-value (Comp. with 20% graphite B)

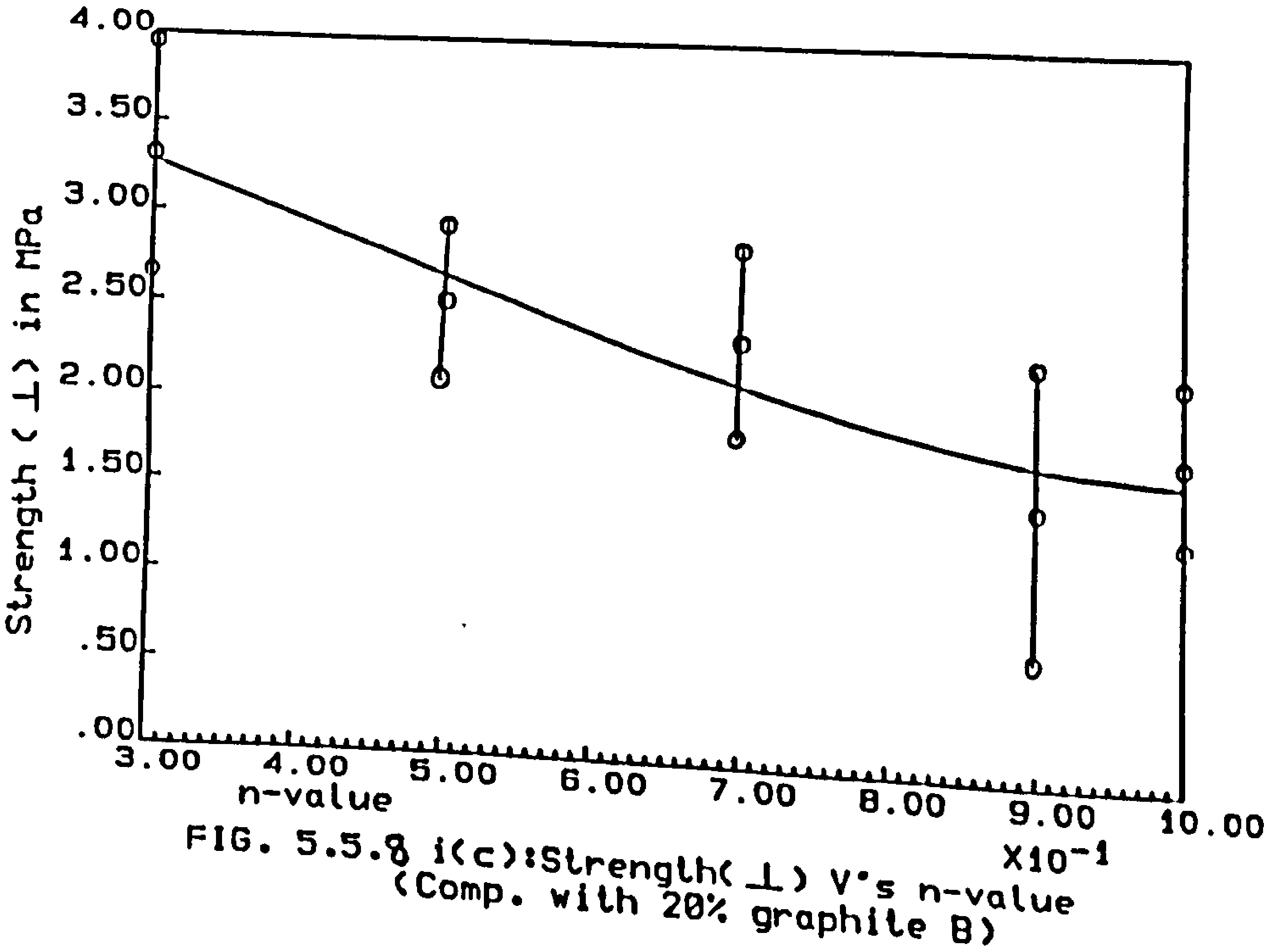

FIG. 5.5.8 i(c):Strength(⊥) V's n-value (Comp. with 20% graphite B)

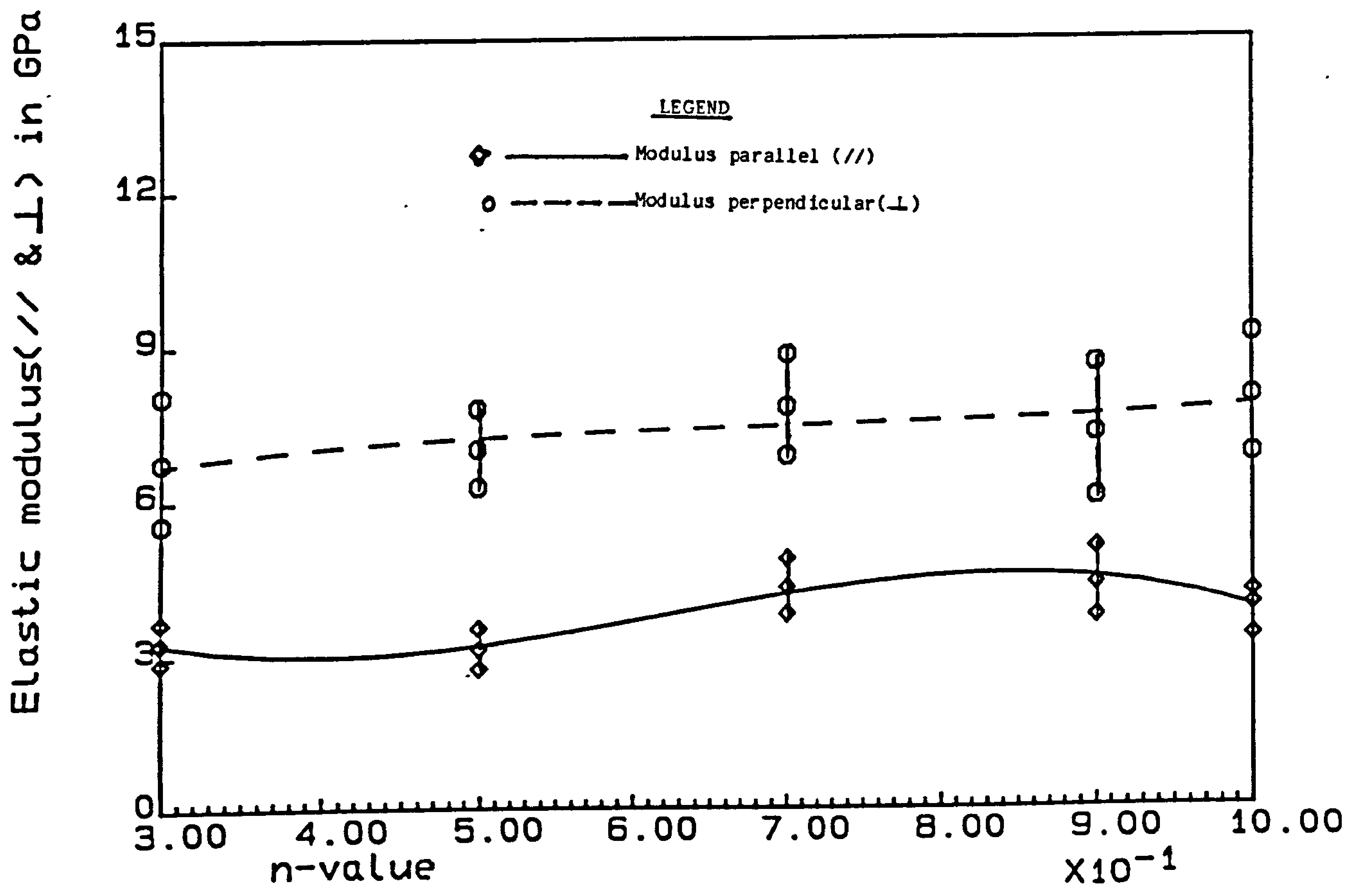

FIG. 5.5.8 i(d):Elastic modulus V's n-value (Comp. with 20% graphite B)

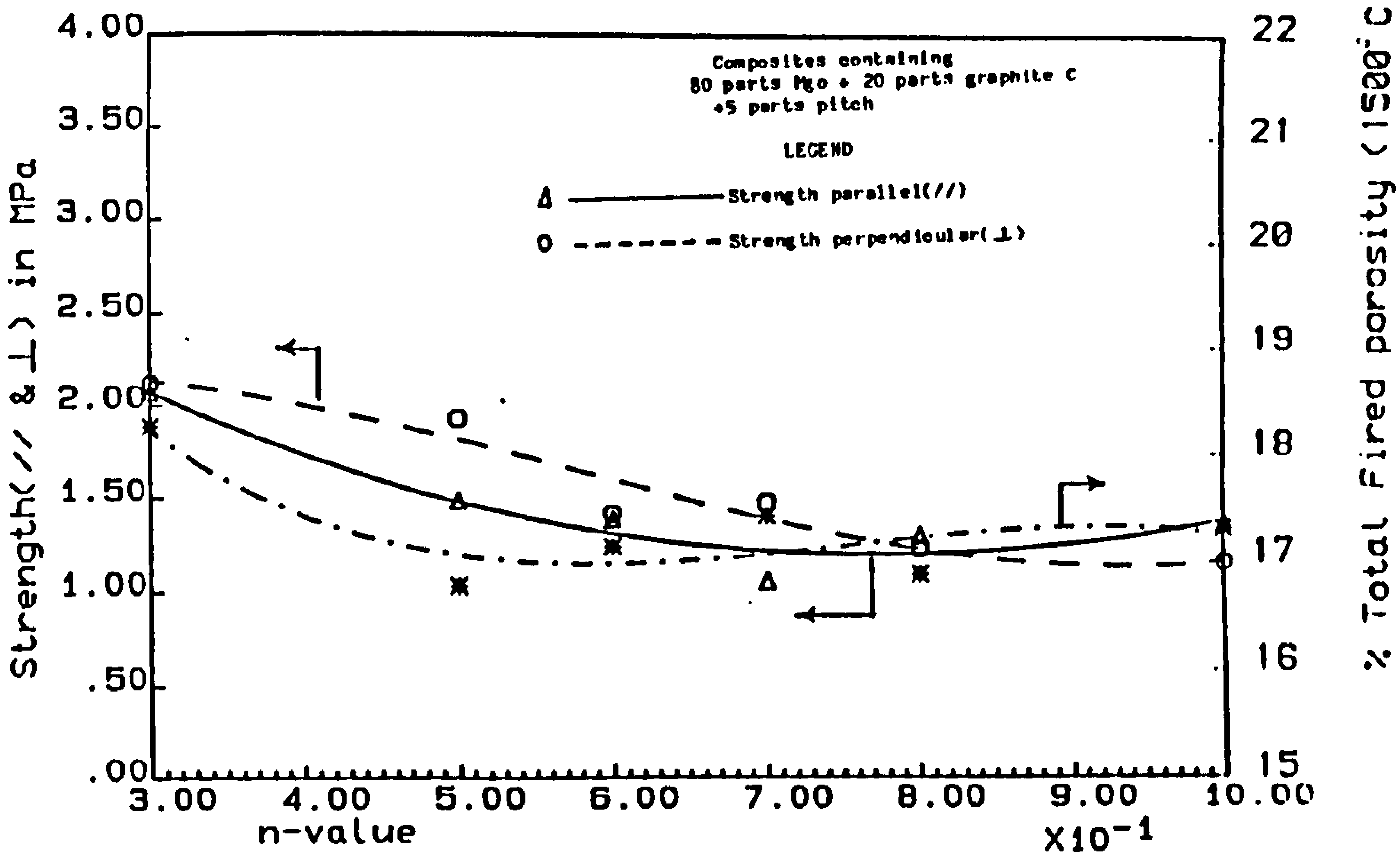

FIG. 5.5.8 ii(a):Strength V's n-value (Comp. with 20% graphite C)

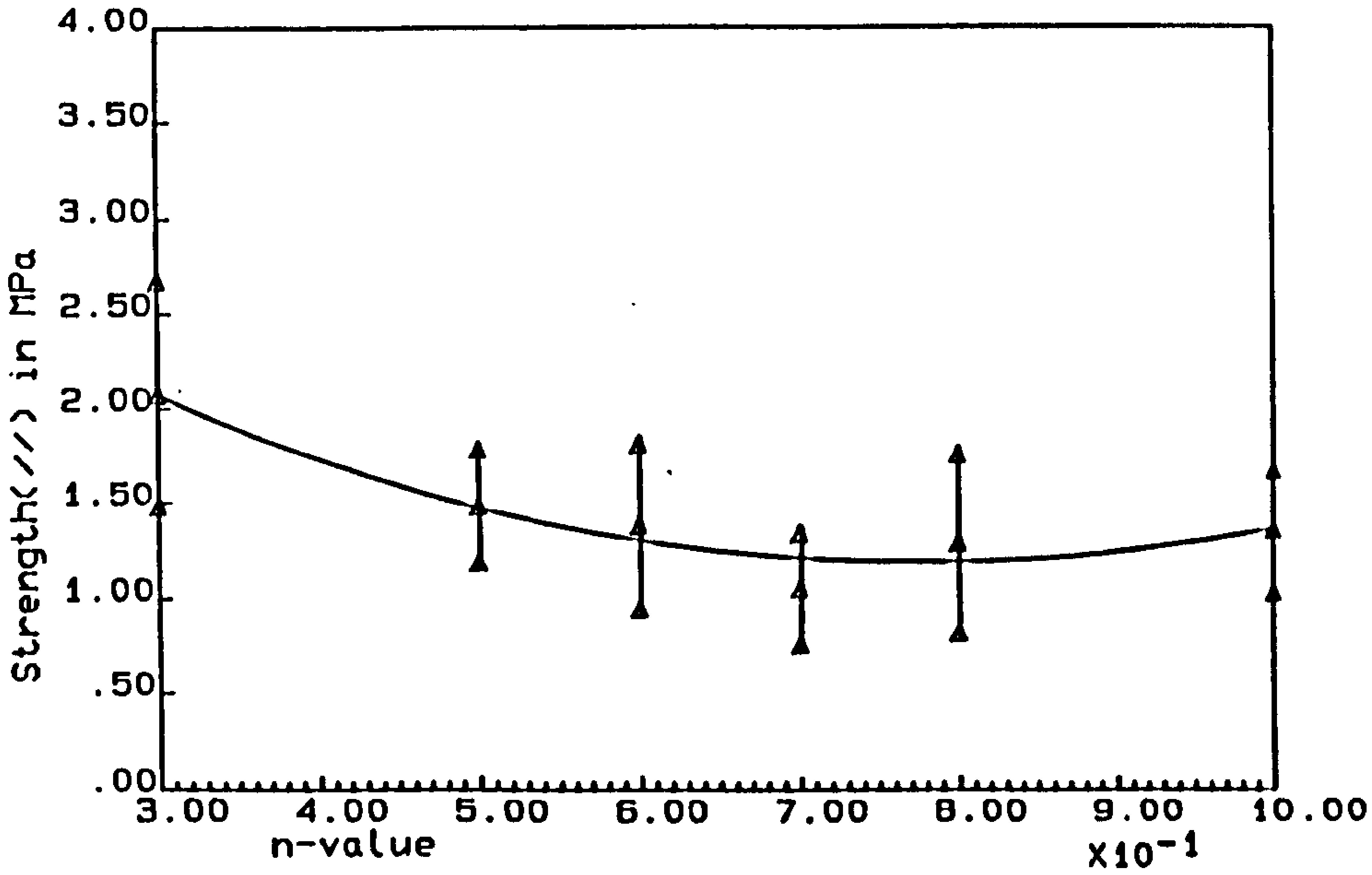

FIG. 5.5.8 ii(b):Strength(//) V's n-value (Comp. with 20% graphite C)

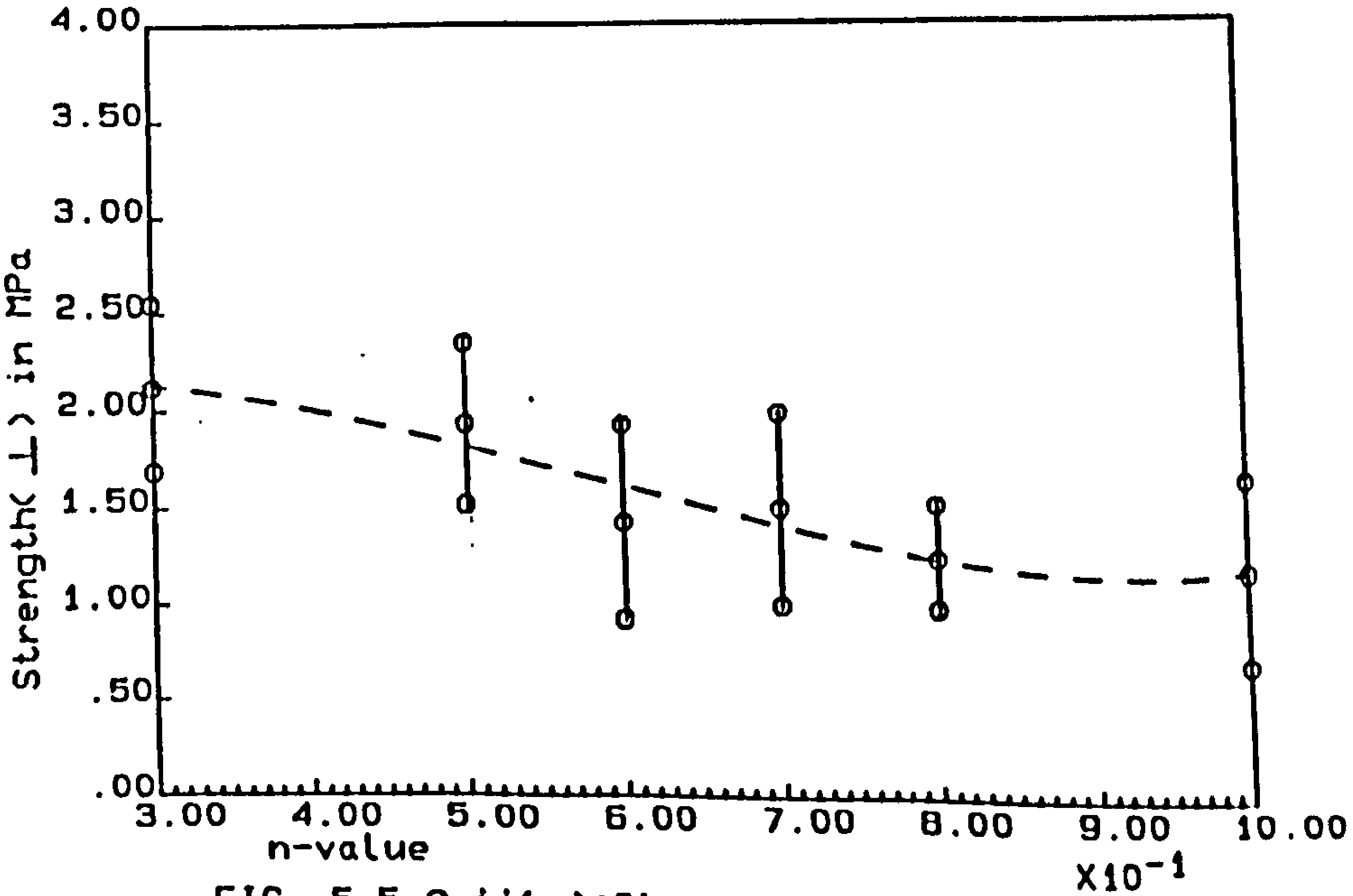

FIG. 5.5.8 ii(c):Strength(⊥) V's n-value (Comp. with 20% graphite C)

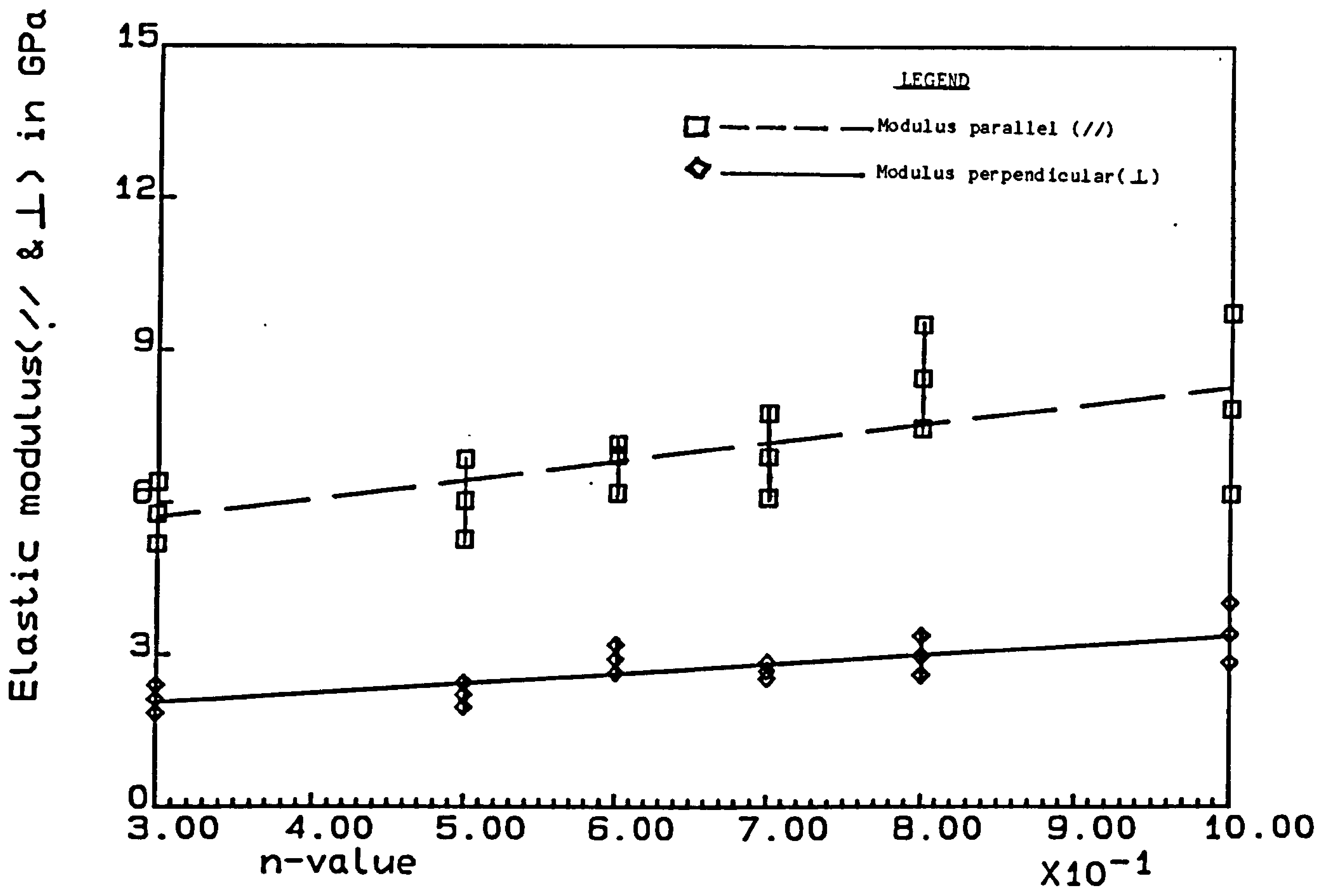

FIG. 5.5.8 ii(d):Elastic modulus V's n-value (Comp. with 20% graphite C)

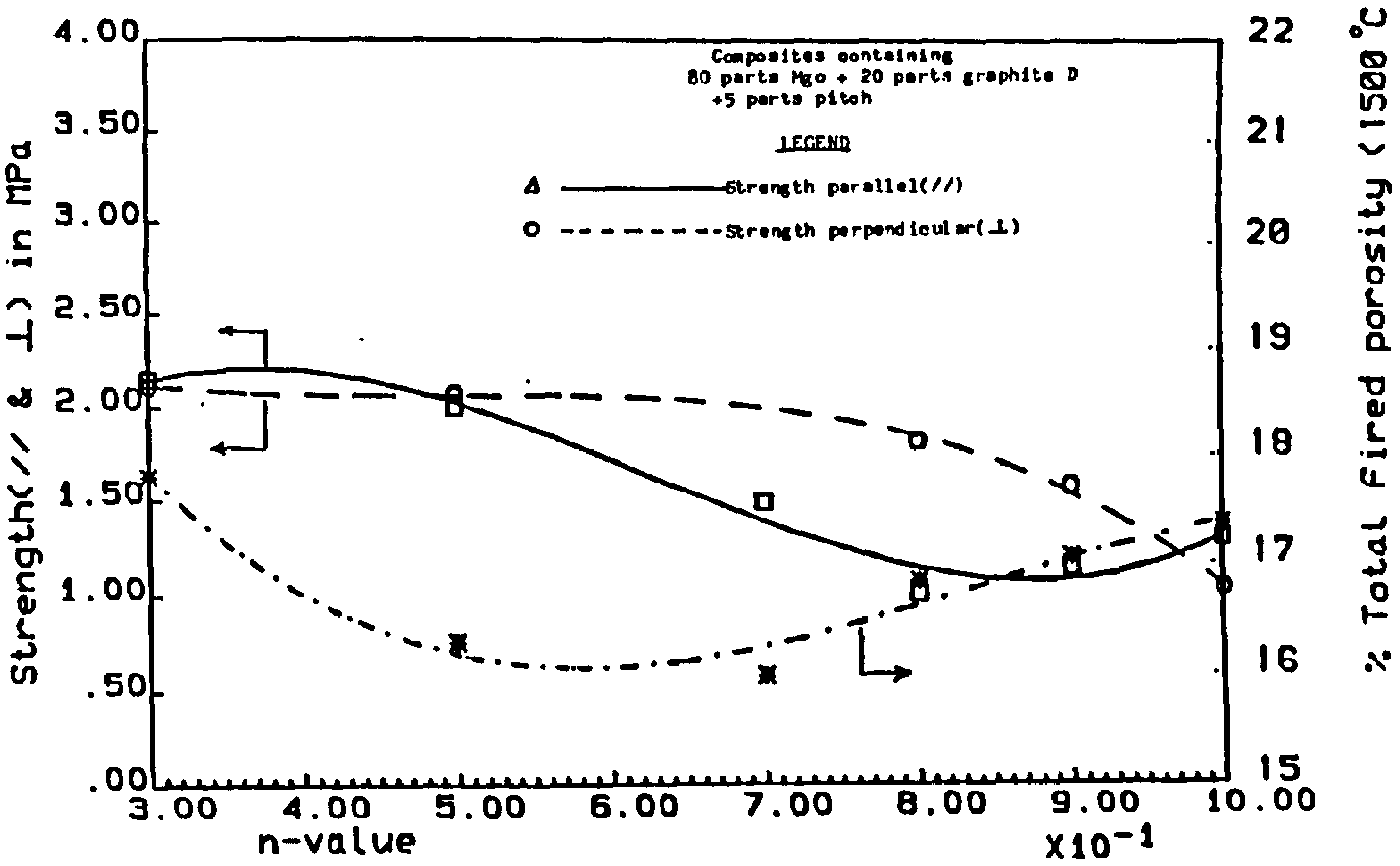

FIG. 5.5.8 iii(a):Strength & porosity V's n-value (Comp. with 20% graphite D)

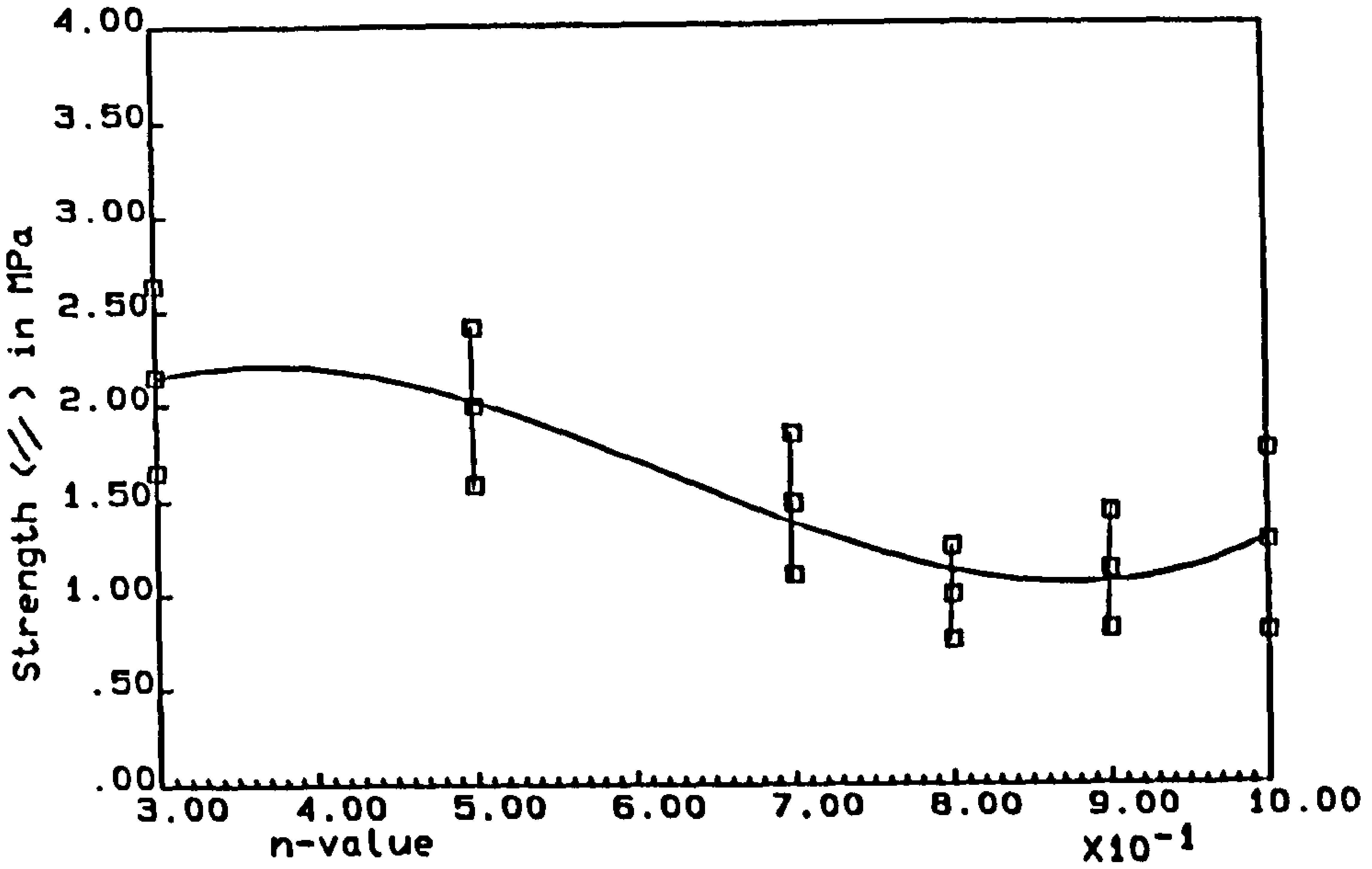

FIG. 5.5.8 iii(b):Strength(//) V's n-value (Comp. with 20% graphite D)

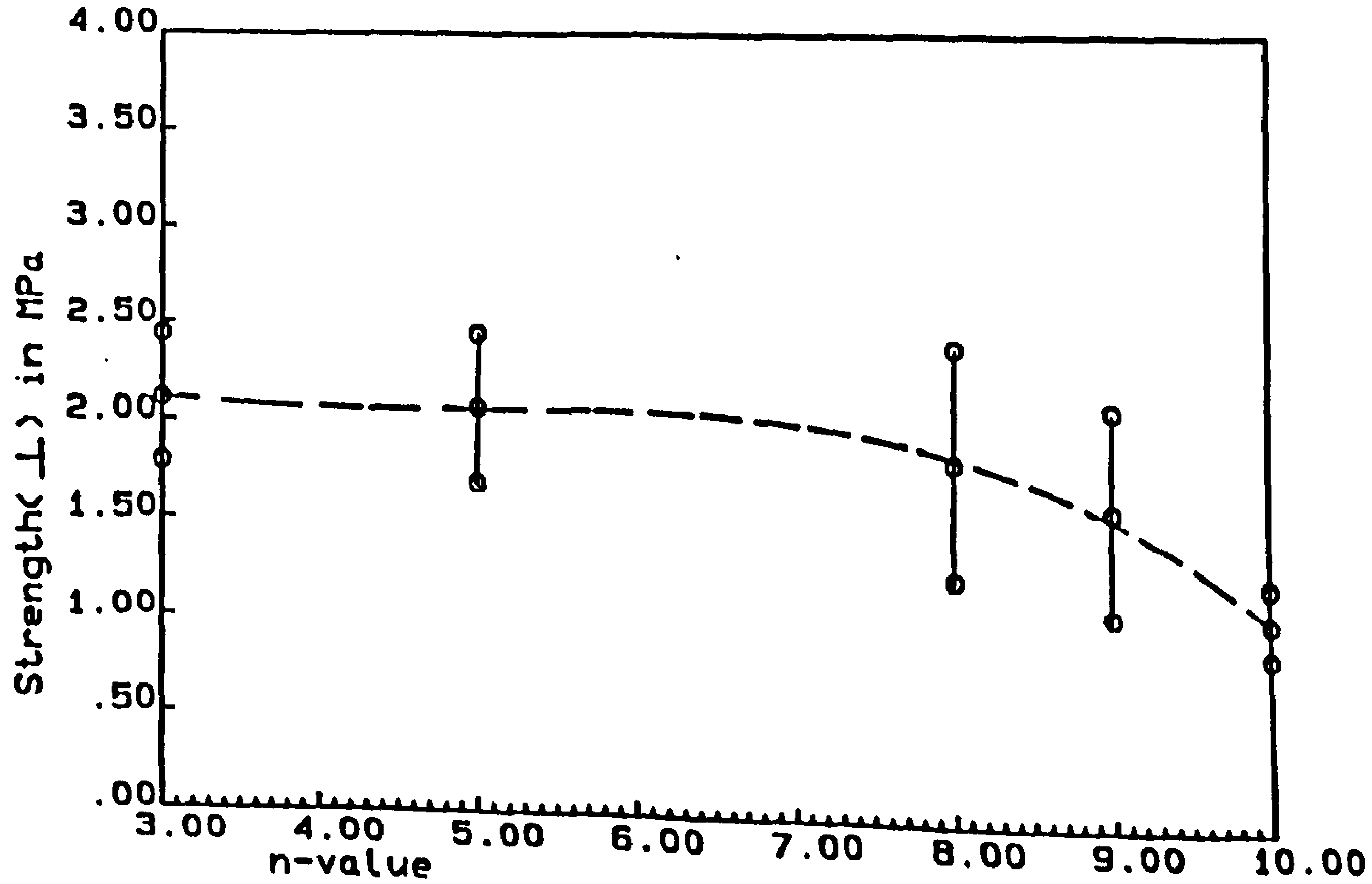

FIG. 5.5.8 iii(c):Strength(⊥) V's n-value (Comp. with 20% graphite D)

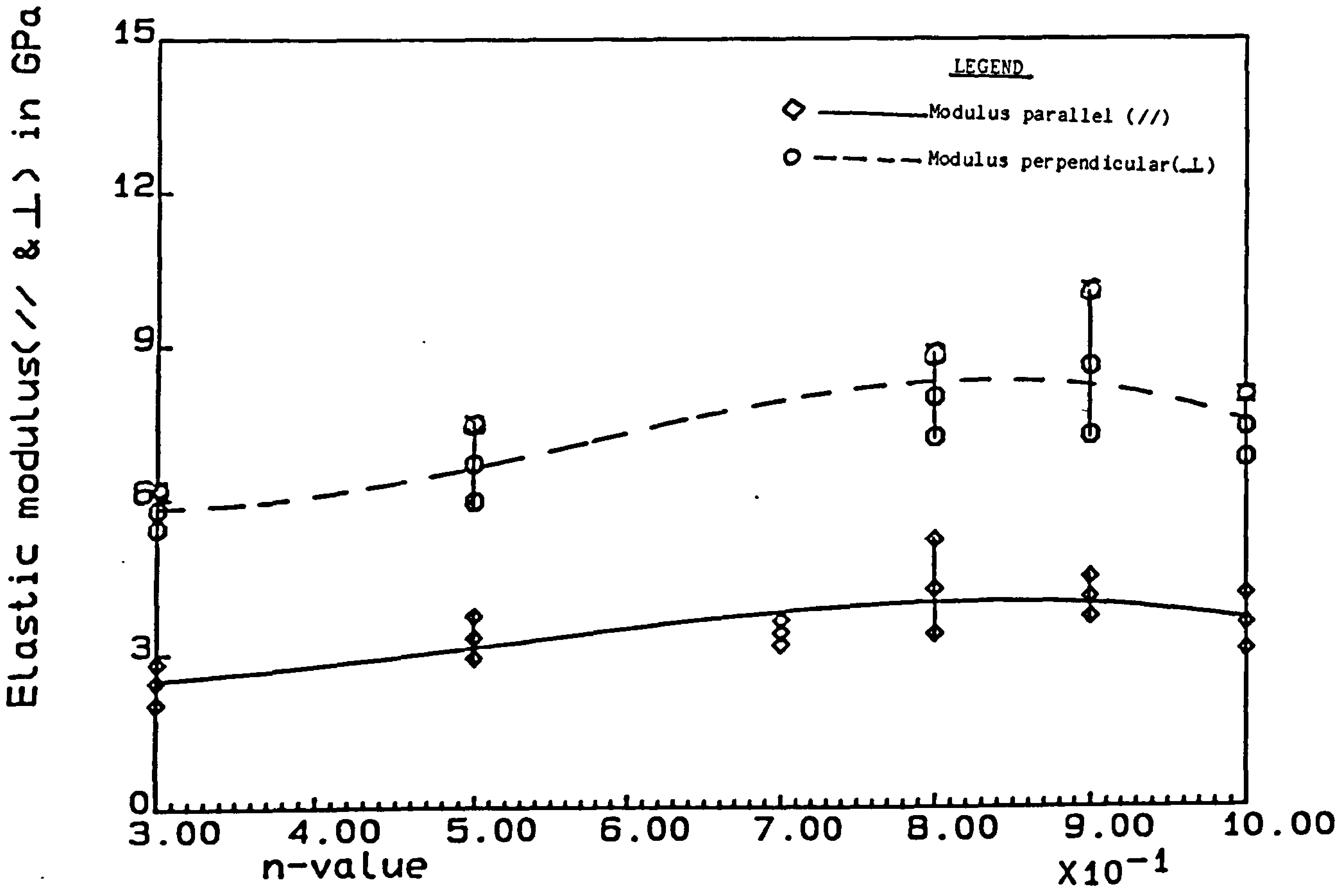

FIG. 5.5.8 iii(d):Elastic modulus V's n-value (Comp. with 20% graphite D)

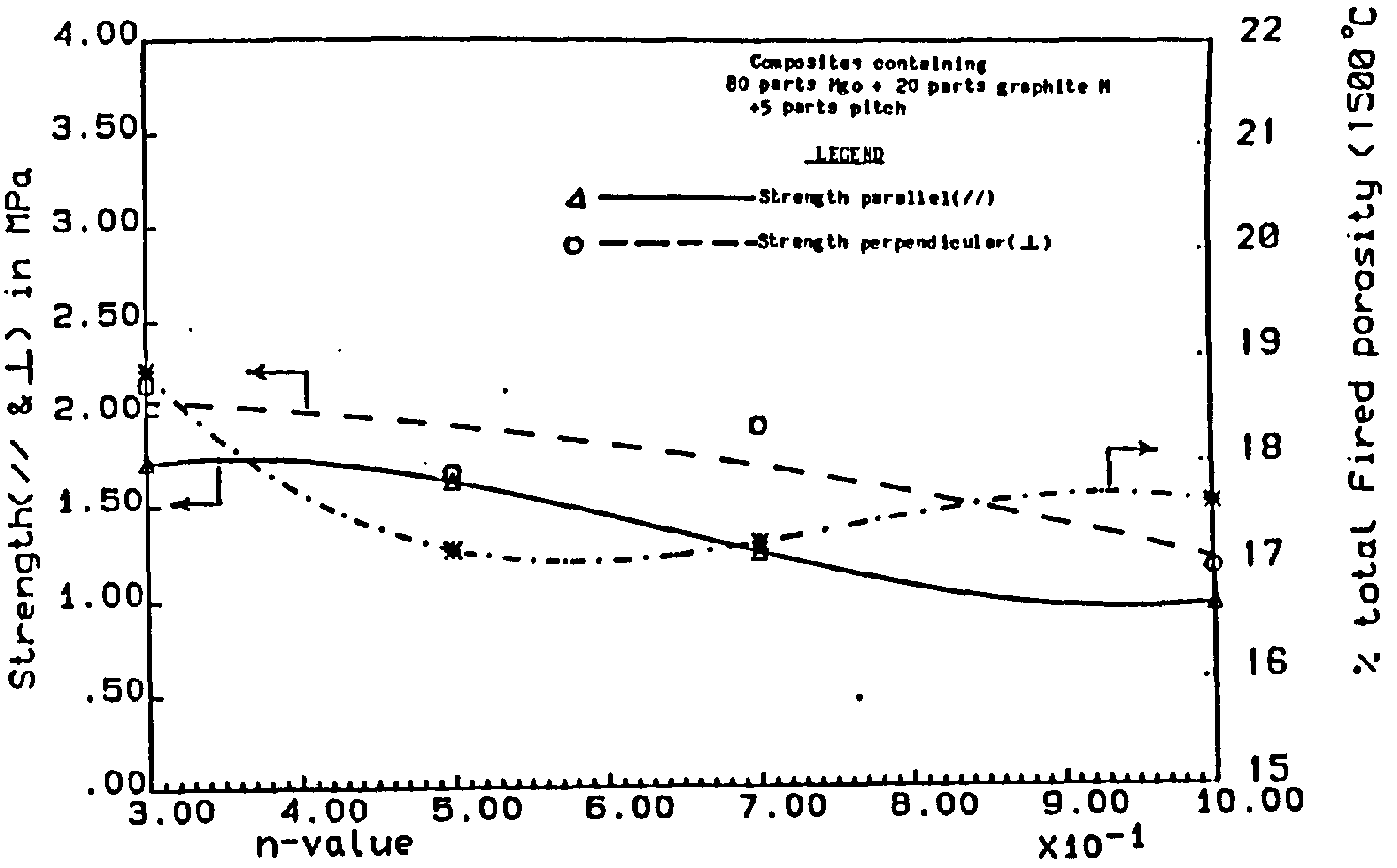

FIG. 5.5.8 iv(a):Strength & porosity V's n-value(Comp. with 20% graphite M)

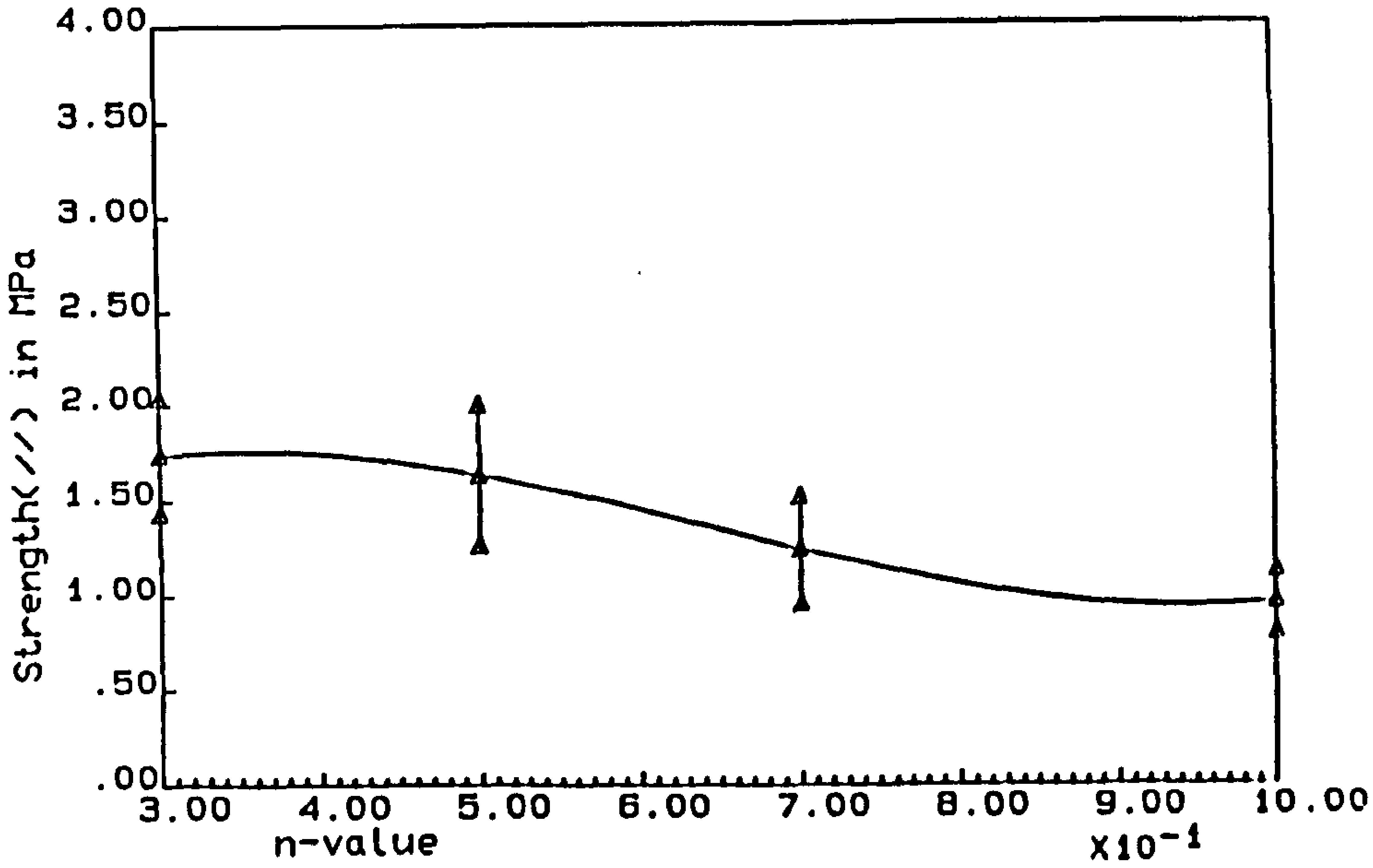

FIG. 5.5.8 iv(b):Strength(//) V's n-value (Comp. with 20% graphite M)

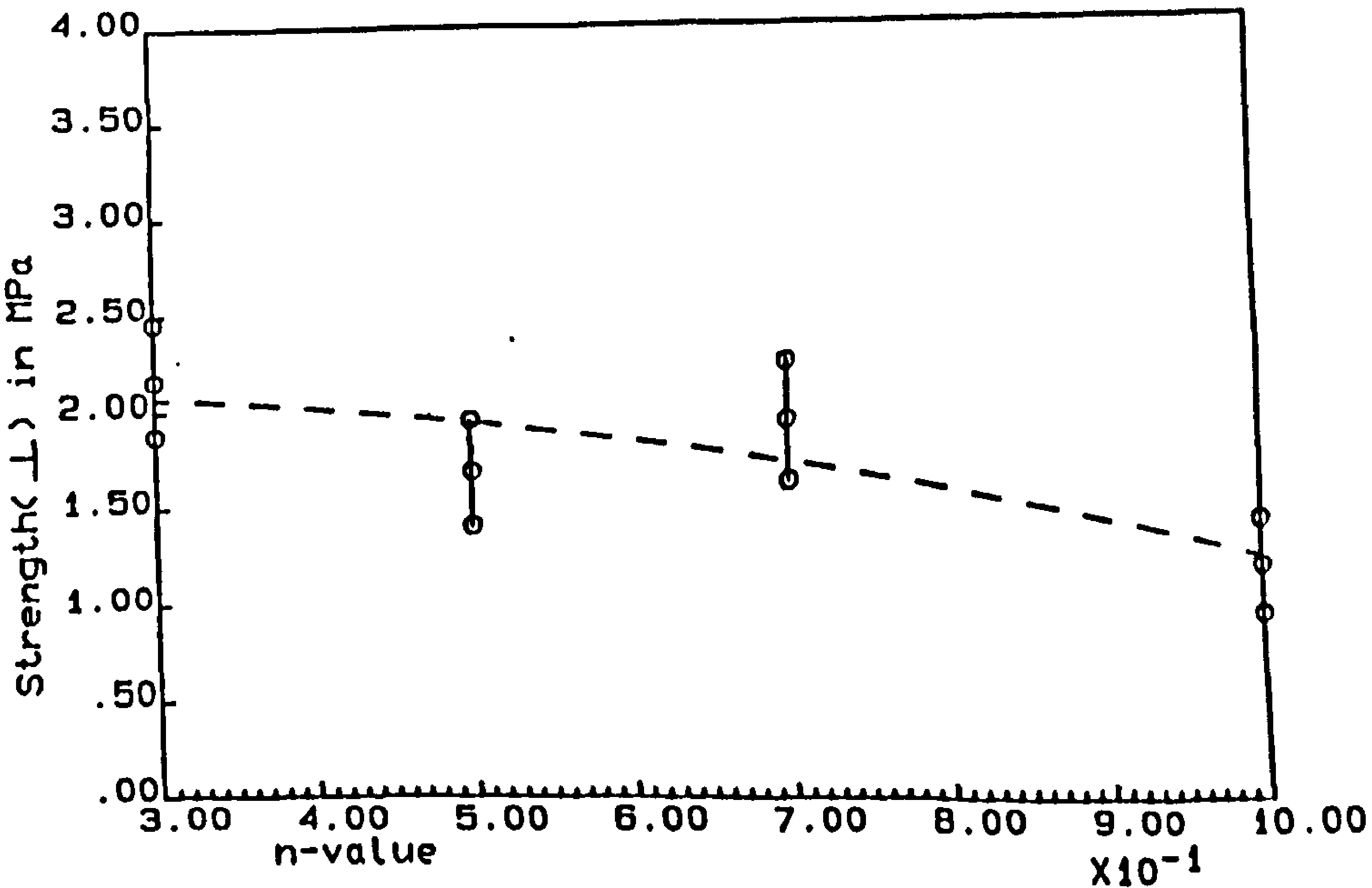

FIG. 5.5.8 iv(c):Strength(⊥) V's n-value (Comp. with 20% graphite M)

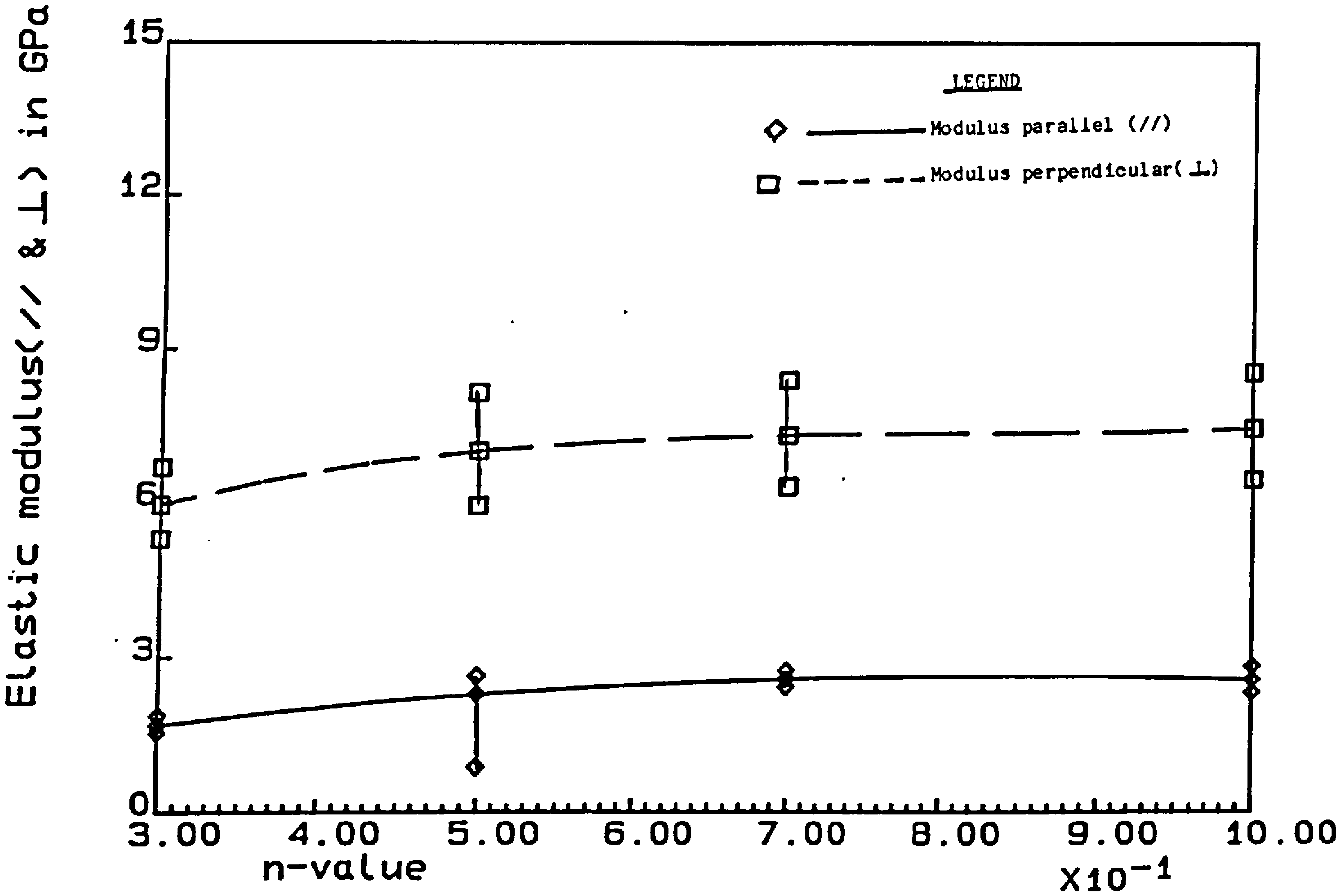

FIG. 5.5.8 iv(d):Elastic modulus V's
n-value (Comp. with 20% graphite M)

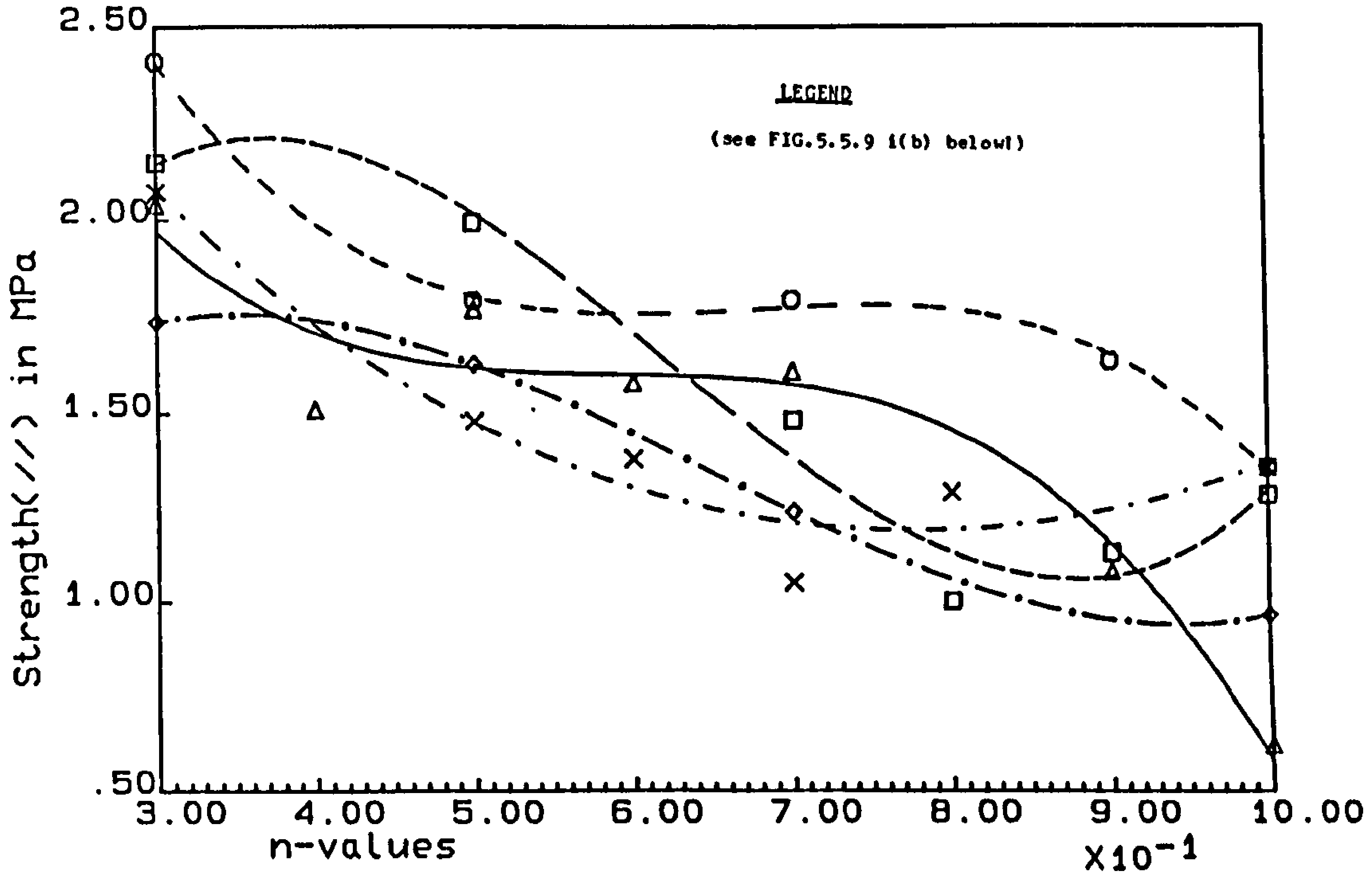

FIG. 5.5.9 i(a):Mean strength V's n-value
(For all Composites with 20% graphite)

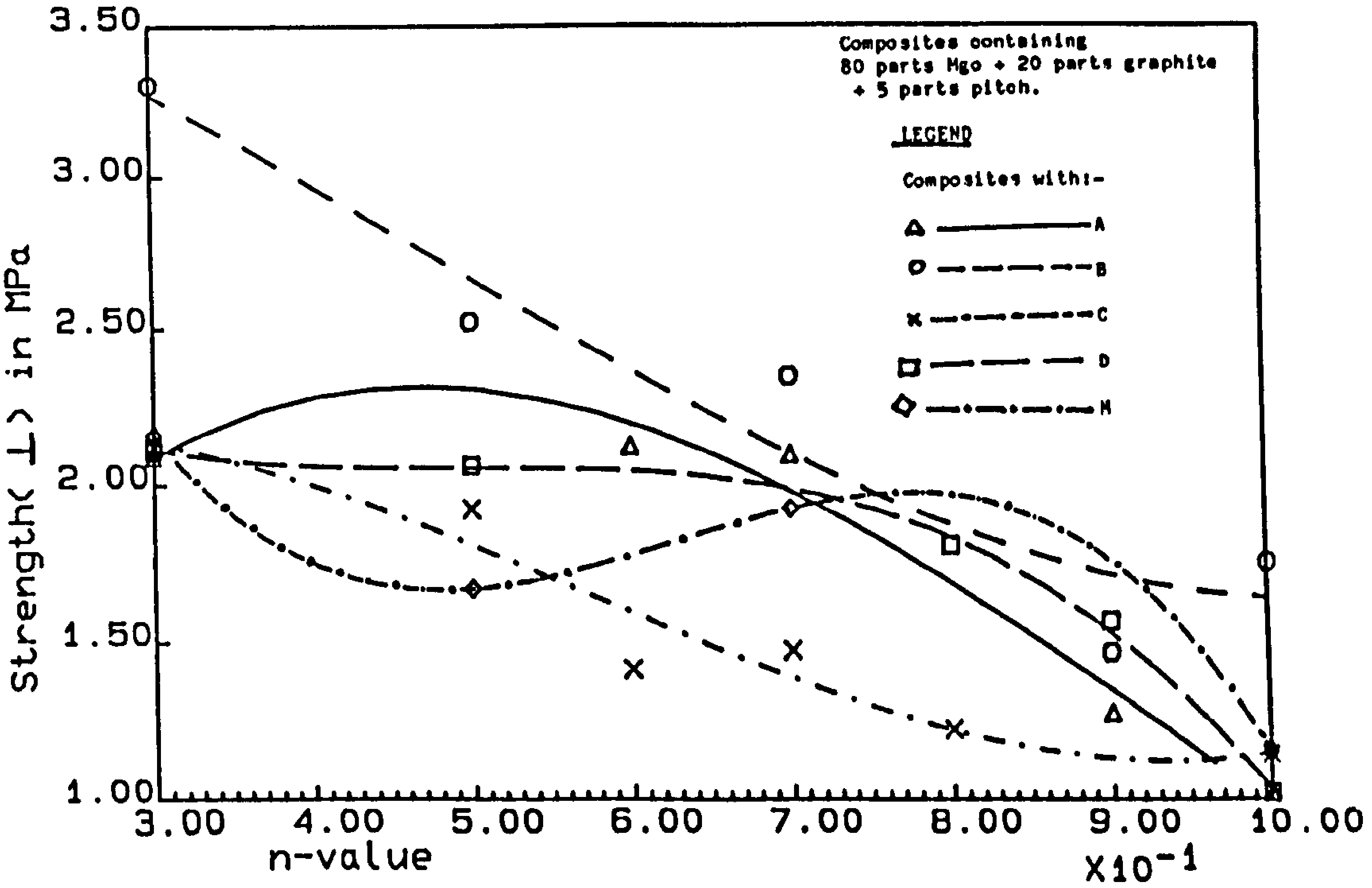

FIG. 5.5.9 i(b):Mean strength V's n-value
(For all composites with 20% graphite)

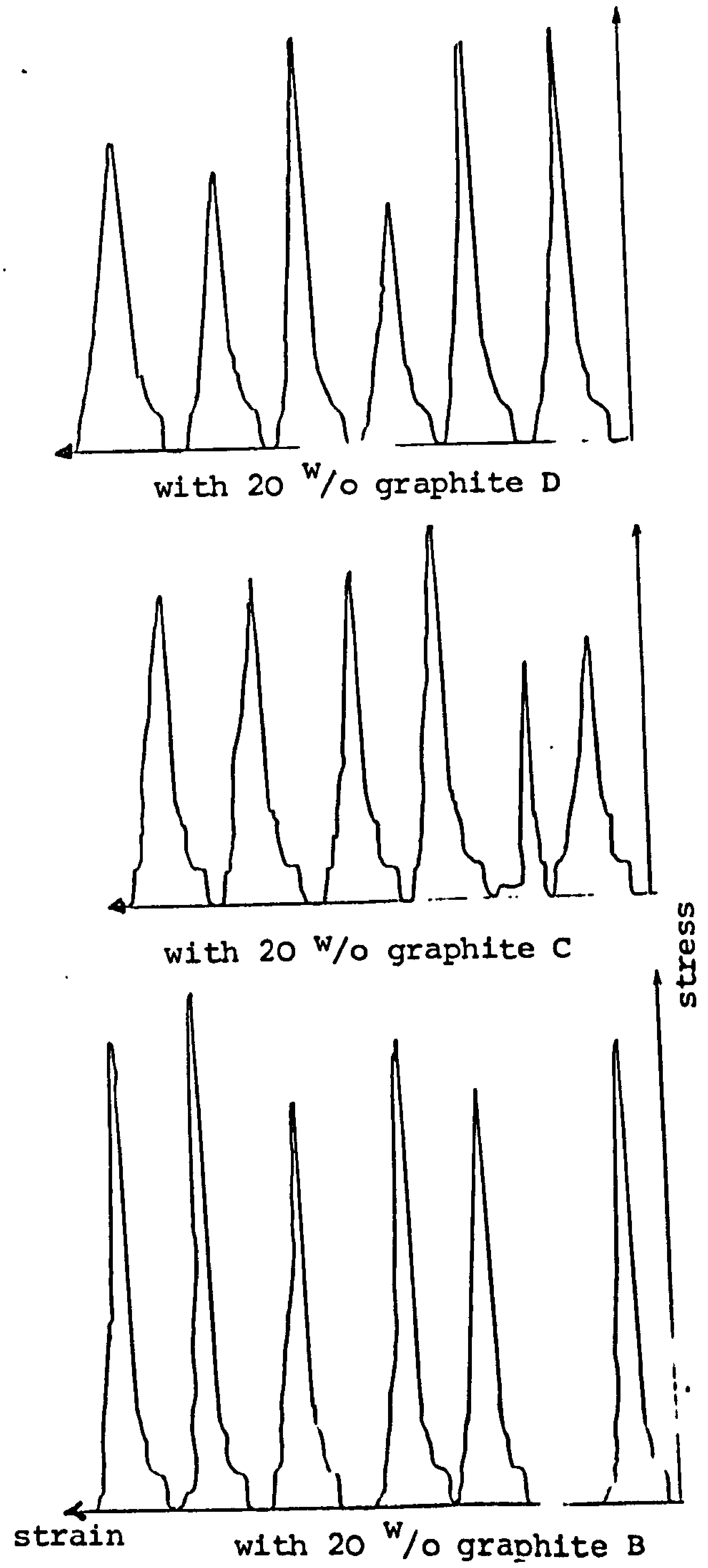

with 20 ^{w}/o graphite D

with 20 ^{w}/o graphite C

with 20 ^{w}/o graphite B

Figure 5.5.9(i)(c) Traces of stress-strain curves of composites containing 80 parts MgO + 20 parts graphite (but of different types) + 5 parts pitch at a fixed n-value of 0.3. (see next Figure for graphites A and M.)

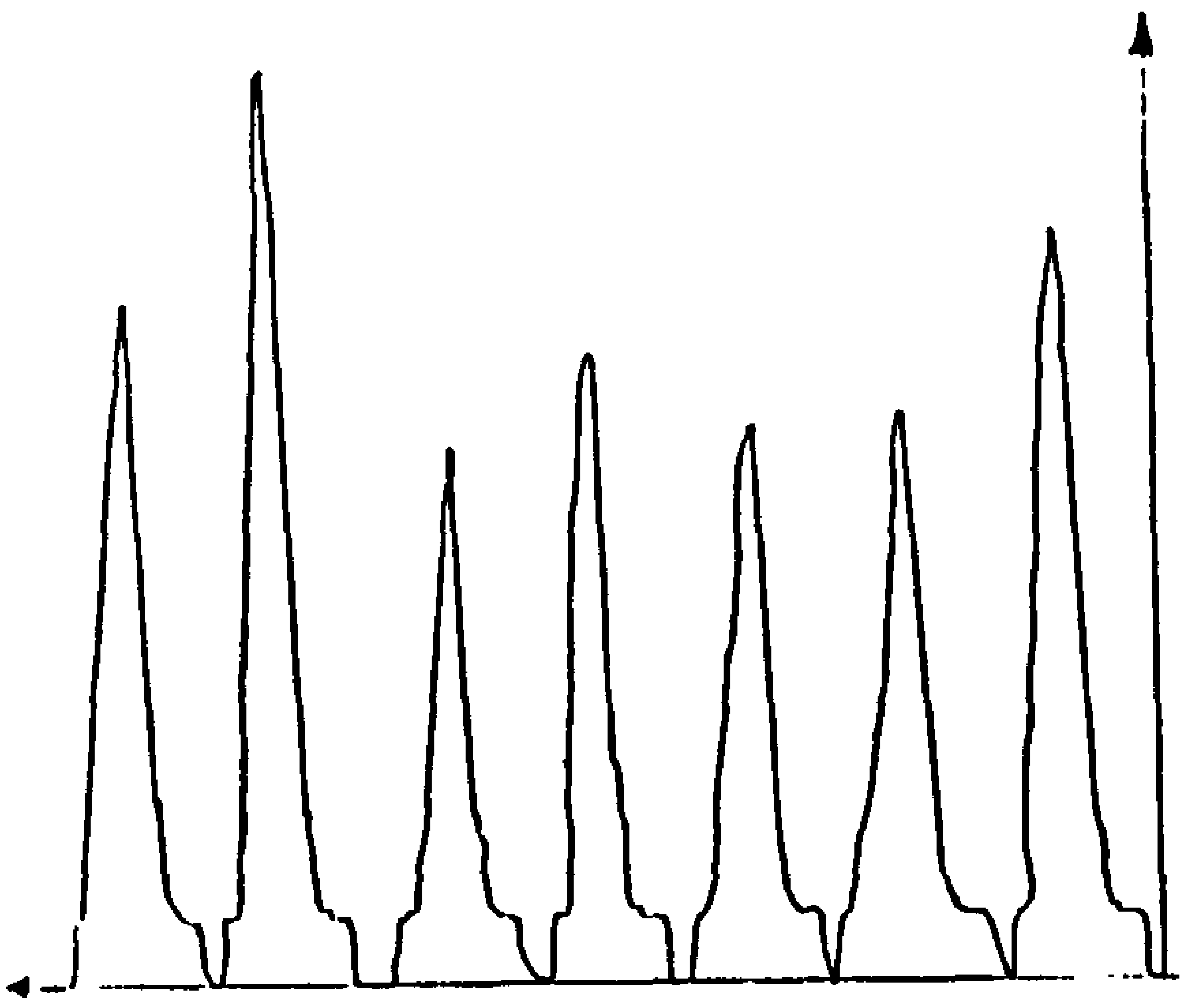

with 20 ^{w}/o graphite M

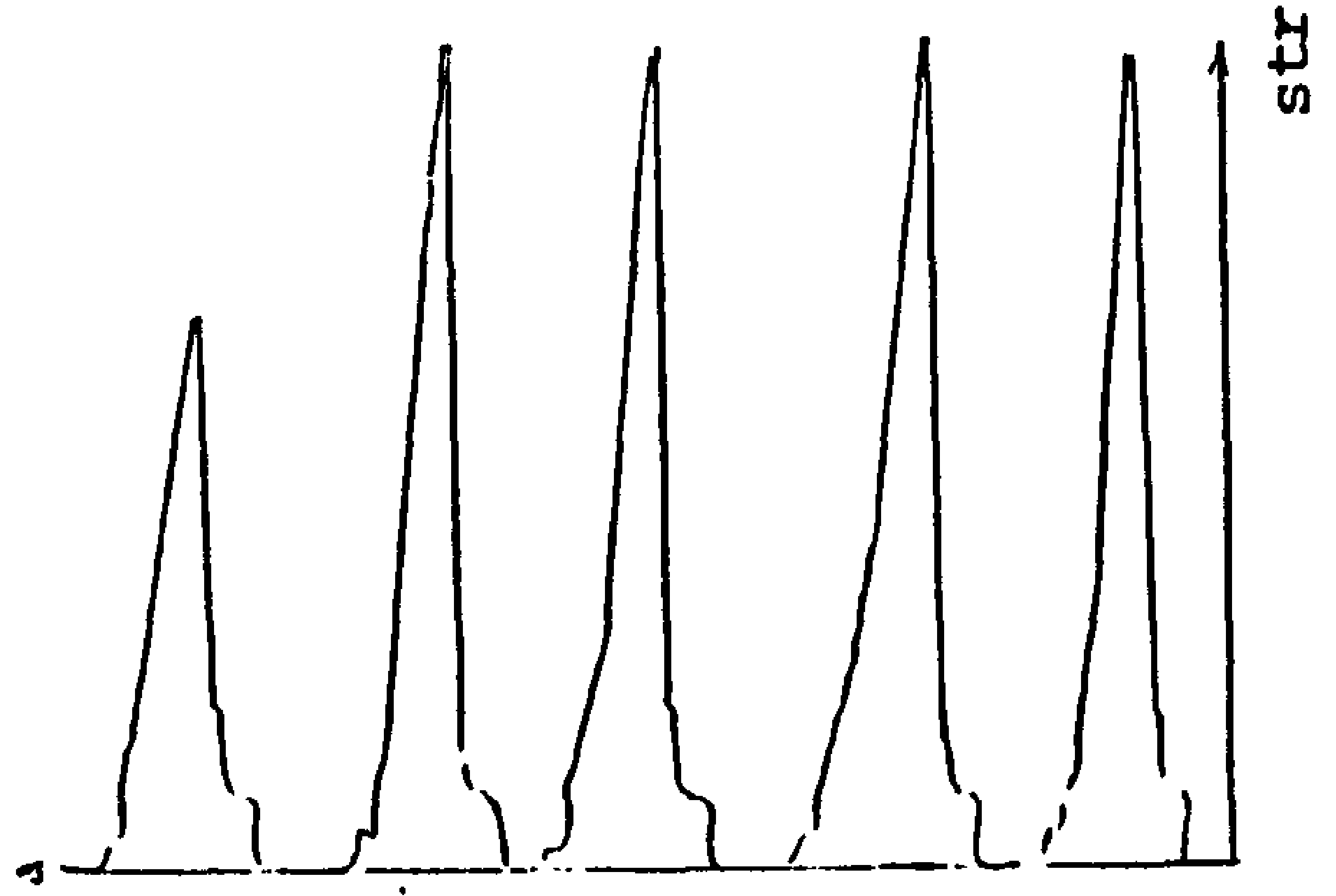

with 20 ^{w}/o graphite A

Figure 5.5.9(i)(c) continued

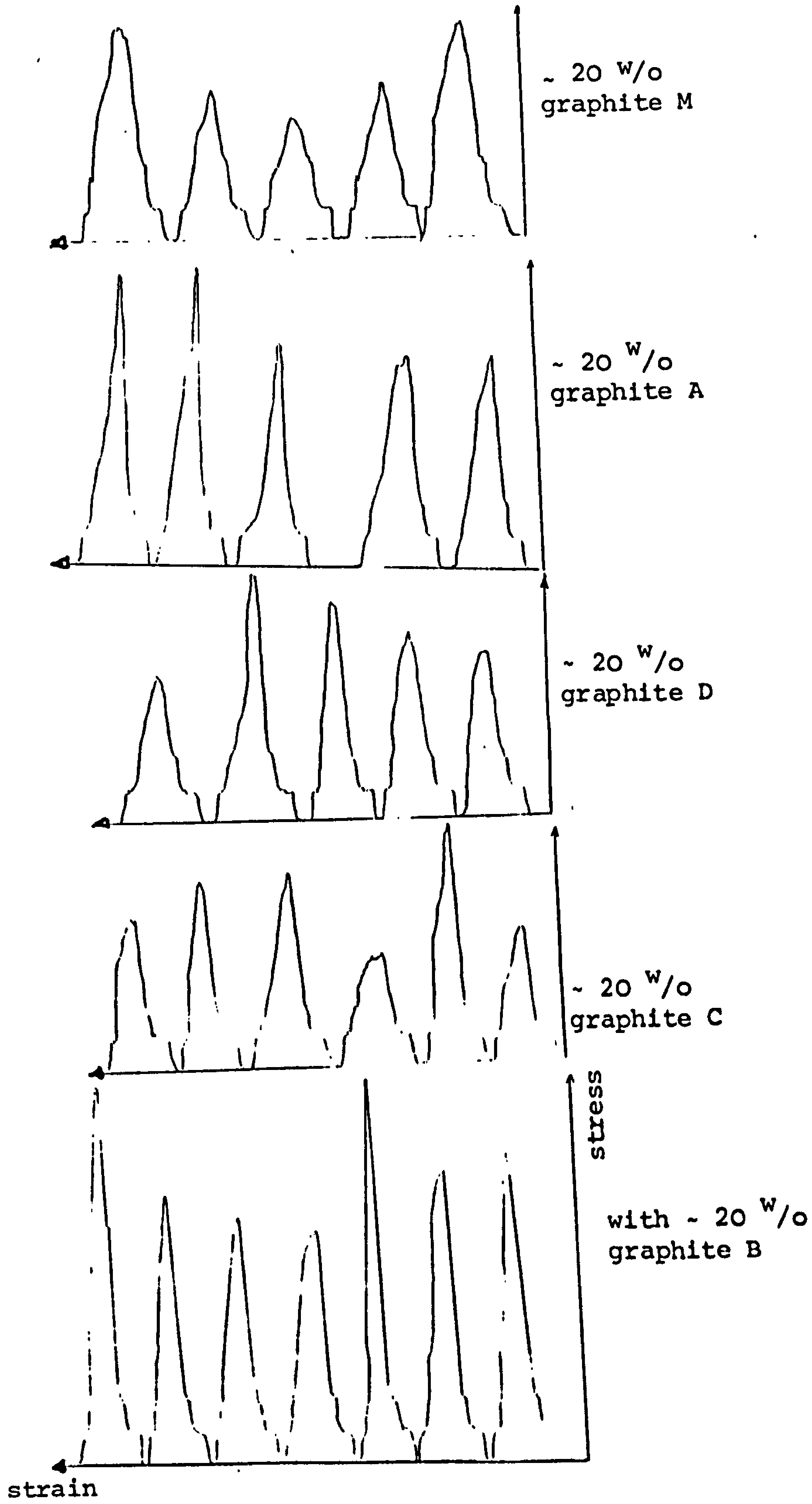

Figure 5.5.9(i)(d) Traces of stress-strain curves of composites containing 80 parts MgO + 20 parts graphite (but of different types) + 5 parts pitch at a fixed n-value of 0.7 and same full scale deflection of 10 kg (not shown here).

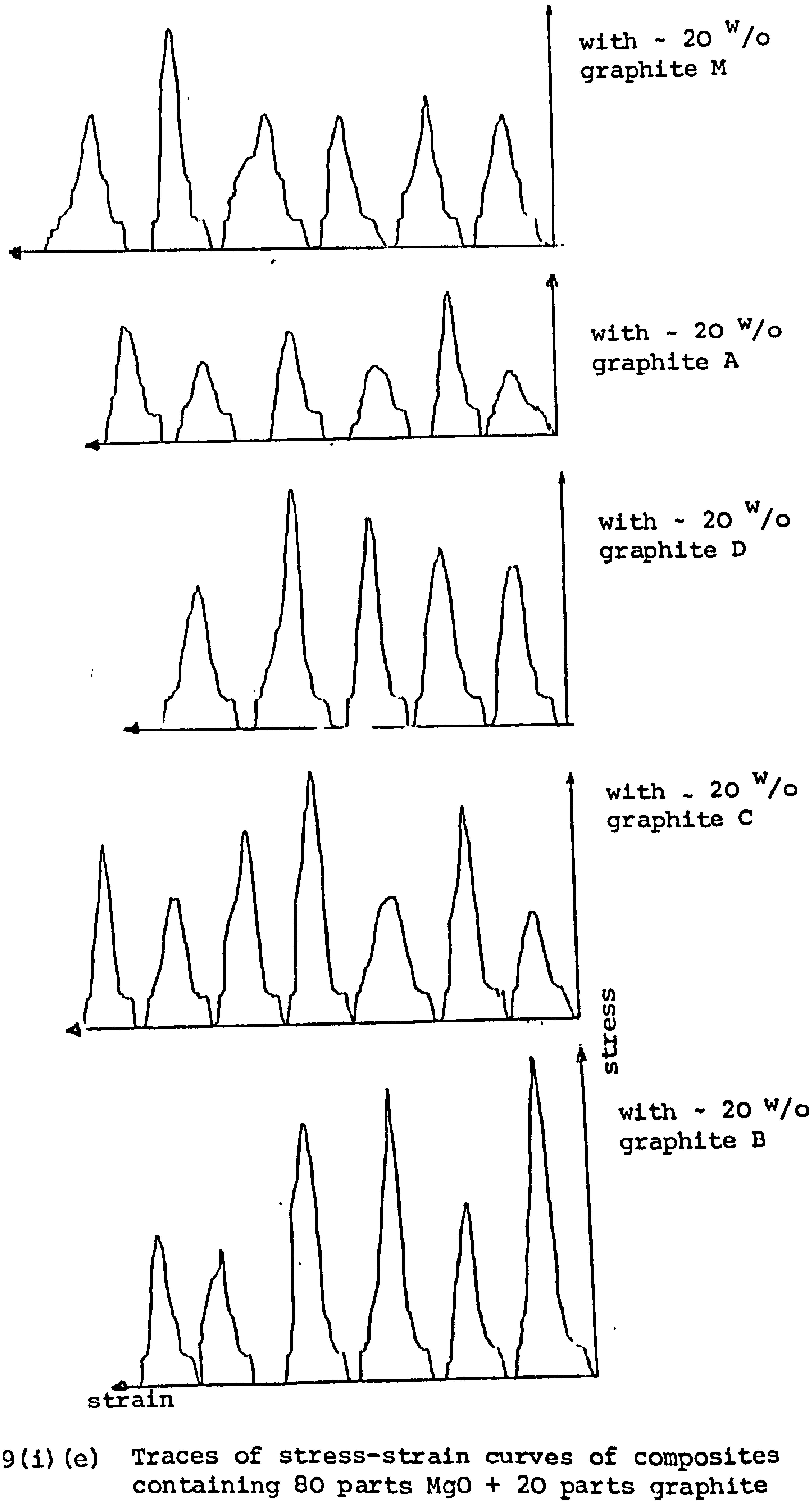

Figure 5.5.9(i)(e) Traces of stress-strain curves of composites containing 80 parts MgO + 20 parts graphite (but of different types) + 5 parts pitch at a fixed n-value of 1.0 and same full scale deflection of 10 kg (not shown here).

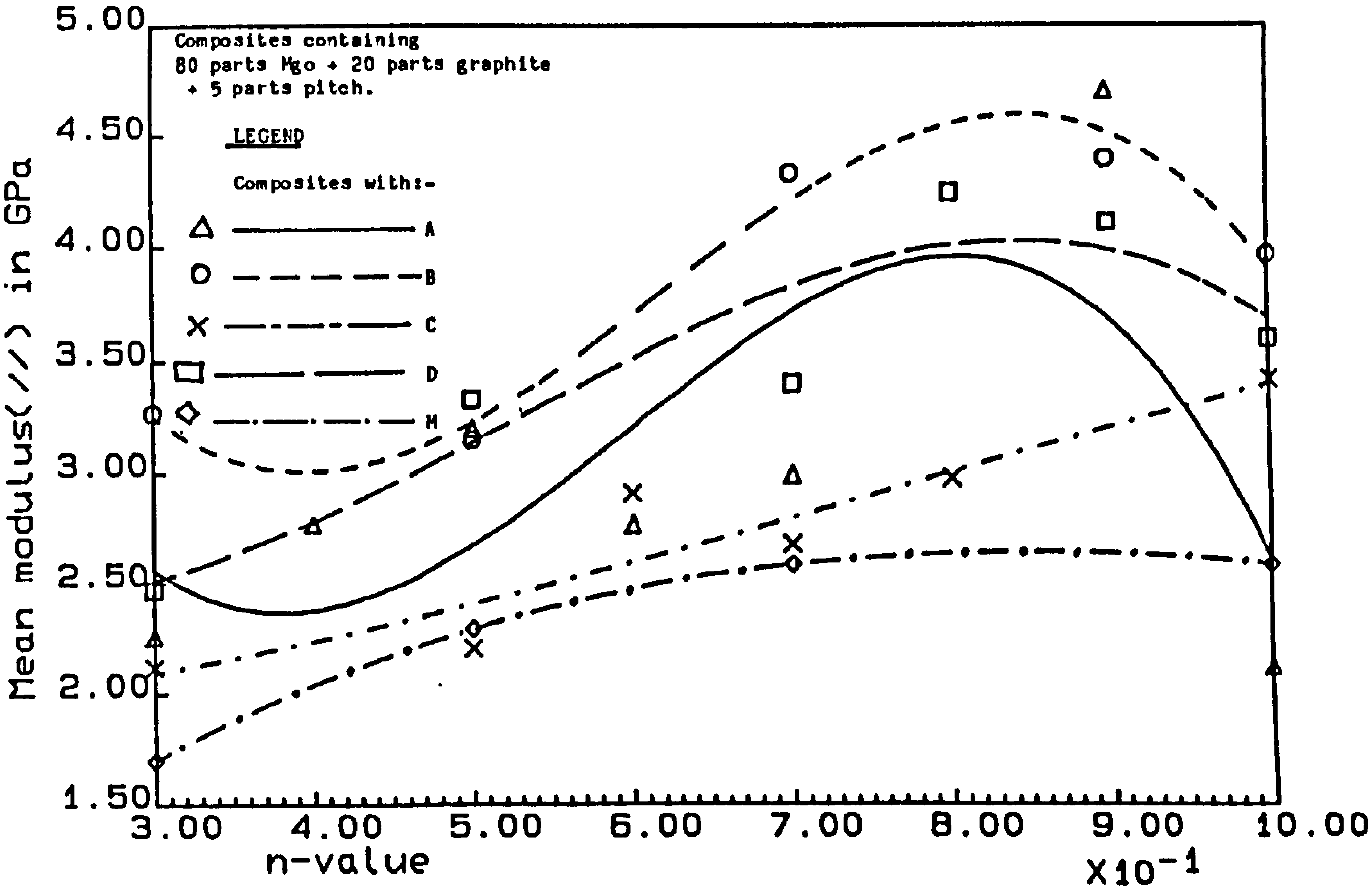

FIG. 5.5.9 ii(a):Elastic modulus V's n-value (For all composites with 20% graphite)

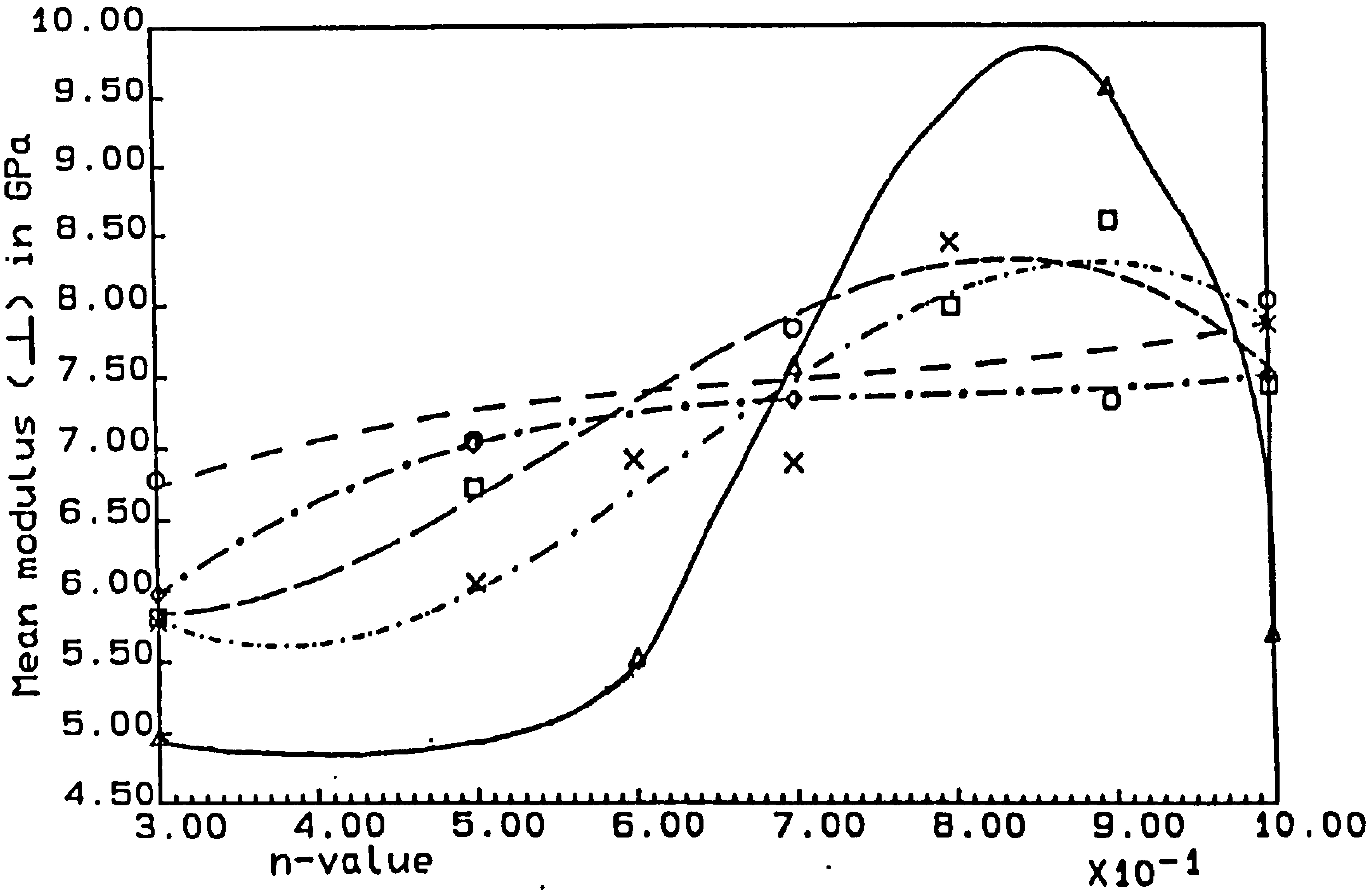

FIG. 5.5.9 ii(b):Mean elastic modulus V's n-value (all composites with 20% graphite)

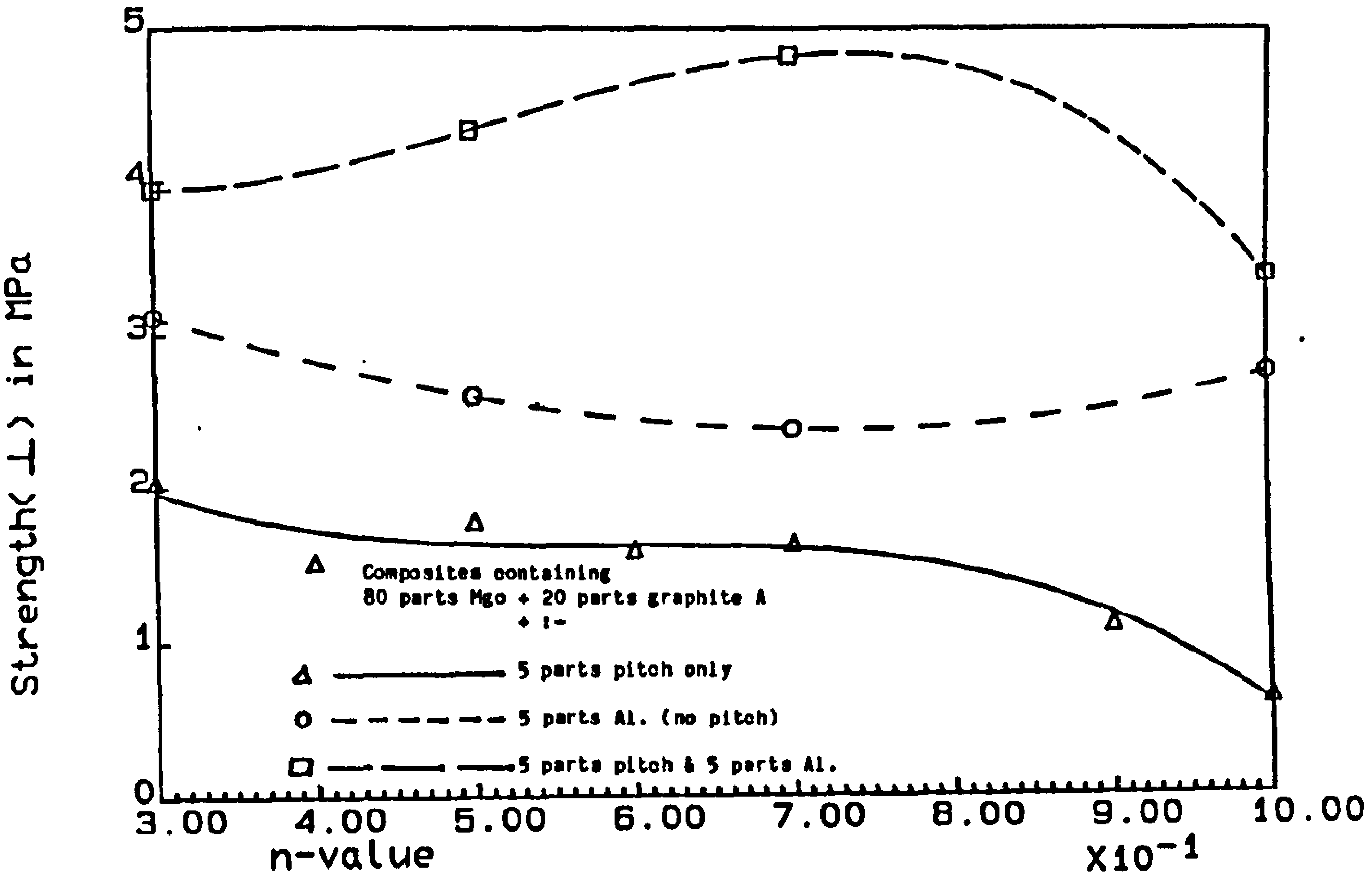

FIG. 5.5.10 i(a):Strength V's n-value
(comp. of 80%Mgo+20/% A +5% pitch or Al.)

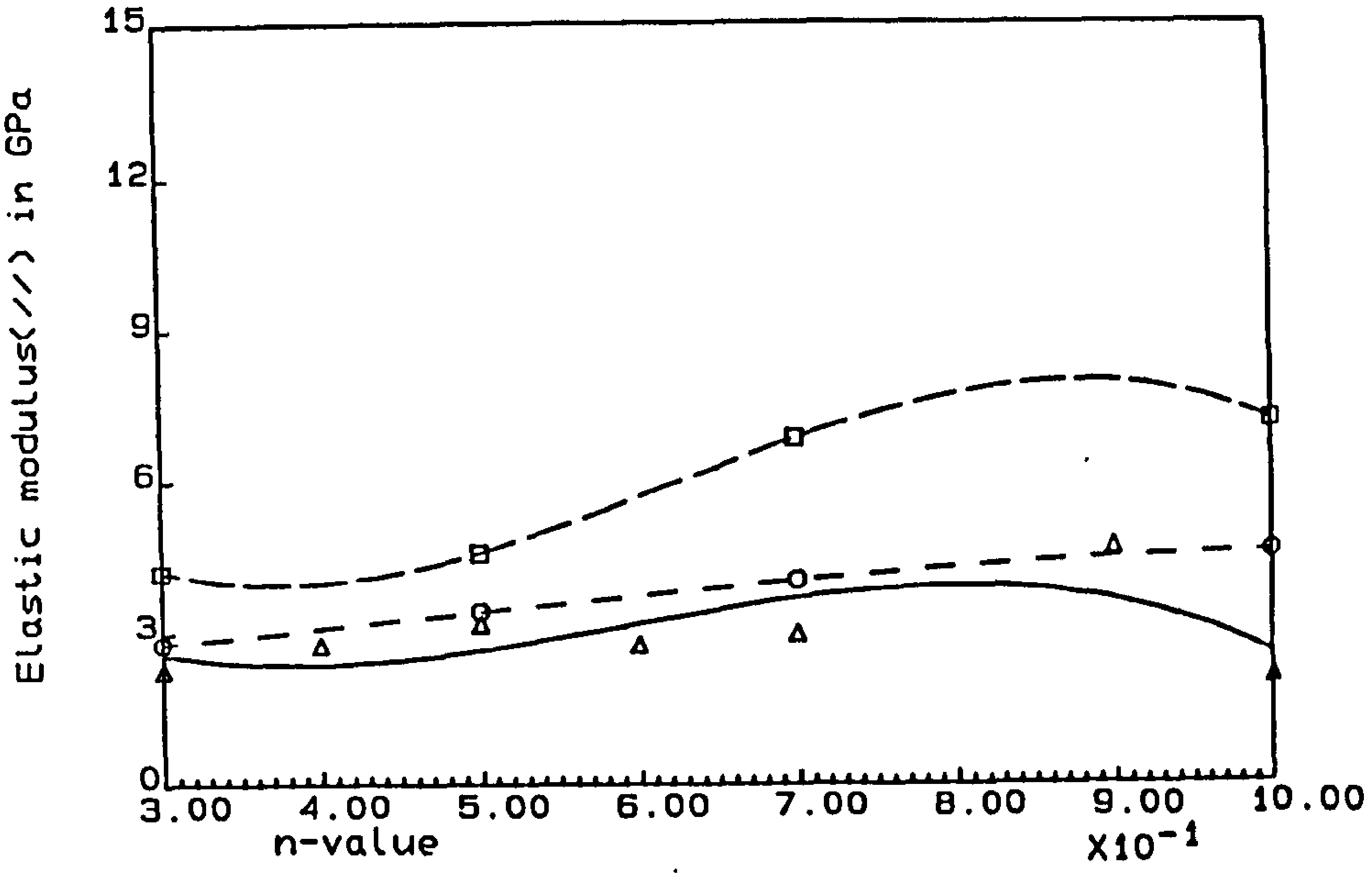

FIG. 5.5.10 i(b):Elastic modulus V's n-value
(Comp. with & without Al.)

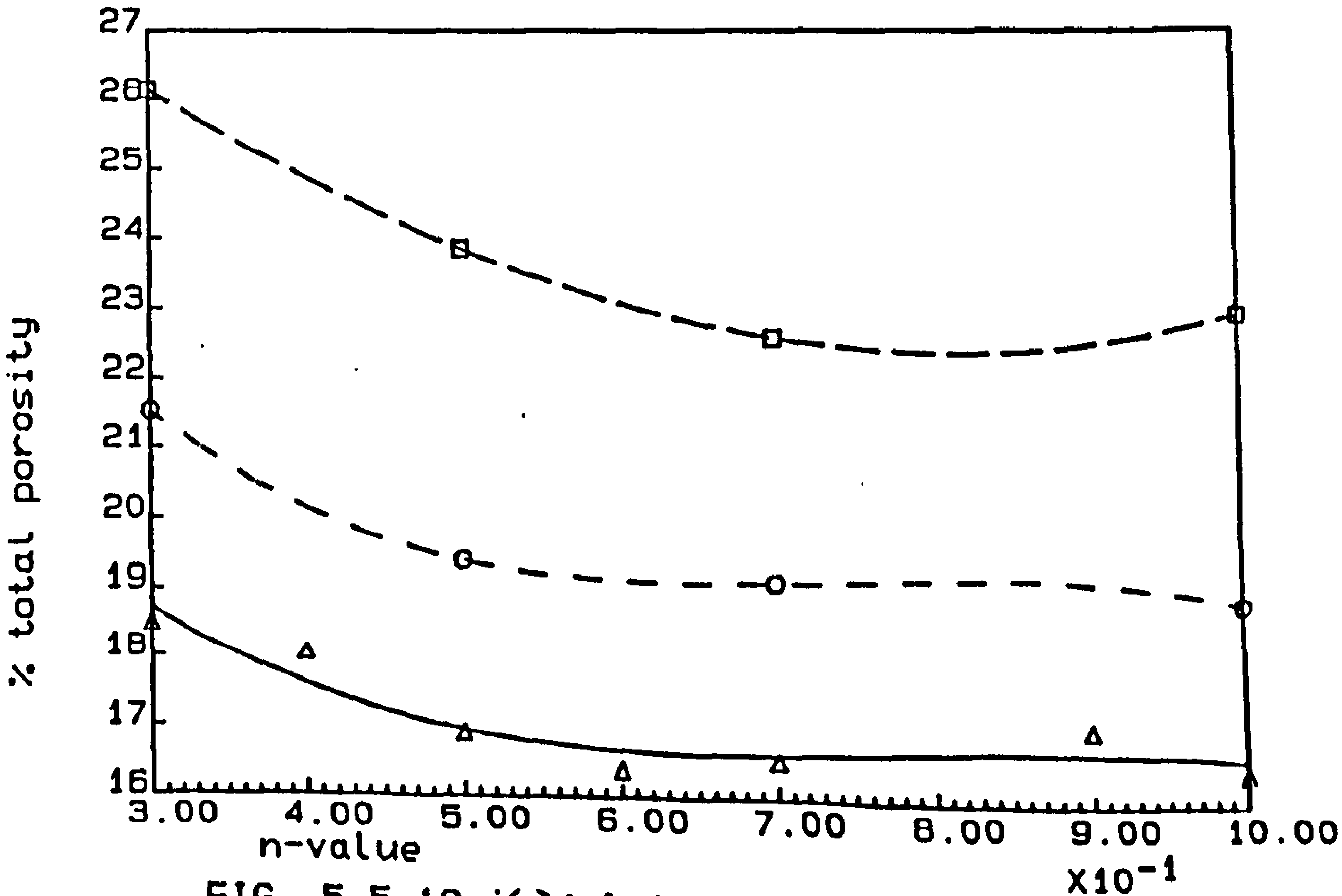

FIG. 5.5.10 i(c): % total porosity V's n-value
(Copm. with & without Al.)

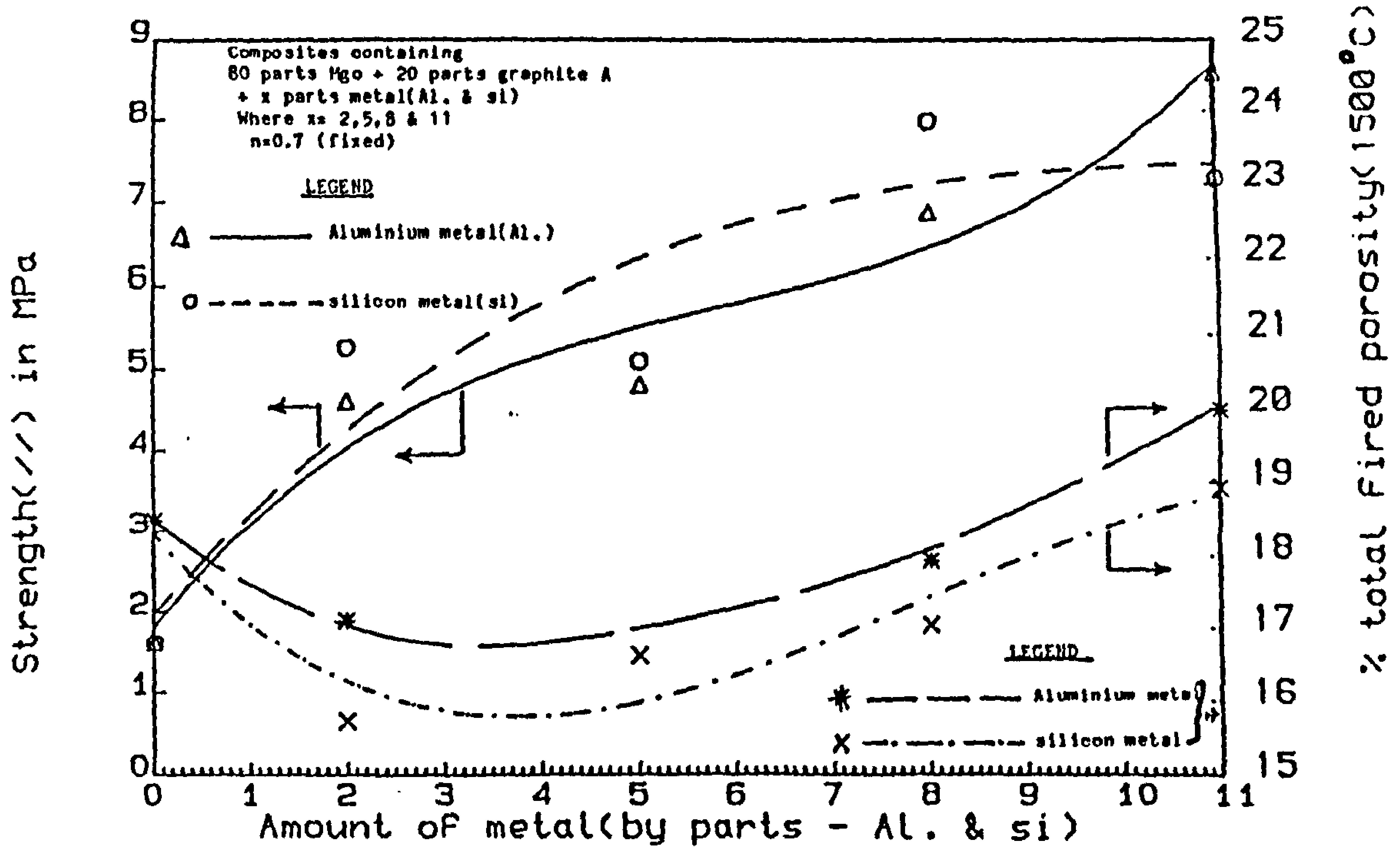

FIG. 5.5.10 ii : Strength V's metal content(by parts)

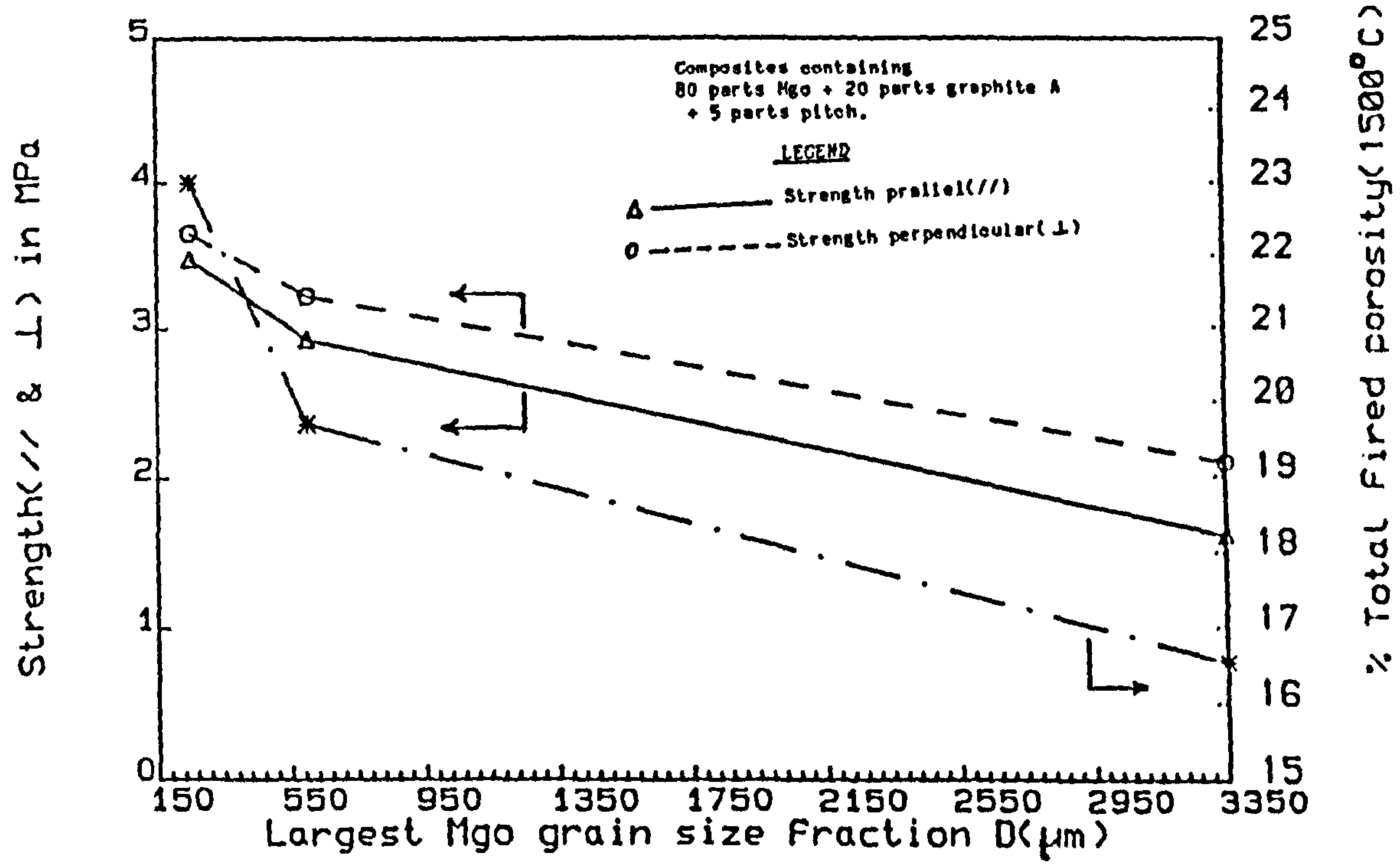

FIG. 5.5.11 : Strength V's D-value (D=topsize in the equation Y=100(d/D)↑n)

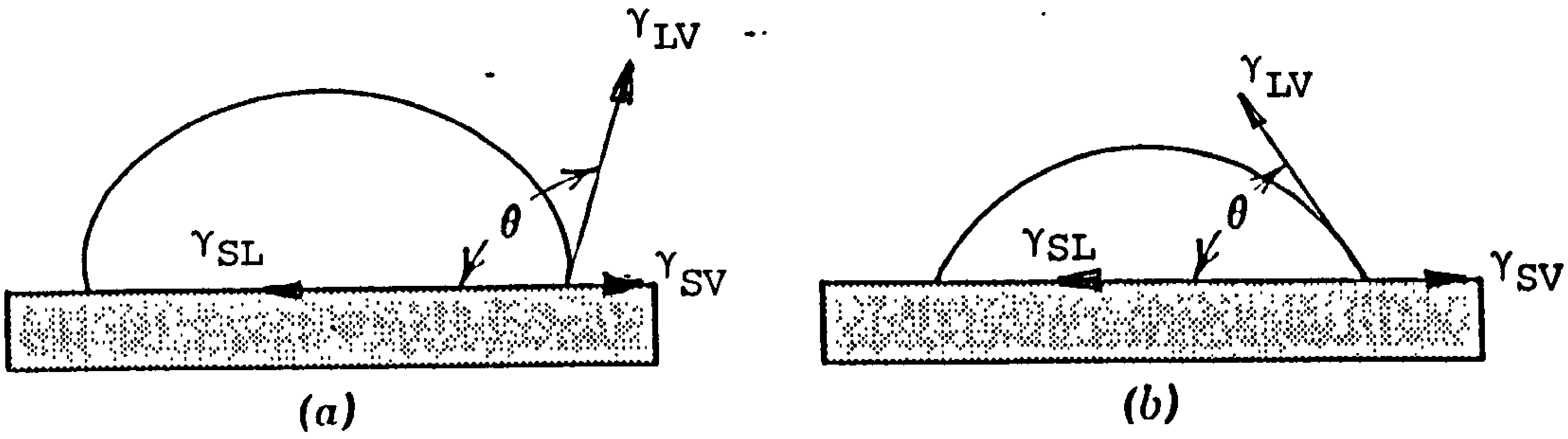

Fig. 6.1.1 The two figures illustrate:-

(a) non-wetting of a solid by a liquid, i.e. $\theta > 90^\circ$

(b) wetting of a solid by a liquid, i.e. $\theta < 90^\circ$

(Ref. 89).

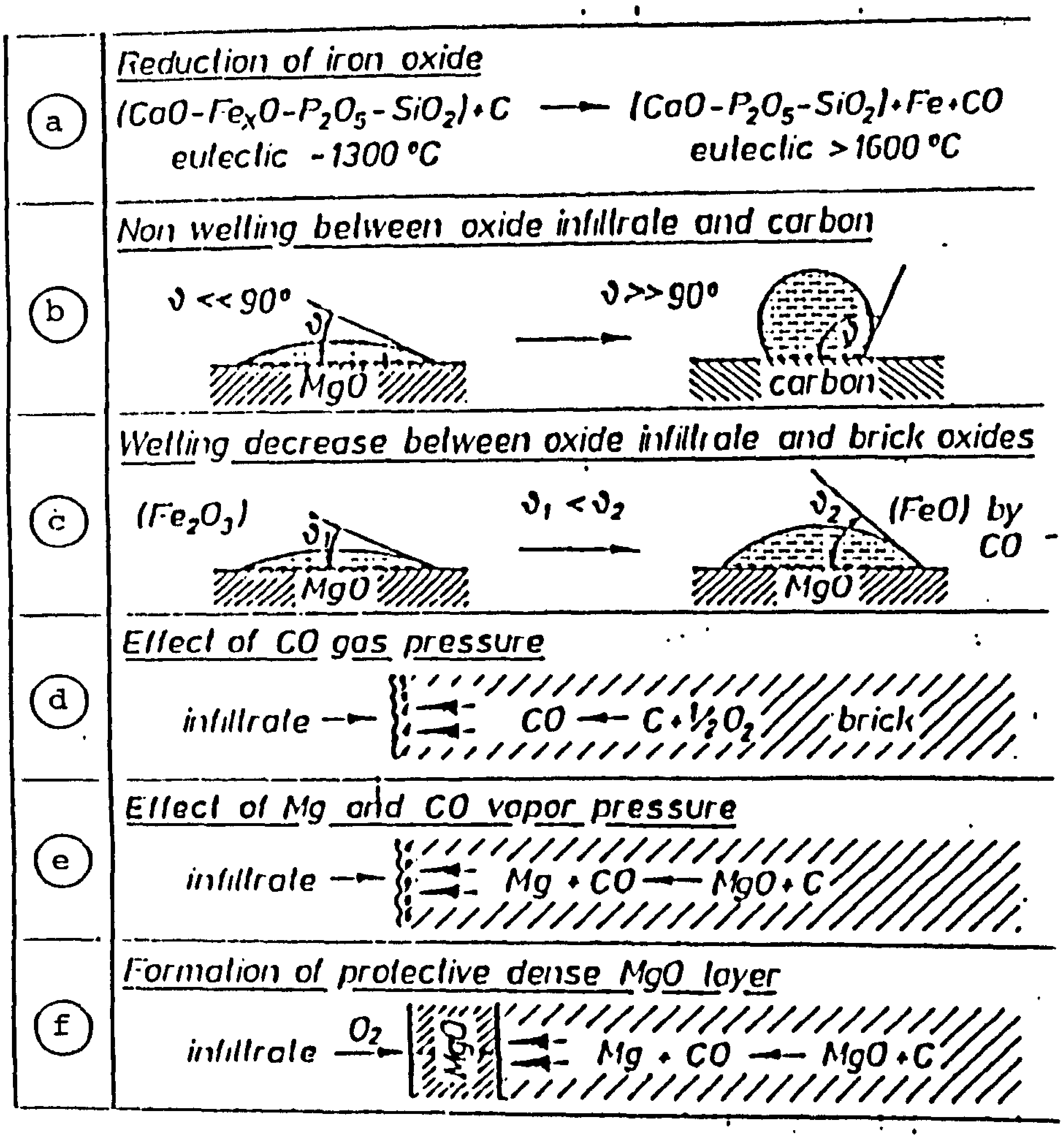

Fig. 6.1.2 Summary of the mechanisms which are thought to be responsible for good slag resistance of magnesia-carbon bricks[103]. (See Section 6.1.2 for details).

PLATES

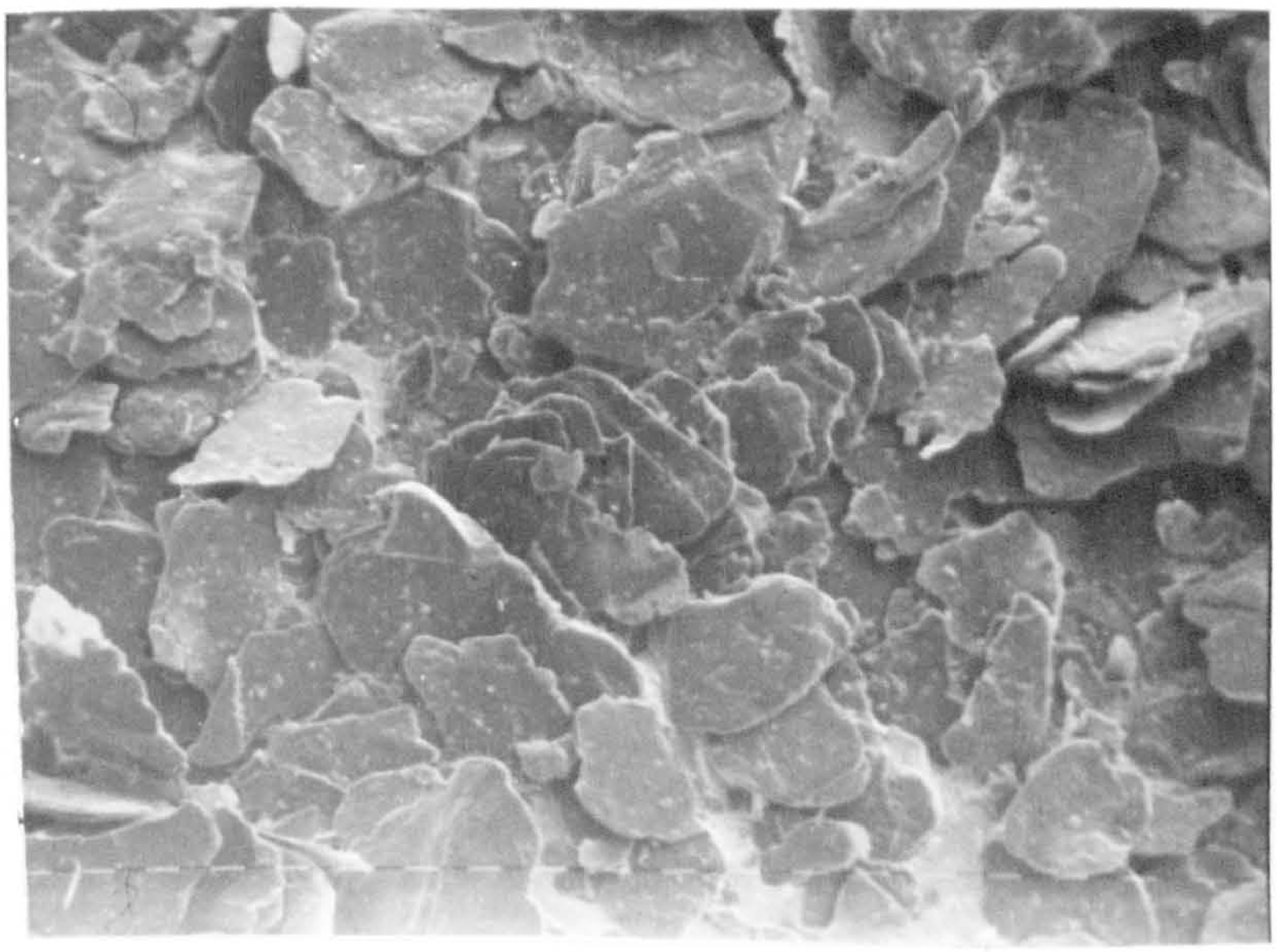

PLATE 1: This scanning electron microscopy(S.E.M) micrograph shows the general appearance of a natural flake graphite.

MAGNIFICATION: One micromark = 100 µm(28x)

Graphite A

Graphite B

Graphite C

PLATES 2.2.2 :Scanning Electron Microscopy (S.E.M) micrographs illustrating the shapes and sizes of graphite flakes used in this work.

MAGNIFICATION: One micromark = 100 microns(28x)

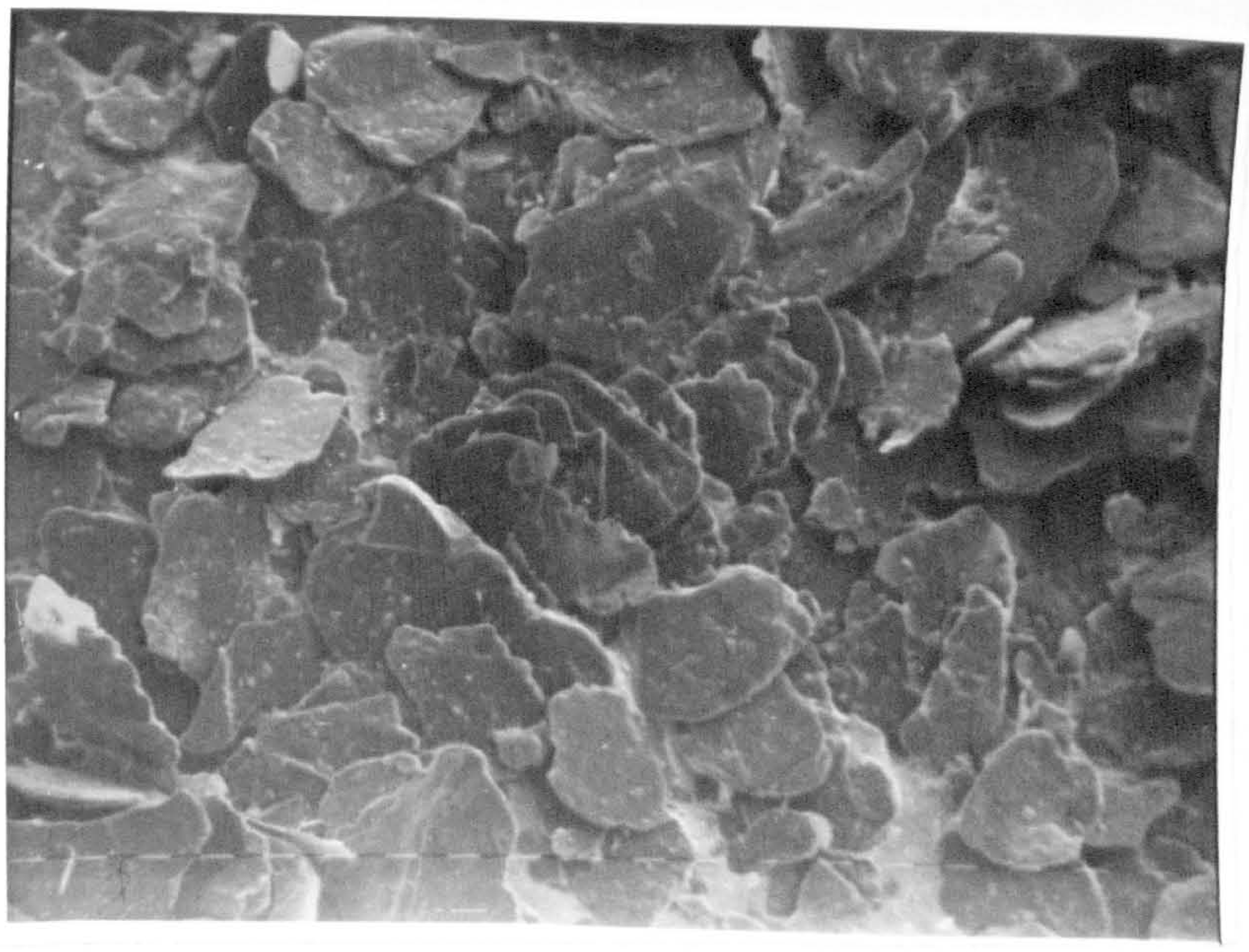

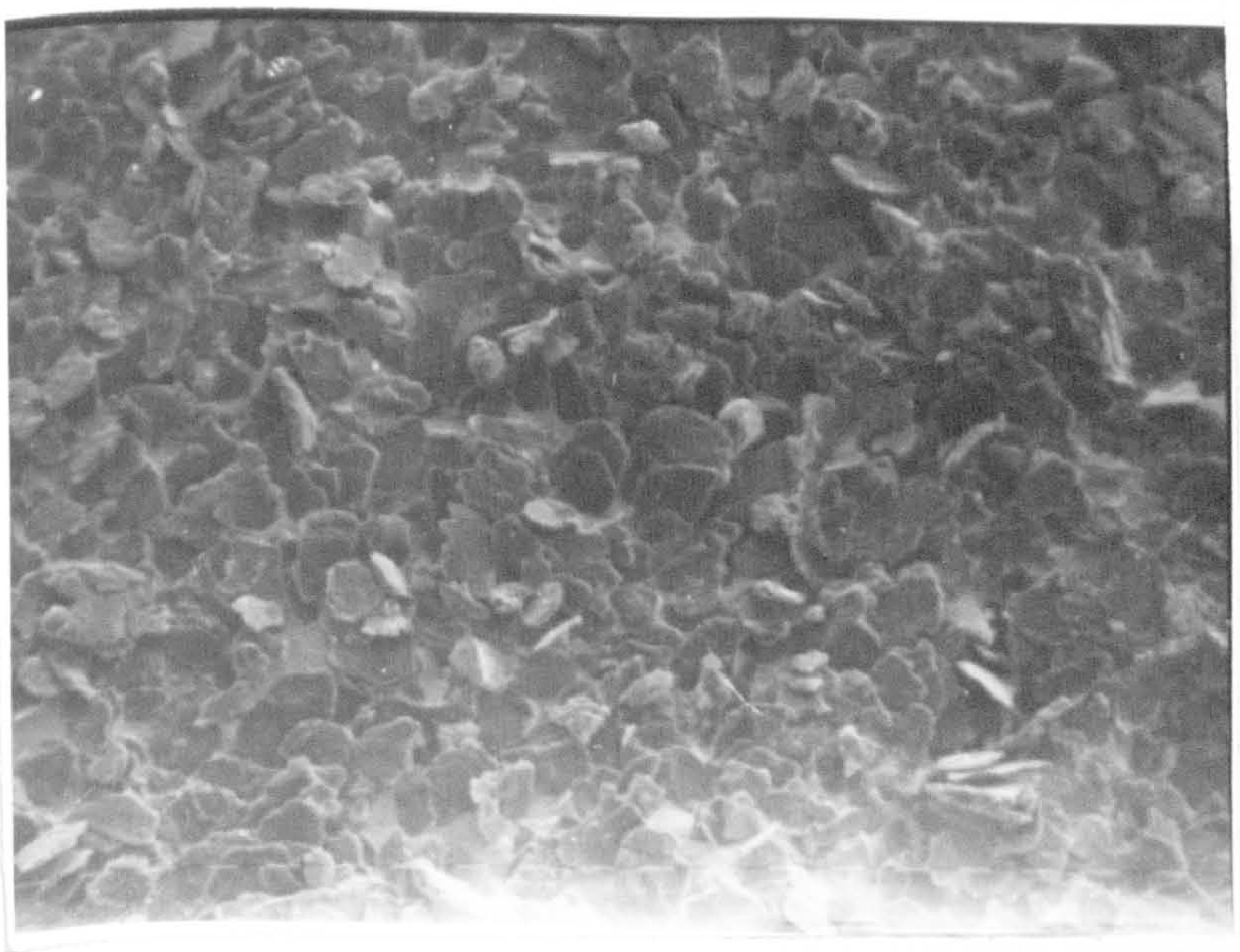

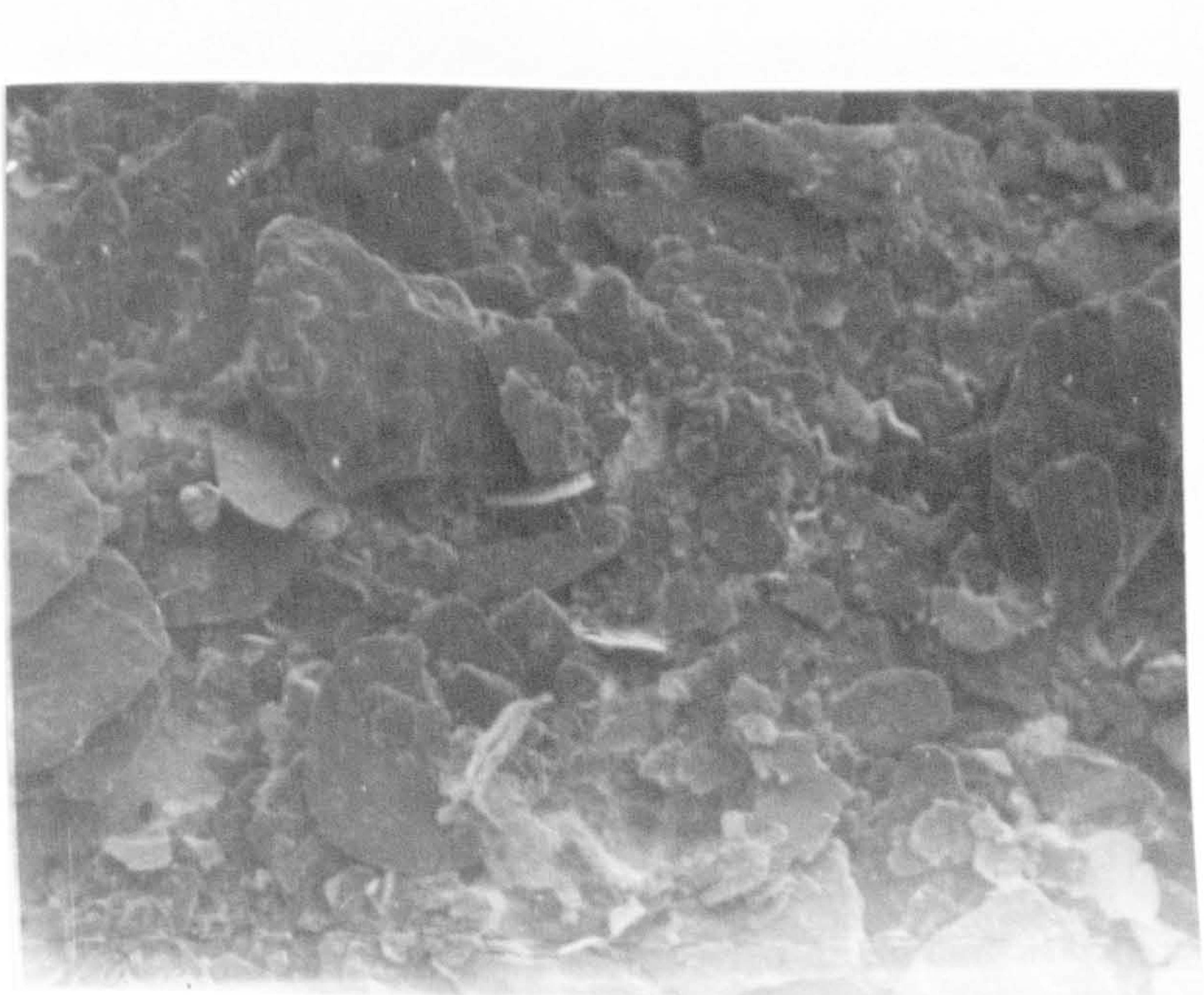

Graphite D

Graphite M

PLATES 2.2.2 Continued (see previous Plates)

MAGNIFICATION: One micromark = 100 microns(28x)

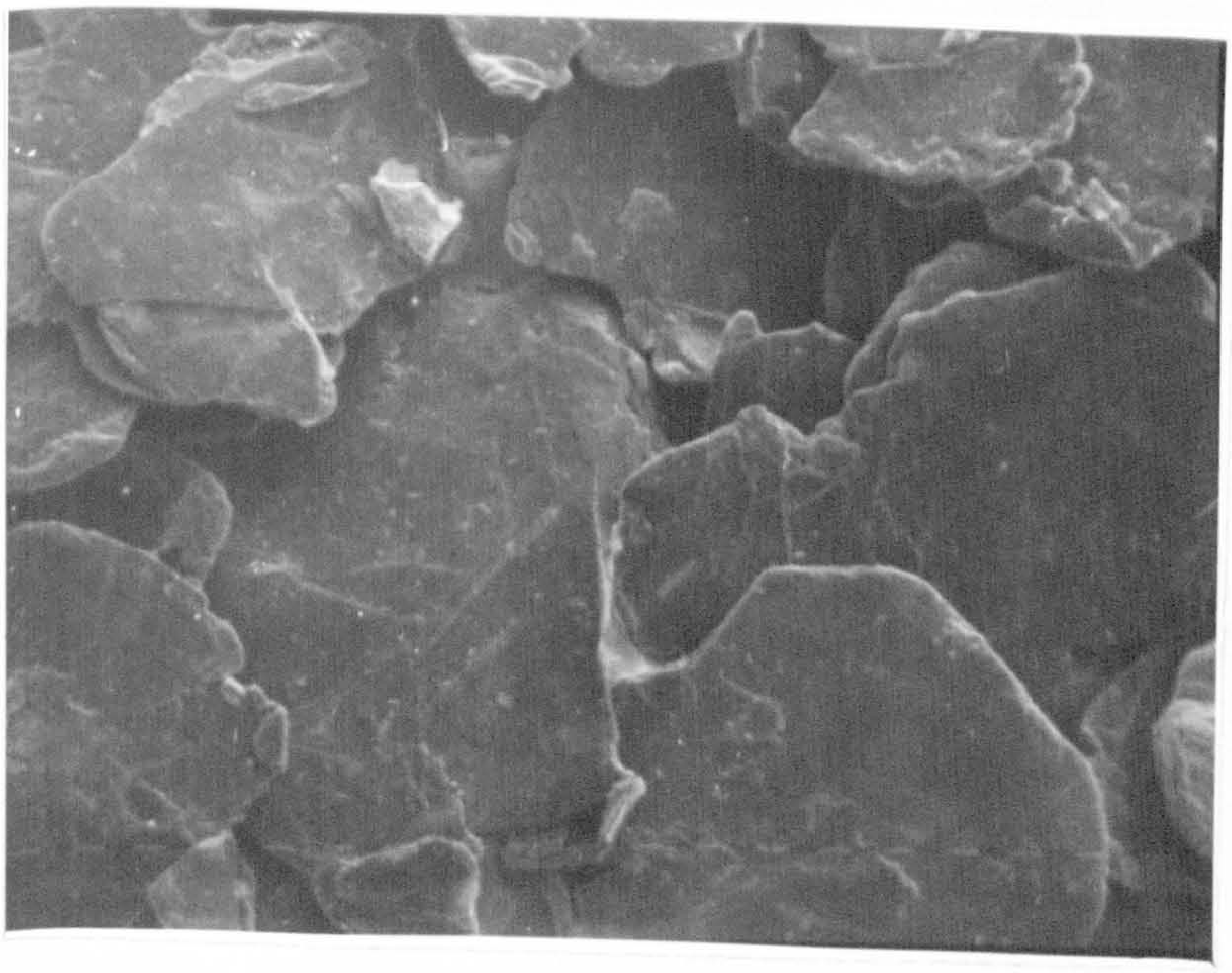

PLATE 2.4.5 ii(a):S.E.M. micrograph of pitch coke
showing the texture of the coke
after coking at 1500°C

PLATE 2.4.5 ii(b):S.E.M. micrograph of coked resin(P41)
showing the texture of the coke after
coking at 1500°C.Large open pores are
evident.
MAGNIFICATION = 57x

PLATE 3.2.3 :Photomicrograph illustrating how a polished
prismatic edge of a graphite flake(Graphite A)
used in thickness determination of
the flakes appeared on the TV screen.
MAGNIFICATION = 84x

PLATE 3.2.3 :Photomicrograph illustrating how a polished
prismatic edge of a graphite flake(Graphite B)
used in thickness determination of
the flakes appeared on the TV screen.
MAGNIFICATION = 84x

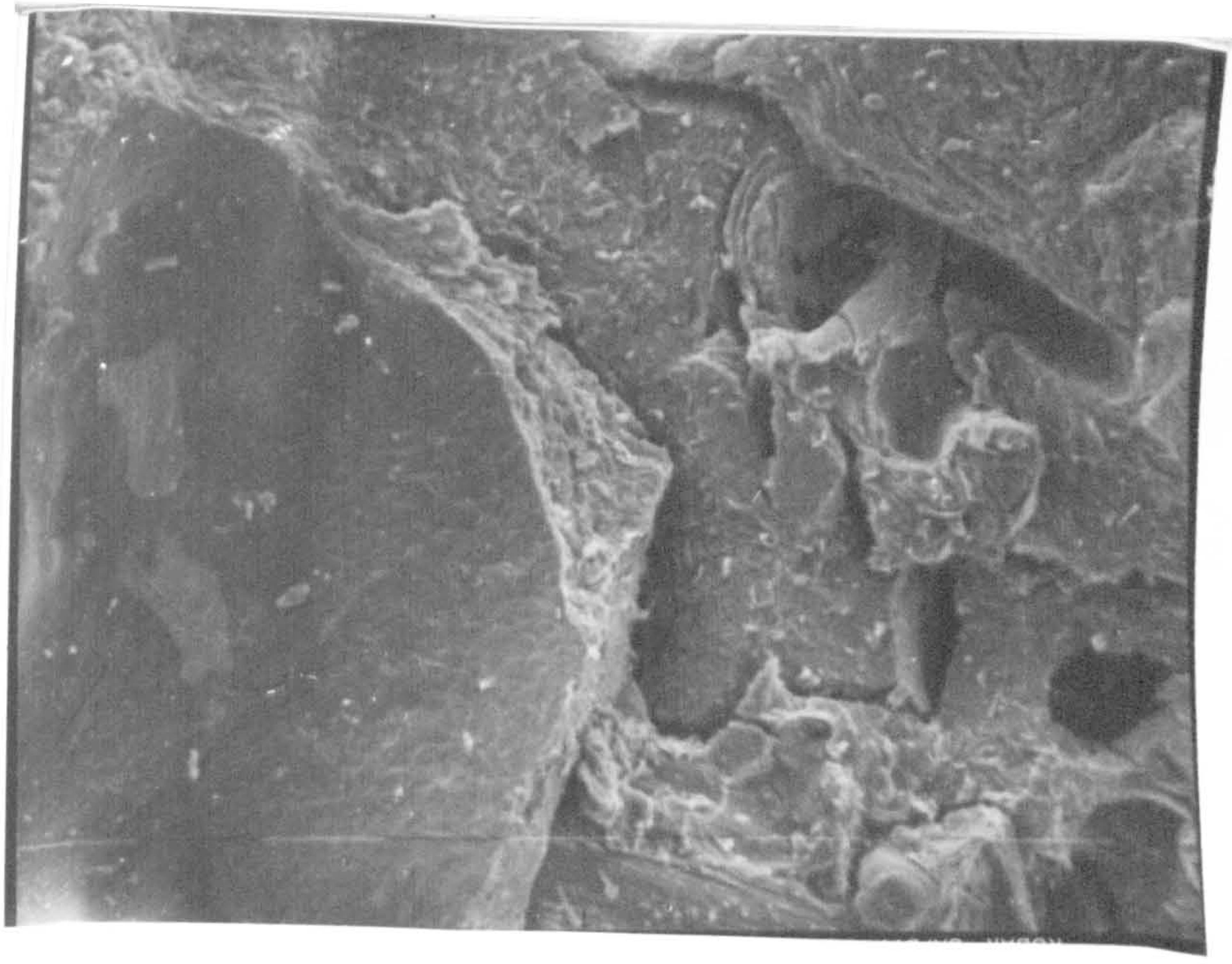

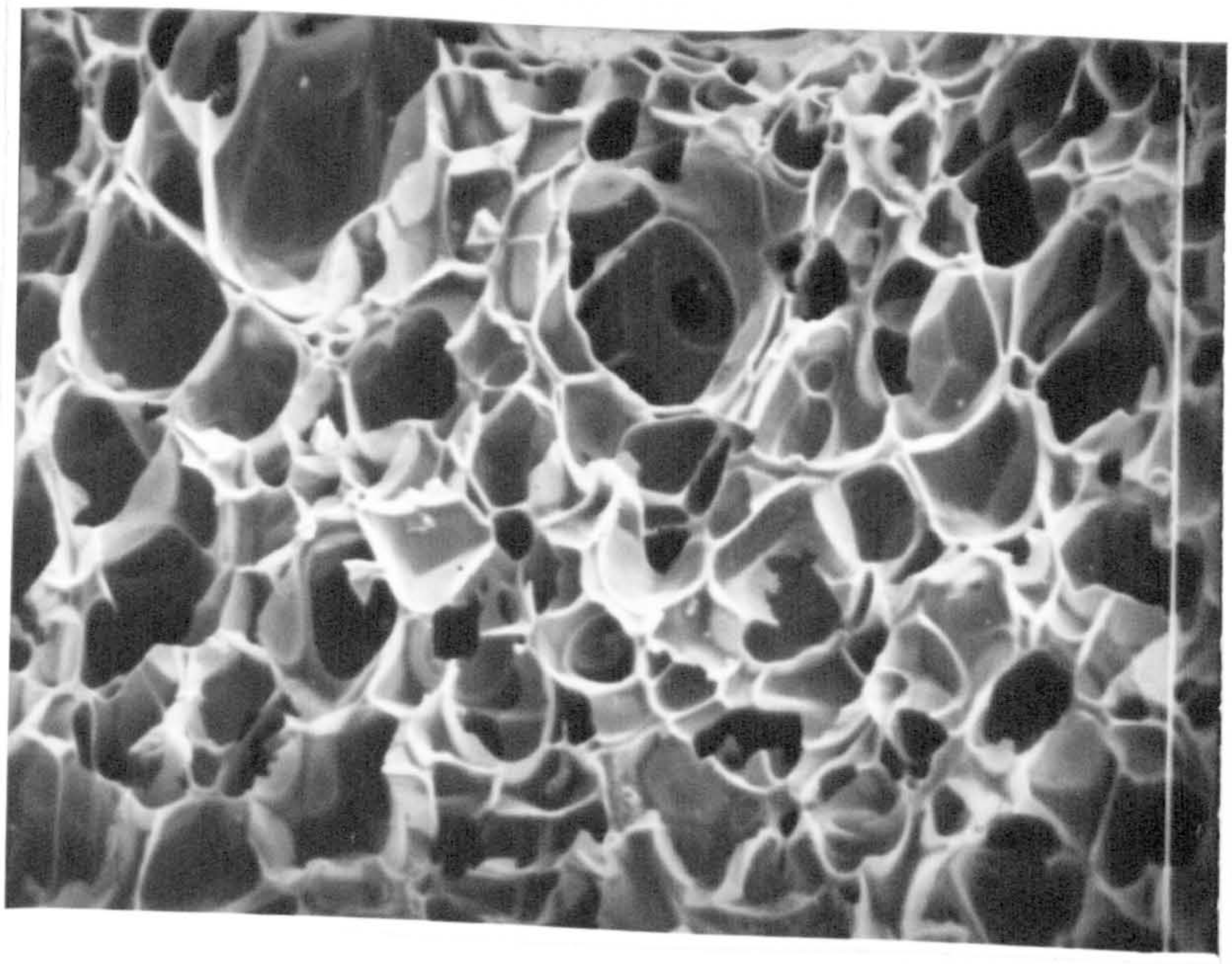

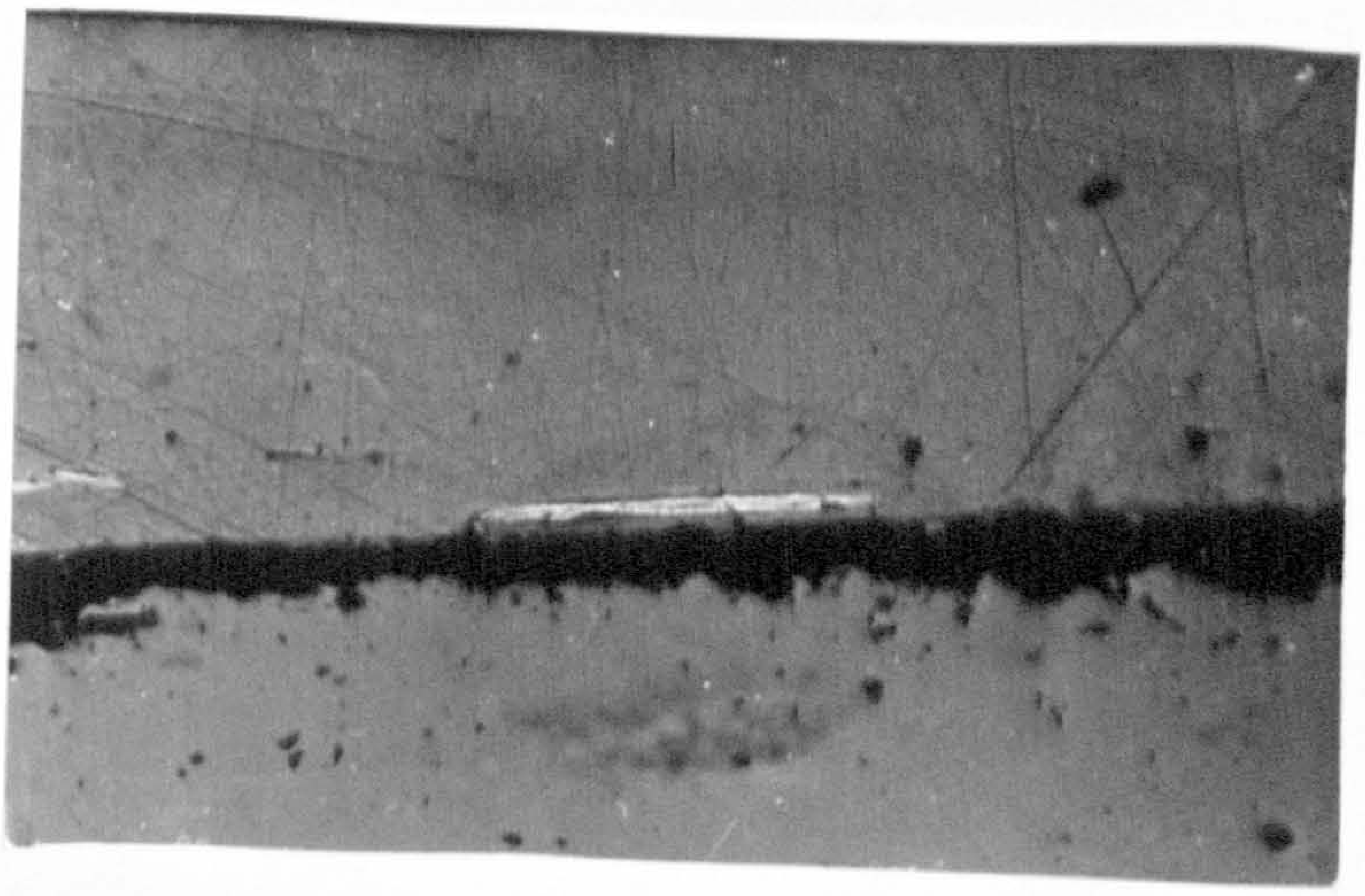

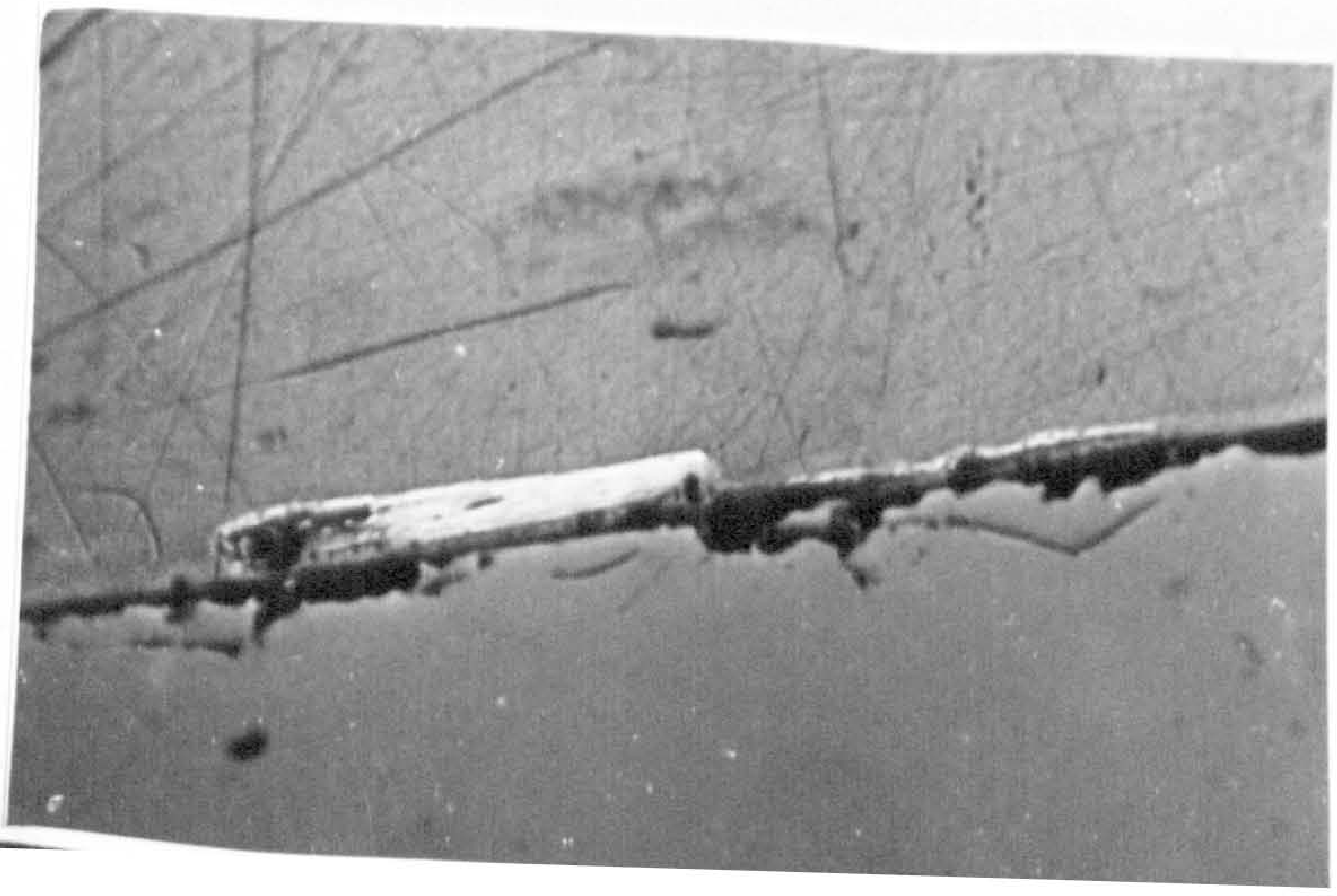

Composite containing
80% Mgo + 20% graphite A
at n=0.4

Composite containing
80% Mgo + 20% graphite B
at n=0.4

Composite containing
80% Mgo + 20% graphite C
at n=0.4

Composite containing
80% Mgo + 20% graphite D
at n=0.4

PLATES 4.4.3 i(a): Photomicrographs showing the texture of composites containing equal amounts of different types of graphite at fixed n-value of 0.4. The composites were formulated by using Method 1 (see section 4.2.2(i)).

The polished surfaces shown in these micrographs are those surfaces perpendicular to the direction of pressing.

MAGNIFICATION = 84x

N.B Notice the similarity of the microstructure

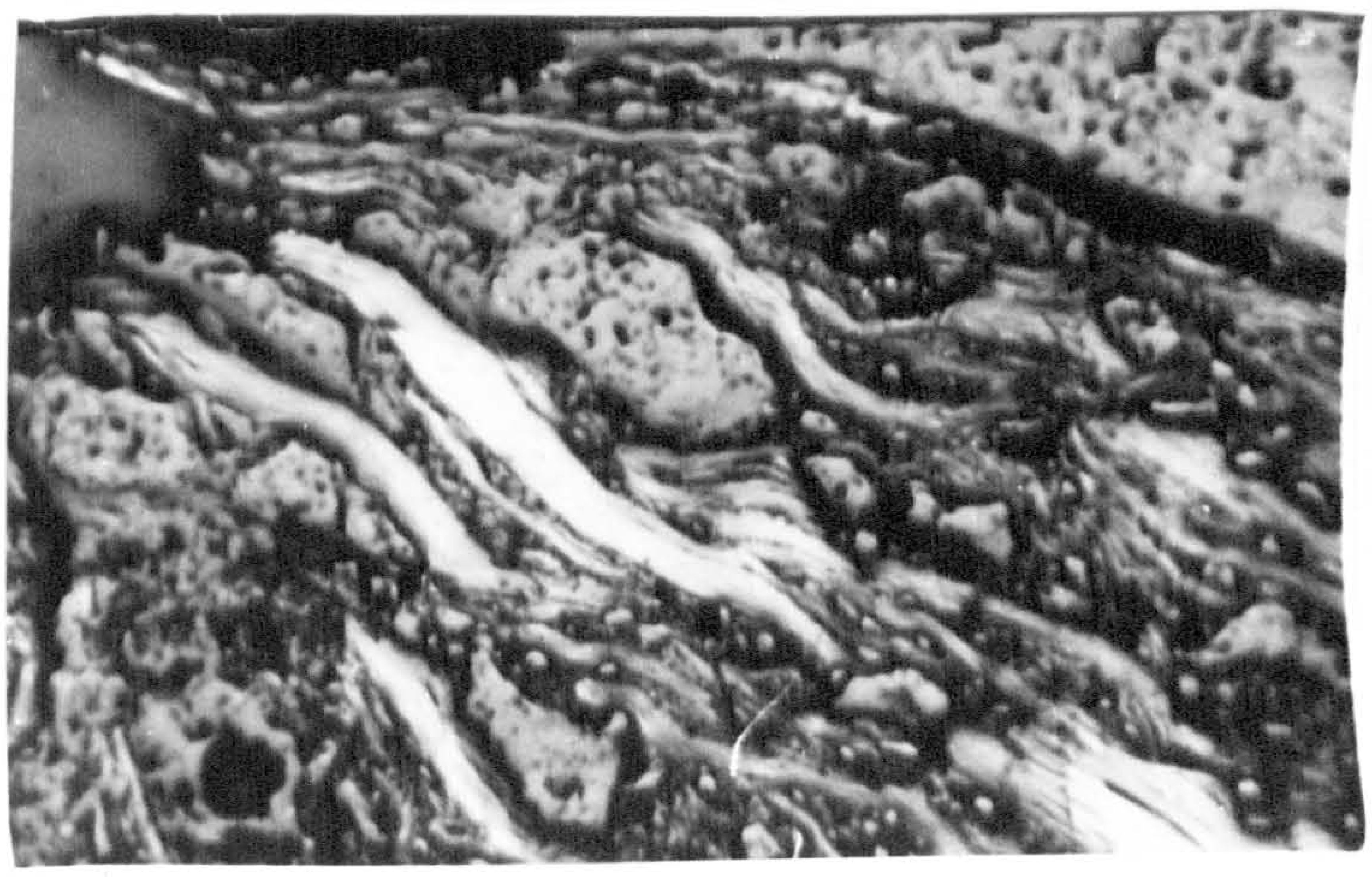

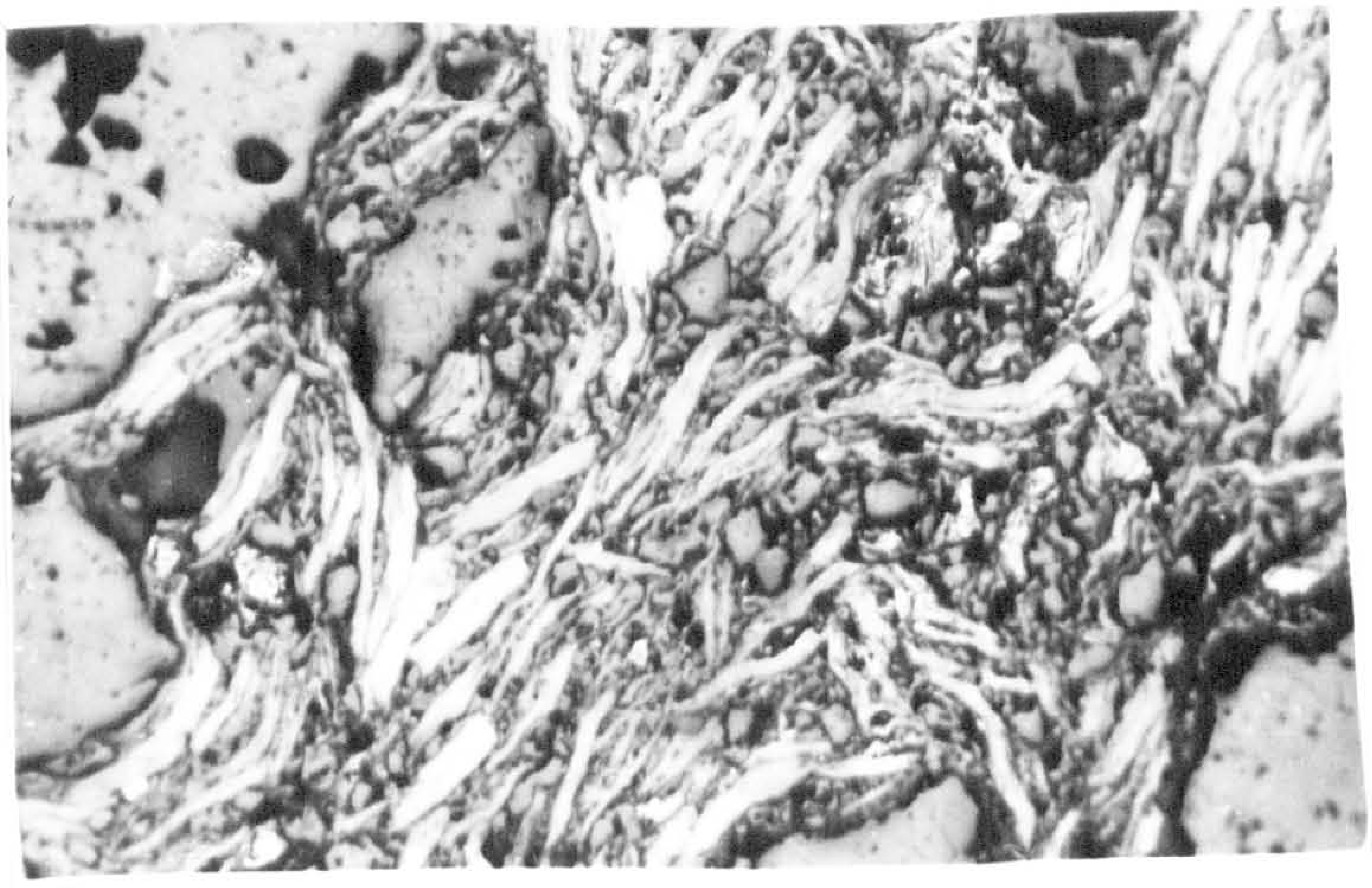

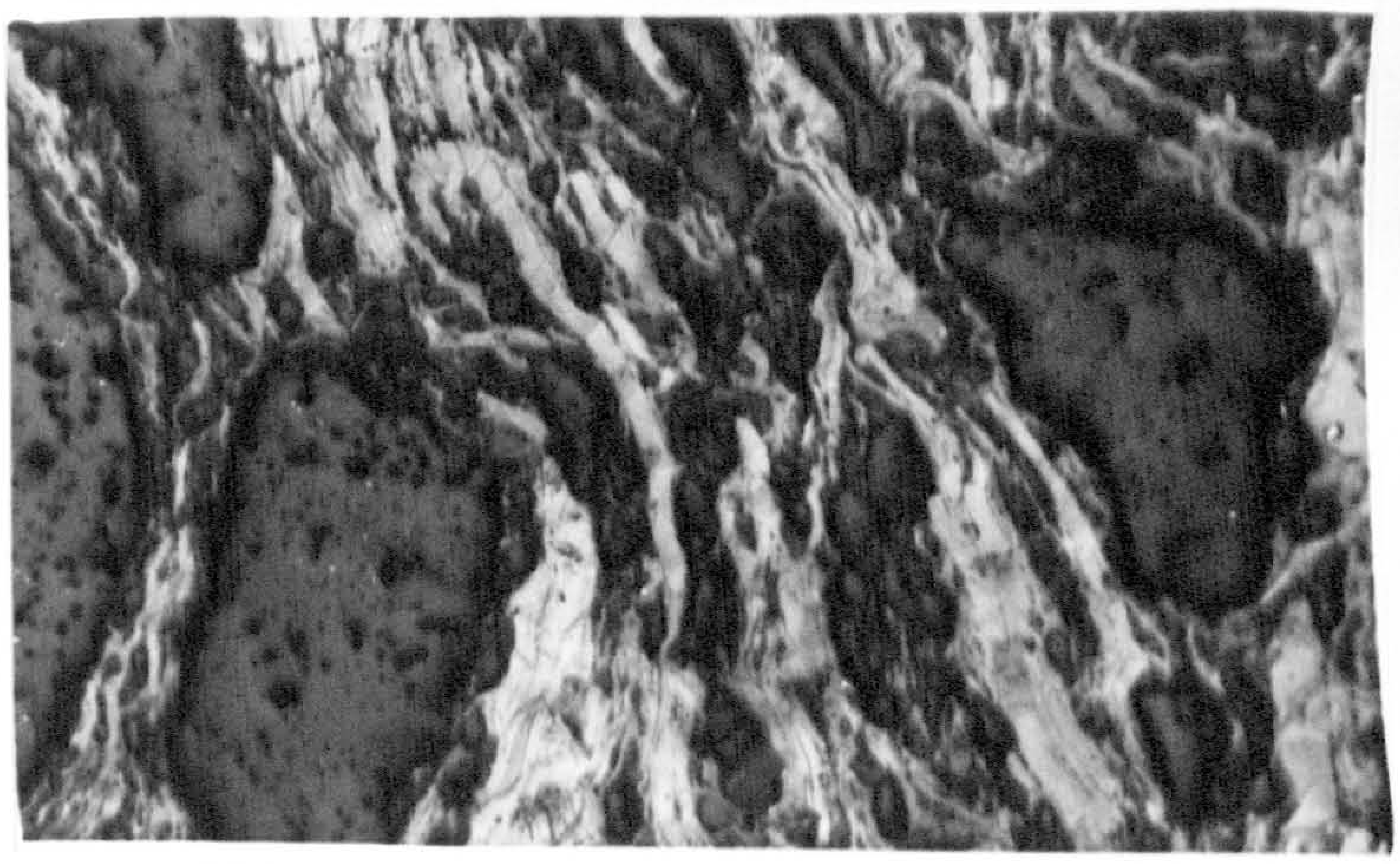

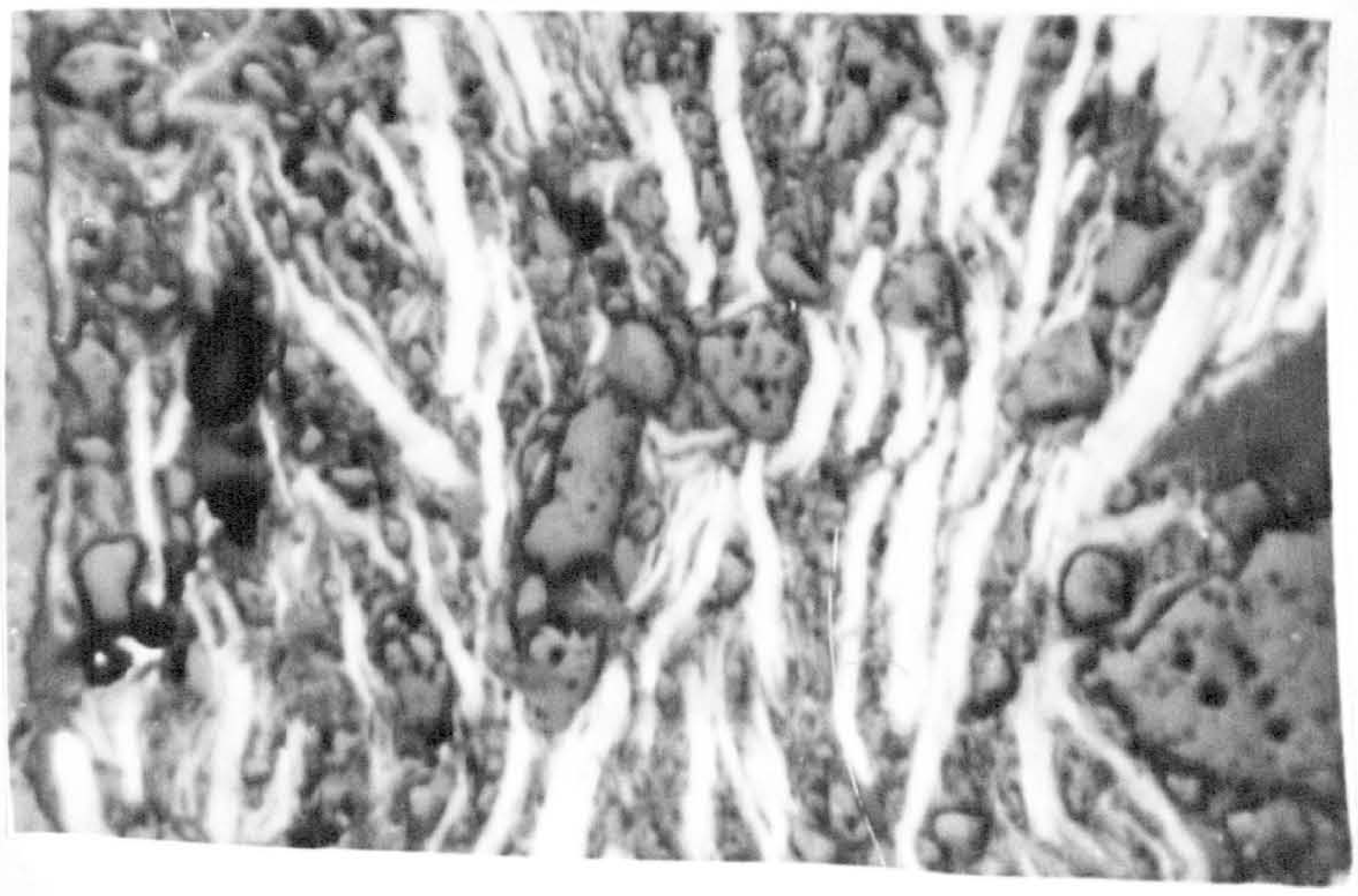

Composite containing
80% Mgo + 20% graphite D
at n=0.4

Composite containing
80% Mgo + 20% graphite D
at n=0.6

Composite containing
80% Mgo + 20% graphite D
at n=1.0

PLATES 4.4.3 i(b): Photomicrographs of composites containing equal amounts of the same graphite but of varying n-value showing the microstructural texture variation as n-value changes. The composites were constituted by Method 1.

The polished surfaces shown in these micrographs are those surfaces perpendicular to the direction of pressing.

MAGNIFICATION = 84x

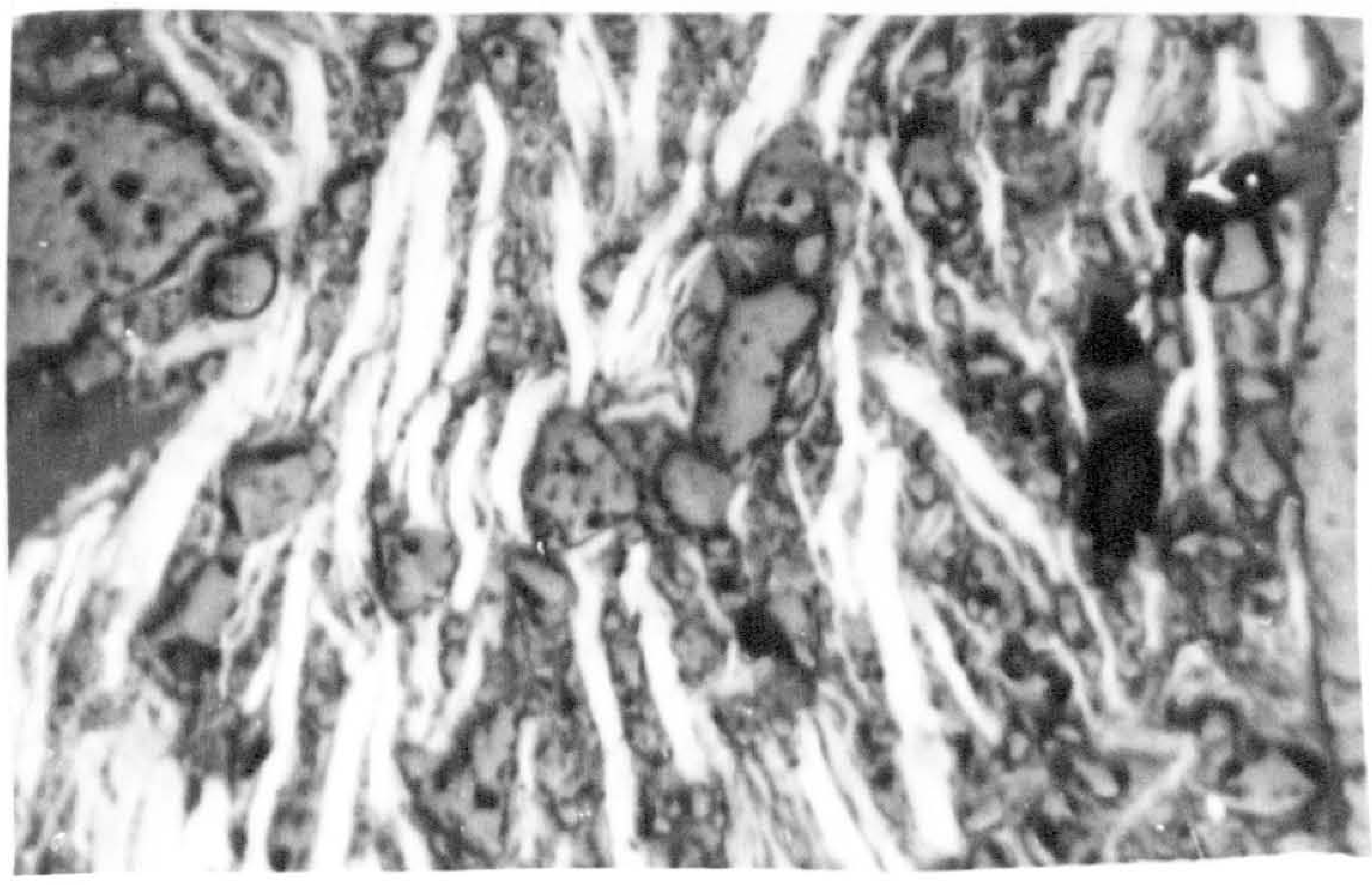

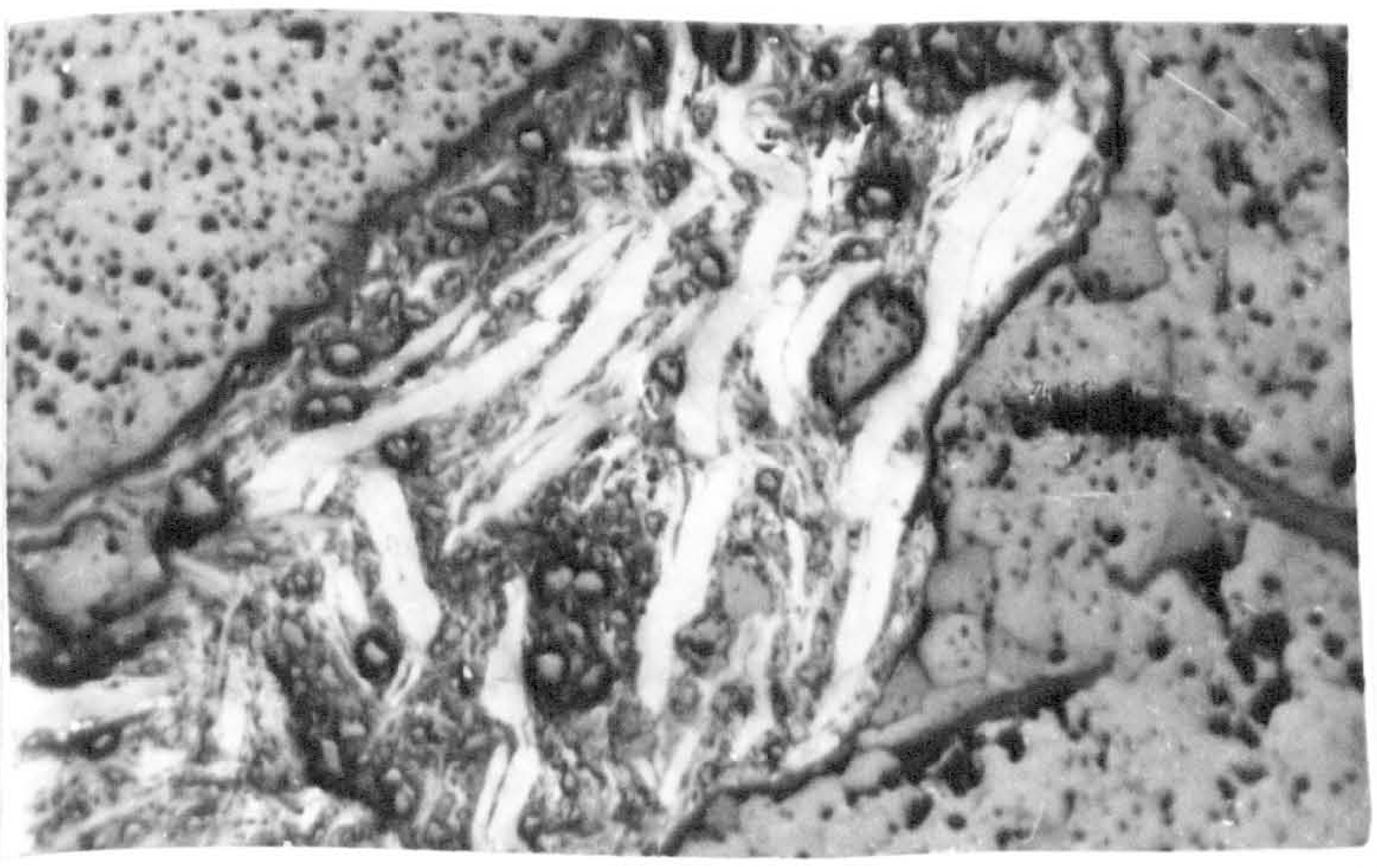

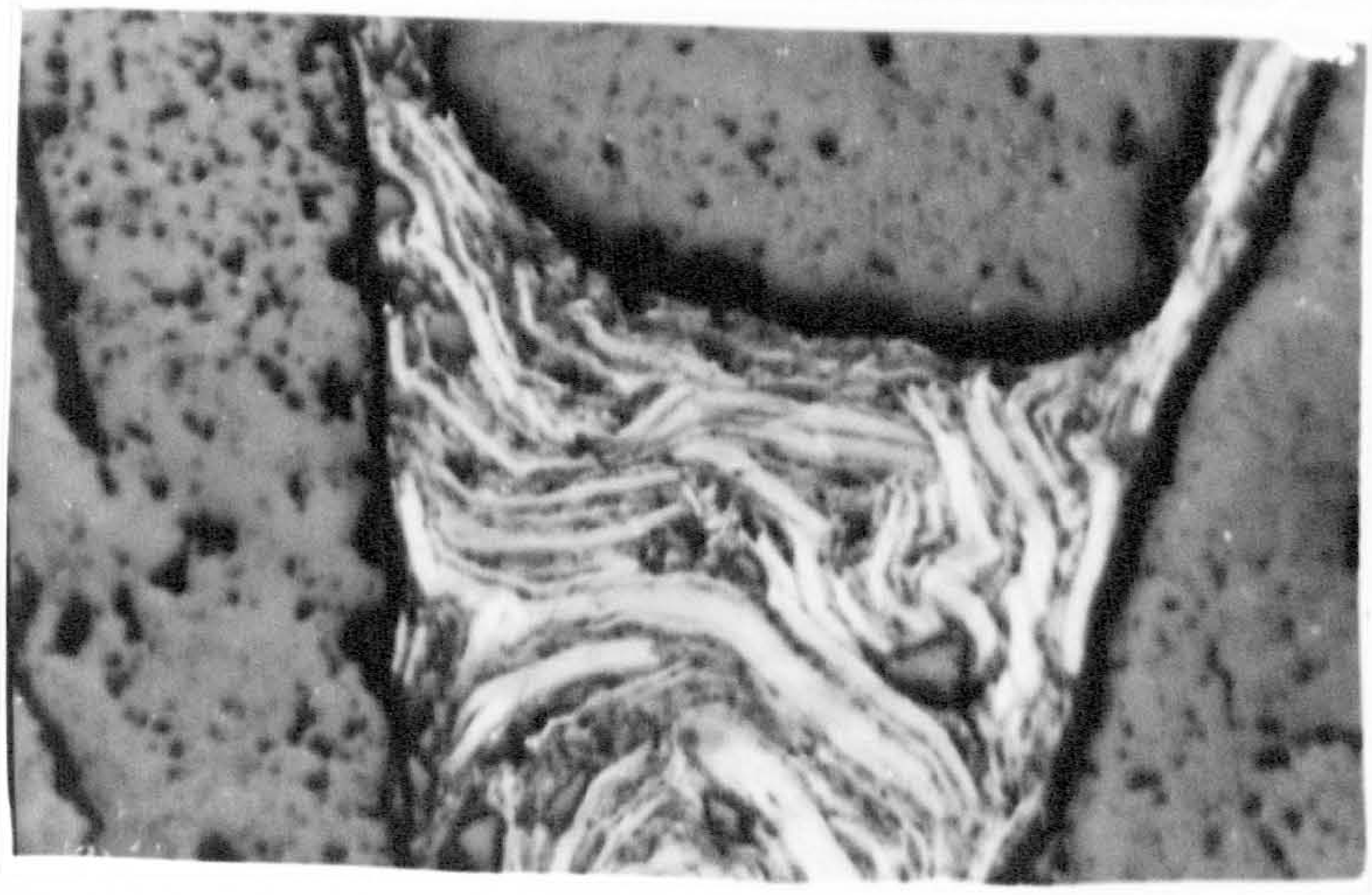

Composite containing
60.62% Mgo + 39.38% graphite A
at n=0.3

Composite containing
78.84% Mgo + 21.16% graphite A
at n=0.5

Composite containing
88.63% Mgo + 11.37% graphite A
at n=0.7

PLATES 4.4.3(ii): These photomicrographs show the microstructural changes as n-value changes. Method 2 was used in compounding these composites and in this Method the graphite content varies with n-value (see section 4.4.3 (ii))

MAGNIFICATION = 84x

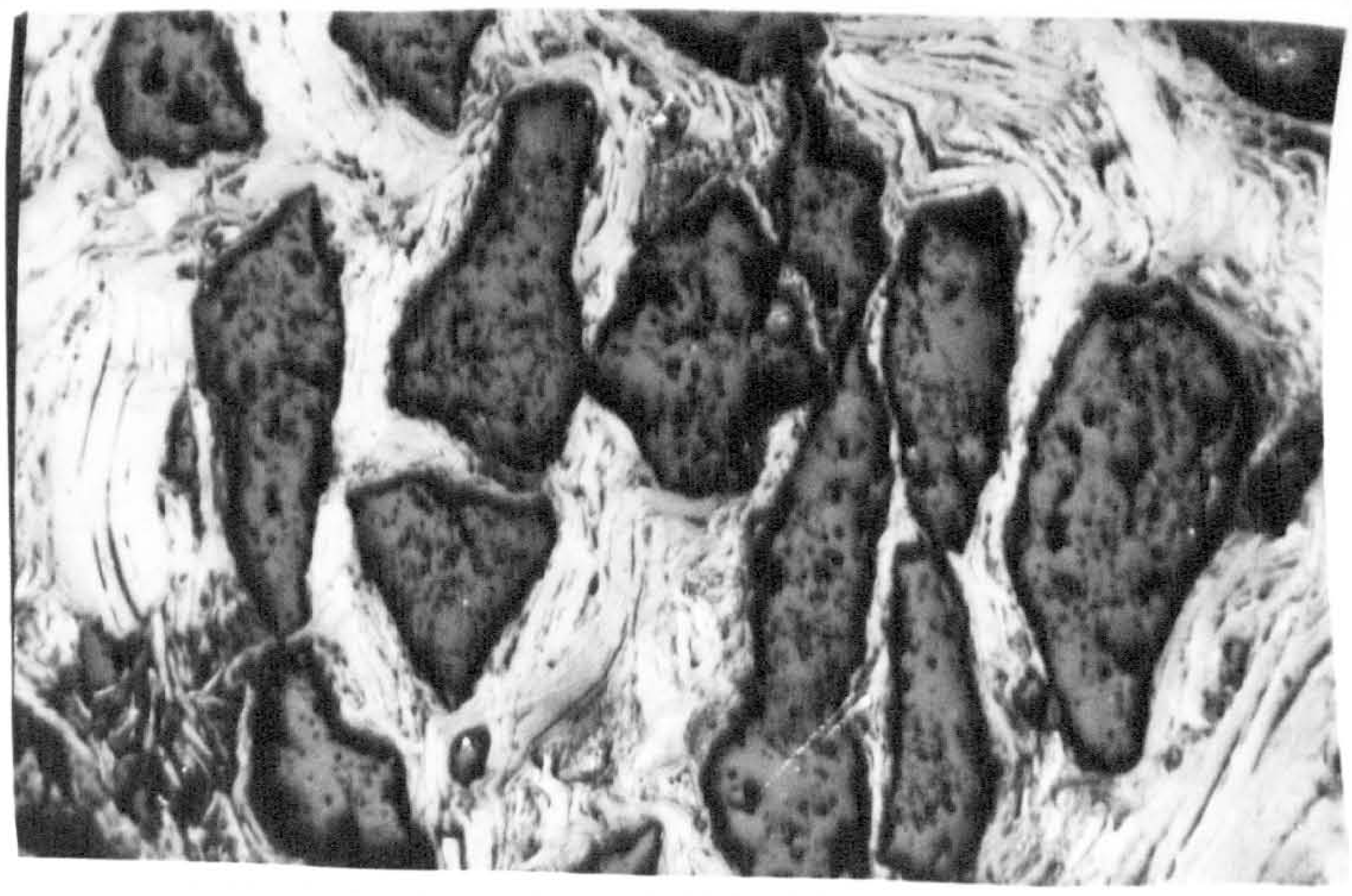

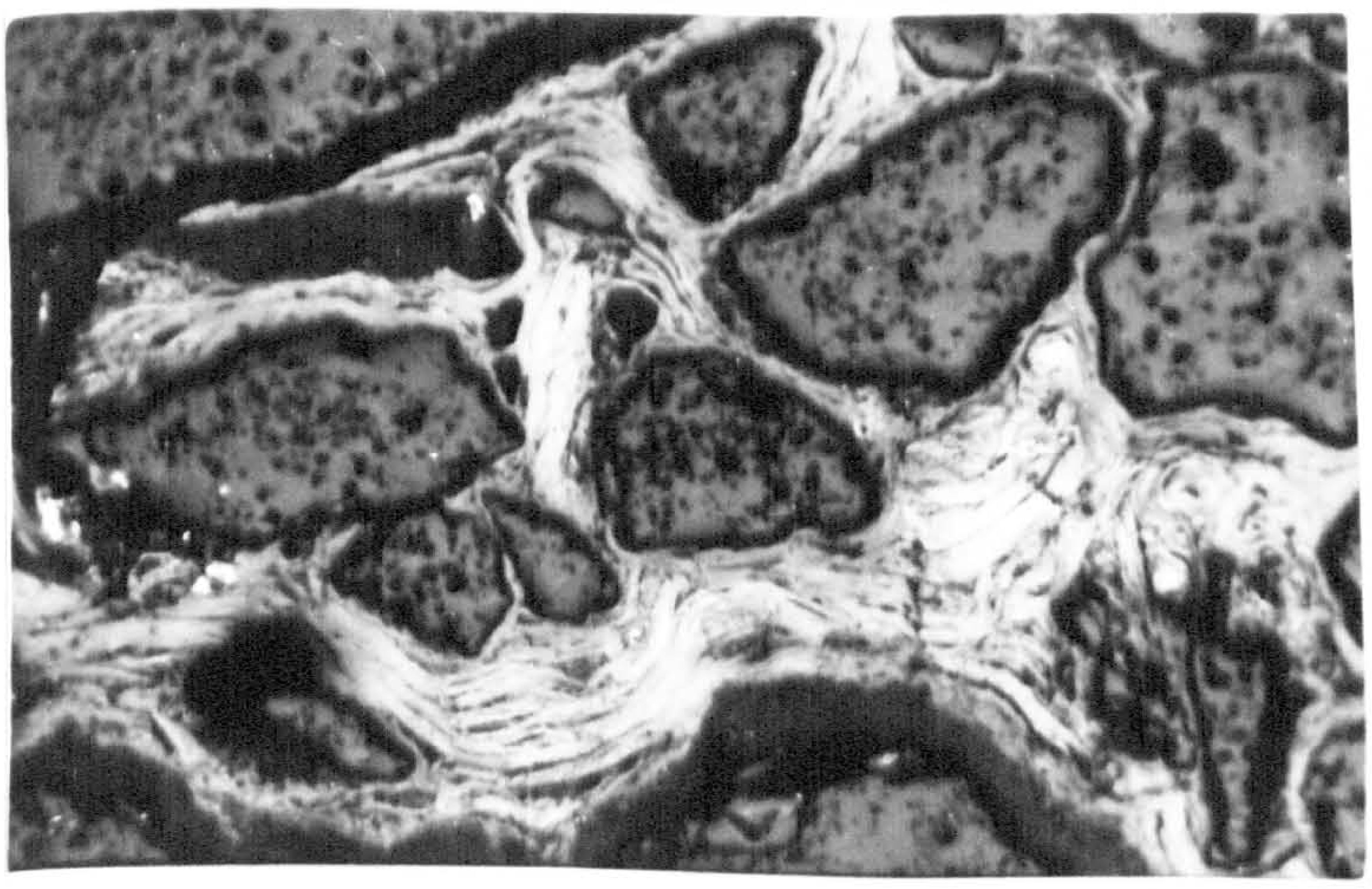

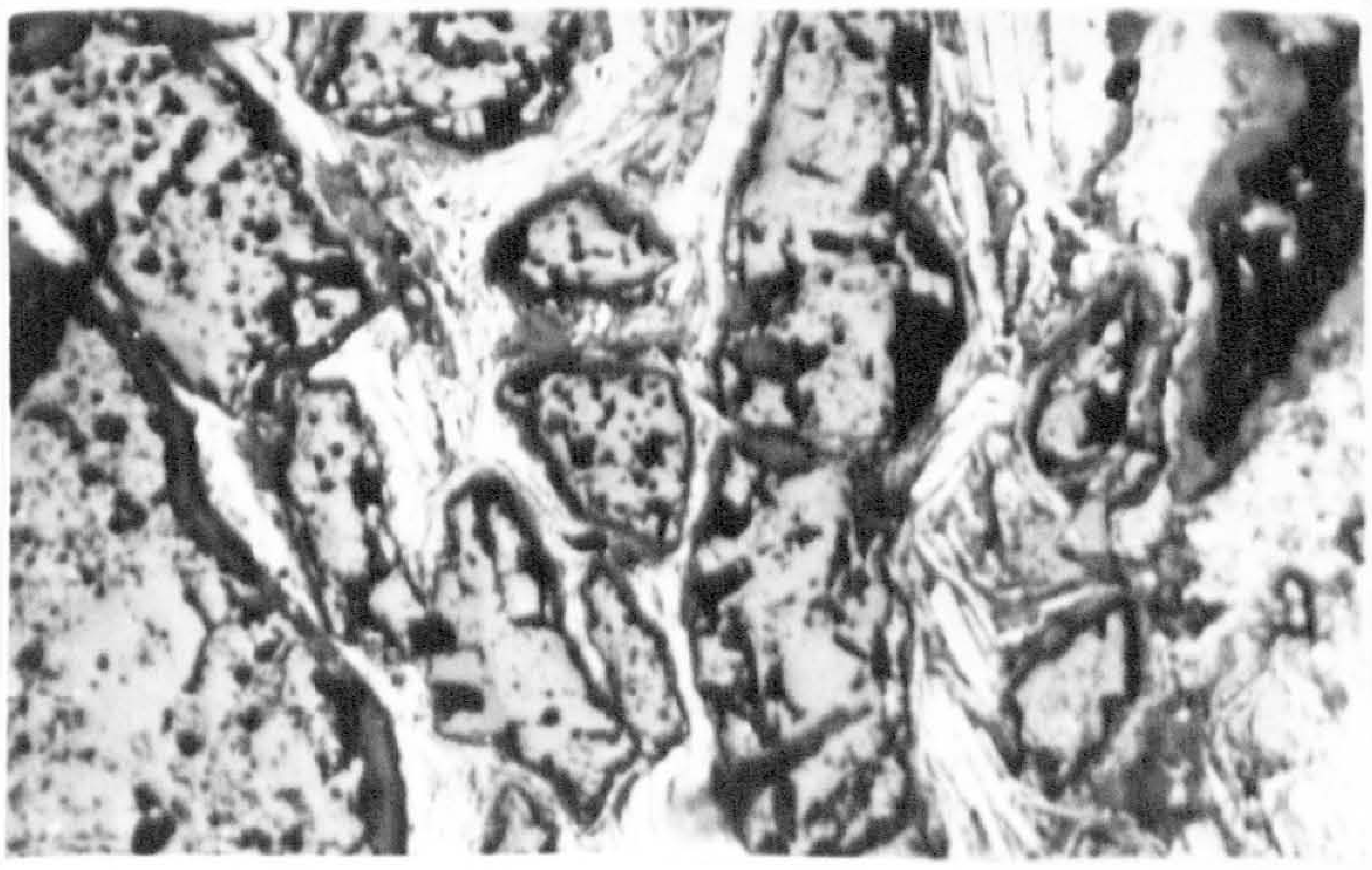

PLATE 4.4.3 iii(a): Composite containing 80% Mgo + 20% graphite B constituted by Method 3 at n=0.3. The surface shown in this micrograph is that perpendicular to the direction of pressing.

PLATE 4.4.3 iii(a) Composite containing 80% Mgo + 20% graphite B constituted by Method 3 at n=0.3. The surface shown in this micrograph is that normal to the direction of pressing.

PLATE 4.4.3 iii(b): Composite containing 80% Mgo + 20% graphite B constituted by Method 3 at n=0.5. The surface shown in this micrograph is that perpendicular to the direction of pressing.

PLATE 4.4.3 iii(b): Composite containing 80% Mgo + 20% graphite B constituted by Method 3 at n=0.5. The surface shown in this micrograph is that normal to the direction of pressing.

PLATES 4.4.3 iii(a & b) above show the texture variation of the composites, constituted by Method 3 and containing the same amount of graphite B, as n-value varies. Two micrographs are presented for each n-value to illustrate the change in the orientation of the graphite flakes normal and perpendicular to the pressing direction.
MAGNIFICATION = 84x

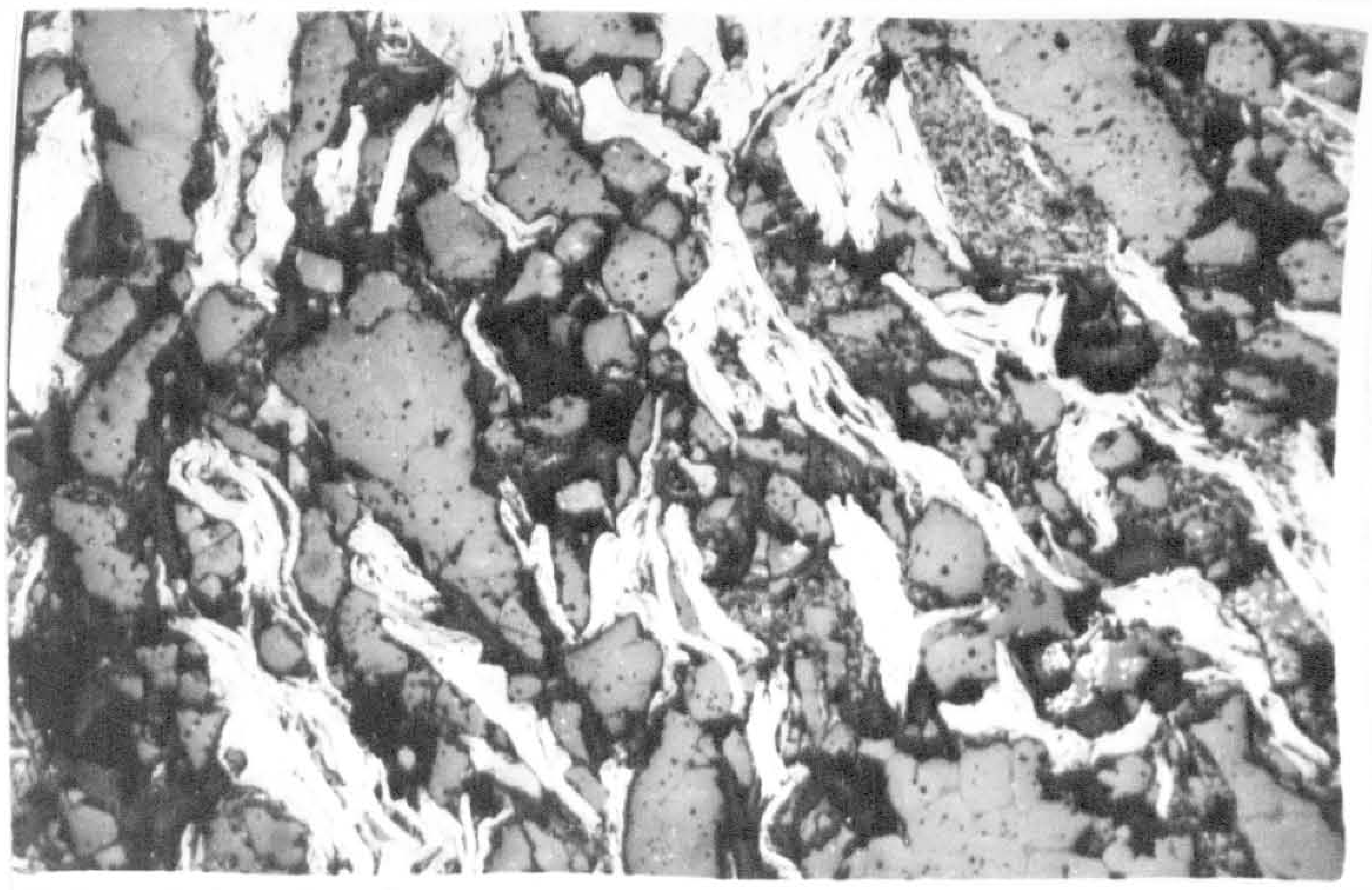

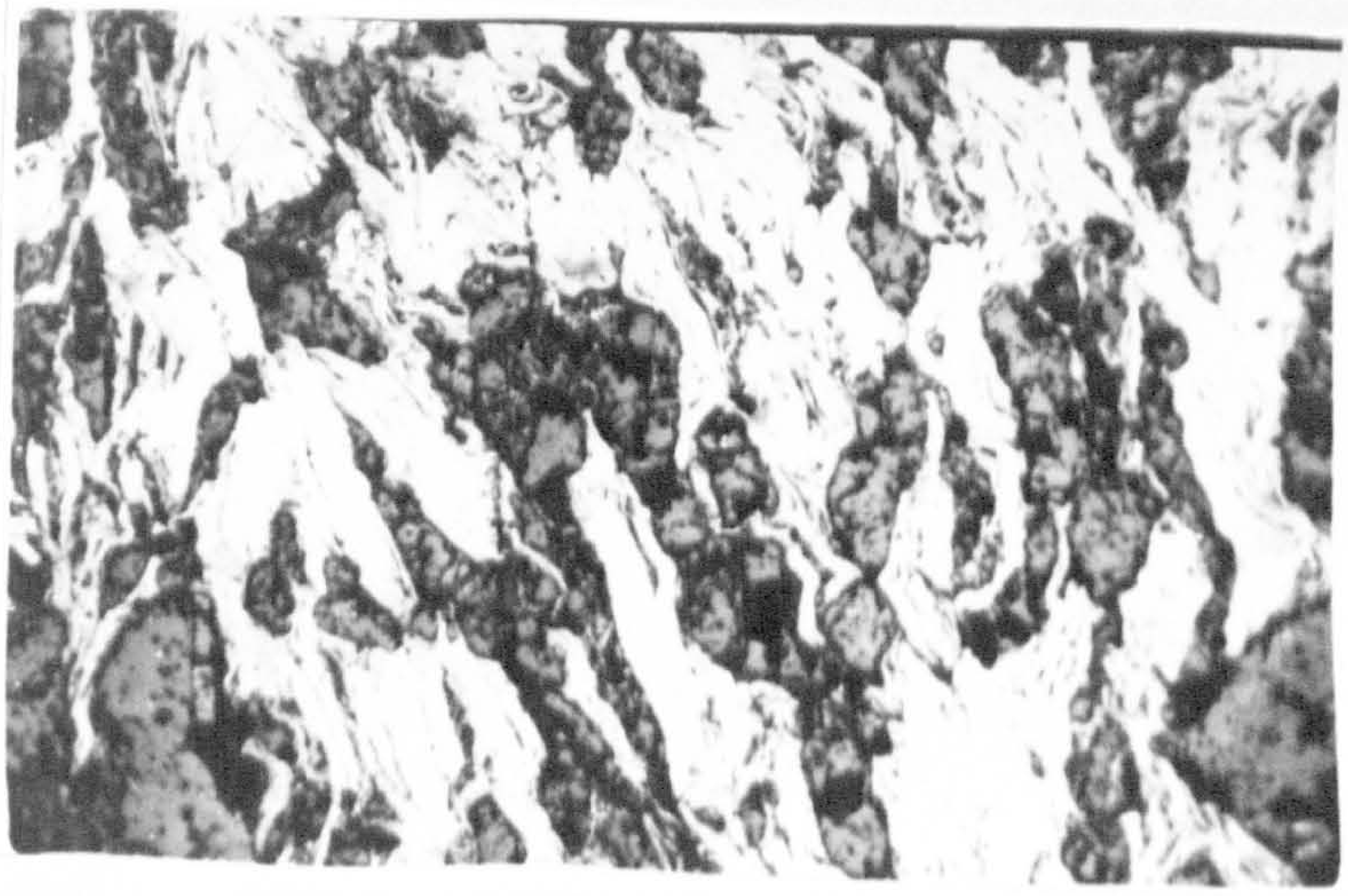

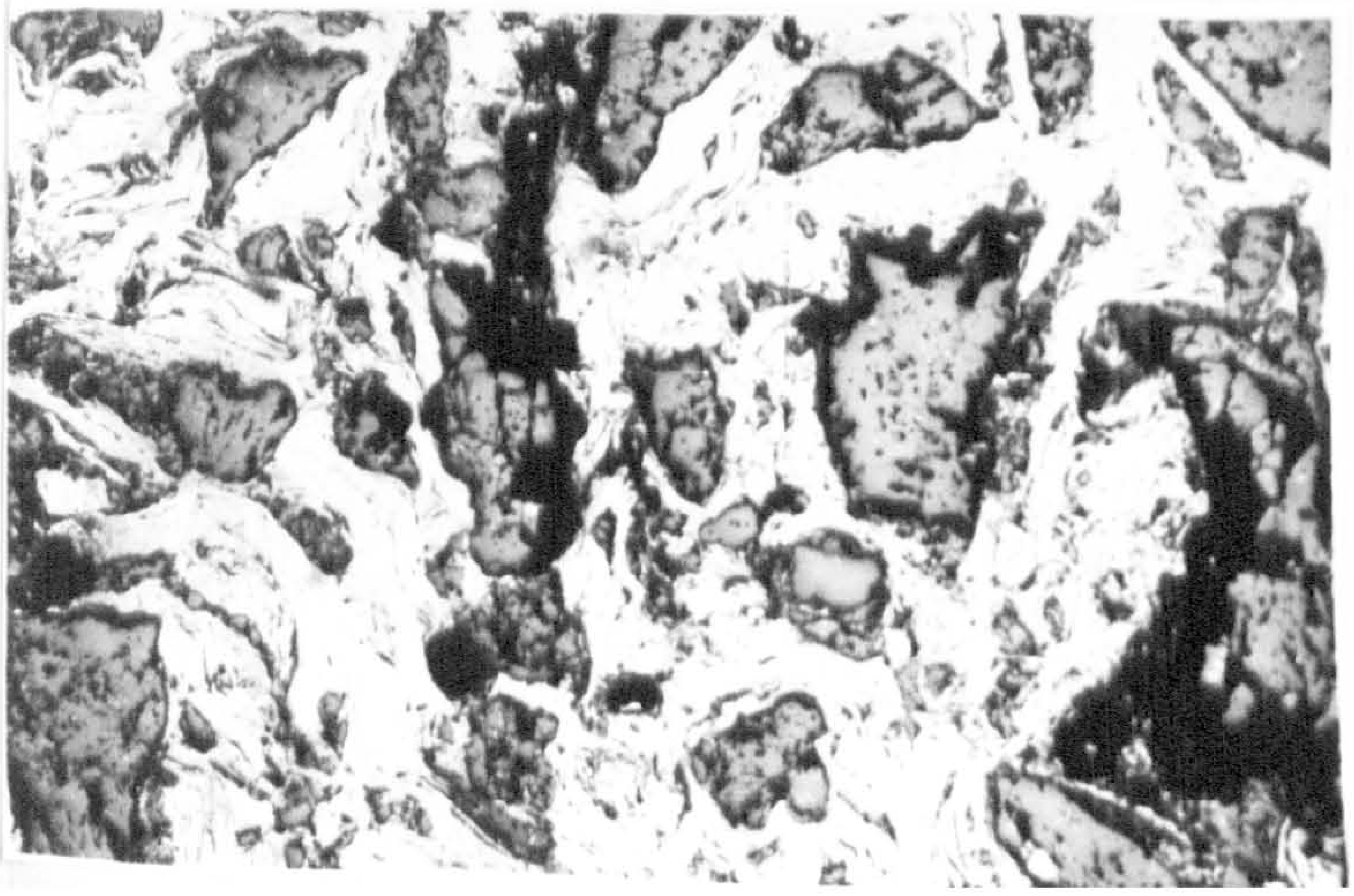

PLATE 4.4.3 iii(c): Composite containing 80% Mgo + 20% graphite B constituted by Method 3 at n=1.0. The surface shown in this micrograph is that perpendicular to the direction of pressing.

PLATE 4.4.3 iii(c): Composite containing 80% Mgo + 20% graphite B constituted by Method 3 at n=1.0. The surface shown in this micrograph is that normal to the direction of pressing.

MAGNIFICATION = 84x

PLATE 4.4.3 iii(d): This Plate shows the texture of a composite(n=0.3) containing the same amount of graphite as those shown in Plates 4.4.3 iii(a - c), but graphite D has been used instead. This photomicrograph has been included to illustrate that there is no textural difference between composites containing the same level of graphite but of different types for the same fabrication conditions. (Compare this Plate to Plate 4.4.3iii(a))

PLATE 4.4.3 iii(d): Composite containing 80% Mgo + 20% graphite D constituted by Method 3 at n=0.3. The surface shown in this micrograph is that normal to the direction of pressing.

MAGNIFICATION = 84x

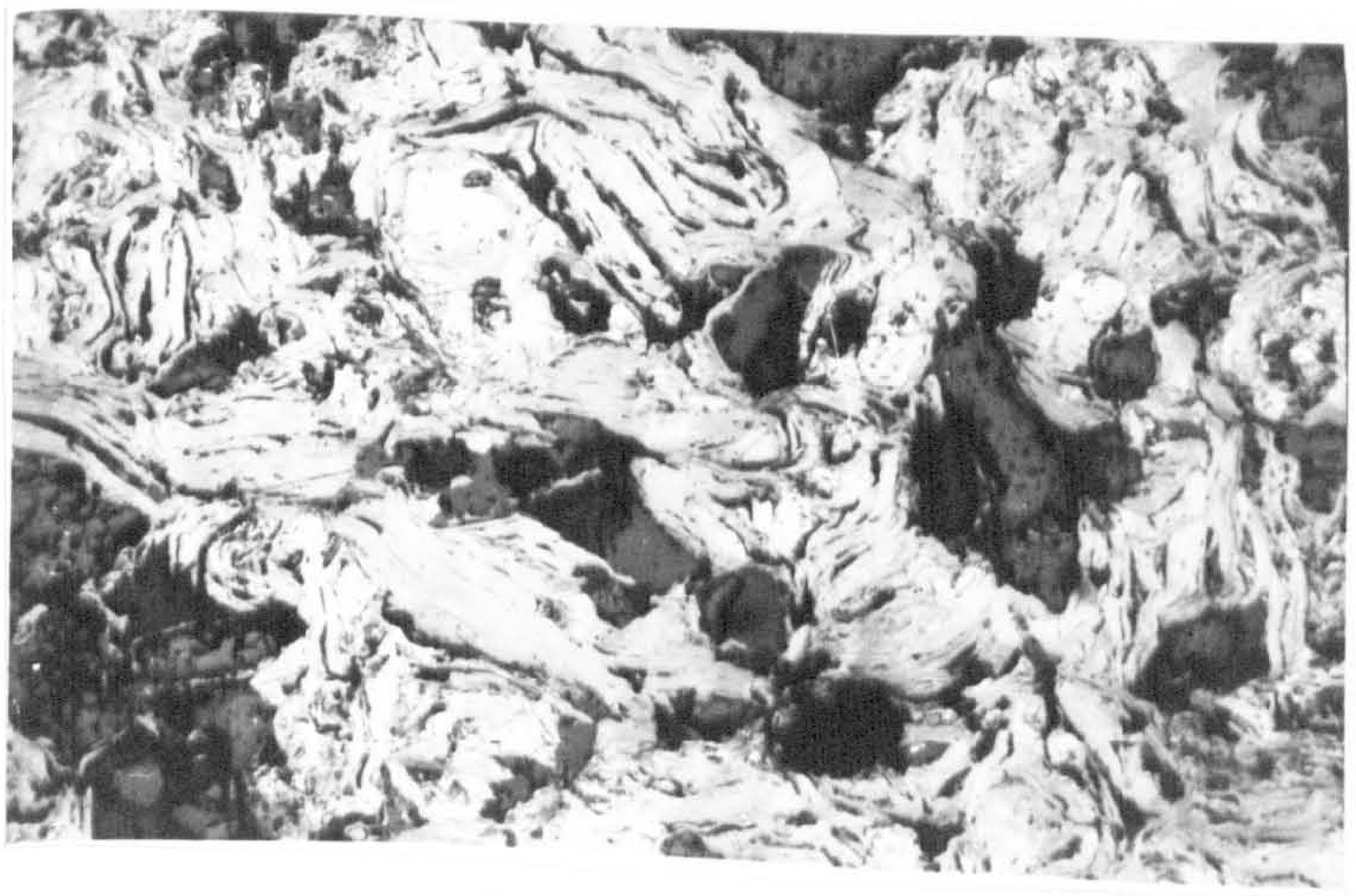

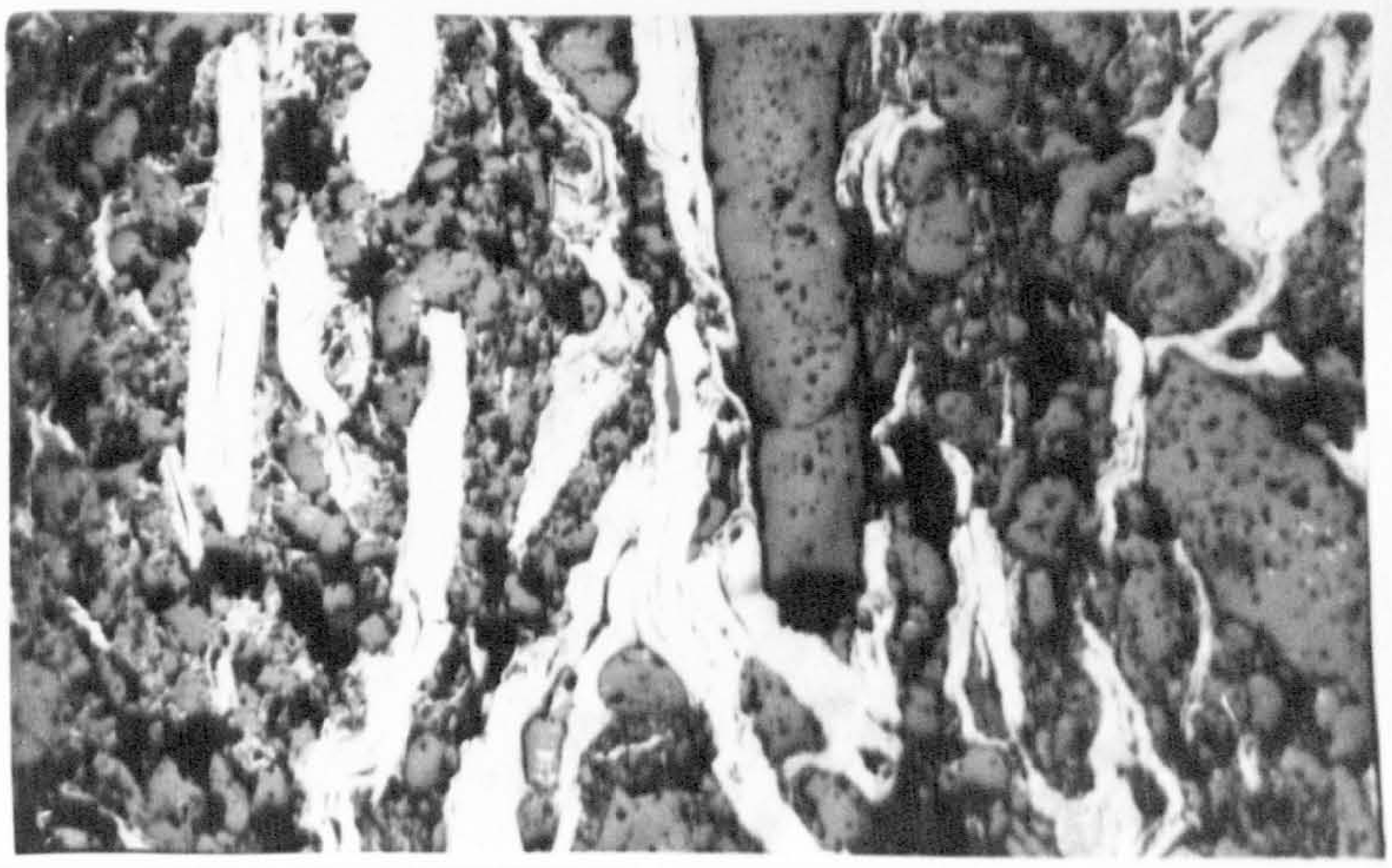

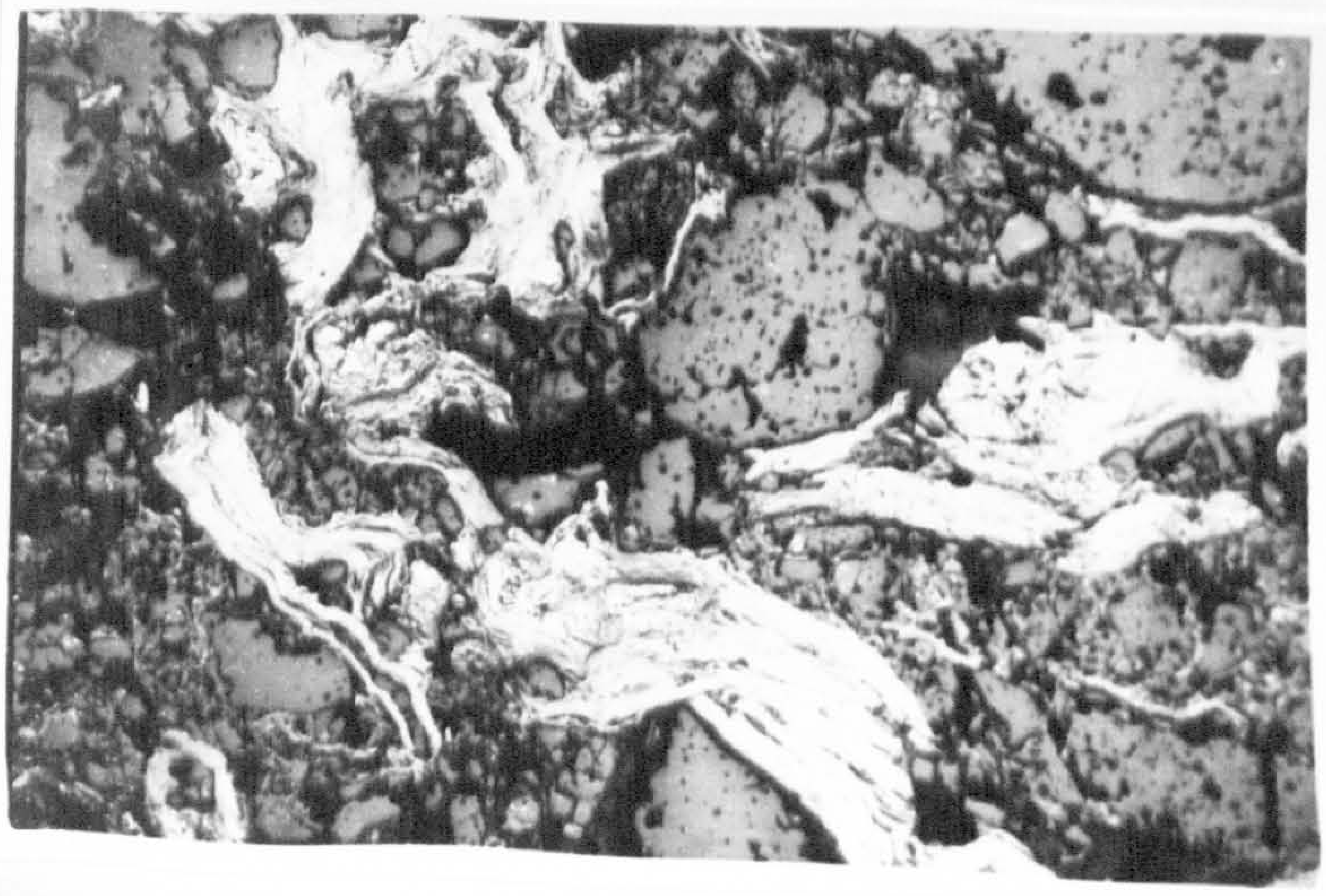

PLATE 5.5.2(a): S.E.M micrograph showing a fractured surface of a specimen containing 100 parts Mgo + 5 parts pitch. The micrograph shows that the Mgo grains are completely covered in pitch coke. There is no evidence of bonding between Mgo grains.

MAGNIFICATION = 222x

PLATE 5.5.2(b): S.E.M micrograph of pitch coke, coked at 1500°C. The shrinkage cracks of the pitch coke are similar to those in Plate 5.5.2(a).

MAGNIFICATION = 890x

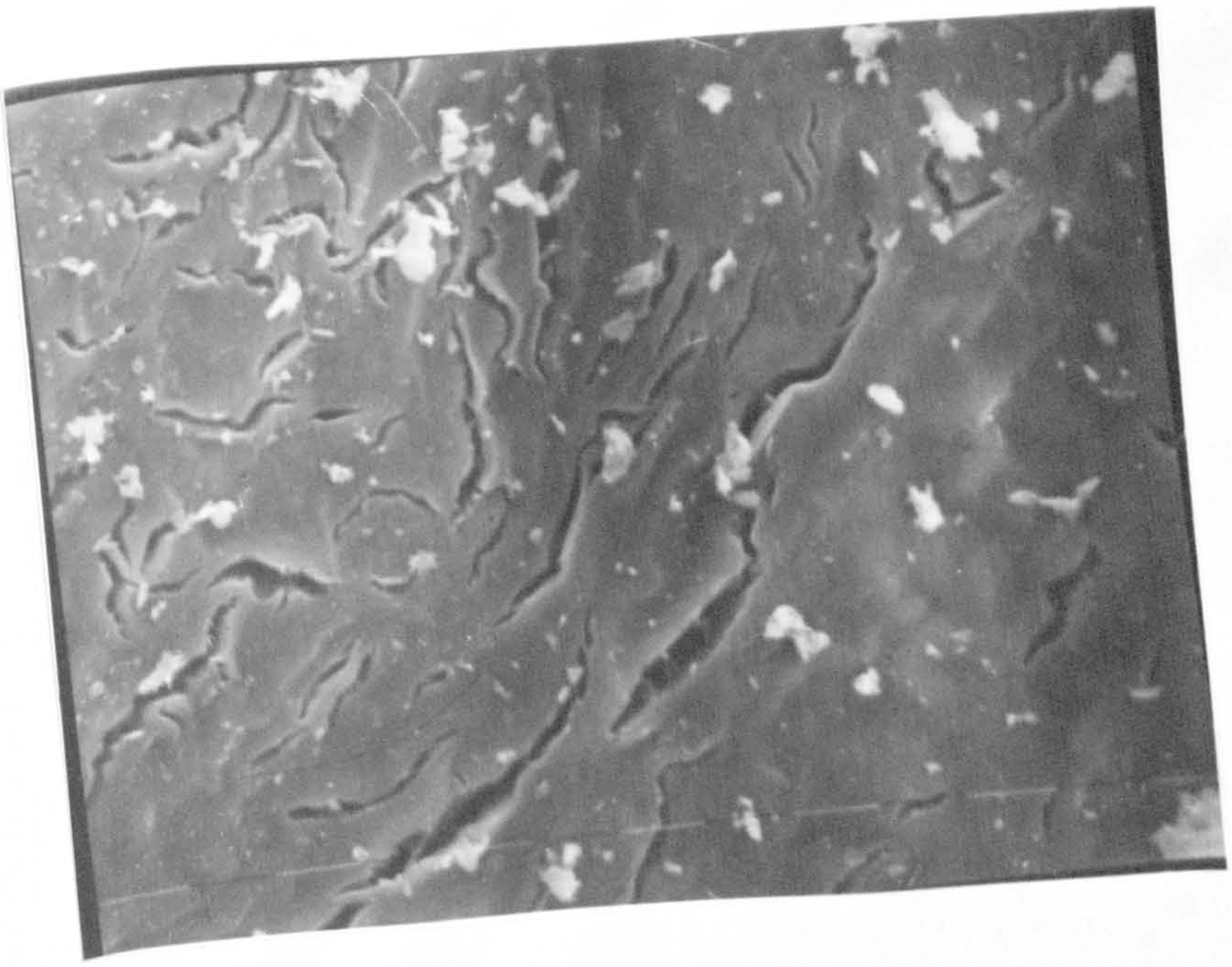

PLATE 5.5.3 i(a): Photomicrograph of a composite containing 80 parts Mgo + 10 parts graphite A + 5 parts pitch at n=0.3 showing that the flakes are dispersed in the matrix, mostly by fine Mgo grains. This surface shown here is the surface perpendicular to the pressing direction.

PLATE 5.5.3 i(b): The same composite as that shown in Plate 5.5.3 i(a) but the surface shown here is that normal to the pressing direction

MAGNIFICATION = 84x

PLATE 5.5.3 ii(a): Photomicrograph of a composite containing 80 parts Mgo + 10 parts graphite A + 5 parts pitch at n=0.5. The graphite-graphite contacts have increased compared with the same composite prepared at n=0.3 shown in Plate 5.5.3 i(a). The polished surface is perpendicular to the pressing direction.

PLATE 5.5.3 ii(b): The same composite as that shown in Plate 5.5.3 ii(a), but the surface shown here is that normal to the pressing direction

MAGNIFICATION = 84x

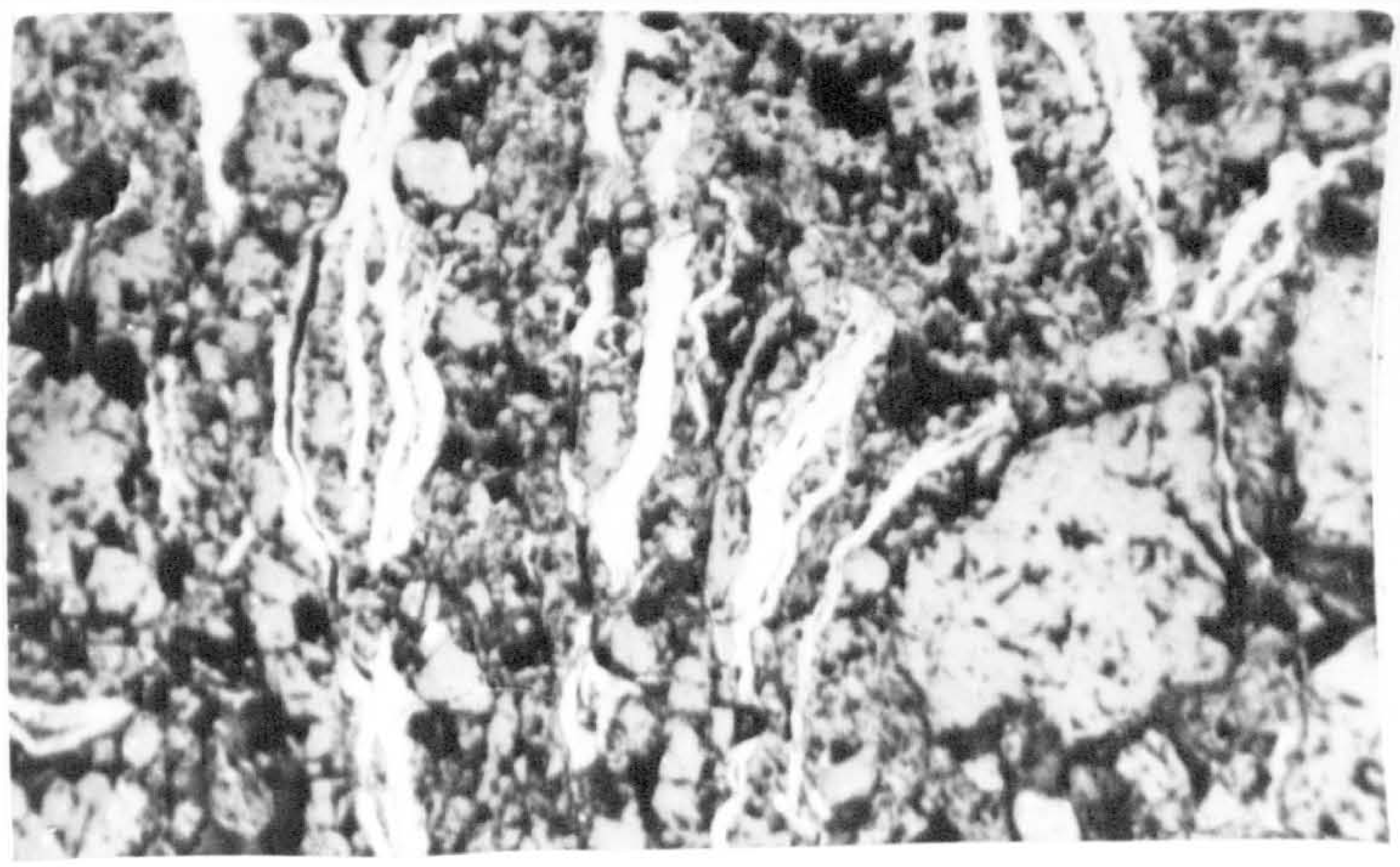

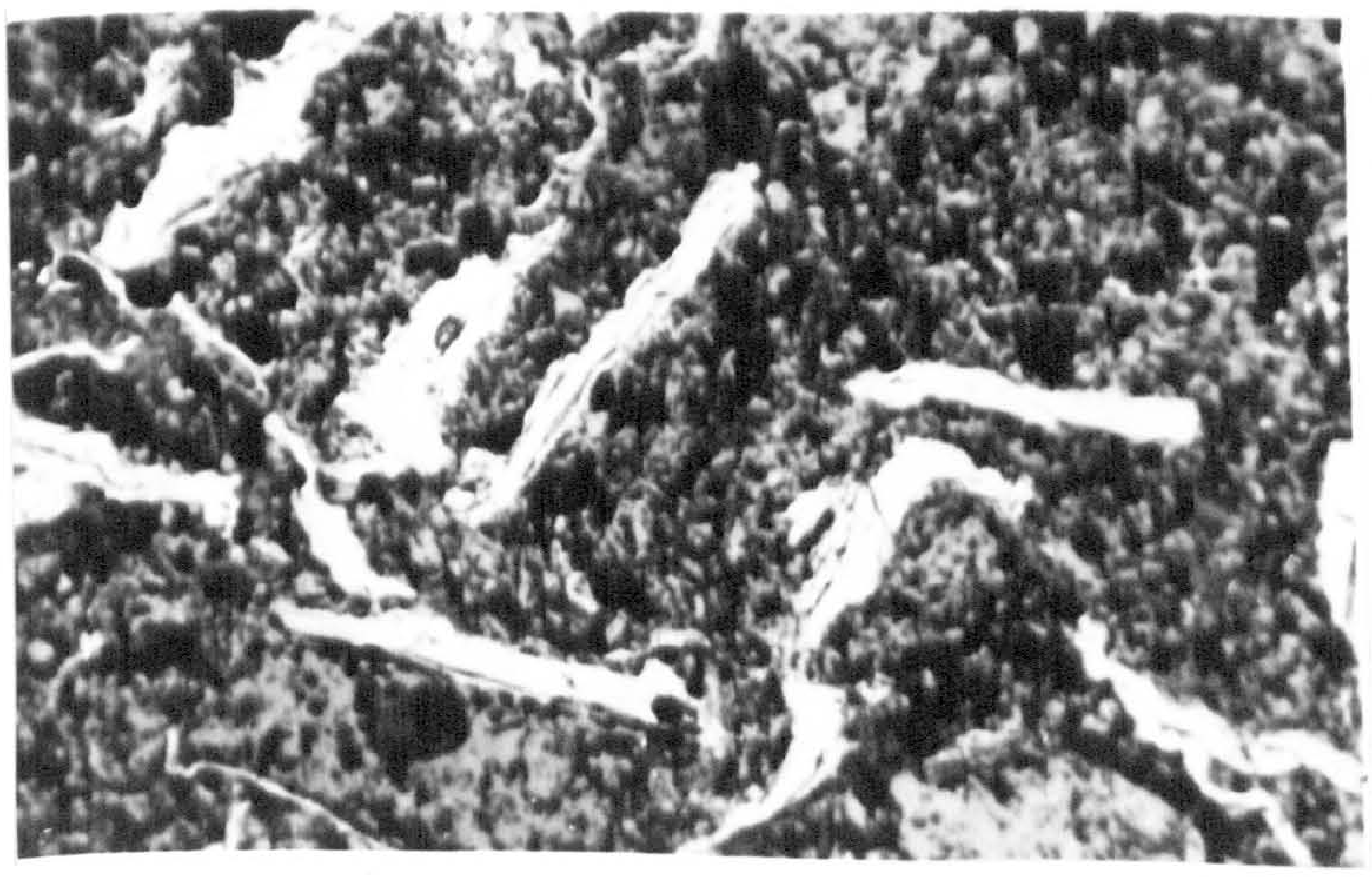

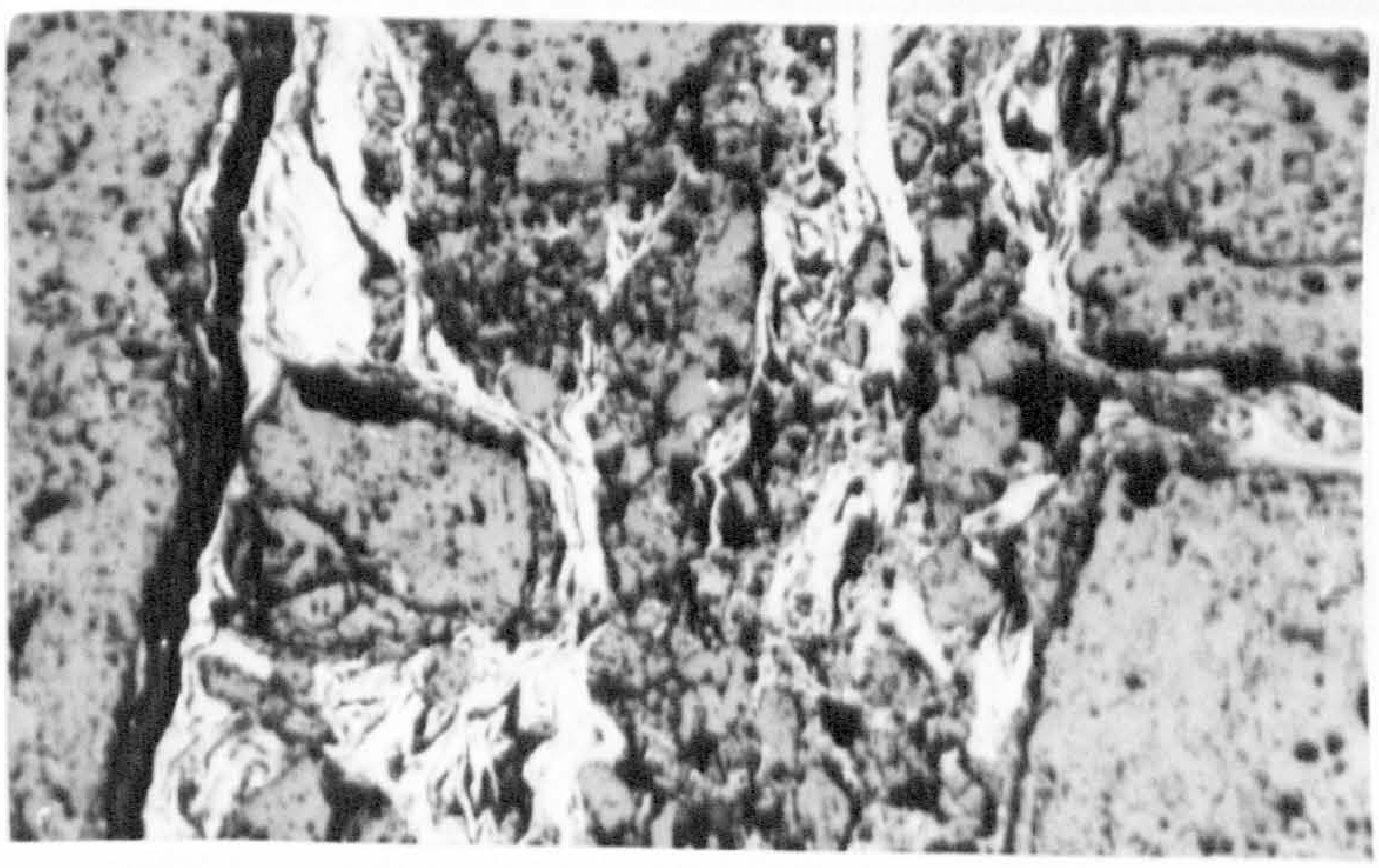

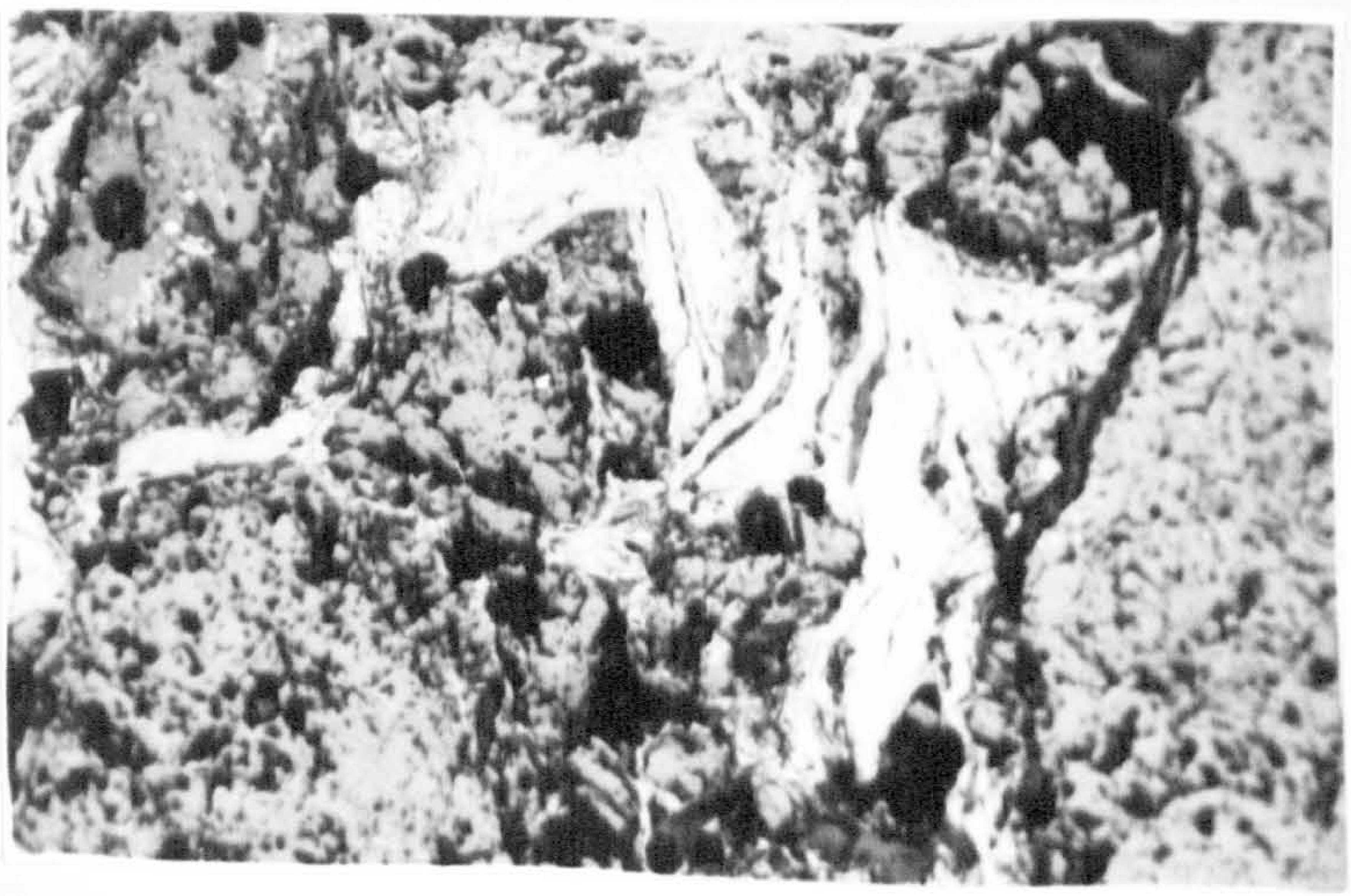

PLATE 5.5.3 iii(a): Photomicrograph of a composite containing 80 parts Mgo + 10 parts graphite A + 5 parts pitch at n=1.0. The graphite flakes now make a continuous matrix between the large Mgo grains.

The polished surface is normal to the pressing direction.

PLATE 5.5.3 iii(b): The same composite as that shown in iii(a) but the surface shown here is that ⊥ to the pressing direction

MAGNIFICATION = 84x

PLATE 5.5.3 iii(c) is a photomicrograph of the same composites as those indicated in the previous two Plates but showing another field of view on a surface normal to the pressing direction.

MAGNIFICATION = 84x

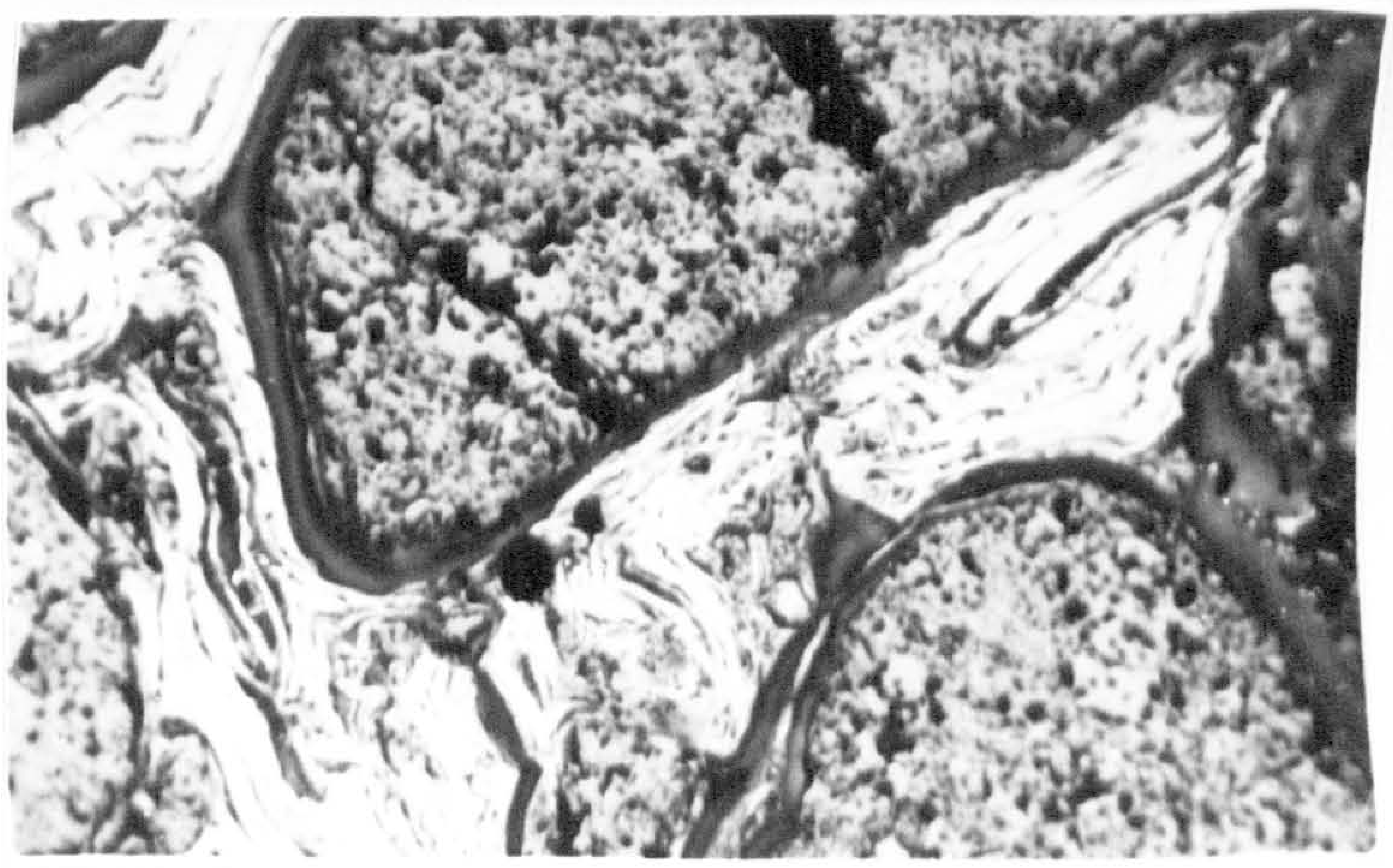

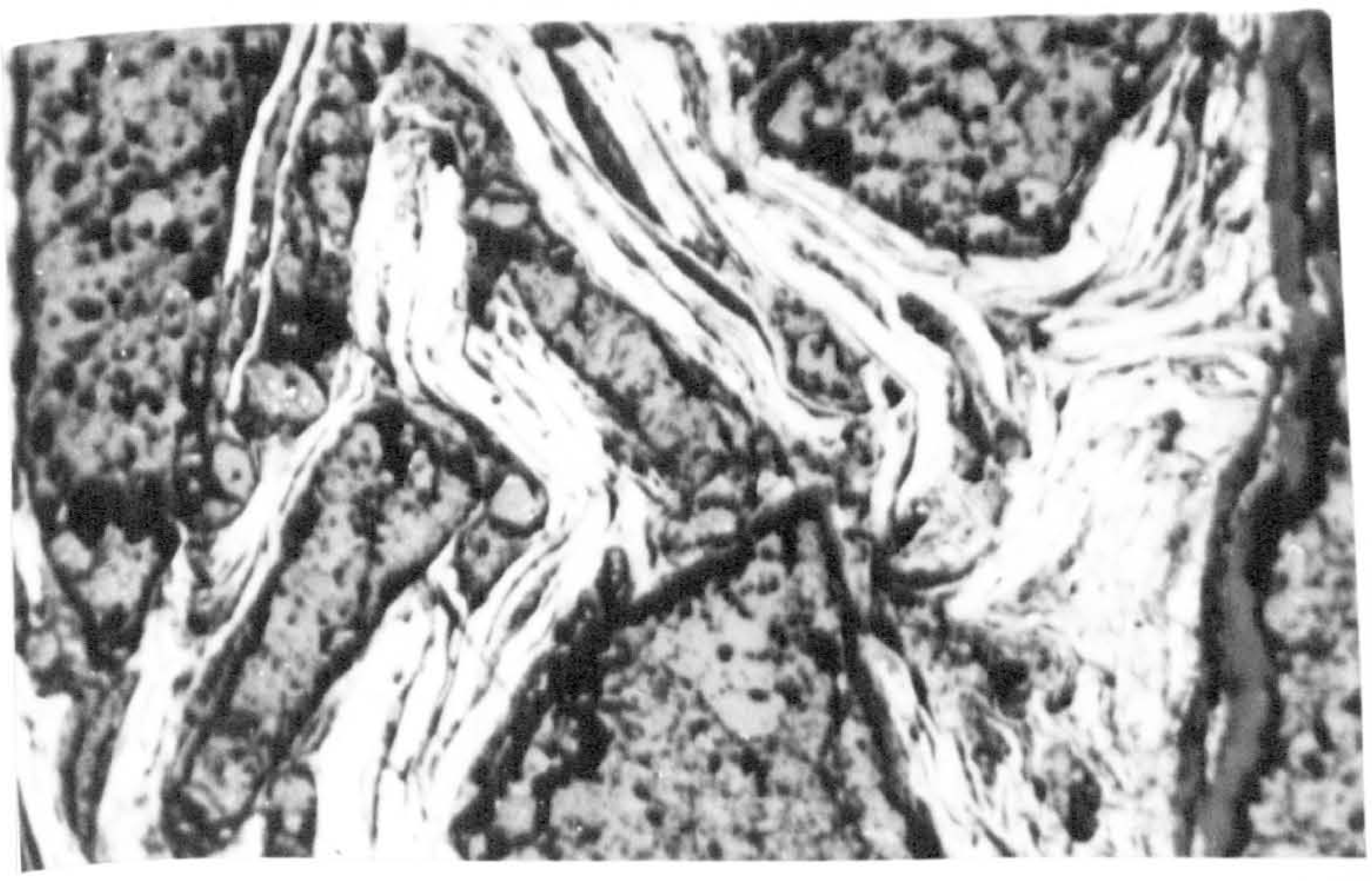

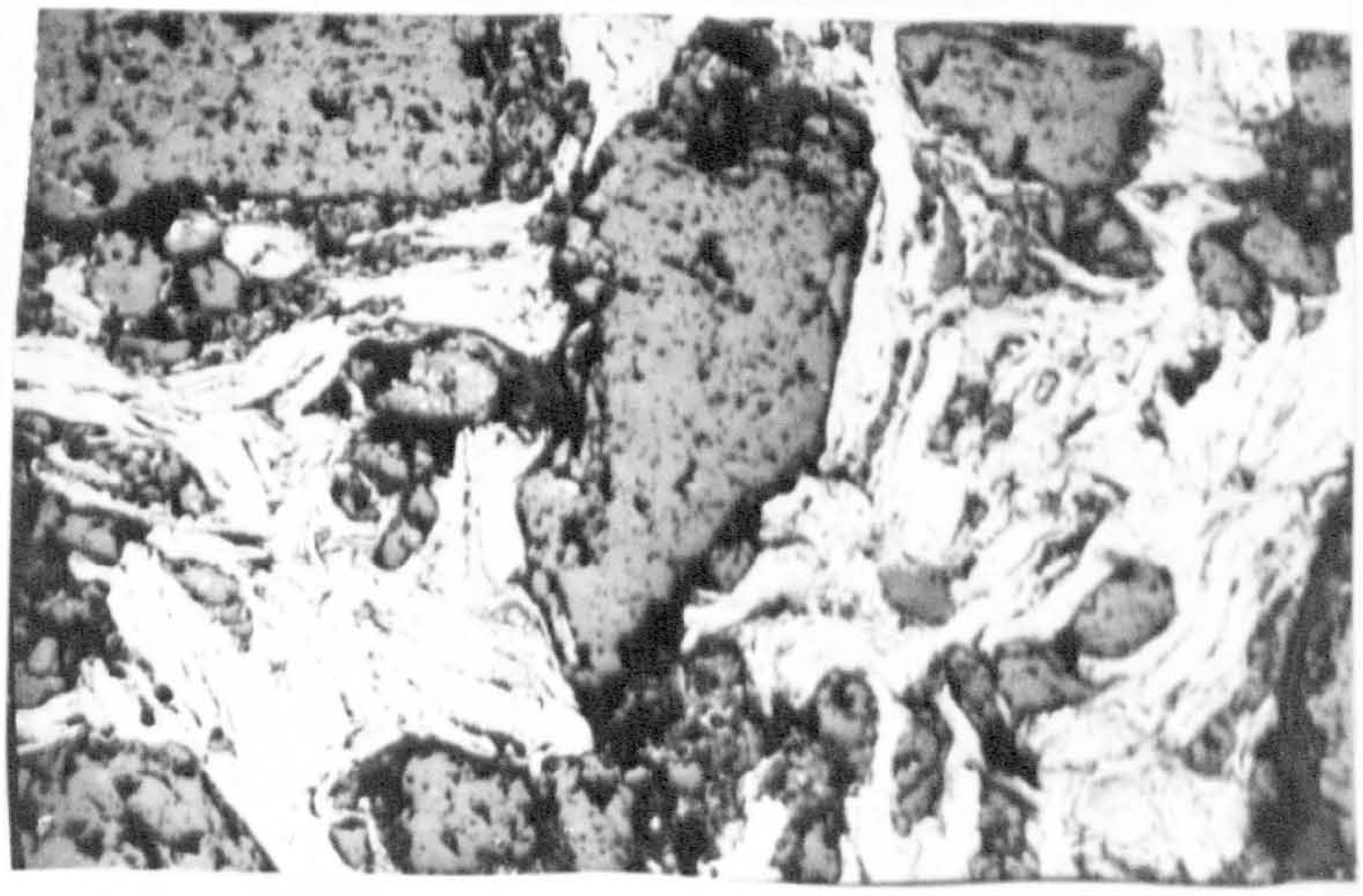

PLATE 5.5.3 iv(a):S.E.M micrograph of fractured specimen showing an unbonded graphite flake to the surrounding magnesia matrix.A gap(crack) between the Mgo grains and the graphite flake can be seen running along the lower part of the flake.Furthermore there is no evidence of a ceramic bond between Mgo-Mgo grains

MAGNIFICATION = 890x

PLATE 5.5.3 iv(b): This is another field of view of the same composite shown in Plate 5.5.3 iv(a) illustrating the lack of bonding between the Mgo-Mgo grains when covered in pitch coke as the case here.

MAGNIFICATION = 222x

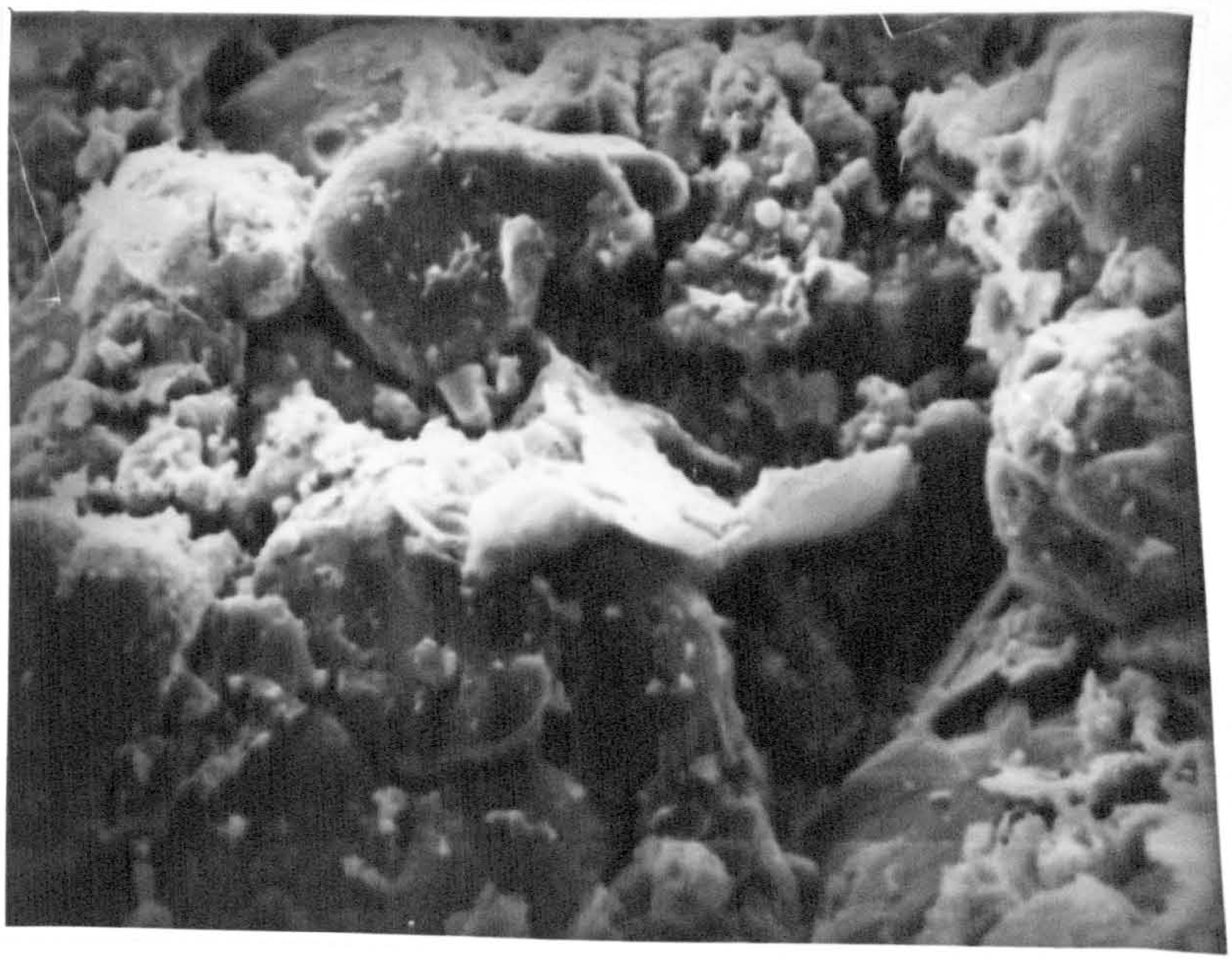

PLATE 5.5.5 i(a): Photomicrograph of a composite containing 70 parts Mgo + 30 parts graphite A + 5 parts pitch at n=0.3. Although the fine magnesia still separates the graphite flakes, the graphite-graphite contacts have increased than has been the case in the previous micrographs shown so far at the same n-value.

MAGNIFICATION = 84x

PLATE 5.5.5 i(b): This micrograph shows the texture of the same composite indicated in Plate 5.5.5 i(a) but prepared at n=0.5. The number of the graphite-graphite contacts is higher than that shown in Plate 5.5.5 i(a).

MAGNIFICATION = 84x

PLATE 5.5.5 i(c): The microstructural texture shown here is that of the composite reported in Plate 5.5.5 i(a) but at n=0.7. In this micrograph, the graphite is the continuous matrix although the graphite content has remained the same.

MAGNIFICATION = 84x

PLATE 5.5.5 i(d): The composite shown here is the same as that indicated above but at n=1.0. The graphite now appears to be the dominant phase and has become continuous.

MAGNIFICATION = 84x

N.B PLATES 5.5.5 i(a - d) show surfaces perpendicular to the pressing direction only.

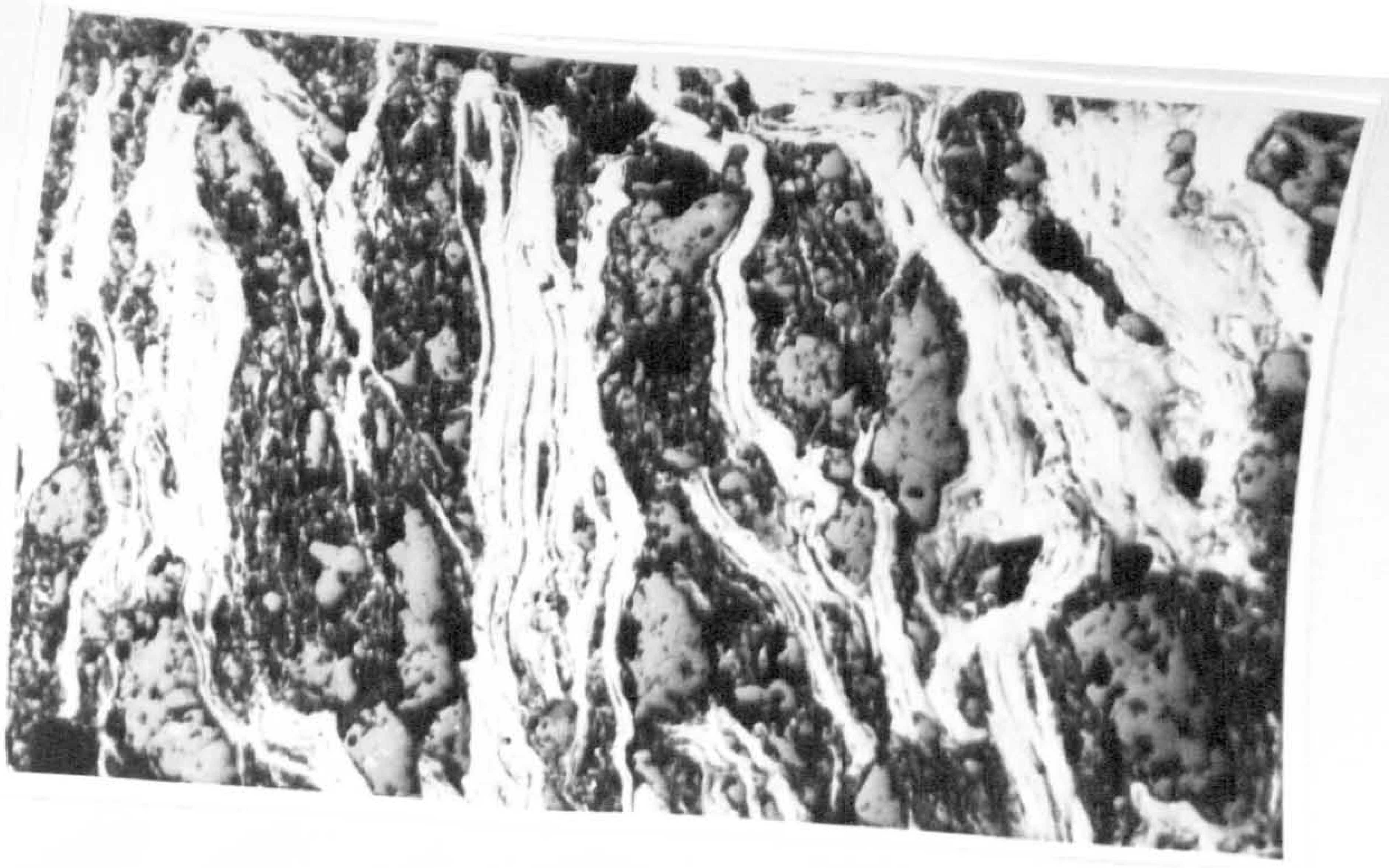

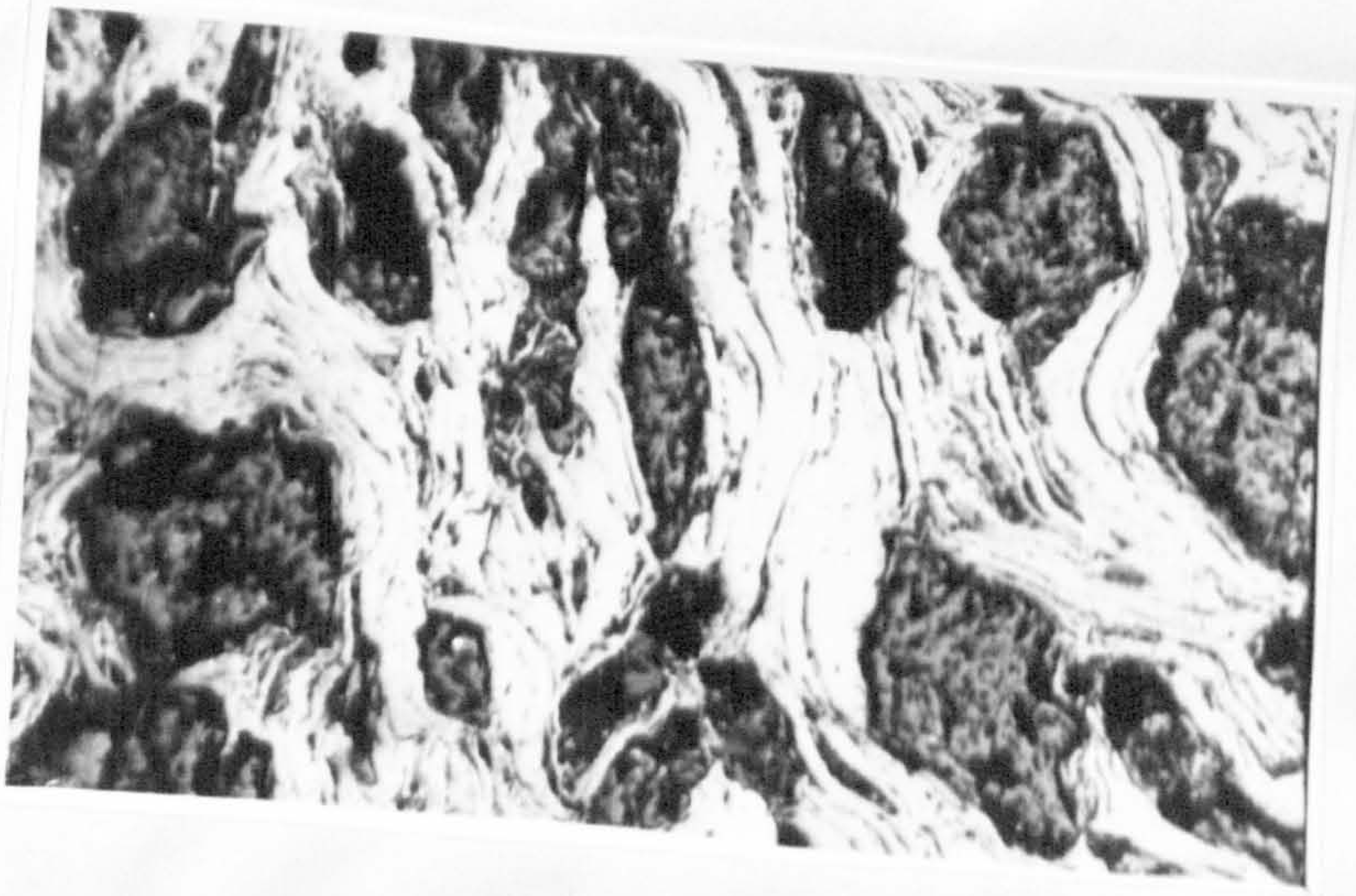

PLATE 5.5.6 (i): S.E.M micrograph showing a tortuous crack round Mgo grains after fracturing a composite specimen containing 80 parts Mgo + 20 parts graphite A + 5 parts pitch.
MAGNIFICATION = 28x

PLATE 5.5.6 (ii): This S.E.M micrograph shows the area encircled in Plate 5.5.6(i) at a higher magnification. The Plate shows some of the flakes which pulled out during fracture.
MAGNIFICATION = 222x

PLATE 5.5.6 (iii): This Plate shows the same field of view as that shown in Plate 5.5.6(ii), boxed, but at a higher magnification. A flake is in the process of being pulled out from the other flakes(a typical example of a flake slipping off).
MAGNIFICATION = 445x

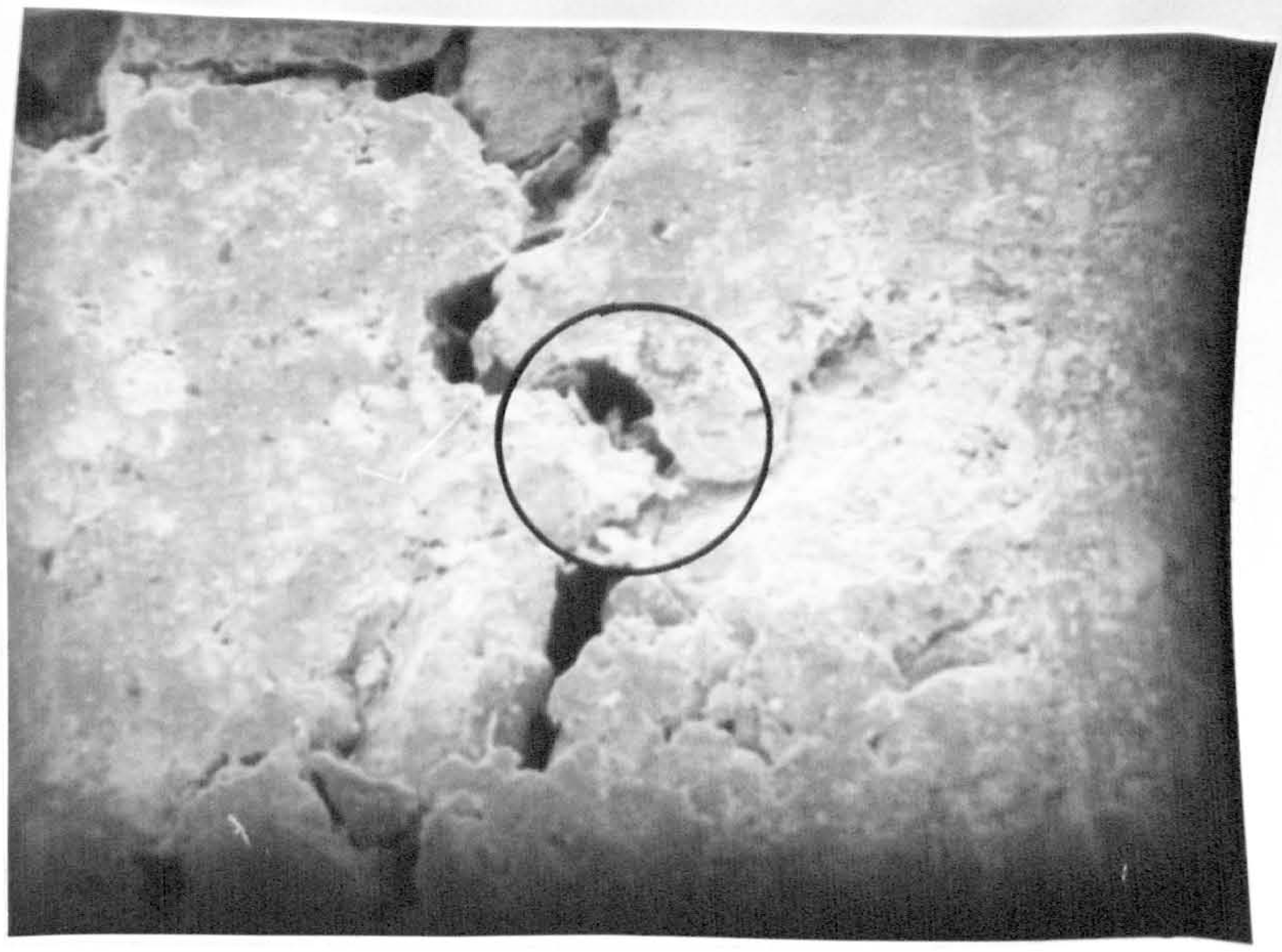

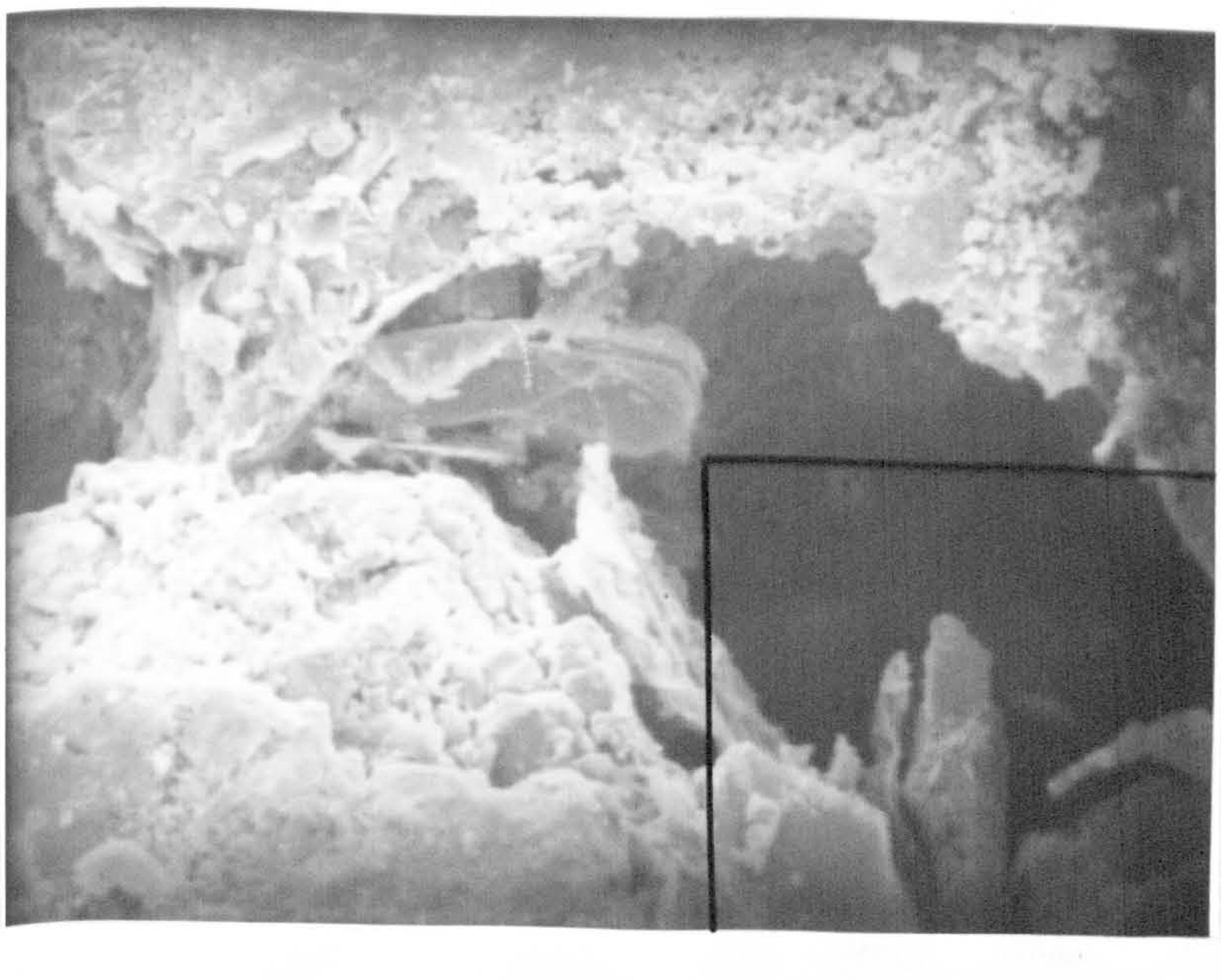

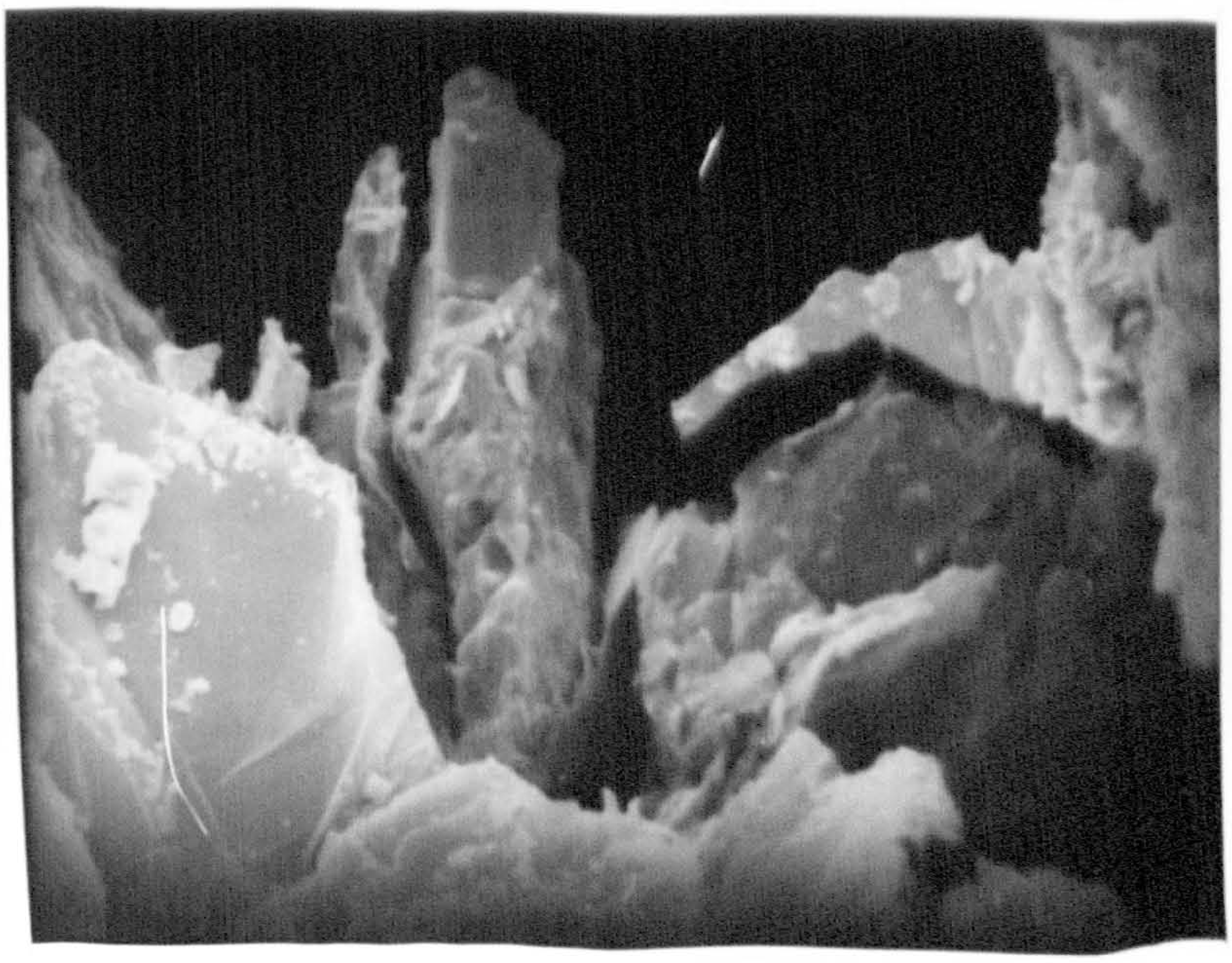

PLATE 5.5.10 i(a):S.E.M micrograph of a fractured surface of a fired composite specimen containing 80 parts Mgo + 20 parts graphite A + 5 parts pitch + 5 parts aluminium metal in the green state.The micrograph shows the aluminium nitride (ALN),the fibrous phase and aluminium carbide (AL_4C_3), the roundish phase.

MAGNIFICATION = 3475x

PLATE 5.5.10 ii(a):S.E.M micrograph of a fractured surface of a fired composite specimen containing 80 parts Mgo + 20 parts graphite A + 5 parts pitch + 5 parts silicon metal in the green state.The micrograph shows the silicon nitride (Si_3N_4),the fibrous phase which is similar to ALN and silicon carbide (SiC),the roundish phase.

MAGNIFICATION = 3475x

PLATE 5.5.10 ii(b): S.E.M micrograph showing cubes of silicon carbide on a graphite flake.This composite contained 11 parts silicon metal in the green state and the other components were the same and of equal amounts as indicated in Plate 5.5.10 iii(a)

MAGNIFICATION = 3475x

PLATE 5.5.10 (iv): A photograph of two fractured fired specimens containing 80 parts Mgo + 20 parts graphite A + 5 parts pitch + 5 parts metal in the green state. The fractured specimens were left in the oven at 60°C for about a week.The specimen containing aluminium (No 1) disintegrated because of moisture hydration by AL_4C_3.Specimen No 2 containing Si was unaffected.

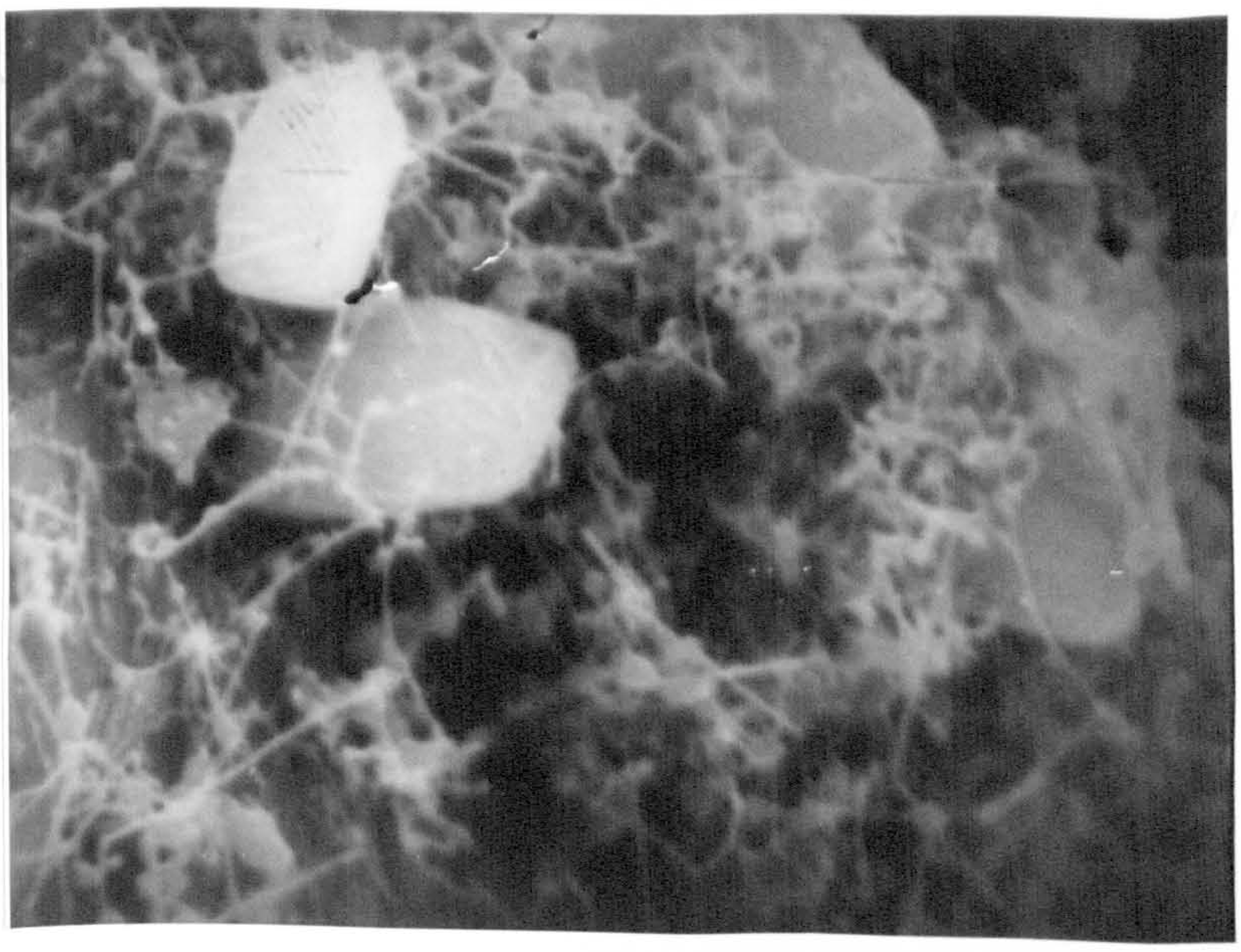

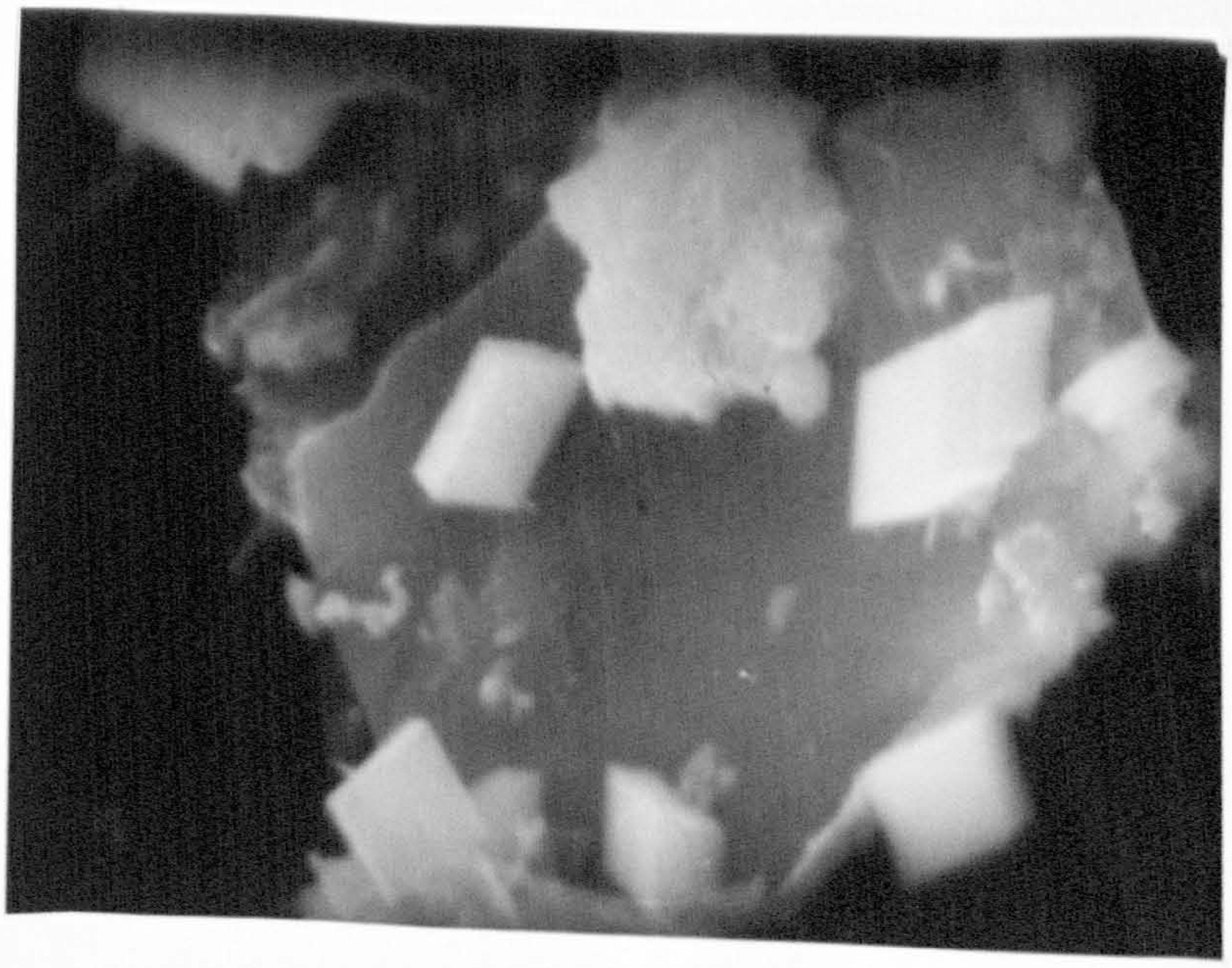

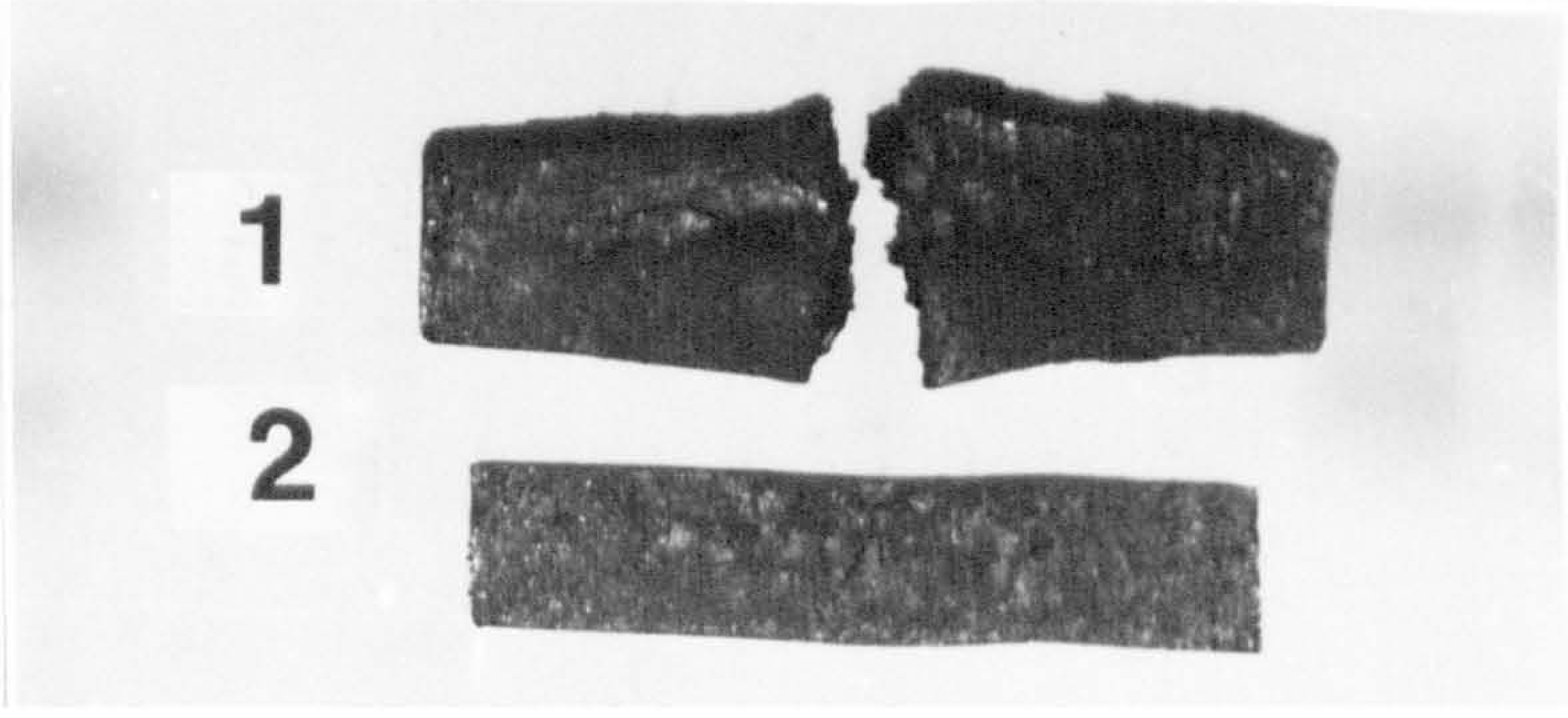
1
2

PLATE 6.2.4 : Photograph of slagged specimens, 1 & 2 reacted at 1500 and 1650 C respectively in non-oxidizing atmosphere. Specimens 1(b) and 2(b) show the depth of slag penetration (visual inspection), while 1(a) and 2(a) show how the slag has covered the top part of the specimens after firing. The slag may have risen to the top by capillary suction.

These specimens were prepared by using Method 3 at n=1.0 and contained 80 parts Mgo + 20 parts graphite A + 5 parts pitch in the green state.

MAGNIFICATION = 1x

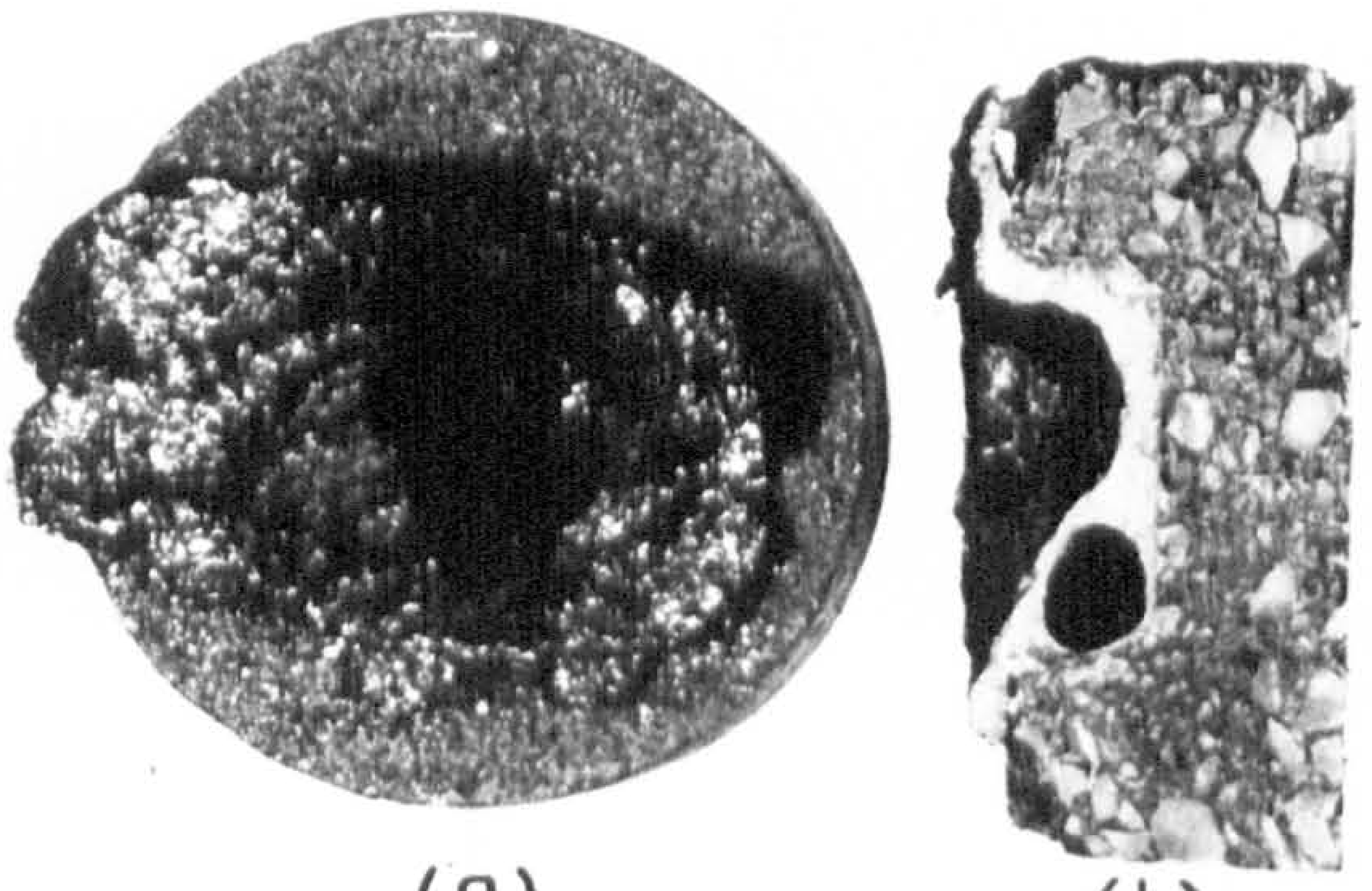

(a) (b)

1

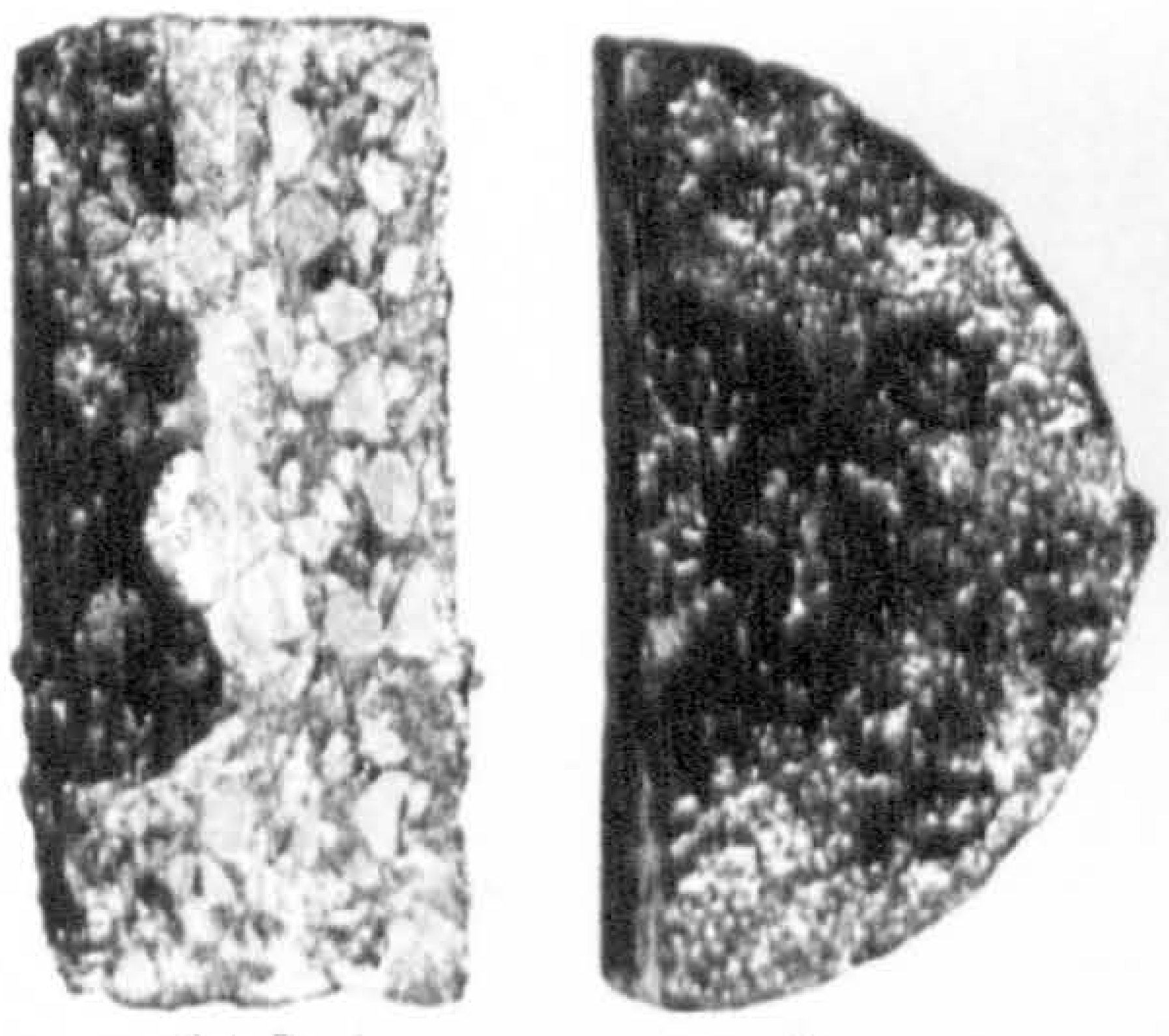

(b) (a)

2

PLATE 6.3.1 i(a): Photomicrograph showing a heavily reacted magnesia/slag interface after a reaction test at 1500°C in non-oxidizing atmosphere.

The specimen was made of magnesia grain mixture only at n=0.3. The fine magnesia grains can be seen floating in the slag.

MAGNIFICATION = 84x

PLATE 6.3.1 i(b): Photomicrograph showing a heavily reacted magnesia/slag interface after a reaction test at 1500 C in non-oxidizing atmosphere. The specimen was made of magnesia grain mixture only at n=1.0. A slag/specimen interface is clearly visible. The extent of slag attack is less in this micrograph than in 6.3.1 i(a) because larger Mgo grains do not dissolve easily in the slag.

The white globules are reduced iron oxides to metal(Fe), while the dendritic phase(slag) is a mixture of phases, such as monticellite, gehlemite, di-calcium ferrite, etc(see section 6.3.1).

MAGNIFICATION = 84x

PLATE 6.3.1 i(c): This micrograph shows the specimen/slag interface after a reaction test at 1500°C. The specimen was made of 100 parts Mgo + 5 parts pitch at n=0.3. From this micrograph it would seem that the slag resistance has improved(compare this to Plate 6.3.1 i(a))

PLATE 6.3.1 i(d): A photomicrograph illustrating the vulnerability of Mgo specimens even though containing a small amount of pitch. The slag easily penetrates between the large Mgo grain boundaries, corrodes the fine grains and eventually loosens the structure.

MAGNIFICATION = 84x

N.B: M = Mgo, S= slag, Fe = reduced iron(metal)

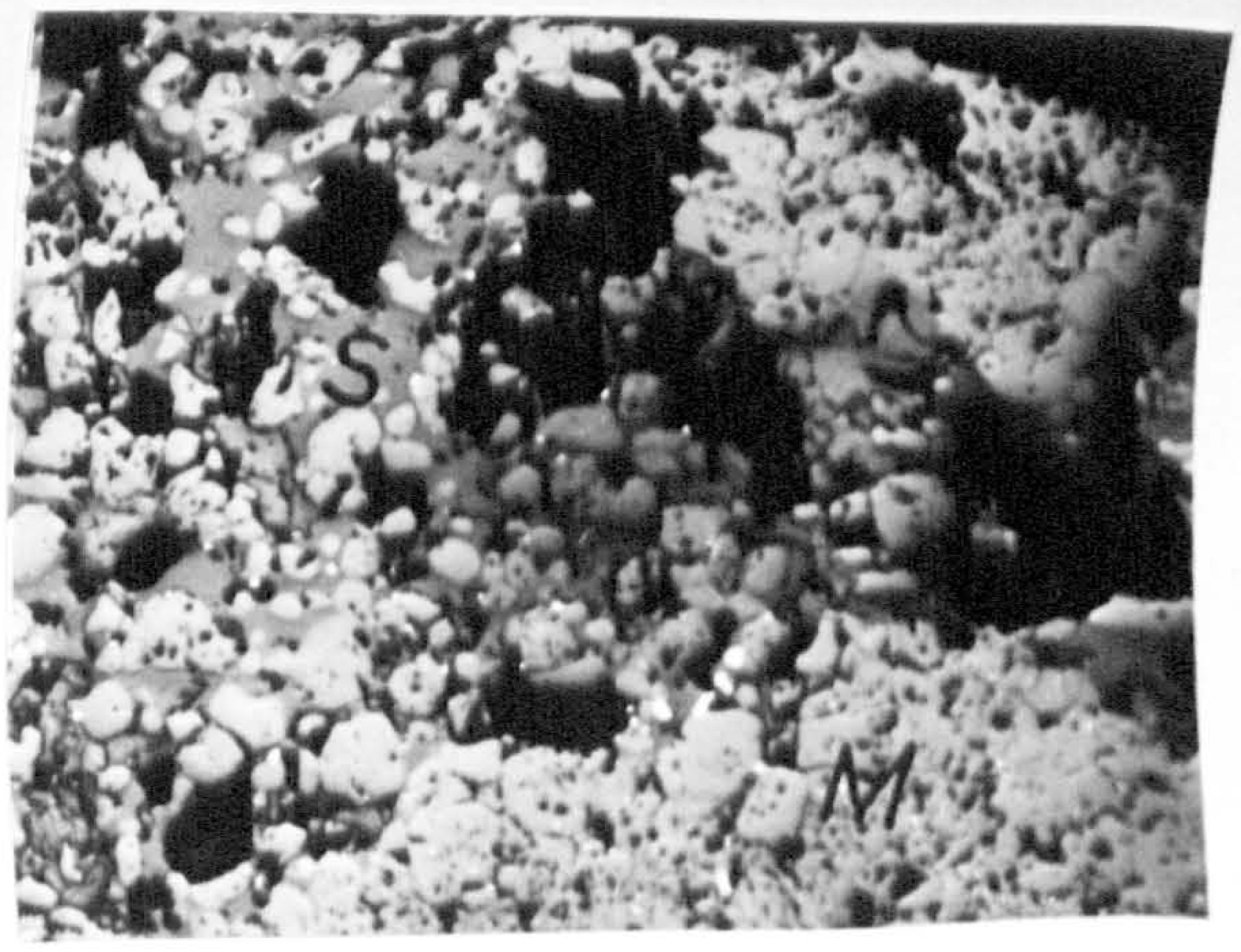
S
M

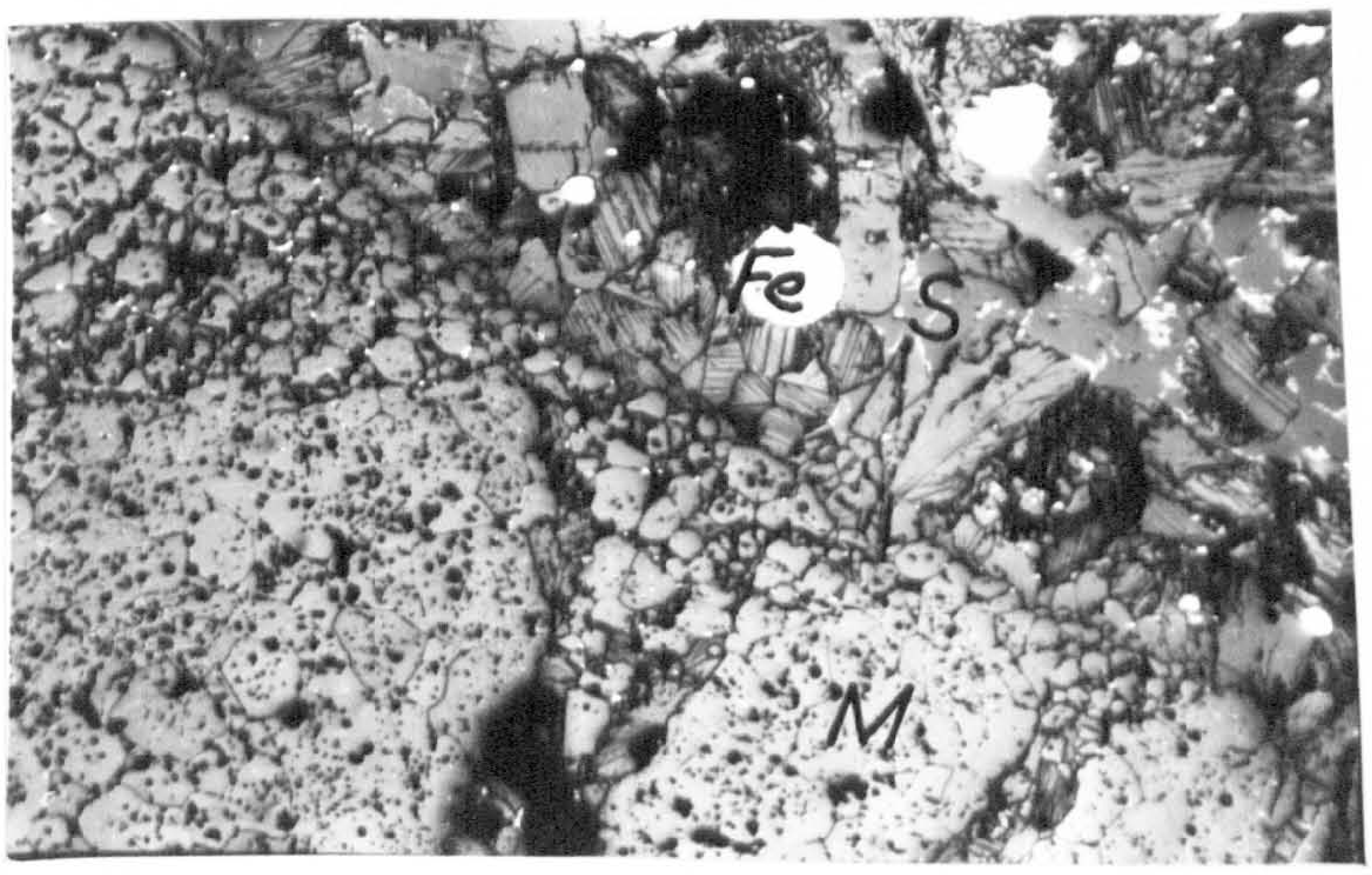
Fe
S
M

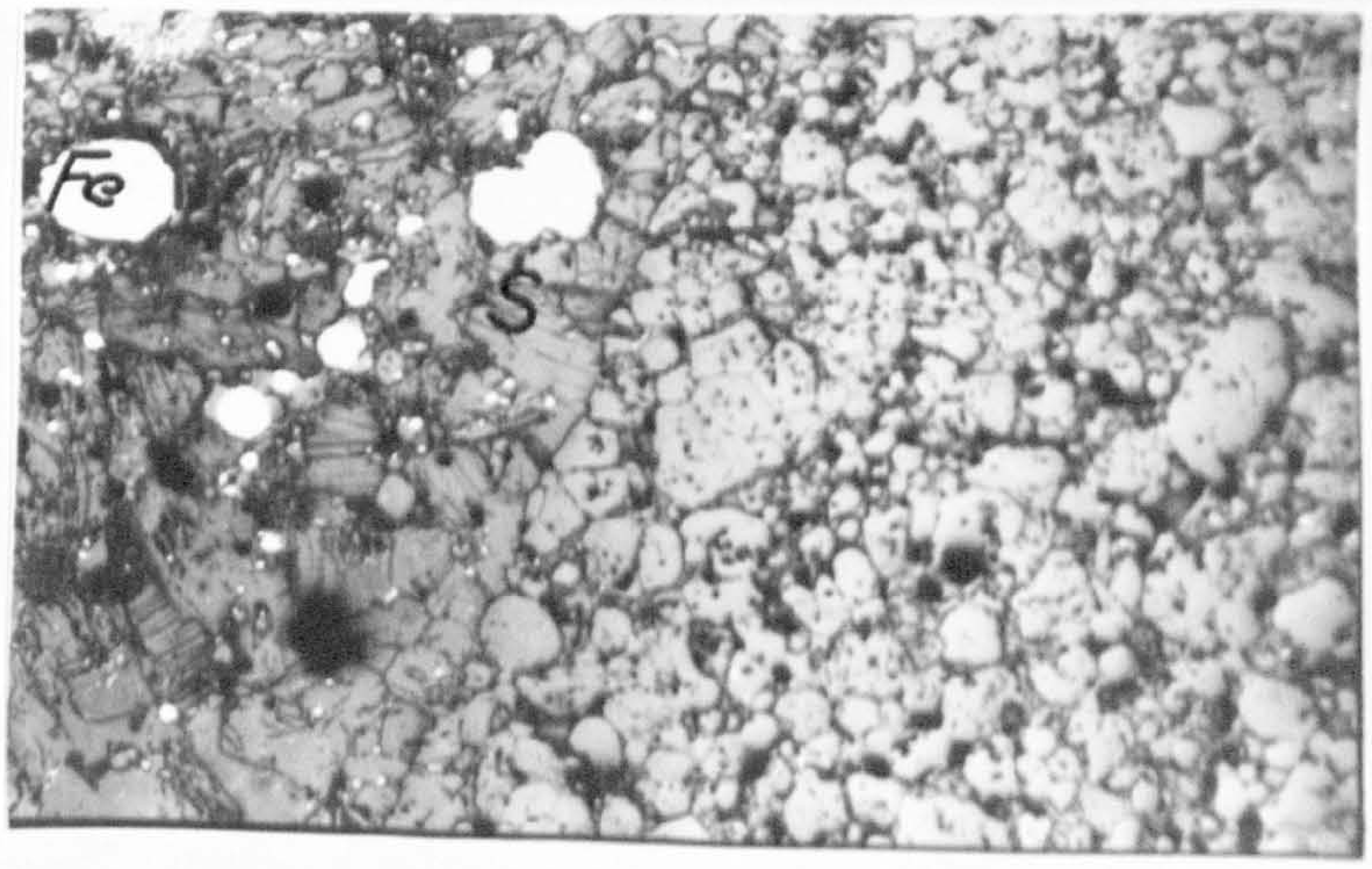
Fe
S

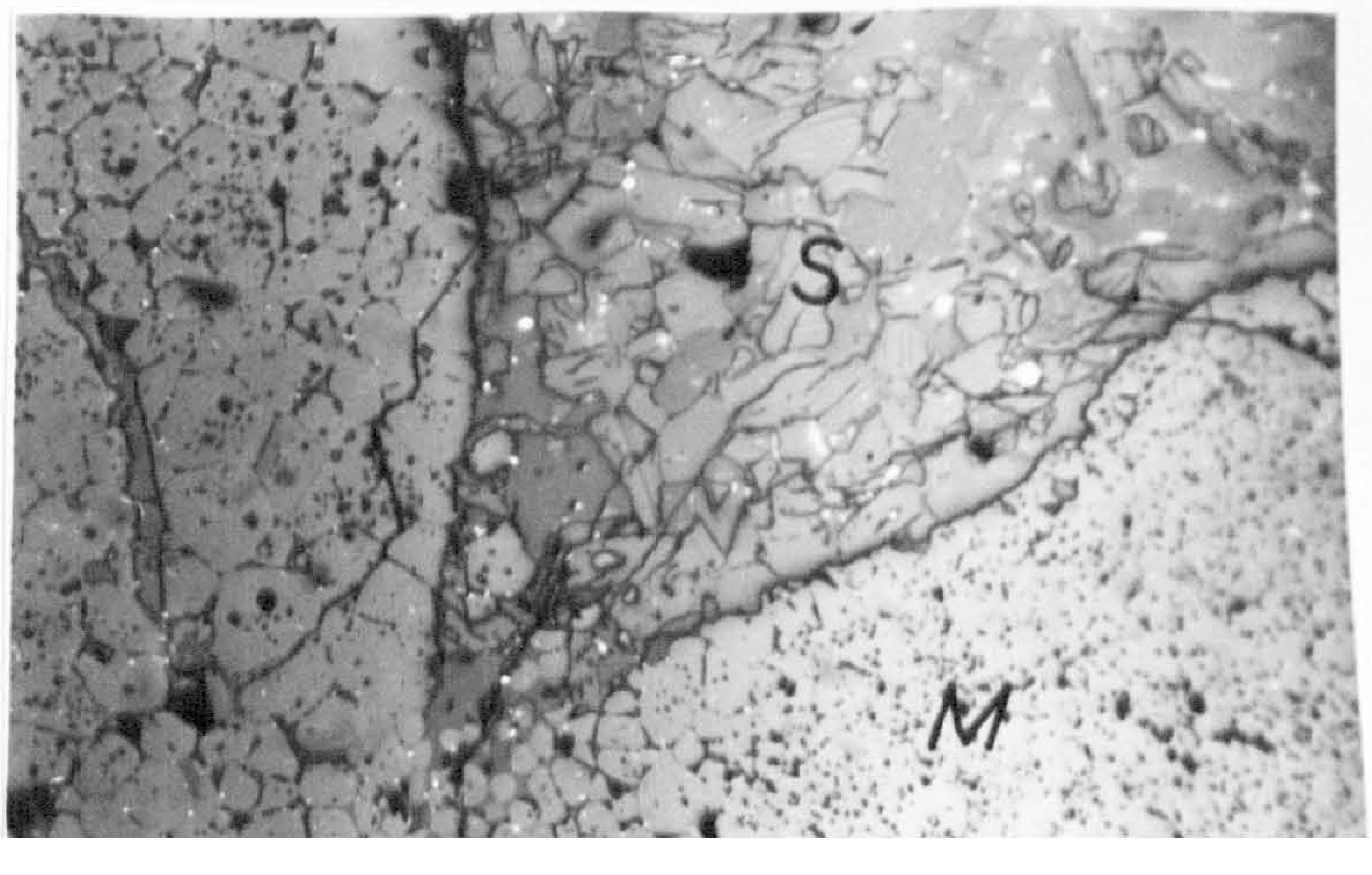
S
M

PLATE 6.3.2 i(a):Photomicrograph showing the slag(s) at the right hand corner of the Plate. The slag has also penetrated down to the bottom right hand corner of the Plate. The magnesia grains are surrounded by the slag. The graphite flakes are so dispersed that they cannot effectively hinder slag penetration.

This specimen contained 80 parts Mgo+ 20 parts graphite D + 5 parts pitch in the green state(n=0.3).

MAGNIFICATION = 84x

PLATE 6.3.2 i(b):This shows the field of view marked in Plate 6.3.2 i(a) above but at a higher mag. The slag(S) can be seen surrounding most of the Mgo grains(M).

MAGNIFICATION = 167x

PLATE 6.3.2 i(c):The microstructure of the composite indicated in Plate 6.3.2 i(a) but prepared at n=1.0. The test was carried out at 1500°C. The slag(S) has not penetrated below the area it is sitting on because of the graphite which it cannot wet.

MAGNIFICATION = 84x

PLATE 6.3.2 i(d):This micrograph emphasizes the increased amount of iron reduced(Fe) in composites containing graphites as opposed to small globules observed in Mgo or Mgo + pitch specimens.

MAGNIFICATION = 84x


Fe
S
M
G

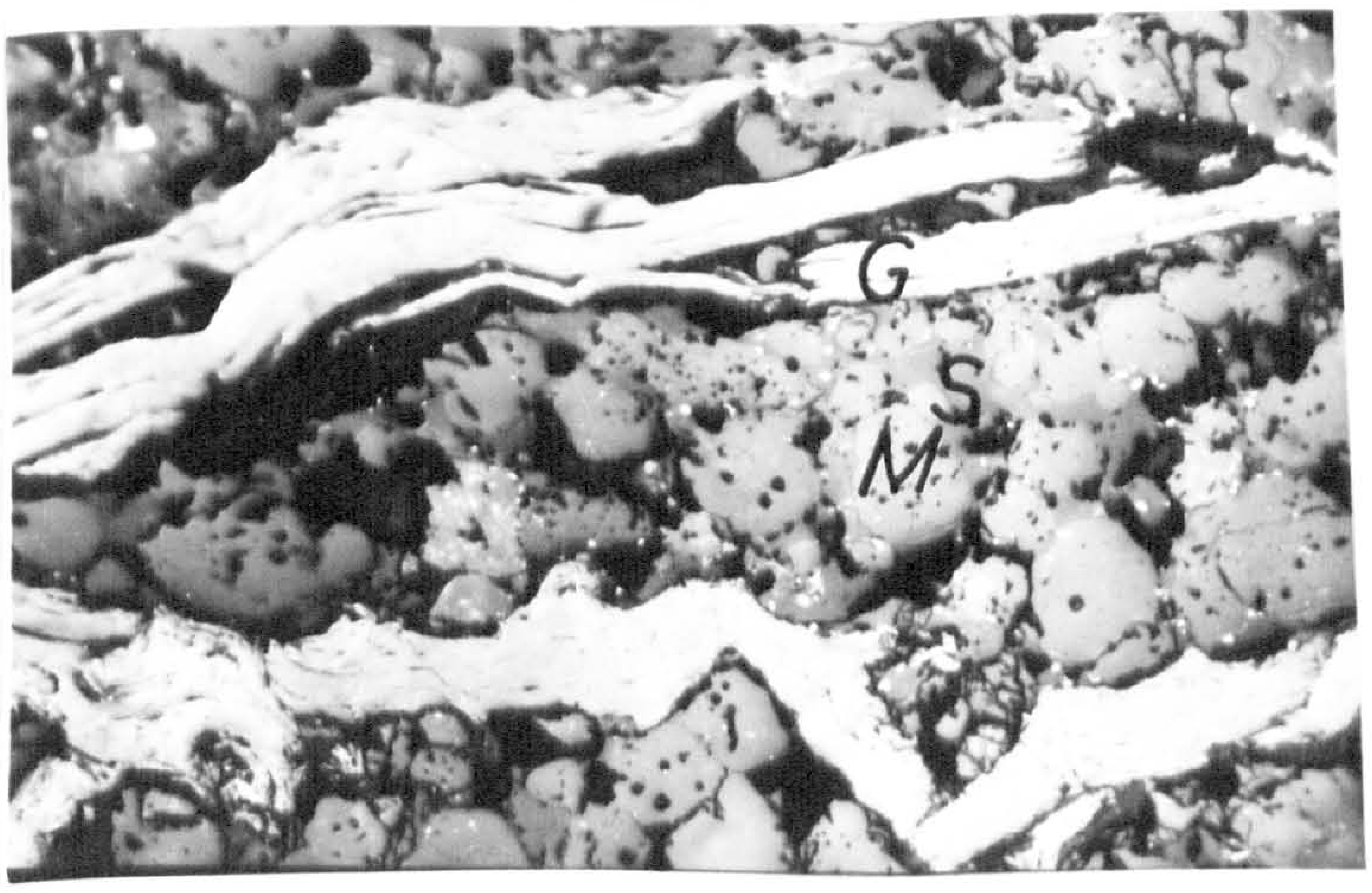
G
S
M

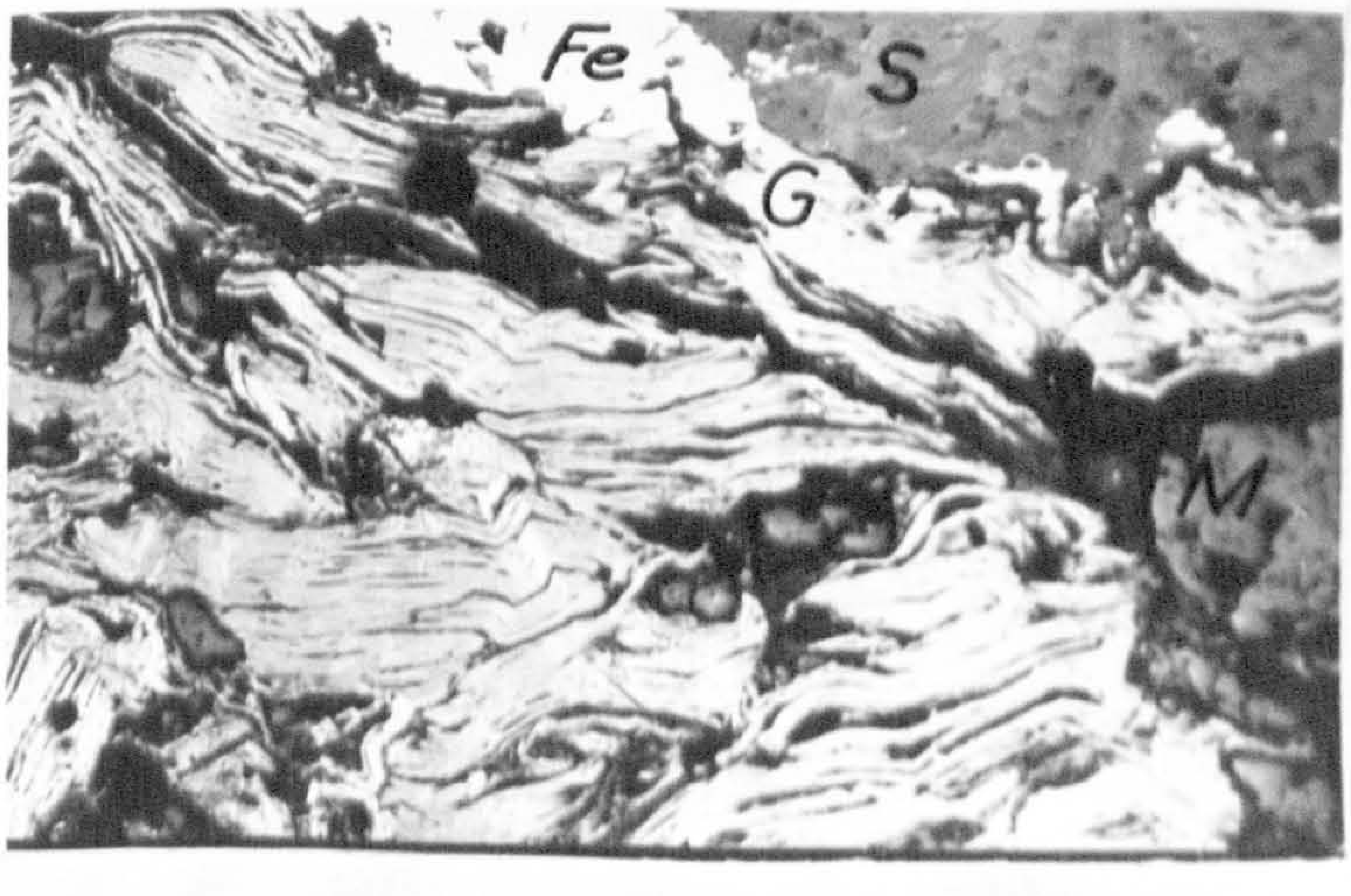
Fe
S
G
M


S
Fe
G
M

PLATE 6.3.2 i(e): This photomicrograph demonstrates the physical blocking of slag infiltration into the specimen by the graphite. The graphite has occupied the the space between two large Mgo grains, and since the slag does not wet the graphite it cannot penetrate between the Mgo grains as it has done in specimens without graphite (see Plate 6.3.1 i(d)). This specimen contained about 20% graphite C (n=1.0).

MAGNIFICATION = 84x

PLATE 6.3.3 (i): This micrograph illustrates the extent of the reaction at the specimen/slag interface after a reaction test at 1650°C in a non-oxidizing atmosphere. The graphite flake(G) seems to be in contact with both the slag(S) and iron(Fe).

The specimen contained 80 parts Mgo + 20 parts graphite M + 5 parts pitch.

MAGNIFICATION = 84x

PLATE 6.3.3 ii(a): This plate shows a field of view about 1mm below the bottom left hand corner of Plate 6.3.3 (i).

This plate shows that the slag did not penetrate deep into the specimen as would have been expected if the specimen did not contain graphite, although the slag/specimen interface (Plate 6.3.3(i)) shows an extensive reaction. The encircled area in this Plate shows the presence of liquid phase but only between the the Mgo grains as would be expected at such high temperatures (1650°C).

MAGNIFICATION = 84x

PLATE 6.3.3 ii(b): This is the same graphite flake shown in Plate 6.3.3(i), but at a higher magnification and reinforces the point that the slag(S) and iron(Fe) are physically in contact with the flake(G). The iron is always between the slag and the specimen because it has a higher density than the slag and therefore it sinks to the bottom of the slag as expected.

MAGNIFICATION = 167x

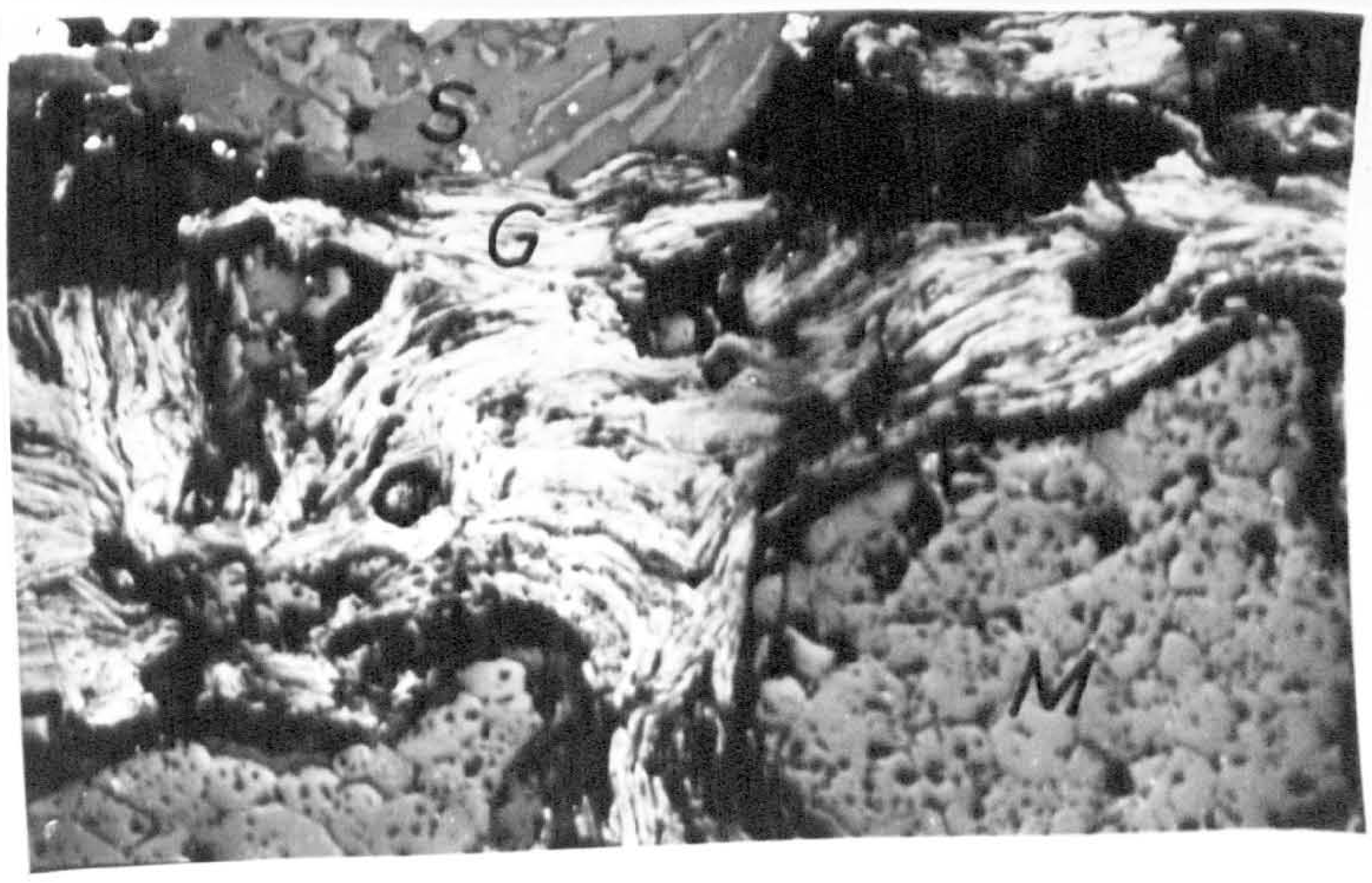
S
G
M

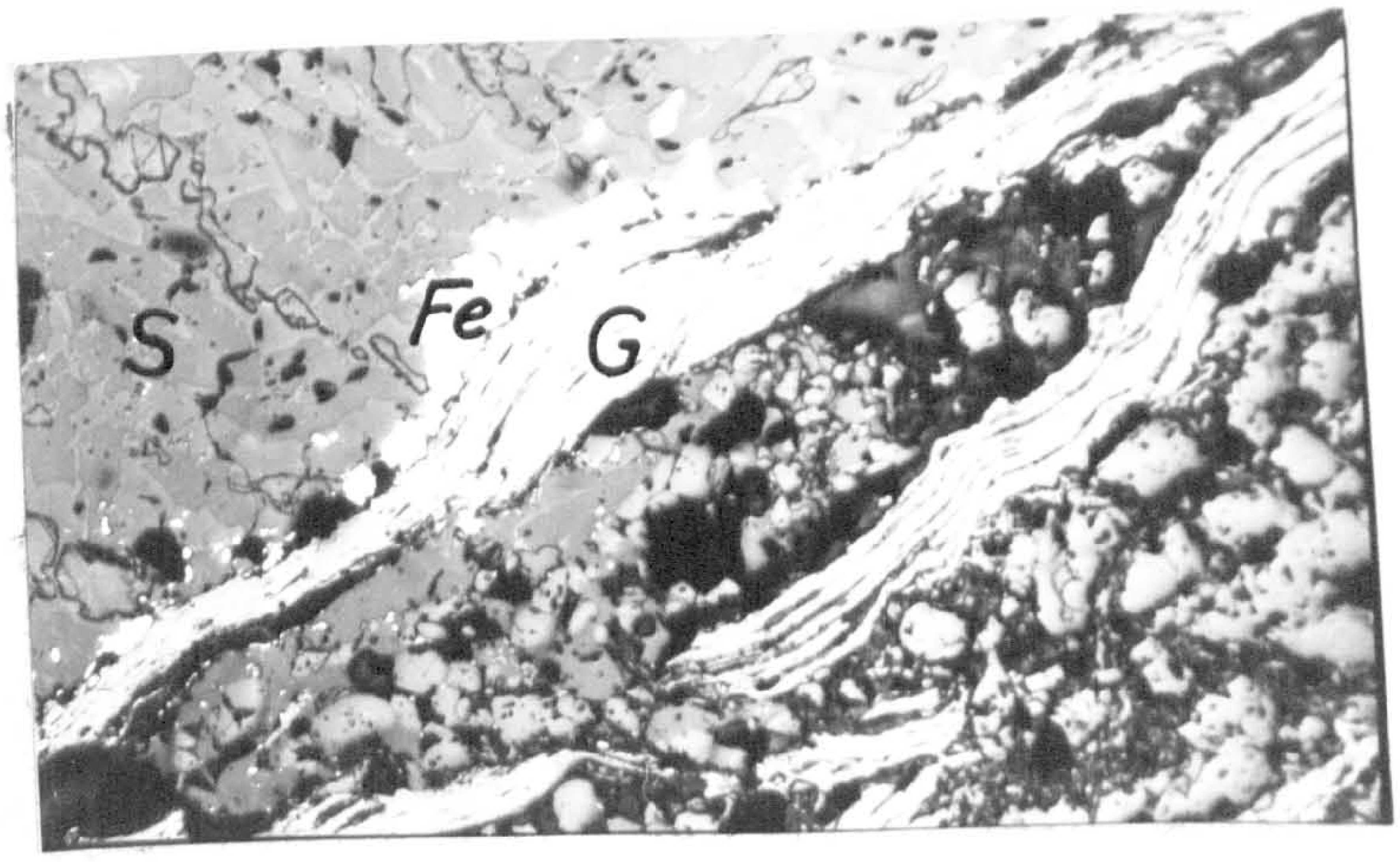
S
Fe
G

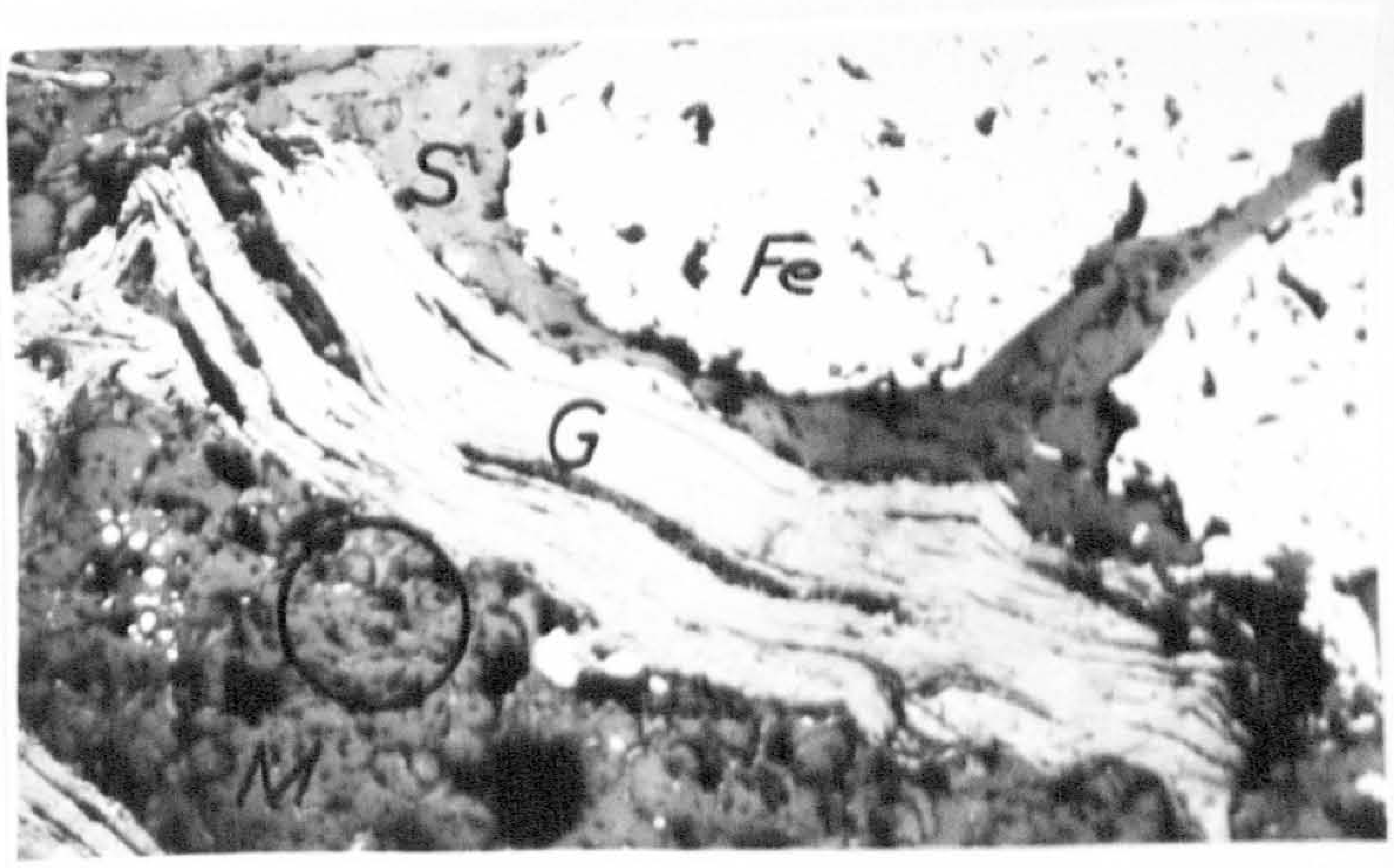
S
Fe
G
M

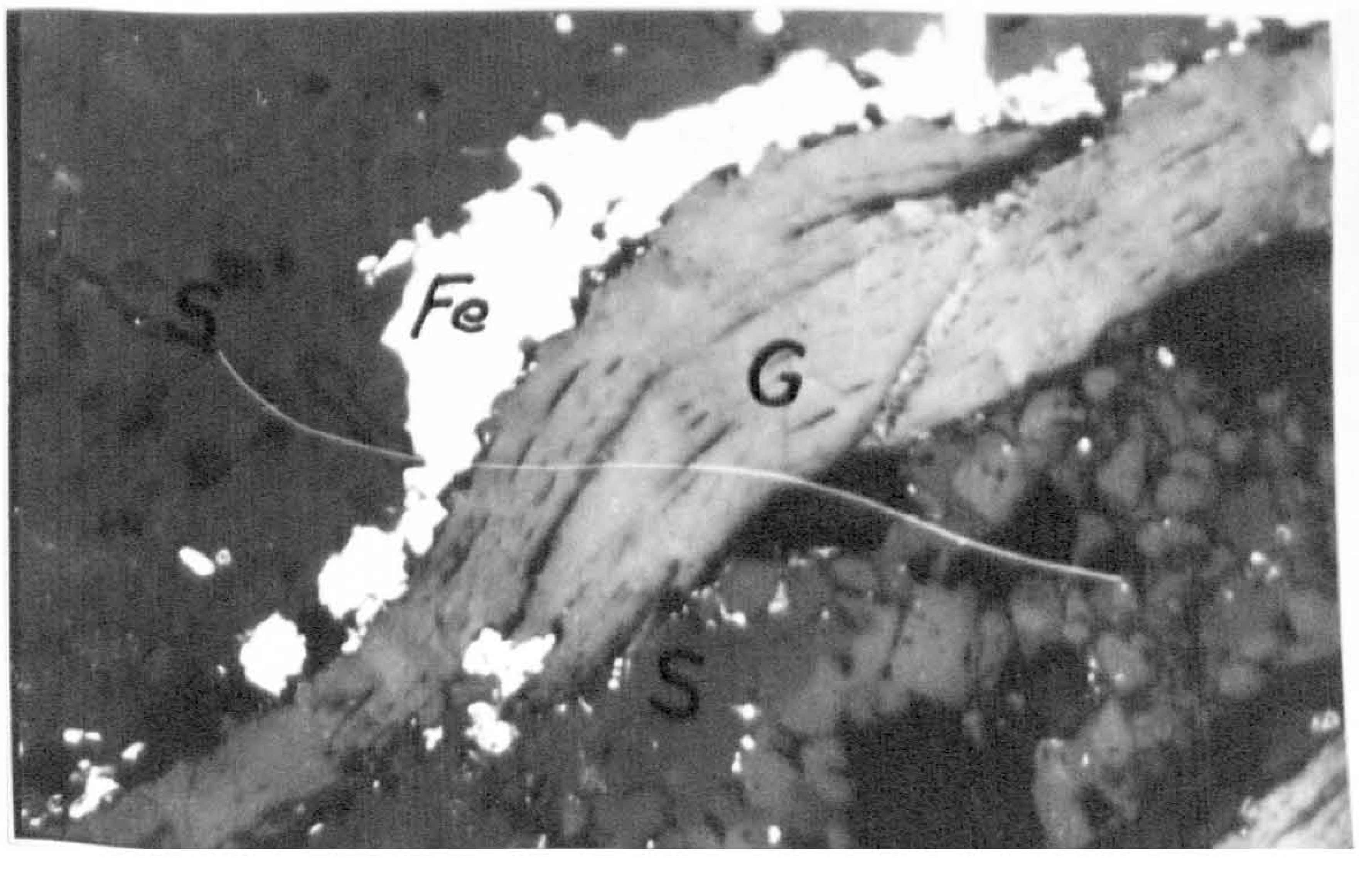
S
Fe
G
S

PLATE 6.3.3 (iii): A photomicrograph showing how the slag has penetrated in-between the interlaminar cracks of a flake. The encircled area shows a globule of iron, while the boxed area shows a slag which has solidified and has conformed to the shape of the crack.

MAGNIFICATION = 167x

PLATE 6.3.3 (iv): This micrograph again shows a graphite flake in the slag(S). The Mgo grains(M) are also shown floating in the slag.

MAGNIFICATION = 167x

PLATE 6.3.3 (v): A micrograph showing a slag/specimen interface reaction after a reaction test at 1650°C. The specimen contained 20% graphite M at n=1.0 and other components being the same as those already indicated in other specimens above.

The slag has completely dissolved the Mgo leaving the graphite flakes floating in the slag.

MAGNIFICATION = 84x

PLATE 6.3.3 (vi): This photomicrograph is a field of view about 1mm below a field of view of Plate 6.3.3(v). The significant thing about this micrograph is that there is no evidence of the slag being present anywhere. The implication being that the slag was able to corrode only a fraction of a millimetre of the specimen from the interface; because at n=1.0 the graphite is the continuous phase, therefore inhibiting slag penetration by its non-wetting behaviour.

MAGNIFICATION = 84x

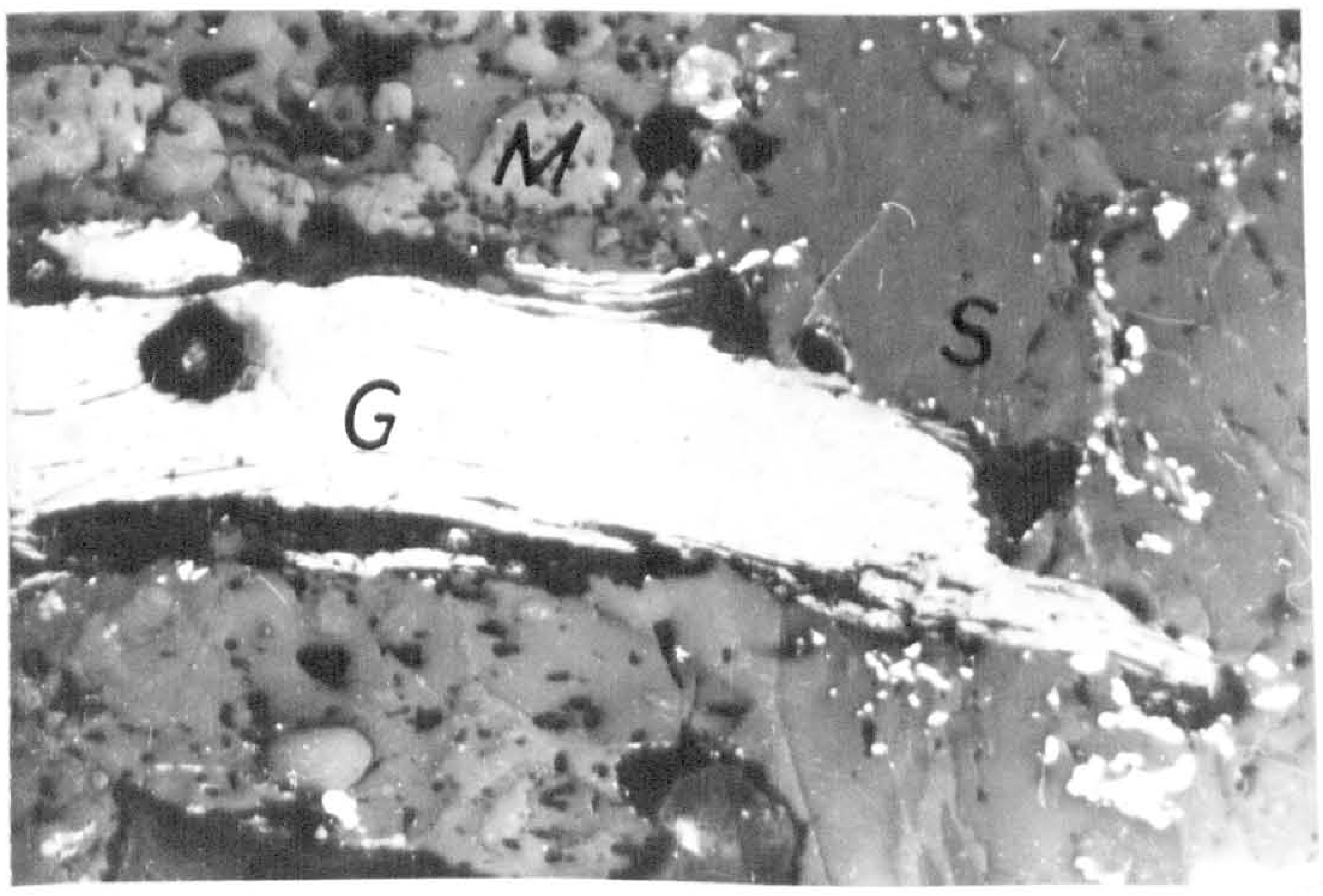
M
S
G


G
S

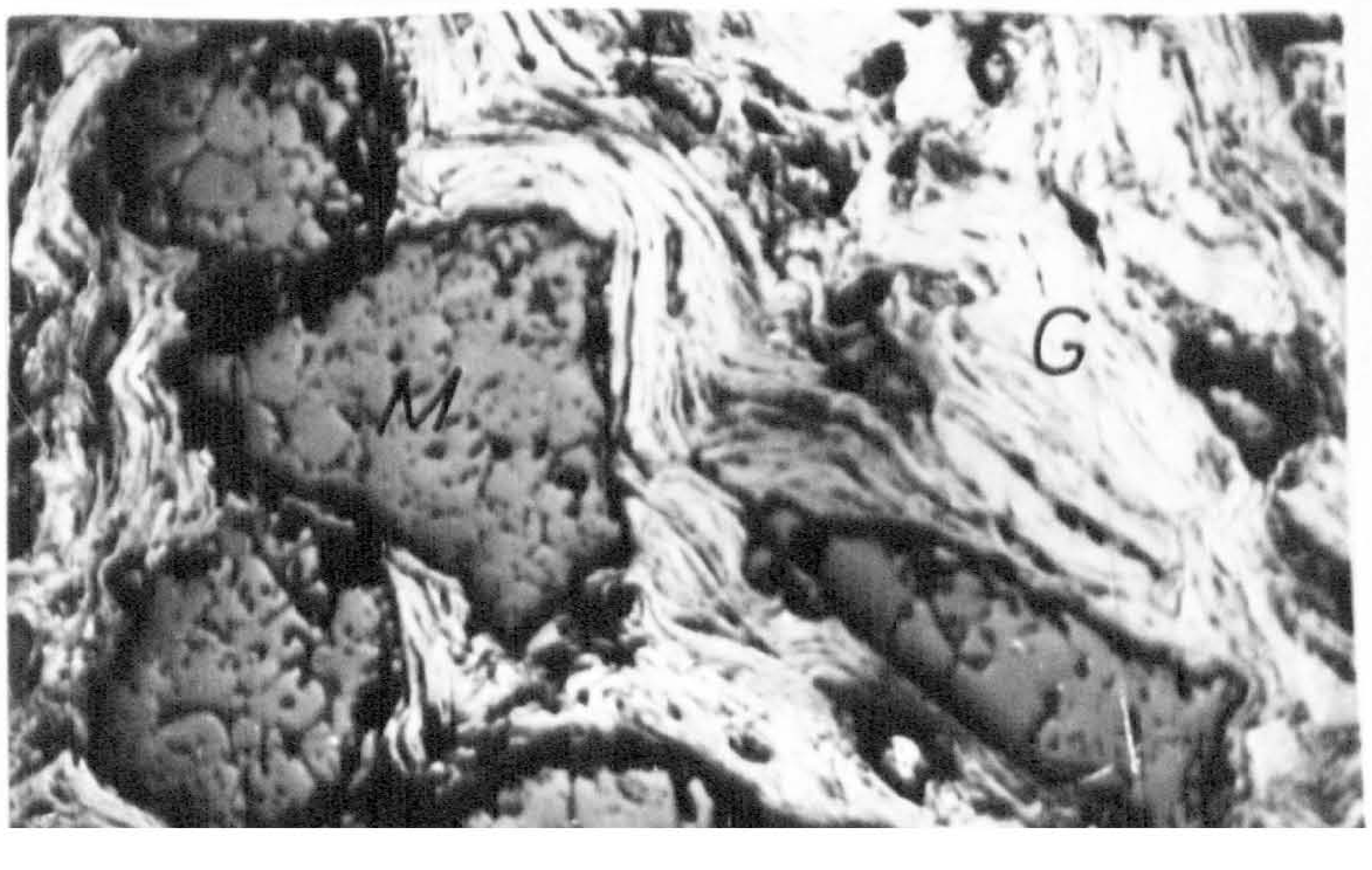
M
G

PLATE 6.3.3 (vii):This S.E.M micrograph shows the slag(S)/specimen boundary after a reaction test at 1650°C.The specimen contained 80 parts Mgo + 20 parts graphite A + 5 parts pitch in the green state at n=0.3.The boundary indicates lack of slag penetration into the specimen.

MAGNIFICATION = 14x

PLATE 6.3.3 (Viii):The same field of view as that shown Plate 6.3.3(vii) where the two lines cross, but at a higher magnification. The micrograph again illustrates the physical contact between the slag(S) and the graphite flake(G) at room temperature,at least,after firing.

MAGNIFICATION = 222x

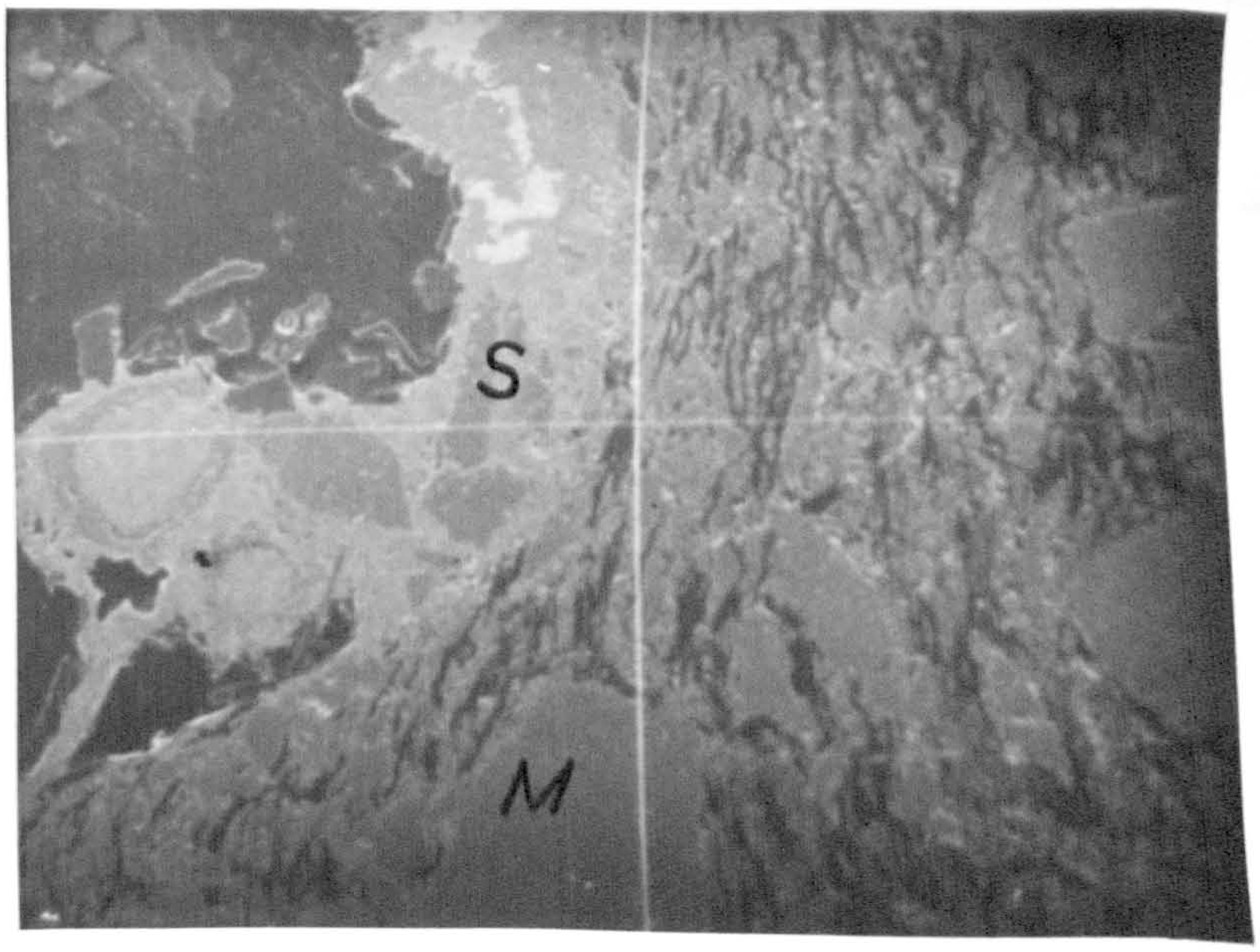
S
M

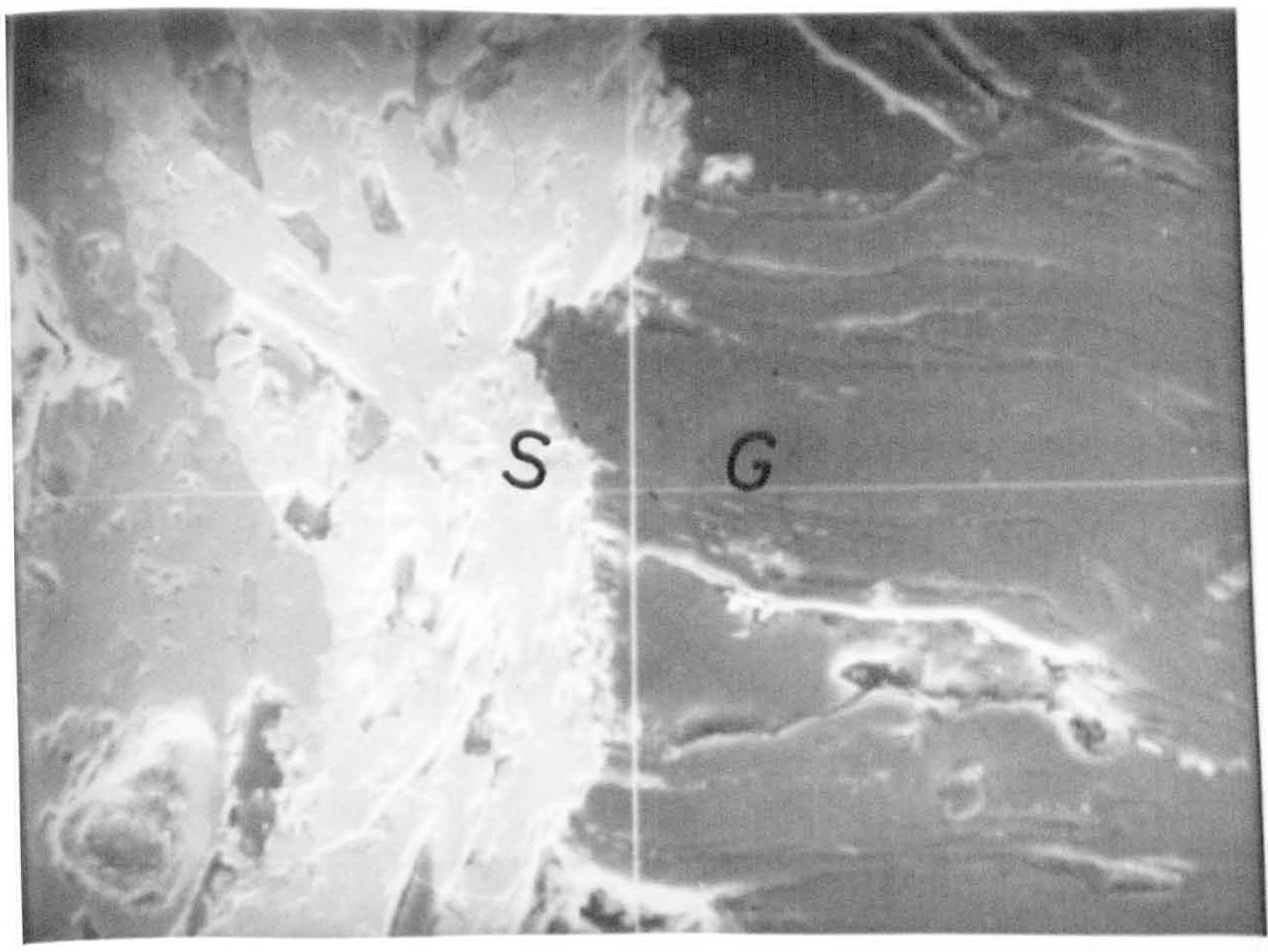
S
G